약학박사 학위논문

Structural and Biophysical Analyses of Aspartyl-tRNA Synthetase from *Homo sapiens* and Triosephosphate Isomerase from *Thermoplasma acidophilum*

Aspartyl-tRNA Synthetase와 Triosephosphate Isomerase의 구조 및 생물학적 분석

2016년 2월

서울대학교 대학원

약학과 의약생명과학전공

박 상 호

Structural and Biophysical Analyses of Aspartyl-tRNA Synthetase from *Homo sapiens* and Triosephosphate Isomerase from *Thermoplasma acidophilum*

Thesis by

Sang Ho Park

Professor: Byung Woo Han

A Thesis Submitted to the Graduate Faculty of Seoul National University in Partial Fulfillment of the Requirements for the Degree of Doctor of Philosophy

2016

Abstract

Structural and Biophysical Analyses of Aspartyl-tRNA Synthetase from *Homo sapiens* and Triosephosphate Isomerase from *Thermoplasma acidophilum*

Sang Ho Park
College of Pharmacy
The Graduate School
Seoul National University

Human cytosolic aspartyl-tRNA synthetase (DRS) catalyzes the attachment of the aspartic acid to its specific tRNA. DRS is a component of the multi-tRNA synthetase complex (MSC) which has been known to be involved in unanticipated signaling pathways. The crystal structure of DRS has been determined at 2.25 Å resolution containing the anticodon binding domain, hinge region, and catalytic domain. The structure also reveals the C-terminal end of the N-helix which is considered as a unique additional domain of DRS, and its conformation further supports the switching model of the N-helix for the transfer of $tRNA^{Asp}$ to elongation factor 1α. From the analyses of the crystal structure and post-translational modification of DRS, I suggest that the phosphorylation of Ser146 could initiate a conformational change of the DRS dimer and provokes the separation

of DRS from the MSC. This structural study provides the binding site for an interaction partner with unforeseen functions.

Thermoplasma acidophilum is one of the most acidophilic organisms that utilize not only non-phosphorylative Entner-Doudoroff (ED) pathway but also Embden-Meyerhof-Parnas (EMP) pathway for glucose degradation. Triosephosphate isomerase (TPI) is structurally and functionally well-known glycolytic enzyme that plays an important role in glycolytic and gluconeogenic metabolism. Crystal structures of apo- and glycerol-3-phosphate-bound TPI from *T. acidophilum* (TaTPI) have been determined at 1.94 and 2.17 Å resolution. TaTPI adopts the canonical TIM-barrel fold with eight α-helices and parallel eight β-strands. Although TaTPI shares ~30% sequence identity to other TPIs from thermophilic species that adopt tetrameric conformation for enzymatic activity in their harsh physiological environments, TaTPI exists as a dimer in solution. Dimeric conformation of TaTPI was further confirmed by analytical ultracentrifugation and size-exclusion chromatography. Helix 5 and helix 4 regions of thermostable tetrameric TPIs are key important tetrameric interface, forming a hydrophobic effects. However, TaTPI contains unique charged-amino acid residues in the helix 5 and adopts dimer conformation. TaTPI exhibits the apparent T_d value of 74.6 ℃ and maintains its overall structure with slight changes in the secondary structure contents under extremely

acidic conditions. Based on the structural and biophysical analyses of TaTPI, more compact structure of the protomer with reduced length of loops and certain patches on the surface could account for the robust nature of *Thermoplasma acidophilum* TPI.

Keywords: aspartyl-tRNA synthetase, multi-tRNA synthetase complex, triosephosphate isomerase, glycolysis, crystal structure

Student number: 2010-21682

Table of Contents

Abstract · · ·

Chapter 2

Structure and stability of the dimeric triosephosphate isomerase from *Thermoplasma acidophilum*

1. Introduction · · ·

References · 83

Abstract (in Korean) · 94

Acknowledgements · 97

Appendix: Printouts of first author publications · · · · · · · · · · · · · · 98

List of Tables

List of Figures

Chapter 1

Chapter 2

Figure 2-1. The isomerization reaction catalyzed by triosephosphate isomerase · · ·

Abbreviations

AARSs	aminoacyl-tRNA synthetases
DRS	aspartyl-tRNA synthetase
KRS	lysyl-tRNA synthetase
MSC	multi-tRNA synthetase complex
NMR	nuclear magnetic resonance
EF-1α	elongation factor 1α
OB-fold	oligonucleotide binding-fold
PTM	post-translational modification
TPI	triosephosphate isomerase
DHAP	dihydroxyacetone phosphate
GAP	glyceraldehyde-3-phosphate
PDB	protein data bank
HEPES	4-(2-hydroxyethyl)-1-piperazineethanesulfonic acid
G3P	glycerol-3-phosphate
CD	circular dichroism
DSC	differential scanning calorimetry
AUC	analytic ultracentrifugation
RMS	root-mean-square errors
T_d	half-denaturation temperature
TSPs	TPI stabilization patches

Chapter 1

Crystal structure of human cytosolic aspartyl-tRNA synthetase

[This chapter was published in PROTEINS.]

Kim KR, Park SH et al. (2013) Crystal Structure of Human cytosolic aspartyl-tRNA synthetase, a component of multi-tRNA synthetase complex.

PROTEINS 81(10):1840-1846

1. Introduction

Aminoacyl-tRNA synthetases (AARSs) catalyze the attachment of specific amino acid to its compatible cognate tRNAs through a two-step reaction.(Normanly and Abelson, 1989, Annual review of biochemistry, 1) In the first step, an intermediate adenylate is formed from amino acid and ATP, then the amino acid is charged to the ribose of the terminal adenine of tRNA (Figure 1-1). Even though AARSs catalyze the same type of reaction, they vary in amino acid sequence, size, three-dimensional structure, and oligomeric state.

This chapter was co-work with Kyung Rok Kim and he equally contributed to this work

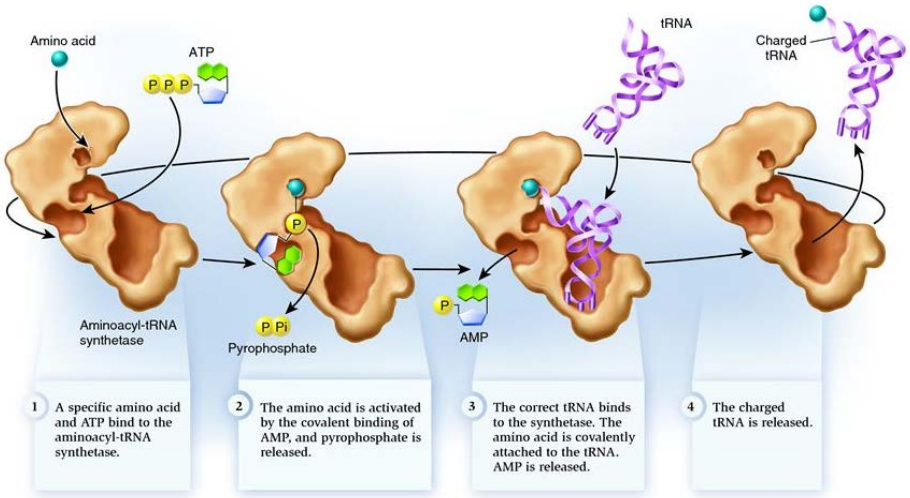

Figure 1-1. Aminoacyl-tRNA synthetase charging a tRNA (biology-forums.com)

AARSs can be classified into two major classes based on conseverd sequence motif; class I and II synthetase.(Eriani, et al., 1990, Nature, 2) Whereas the class I synthetase adopts the representative Rossmann fold that binds ATP, the class II synthetase contains a core antiparallel β-sheet surrounded by α-helices and three unique conserved motifs; motif 1, 2, and 3 (Figure 1-2).(Eriani, et al., 1990, Nature, 2)

There are cytosolic or mitochondrial AARSs that play an essential cellular role not only in cytosol but also in mitochondria and most AARSs function distinctively in either location for protein synthesis. In human, there are cytosolic and mitochondrial aspartyl-tRNA synthetases (DRS and DRS2), which share only 22.9% sequence identity. It has been known that DRS2 is associated with neurodegenerative disorder; leukoencephalopathy with brain stem and spinal cord involvement and high lactate (LBSL). (Scheper, et al., 2007, Nature genetics, 3) Structure of DRS2 revealed the function of the additional motif in the catalytic domain.(Neuenfeldt, et al., 2012, Nucleic acids research, 4) In the case of DRS, it has been known to the component of multi-tRNA synthetase complex (MSC) in higher eukaryotes.(Deutscher, 1984, The Journal of cell biology, 5)

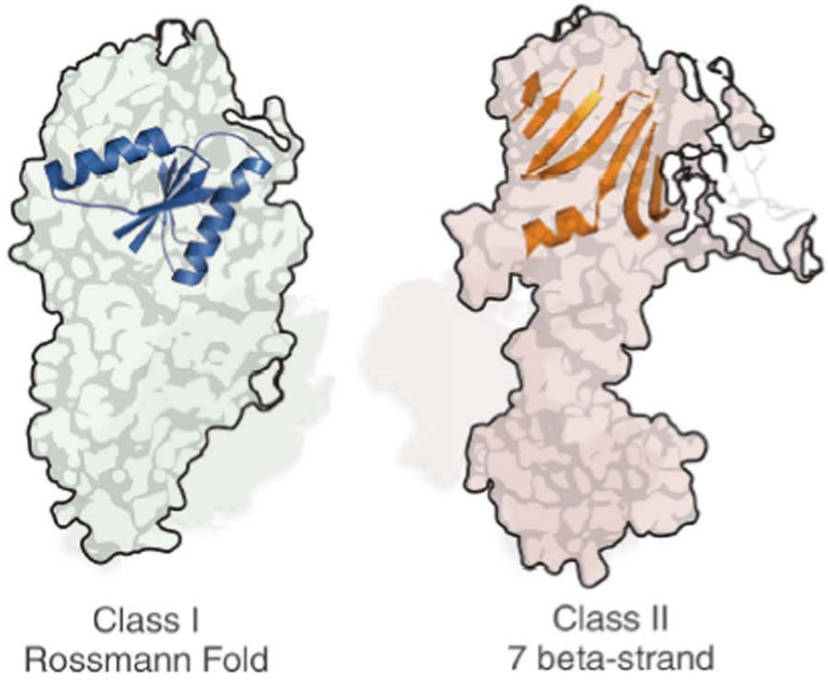

Figure 1-2. Architectures of the catalytic domains for aminoacylation – class I versus class II (Lo, et al., 2014, Science, 6)

The conserved core Rossmann fold is represented on the structure of MRS (PDB ID: 2CT8) in class I, and the conserved core 7 beta-strand with motif-3 helix is represented on the structure of KRS (PDB ID: 4DPG) in class II.

The MSC consists of nine cytosolic tRNA synthetases (DRS, KRS, MRS, RRS, QRS, IRS, LRS, and EPRS) with three auxillary proteins (AIMP1/p43, AIMP2/p38, and AIMP3/p18) and it has been known to switch the canonical translational function and additional functions which are often observed in higher eukaryotes (Figure 1-3).(Ray, et al., 2007, Trends Biochem Sci, 7; Park, et al., 2005, Trends Biochem Sci, 8) In the MSC, DRS is known to interact with the aminoacyl-tRNA synthetase-interacting multifunctional protein 2 (AIMP2/p38) (Robinson, et al., 2000, J Mol Biol, 9; Kaminska, et al., 2009, J Biol Chem, 10) and the lysyl-tRNA synthetase (KRS).(Guzzo and Yang, 2008, Biochemical and biophysical research communications, 11) The N-terminal extension of DRS, KRS, and asparaginyl-tRNA synthetase (NRS) is unique additional region in the class II synthetases and further classifies them into the subclass IIb.(Woese, et al., 2000, Microbiology and molecular biology reviews : MMBR, 12) The NMR structure of the N-terminal extension region in DRS revealed that the N-terminal flexible β-turn followed by the amphipathic C-terminal helix induces the nonspecific tRNA binding and gives a force to transfer its charged tRNA to elongation factor 1α (EF-1α).(Reed and Yang, 1994, J Biol Chem, 13; Reed, et al., 1994, J Biol Chem, 14; Cheong, et al., 2003, The international journal of biochemistry & cell biology, 15)

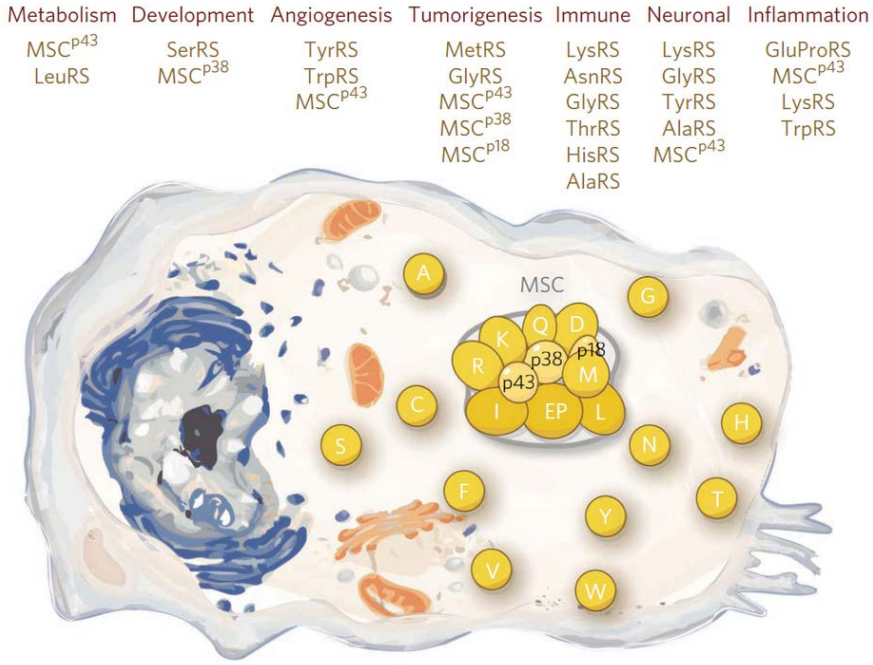

Figure 1-3. The nontranslational functions of AARs (Guo and Schimmel, 2013, Nature chemical biology, 16)

In this work, I present the crystal structure of human cytosolic DRS at 2.25 Å. I show that DRS forms a homodimer with the N-terminal extension, anticodon binding domain, and catalytic domain. Analyses of the crystal structure and post-translational modification shed lights on the molecular basis of the association and dissociation of DRS with the MSC.

2. Material and methods

2.1. Cloning, protein expression, and purification

Full-length sequence of human cytosolic DRS (501 amino acids) was amplified using PCR and cloned into the pET-28a(+) vector containing the N-terminal His_6-tag (Novagen). The recombinant protein was transformed into *Escherichia coli* Rosetta2(DE3)pLysS strain. DRS was induced by 0.5 m*M* isopropyl 1-thio-β-D-galactopyranoside and incubated for 6 hours at 310 K using Luria Broth culture medium. The harvested cells were lysed by cell sonicator (SONICS) in lysis buffer containing 20 m*M* Tris-HCl (pH 7.5), 500 m*M* NaCl, 35 m*M* imidazole, and 1 m*M* phenylmethanesulfonyl fluoride. The lysates were centrifuged at 35,000g for 50 min to remove the cell debris and denatured proteins. The supernatant was applied to a HiTrap Chelating HP column (GE Healthcare) for affinity chromatography and eluted with linear gradient 50-500 m*M* imidazole following equilibration with 50 m*M* imidazole. The eluted protein was diluted with a buffer containing 50 m*M* HEPES-NaOH (pH 7.0), 50 m*M* NaCl, 1 m*M* dithiothreitol, and 5% (v/v) glycerol, and further purified using the ion exchange chromatography with a HiTrap Q HP column (GE Healthcare). For the final purification step, size-exclusion chromatography was performed with a HiLoad 16/600 Superdex 200

prep grade column (GE Healthcare) equilibrated with 50 m*M* HEPES-NaOH (pH 7.0), 200 m*M* NaCl, 5% (v/v) glycerol, and 1 m*M* dithiothreitol. For crystallization, the purified DRS proteins were concentrated to 11.1 mg ml^{-1}.

2.2. Crystallization

Initial DRS crystals were searched using commercial screen solutions, Crystal screen I, II, PEG/Ion I, II (Hampton Research), and Wizard classic I, II, III, IV (Rigaku), by the sitting-drop vapor-diffusion method at 295 K. DRS crystals were grown by the sitting-drop vapor-diffusion method at 295 K by mixing equal volumes of the purified protein and the reservoir solution containing 8% (v/v) tacsimate (pH 8.0), and 20% (w/v) polyethylene glycol 3350 (Figure 1-4).

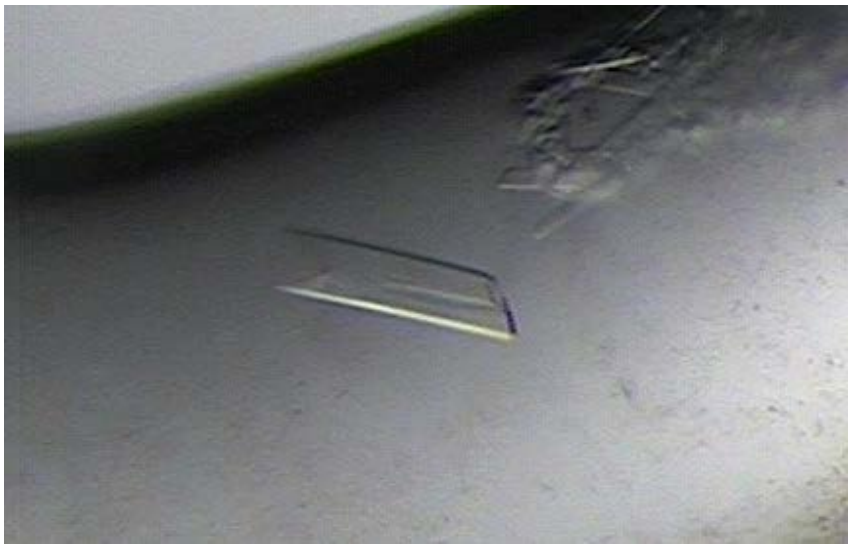

Figure 1-4. Crystals of human cytosolic DRS

Crystals of human cytosolic DRS with approximate dimensions of 0.3 mm × 0.1 mm × 0.05 mm.

2.3. X-ray data collection and structure determination

For X-ray diffraction data collection, crystals were soaked in the cryoprotectant solution containing 20% (v/v) glycerol added to the reservoir solution. X-ray diffraction data of the crystal were collected at the synchrotron BL-5A at the Photon Factory, Japan. The DRS crystals belong to the space group $P2_1$, with unit cell parameters of a = 54.89, b = 141.92, c= 98.50, $\alpha = \gamma = 90^{\circ}$, and $\beta = 102.19^{\circ}$. The structure was solved by molecular replacement method with the structure of *S. cerevisiae* DRS containing the anticodon binding domain, hinge region, and catalytic domain (PDB ID: 1ASZ)(Cavarelli, et al., 1994, The EMBO journal, 17) as a phasing model using *MOLREP*.(Vagin and Teplyakov, 2010, Acta Crystallogr D Biol Crystallogr, 18) The structure was completed using alternate cycles of manual building in *WinCoot*(Emsley, et al., 2010, Acta Crystallogr D Biol Crystallogr, 19) and refinement in *REFMAC*(Murshudov, et al., 1997, Acta Crystallogr D Biol Crystallogr, 20). All refinement steps were monitored using an R_{free} value based on 5.0% of the independent reflections. The stereochemical quality of the final model was assessed using *MolProbity*(Lovell, et al., 2003, Proteins, 21). The data collection and refinement statistics are summarized in Table1-1; 1-2.

Table 1-1. Statistics for data collection

Data collection[a]	**Human cytosolic DRS**
Space group	$P2_1$
Cell dimensions	
a, b, c (Å)	54.89, 141.92, 68.50
α, β, γ (°)	90, 102.19, 90
Data set	
X-ray wavelength (Å)	1.0000
Resolution (Å)[b]	50.00–2.25 (2.29–2.25)
Total / unique reflections	177,246 / 48,428
Completeness (%)	99.3 (95.4)
R_{merge} (%)[c]	11.0 (50.2)

Footnotes to Table 1-1

[a]Data collected at the synchrotron BL-5A at the Photon Factory.

[b]Numbers in parentheses indicate the highest resolution shell.

[c]$R_{merge} = \Sigma_h \Sigma_i |I(h)_i - \langle I(h) \rangle| / \Sigma_h \Sigma_i I(h)_i$, where $I(h)$ is the observed intensity of reflection h, and $\langle I(h) \rangle$ is the average intensity obtained from multiple measurements.

Table 1-2. Refinement statistics

Refinement	Human cytosolic DRS
Resolution (Å)	50.00–2.25
R_{work}[a] / R_{free}[b] (%)	19.7 / 22.8
No. of non-hydrogen atoms / mean B-factor (Å^2)	
Protein	6,968 / 33.7
Water	354 / 40.2
Glycerol	48 / 52.5
Poor rotamers (%)[c]	3.1
Ramachandran plot analysis (%)	
Most favored regions	96.9
Additional allowed regions	3.1
Disallowed regions	0
R.m.s.d. from ideal geometry	
Bond lengths (Å)	0.010
Bond angles (°)	1.290

Footnotes to Table 1-2

[a]$R_{work} = \Sigma \mid |F_o| - |F_c| \mid / \Sigma |F_o|$, where $|F_o|$ is the observed structure factor amplitude and $|F_c|$ is the calculated structure factor amplitude.

[b]R_{free} = R-factor based on 5.0% of the data excluded from refinement.

[c]Values obtained using MolProbity.

2.4. Post-translational modification analysis

Purified N-terminal OneSTrEP-tagged DRS and co-eluted interaction partners of that, overexpressed and purified from HEK293T cells, were digested with sequencing grade gold-trypsin (Promega) after 1D-SDS PAGE/Coomassie blue staining. Tryptic peptides were analyzed with the LTQ Velos Orbitrap mass spectrometer equipped with an electron transfer dissociation source after an online reversed-phase chromatography. To improve sequencing coverage, I applied a data dependent decision tree to select for collision induced dissociation or electron transfer dissociation fragmentation depending on the charged states, respectively. Protein identification was accomplished using the Sorcerer™-SEQUEST® (Sage-N Research), and searches were performed against the IPI human DB v3.87 fasta. The carbamidomethylation (+57.021 Da) of Cys is set as a static modification, and the following variable modification were allowed: GlyGly / +114.043 Da (Lys), Acetyl / +42.011 Da (Lys), HexNAc / +203.079 Da (Asn, Ser, Thr), Phospho / +79.966 Da (Ser, Thr, Tyr), Oxidation / +15.995 Da (Met), deamidated / +0.984 Da (Asn, Gln).

2.5. Data deposition

The coordinate and structure factors for human cytosolic DRS have been deposited in the RCSB Protein Data Bank, accession code **4J15**.

3. Results and discussion

3.1. Overall structure and oligomeric state of DRS

The crystal structure of human cytosolic DRS has been determined at 2.25 Å resolution by molecule replacement method with the structure of *S. cerevisiae* DRS containing the anticodon binding domain, hinge region, and catalytic domain (PDB ID: 1ASZ) (Cavarelli, et al., 1994, The EMBO journal, 17) as a phasing model. R_{work}/R_{free} values for the final models of DRS was 19.7%/22.8%. Crystal structure of DRS contains a homodimer in the asymmetric unit and the dimer interface area is 3,750.5 $Å^2$ which comprises of 16.6% of the monomeric surface area calculated from Protein Interfaces, Surfaces and Assemblies service.(Krissinel and Henrick, 2007, Journal of molecular biology, 22) The crystal structure of DRS contains anticodon binding domain, hinge region, and catalytic domain. In addition, the N-terminal extension region, which is a distinct domain in mammalian DRS, could be partially modeled including the C-terminal three residues of the characteristic helix motif (Figure 1-5). Structural analyses on this N-terminal extension region will be further discussed with the previous NMR structure below.

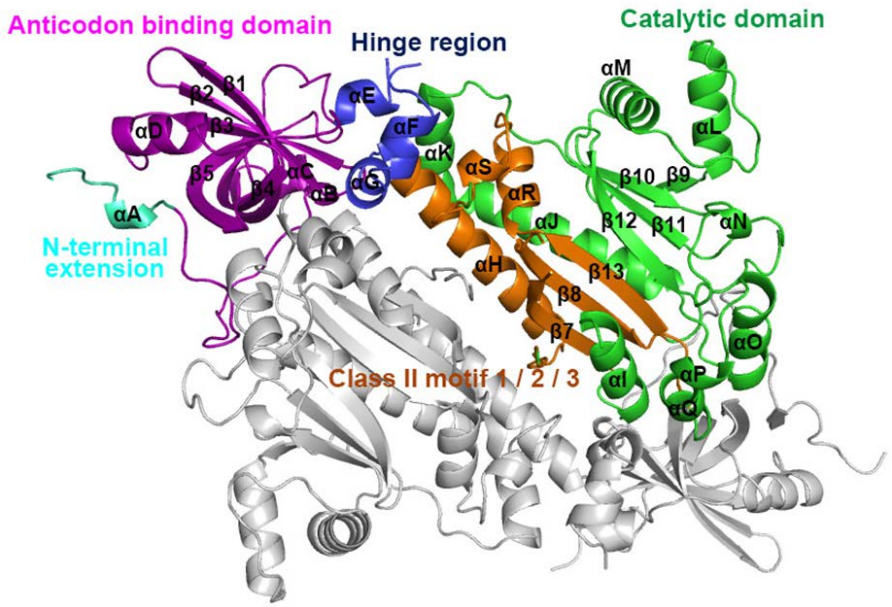

Figure 1-5. Crystal structure of DRS dimer

The N-terminal extension, anticodon binding domain, hinge region, catalytic domain, and motifs are colored and labeled in cyan, magentas, blue, green, and orange respectively.

The anticodon binding domain of DRS (residues 57-146) contains the oligonucleotide binding-fold (OB-fold) that is composed of a five-stranded antiparallel β-sheet connected by helices and loops (β1-β5) to form a closed β-barrel. The catalytic domain (residues 189-497) adopts thirteen α-helices (αH-αT) and eight β-strands (β6-β13) which comprise all the three conventional class II aminoacyl-tRNA synthetase motifs; motif 1, 2, and 3.(Eriani, et al., 1990, Nature, 2) The hinge region (residues 156-188) plays a fundamental role in the connection of the anticodon binding domain and the catalytic domain. In the middle of the hinge region, residues 163-172 could not be observed due to the lack of the electron density and the disordered residues are considered as a part of binding region to the ribose-phosphate backbone in the D-stem of $tRNA^{Asp}$, compared with the known *S. cerevisiae* DRS-$tRNA^{Asp}$ complex structure.(Cavarelli, et al., 1994, The EMBO journal, 17) In addition, residues 224-247 in the flipping loop and residues 273-282 in the motif 2 could not be modeled in the crystal structure of DRS. These regions are known to be dynamic without its cognate tRNA and recognize its tRNA in an induced-fit manner.(Sauter, et al., 2000, J Mol Biol, 23)

When the anticodon binding domain, hinge region, and catalytic domain in the structure were independently superimposed with those of the *S. cerevisiae* DRS-$tRNA^{Asp}$ complex structure, the three domains

were structurally well-conserved with the r.m.s.d. values of 1.08 Å, 1.80 Å, and 0.97 Å, respectively. In the anticodon binding domain, three β-strands (β1, β2, and β3) could bind to the anticodon loop of $tRNA^{Asp}$ which is composed of GUC elements. In the hinge region, short helices containing Asp158 and Asn175 could interact with the D-stem (U11, U12) of $tRNA^{Asp}$. In the catalytic domain, the flipping loop and the class II motif 2 play a key role in the interaction of DRS with the 3'-end of $tRNA^{Asp}$ (Figure 1-6).

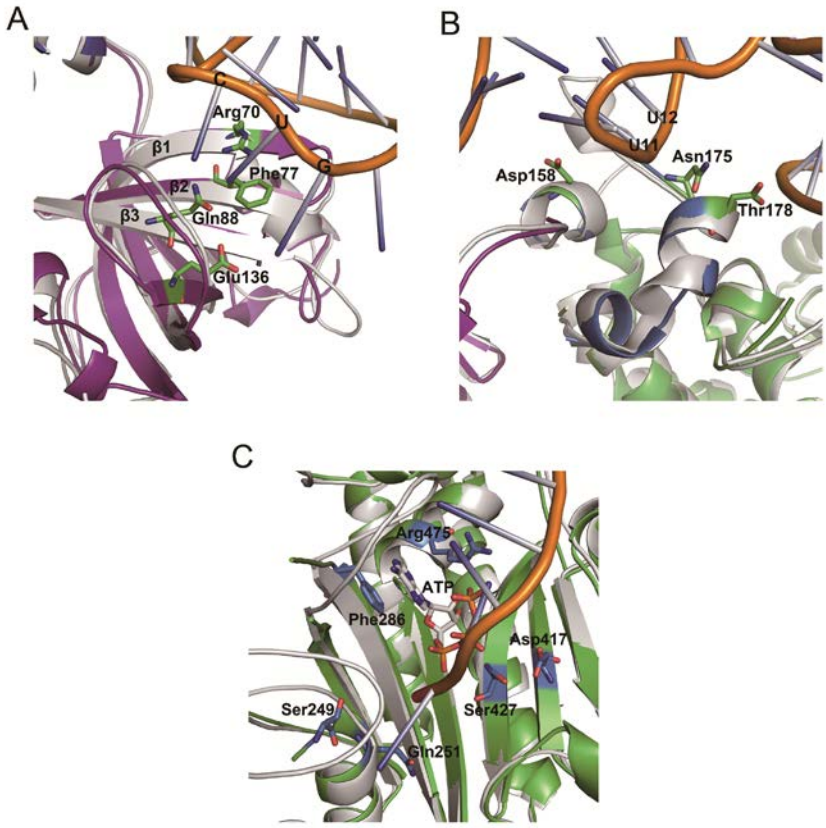

Figure 1-6. Superposition of human DRS with *S.cerevisiae* DRS-tRNA^{Asp}

The anticodon binding domain (**A**) and the hinge region (**B**) of human DRS are colored as in Figure 1-5 and the catalytic domain (**C**) of human DRS is represented in green. *S. cerevisiae* DRS is colored in gray and tRNA^{Asp} is shown in orange. Carbon, oxygen, nitrogen and phosphorus atoms of ATP are shown with stick model in gray, red, blue, and orange, respectively. The predicted interaction residues of human DRS with tRNA^{Asp} are labeled and shown in stick model.

3.2. Structural comparison of human cytosolic and mitochondrial DRSs

Recently, the crystal structure of human mitochondrial DRS (DRS2) has been determined at 3.7 Å resolution (PDB ID: 4AH6).(Neuenfeldt, et al., 2012, Nucleic acids research, 4) Even though human DRS and DRS2 share only 22.9% sequence identity (Figure 1-7), two structures are structurally similar to each other with the r.m.s.d. distance of 1.7 Å. The anticodon binding domain, hinge region, and catalytic domain of DRS and DRS2 are structurally well-conserved, with the exception of an additional motif in the catalytic domain of DRS2 which is known as the insertion domain (Figure 1-8). The insertion domain of DRS2 adopts the enlarged catalytic groove with more electropositive surface potential, which enables an alternate interaction network at the subunit interface between tRNA and DRS2.(Neuenfeldt, et al., 2012, Nucleic acids research, 4) Interestingly, DRS2 showed a higher sensitivity than DRS for inhibitors with a non-hydrolysable adenylate moiety and its correlation with structural features has not been well understood. (Messmer, et al., 2009, Biochimie, 24) Structural analyses of DRS and DRS2 in complex with same adenylate analogs would elucidate a subtle role of the domain difference with respect to substrate specificity and evolutionary advantages.

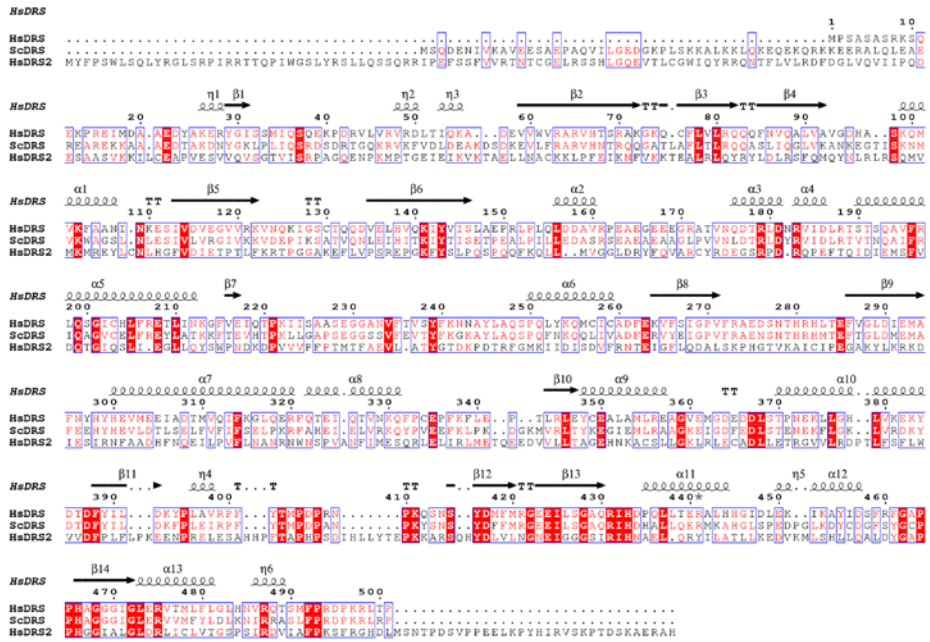

Figure 1-7. Sequence alignment of human cytosolic DRS with *S.cerevisiae* DRS and human mitochondrial DRS

Strictly conserved amino acid residues are highlighted in red shaded boxes and moderately conserved amino acid residues are colored in red. The alignment figure was prepared using *ESPript* program (Robert and Gouet, 2014, Nucleic acids research, 25).

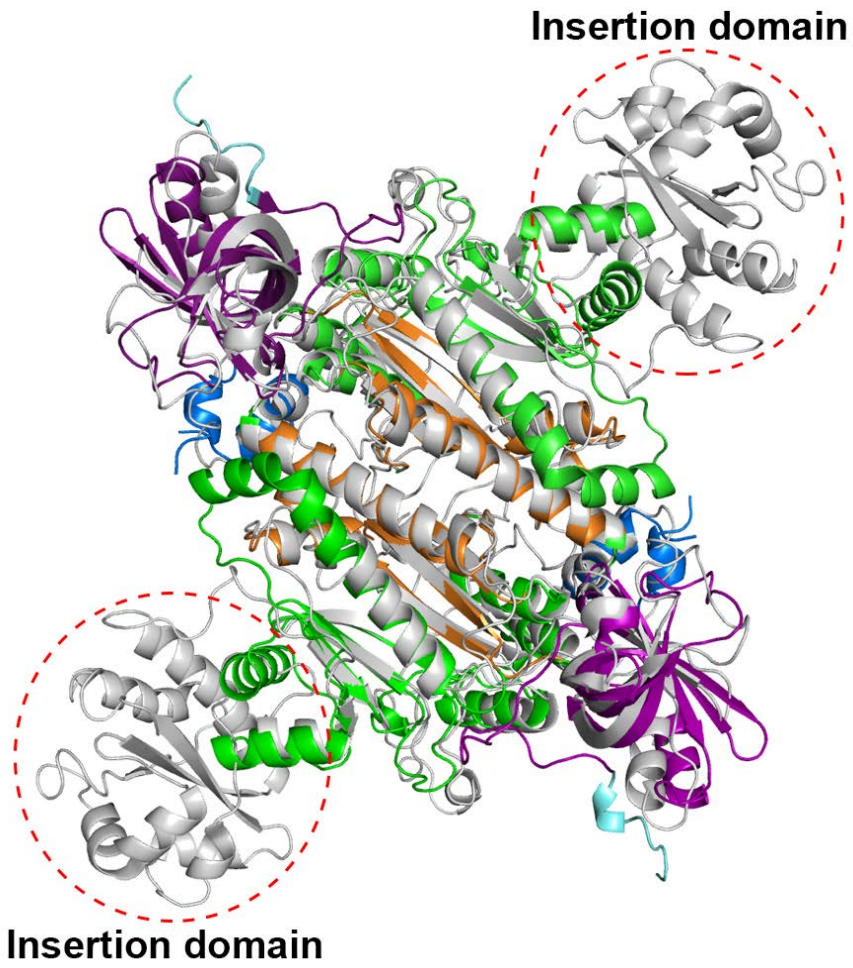

Figure 1-8. Structural comparison of human cytosolic DRS and mitochondrial DRS

Human cytosolic DRS is shown as in Figure 1-5 and mitochondrial DRS is colored in gray. The red dotted ovals indicate the insertion domain of mitochondrial DRS.

3.3. Flexible N-terminal extension of DRS

In higher eukaryotes, additional domains or motifs in a specific AARS result in additional functions. In the case of DRS, KRS, and NRS, they contain the N-helix that is named after the helical conformation in part of their N-terminal extension region.(Woese, et al., 2000, Microbiology and molecular biology reviews : MMBR, 12; Guo, et al., 2010, Nature reviews Molecular cell biology, 26) The previously determined NMR structure of the N-terminal extension of DRS revealed the conformational flexibility caused by the β-turn followed by one α-helix and the N-terminal extension plays a crucial role in the interaction between $tRNA^{Asp}$ and EF-1α.(Reed and Yang, 1994, J Biol Chem, 13; Reed, et al., 1994, J Biol Chem, 14; Cheong, et al., 2003, The international journal of biochemistry & cell biology, 15) In the crystal structure of DRS, the C-terminal end of the α-helix in the N-terminal extension was observed, comprising of Lys26, Glu27, and Arg28, even though the N-terminal region was less-ordered. To get a glimpse of the whole N-helix structure, the structurally well-resolved C-terminal end of the N-terminal extension residue Glu27 and Arg28 was superposed with the α-helix of the NMR structure, considering the helical wheel conformation (Figure 1-9). The α-helix in the N-terminal extension is amphipathic and the hydrophilic face of the amphipathic helix could interact with positively charged residues Arg8 and Lys9 in

the N-terminus by the conformational change on the flexible β-turn.(Cheong, et al., 2003, The international journal of biochemistry & cell biology, 15) Consequentially, the crystal structure further supports the structural switching model of the N-terminal extension of DRS in the aid of the direct transfer of $tRNA^{Asp}$ to EF-1α (Figure 1-10).

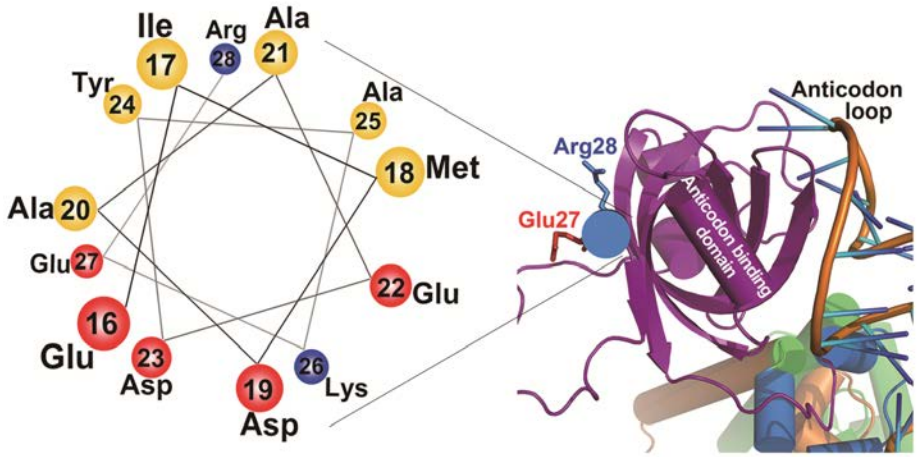

Figure 1-9. Helical wheel of the α-helix in the N-terminal extension

Helical wheel represent the α-helix in the N-terminal extension and the anticodon binding domain. The hydrophobic, negative-charged, and positive-charged residues in the helical wheel are colored yellow, red, and blue, respectively.

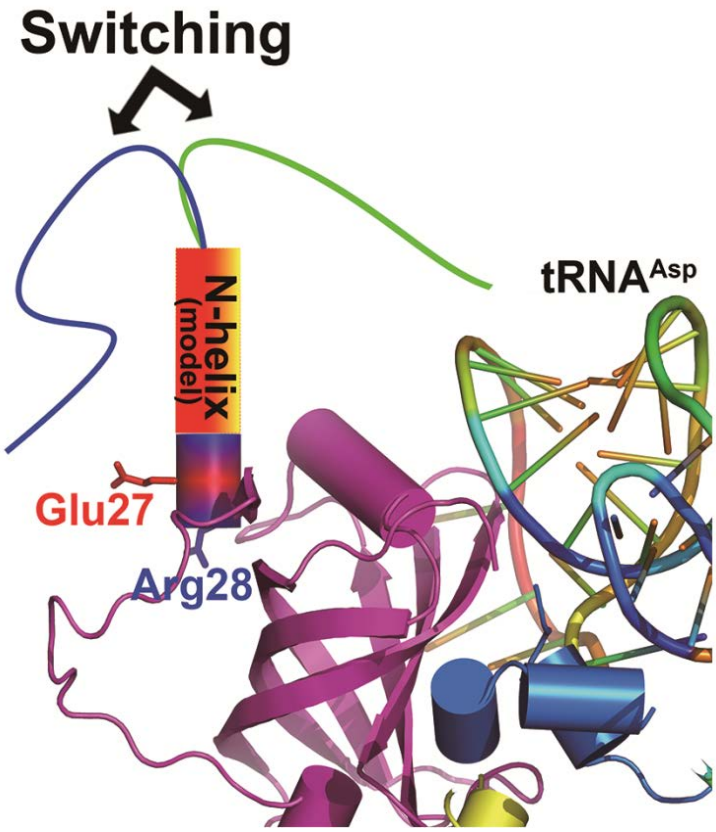

Figure 1-10. The switching model of the N-helix with DRS structure

From the helical wheel model, the switching model of the N-helix with the DRS structure is suggested.

3.4. Post-translational modification of DRS

To speculate the organization of DRS as a main interacting component with AIMP2/p38 in the MSC assembly, all the known post-translational modification (PTM) data was searched and independently implemented the PTM analyses of DRS. The liquid chromatography tandem mass spectrometry analysis was performed and two phosphorylation sites (Tyr239 and Ser249) and six acetylation sites (Lys55, 110, 213, 241, 330 and 453) were identified. Among the results, the phosphorylation of Tyr239 and the acetylation of Lys55, 213 and 453 were firstly identified. These findings and other PTM sites information of DRS from PhosphoSite Plus database (http://www.phosphosite.org) indicated that the residues 238-254 region of the class II aminoacyl-tRNA synthetase are dynamically regulated by various types of modifications such as phosphorylation, acetylation and ubiquitination (Figure 1-11). For instance, while Lys241 was identified with its acetylation modification in the analysis, collected six independent MS-analysis data of ubiquitin branch motif (K-e-GG) immunoaffinity beads purification studies showed that Lys241 is also modified with ubiquitin. Thus it seems that the phosphorylation status of Ser238, Tyr239 and/or Ser249 could affect the catalytic activity, stability or partner binding affinity of DRS through a competitive modification event between acetylation and

ubiquitination of Lys241 and/or Lys254, though it should be clarified with further studies. PTM sites mapped on the surface representation of human DRS dimer modeled with $tRNA^{Asp}$ are shown in Figure 1-12. A large numer of PTM sites locate in tRNA interaction region, or surface of DRS. These results suggest that the PTM sites could affect on interaction between DRS and tRNA.

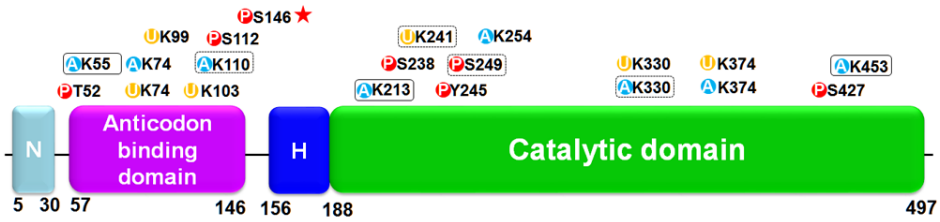

Figure 1-11. PTM analyses

Acetylation, phosphorylation, and ubiquitination sites are shown as blue, red, and yellow circles, respectively. PTM sites uniquely observed in this study and residues observed both in the database and in this study are surrounded by black boxes and dotted boxes, respectively. Ser146, which is expected to play a key role in the organization of DRS, is marked with a red asterisk.

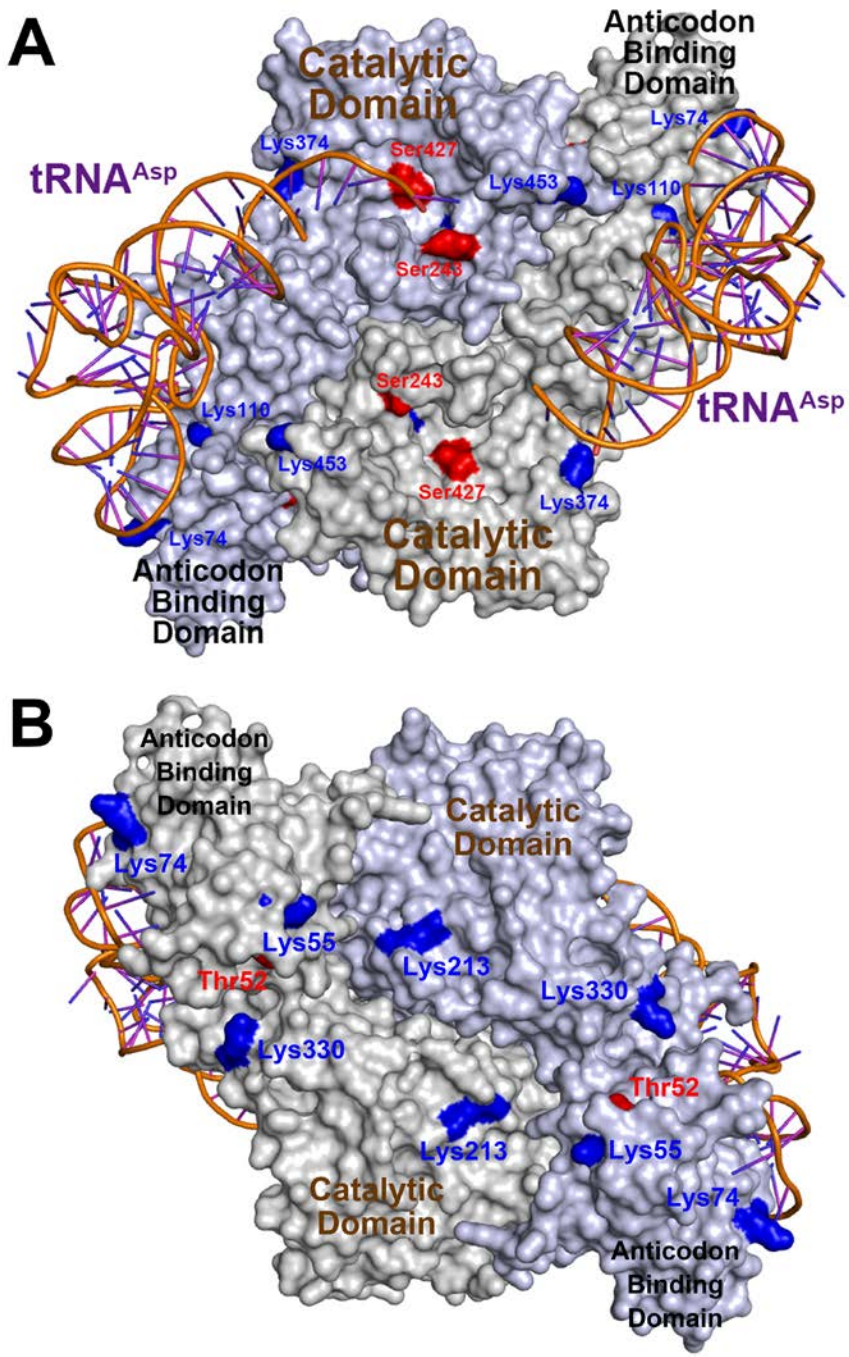

Figure 1-12. PTM sites mapped on the surface representation of human DRS dimer modeled with tRNA^{Asp}

The crystal structure of human DRS dimer was superposed with that of *S. cerevisiae* DRS dimer in complex with $tRNA^{Asp}$ and human DRS is shown as surface representation. (**A**) tRNA binding face of DRS dimer. (**B**) Bottom and symmetric groove of the DRS dimer. Acetylation and phosphorylation sites are colored in blue and red, respectively.

3.5. Implication on the MSC assembly

In the MSC, AIMP2/p38 has been known to interact with two subcomplexes of the MSC (I: MRS, AIMP3/p18, EPRS, IRS, LRS; II: AIMP1/p43, QRS, RRS, DRS, and KRS), and the N-terminal domain of AIMP2/p38 interacts with the subcomplex II, DRS, and KRS.(Kaminska, et al., 2009, J Biol Chem, 10) The N-terminal motif 1 and 2 of AIMP2/p38 have been recently shown to interact with the bottom groove and the symmetric groove on the KRS dimer, respectively.(Ofir-Birin, et al., 2012, Molecular cell, 27) Based on the situational and structural similarity between KRS and DRS, two dimers of DRS would interact with AIMP2/p38 in the similar manner of KRS regarding the association and dissociation from the MSC. In the case of KRS, Ser207 establishes the major intermolecular interaction of the KRS dimer through three hydrogen bonds between the hydroxyl group of Ser207 and the backbone of Gly540 and Leu541. Interestingly, a conformational change triggered by the phosphorylation of Ser207 switches the function of KRS from translation to transcription, provoking a new conformer and releasing KRS from the MSC.(Ofir-Birin, et al., 2012, Molecular cell, 27) To this surprise, DRS also contains the equivalent Ser146, Gly462, and Ala463, which are highly conserved in the amino acid sequence and three-dimensional structure in higher eukaryotes (Figure 1-13). In addition, the PTM information of

DRS from the PhosphoSite Plus database shows that the phosphorylation of Ser146 was already observed with the phosphoproteome analyses of the human cell cycle using the mass spectrometry.(Olsen, et al., 2010, Science signaling, 28) Thus, the phosphorylation of Ser146 could initiate a conformation change of the DRS dimer and trigger an unpredicted function of DRS by releasing it from the MSC. The structural study and PTM analyses of DRS extend the knowledge about the interaction of components in the MSC and provide fundamental information for human physiological signaling pathways related to the MSC.

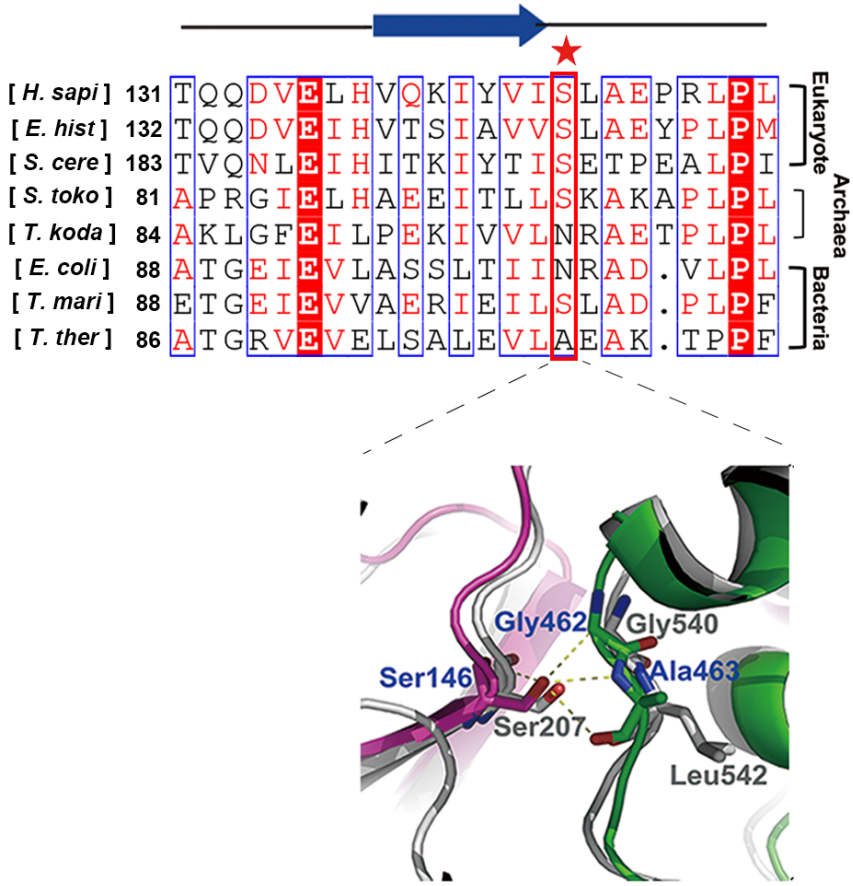

Figure 1-13. Key intermolecular interaction of DRS

Sequence alignment of the interface residues of anticodon binding domain and catalytic domain of DRSs from various organisms. Ser146 of human DRS are marked with red asterisks. Close-up view of Ser146 and the intermolecular interaction of DRS dimer. The structure of human DRS is superimposed with that of human KRS shown in a gray cartoon model.

Chapter 2

Structure and stability of the dimeric triosephosphate isomerase from *Thermoplasma acidophilum*

[This chapter was published in *PLoS One*.]

Park SH et al. (2015) Structure and Stability of the Dimeric Triosephosphate Isomerase from the Thermophilic Archaeon *Thermoplasma acidophilum*. *PLoS One* 10(12):e0145331. doi: 10.1371/journal.pone.

1. Introduction

Triosephosphate isomerase (TPI or TIM) is a functionally and structurally well-known enzyme that plays a crucial role in glycolytic and gluconeogenic metabolism. TPI accurately and efficiently interconverts dihydroxyacetone phosphate (DHAP) and glyceraldehyde-3-phosphate (GAP) (Figure 2-1). Missense mutations of TPI genes result in TPI deficiency through loss-of-function (Schneider, 2000, Bailliere's best practice & research Clinical haematology, 29). TPI deficiency has been known to cause metabolic diseases, glycolytic enzymopathies, in which neurological pathogenesis is uniquely severe (Celotto, et al., 2006, Genetics, 30). Pathogenic TPI

deficiency mutations dramatically affect TPI activity owing to either catalytic interruption or oligomeric state alteration (Arya, et al., 1997, Hum Mutat, 31; Hollan, et al., 1993, Hum Genet, 32; Daar, et al., 1986, Proc Natl Acad Sci U S A, 33).

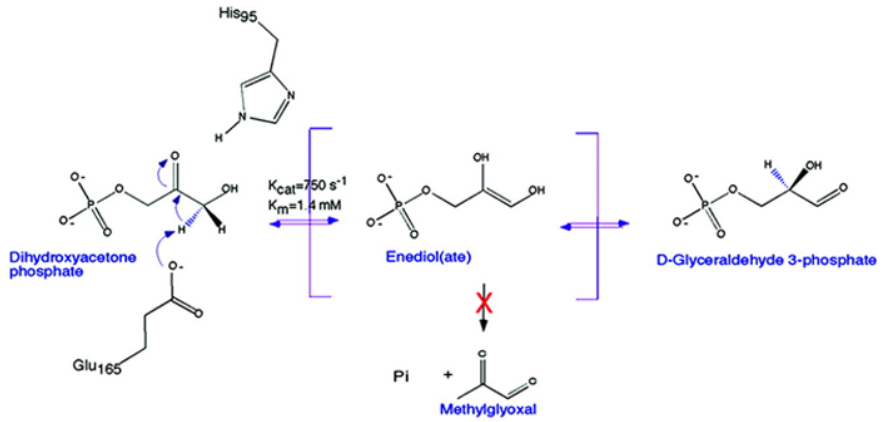

Figure 2-1. The isomerization reaction catalyzed by triosephosphate isomerase (Jogl, et al., 2003, Proceedings of the National Academy of Sciences of the United States of America, 34)

The reaction pathway from DHAP to GAP, including the putative reaction intermediate, an enediol.

Thermoplasma acidophilum is one of the most acidophilic organisms among known thermophilic archaea. It optimally grows at 55 – 60 ℃ and pH 0.5 – 2.0. For glucose degradation, *T. acidophilum* has been known to utilize not only non-phosphorylative Entner-Doudoroff (ED) pathway but also canonical glycolysis/gluconeogenesis pathway (Embden-Meyerhof-Parnas pathway) (Ruepp, et al., 2000, Nature, 35). Although one of the glycolysis/gluconeogenesis pathway enzymes, phosphofructokinase, has not been identified in *T. acidophilum*, TPI has been considered to play a crucial role in the glycolysis/gluconeogenesis pathway in *T. acidophilum*.

TPI is a representative α/β protein with eight α-helices and eight β-strands connected by loops, forming a TIM-barrel fold (Wierenga, 2001, FEBS Lett, 36). The active site of TPI is highly conserved in all kingdoms and located inside of the TIM-barrel fold with three catalytic residues (Lys9, His89, and Glu137 in TaTPI numbering). Most TPIs are optimally active in their dimeric forms. In contrast, archaeal TPIs that withstand high temperatures are tetrameric in their active states (Maes, et al., 1999, Proteins, 37). Thermostable proteins have been known to adapt to high temperature in various ways: increased electrostatic interactions, hydrogen bonds, and hydrophobic effects, resulting in fortified subunit contacts, more compact packing, higher oligomerization state, and two-state equilibrium reversibility (Xiao and

Honig, 1999, Journal of molecular biology, 38; Dams, et al., 2000, Journal of molecular biology, 39; Szilagyi and Zavodszky, 2000, Structure, 40; Delboni, et al., 1995, Protein science : a publication of the Protein Society, 41; Romero-Romero, et al., 2015, Physical chemistry chemical physics : PCCP, 42).

In the Protein Data Bank (PDB), structures of one bacterial TPI (*Thermotoga maritima;* Tm) and three archaeal TPIs (*Pyrococcus woesei;* Pw, *Thermoproteus tenax;* Tt, and *Methanocaldococcus jannaschii;* Mj) that have been deposited are in tetrameric form. *P. woesei*, *M. jannaschii*, and *T. acidophilum* belong to Euryarchaeota and *T. tenax* is affiliated to Crenarchaeota in phylogeny. Among tetrameric TPIs in PDB, tetrameric conformation of bacterial TmTPI is maintained by disulfide bonds between two classical TPI dimers (Maes, et al., 1999, Proteins, 37). In archaeal TPIs, helix 4 and helix 5 in the tetrameric interface are of key importance for their tetrameric forms. Especially, helix 5 in thermostable TPIs has been considered as a major contributor for tetramer formation via dominant hydrophobic effects (Walden, et al., 2001, Journal of molecular biology, 43).

In this work, I report crystal structures of apo- and glycerol-3-phosphate (G3P)-bound TaTPI, each representing open and closed form. Unlike other thermostable archaeal TPIs, TaTPI forms a stable dimer in solution, which I confirmed using analytical ultracentrifugation and

size-exclusion chromatography. I also show the effect of pH on the secondary structure and temperature-induced unfolding of TaTPI. Through systematic comparison of TaTPI with available dimeric and tetrameric TPIs, I suggest that TPI stabilization patches can be targeted for the design of more stable TIM-barrel fold proteins.

2. Material and methods

2.1. Cloning, expression, and purification of TaTPI and MjTPI

Full-length sequences of *Thermoplasma acidophilum* TPI (TaTPI, 216 amino acid residues) and *Methanocaldococcus jannaschii* TPI (MjTPI, 219 amino acid residues) were amplified using PCR and cloned into pET-28a(+) vector (Novagen) containing C-terminal His_6-tag. Cloned plasmids were transformed into *Escherichia coli* Rosetta2(DE3)pLysS strain. Recombinant proteins were overexpressed by adding 0.5 m*M* isopropyl 1-thio-ß-D-galactopyranoside at $O.D._{600nm}$ 0.5 and cells were further incubated at 20 ℃ overnight (16 h) using Luria Broth culture media. Harvested cells were lysed by cell sonicator (SONICS) in lysis buffer (20 m*M* Tris-HCl, pH 7.5, 500 m*M* NaCl, 35 m*M* imidazole, and 1 m*M* phenylmethylsulfonyl fluoride). After incubation of cell lysate at 60 ℃ for 10 minutes, cell debris and denatured proteins were removed by centrifugation at 35,000 xg for 50 minutes. Supernatant was applied to HiTrap Chelating HP column (GE Healthcare) for affinity chromatography. Loaded sample was eluted with elution buffer (20 m*M* Tris-HCl, pH 7.5, 500 m*M* NaCl, and 500 m*M* imidazole) following equilibration with washing buffer (20 m*M* Tris-HCl, pH 7.5, 500 m*M* NaCl, and 50 m*M* imidazole). Eluted sample was further purified by size-exclusion chromatography with

HiLoad 16/600 Superdex 200 prep grade column (GE Healthcare) equilibrated with 20 m*M* Tris-HCl, pH 7.5, and 200 m*M* NaCl. Fractions containing TPI proteins were further purified by anion exchange chromatography with HiTrap Q HP column (GE Healthcare) after 2 X dilution of the fractions with 20 m*M* Tris-HCl, pH 7.5, and 100 m*M* NaCl. Linear gradient of 0-500 m*M* NaCl in 20 m*M* Tris-HCl, pH 7.5, was applied for elution. For the final purification step, second size-exclusion chromatography was performed with HiLoad 16/600 Superdex 200 prep grade column (GE Healthcare) equilibrated with 20 m*M* Tris-HCl, pH 7.5, and 200 m*M* NaCl for TaTPI or 50 m*M* HEPES (4-(2-hydroxyethyl)-1-piperazineethanesulfonic acid), pH 7.5, for MjTPI. For crystallization, purified TaTPI proteins were concentrated to 30 mg ml^{-1}.

2.2. Crystallization

Initial crystals of apo-TaTPI were grown at 22 ℃ by sitting drop vapor diffusion method with crystallization solution containing 2 *M* NaCl and 10% (w/v) polyethylene glycol 6000. Apo-TaTPI crystals suitable for diffraction data collection were grown at 4 ℃ using hanging-drop vapor diffusion method after mixing apo-TaTPI proteins with 2 times volume of crystallization solution containing 0.5 *M* NaCl, 10% (w/v) polyethylene glycol 6000, and 0.1 *M* Tris-HCl, pH 8.5. Crystals of TaTPI in complex with glycerol-3-phosphate (G3P) were obtained from crystallization solution with 0.6 *M* NaCl, 9% (w/v) polyethylene glycol 6000, and 0.1 *M* Tris-HCl, pH 8.5, after incubating purified apo-TaTPI proteins with 20 m*M* G3P for 4 h at 4 ℃ (Figure 2-2).

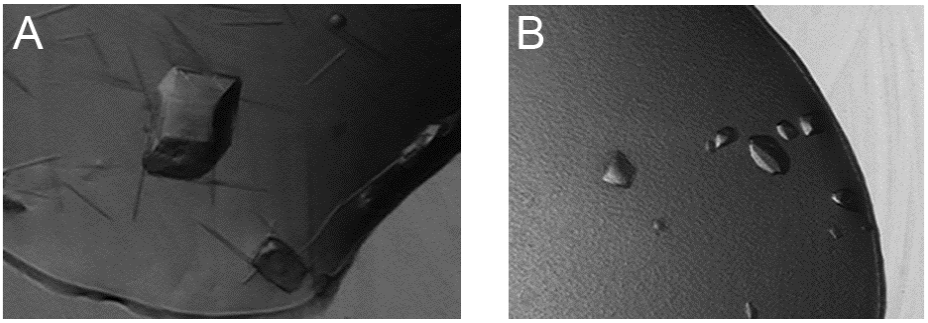

Figure 2-2. Crystals of TaTPI from *T.acidophilum*

(A) Crystals of the apo-TaTPI. (B) Crystals of the TaTPI in complex with glycerol-3-phosphate (G3P).

2.3. X-ray data collection and structure determination

For X-ray diffraction data collection, crystals were frozen in liquid nitrogen following cryoprotection by soaking TaTPI crystals in crystallization solution supplemented with 20% (v/v) glycerol. X-ray diffraction data for apo- and G3P-bound complex TaTPI crystals were collected at BL-7A synchrotron beamline at the Pohang Light Source, Korea, and at BL-1A synchrotron beamline at the Photon Factory, Japan, respectively. Collected data were processed using *HKL*2000 program suite (Otwinowski and Minor, 1997, Methods Enzymol, 44). The apo- and G3P-bound TaTPI crystals belong to the space group $P2_12_12_1$, with unit cell parameters of a = 75.49, b = 113.96, c= 114.80, and a = 72.63, b = 84.08, c = 143.54, respectively (Figure 2-3; 2-4). The crystal structure of apo-TaTPI was solved by molecular replacement method using MOLREP program (Vagin and Teplyakov, 2010, Acta Crystallogr D Biol Crystallogr, 18), with the crystal structure of *Pyrococcus woesei* TPI (PDB ID: 1HG3) as a phasing model (Walden, et al., 2001, Journal of molecular biology, 43). The crystal structure of G3P-bound TaTPI was solved with the apo-TaTPI structure as a phasing model. The initial models building were carried out by *WinCoot* program (Emsley, et al., 2010, Acta Crystallogr D Biol Crystallogr, 19) and further refined with *REFMAC*5 program (Murshudov, et al., 1997, Acta Crystallogr D Biol Crystallogr, 20). All

refinement steps were monitored using R_{free} value based on 5.0% of independently saved reflections. The final models were evaluated with *MolProbity* program (Lovell, et al., 2003, Proteins, 21). Data collection and refinement statistics are summarized in Table 2-1; 2-2.

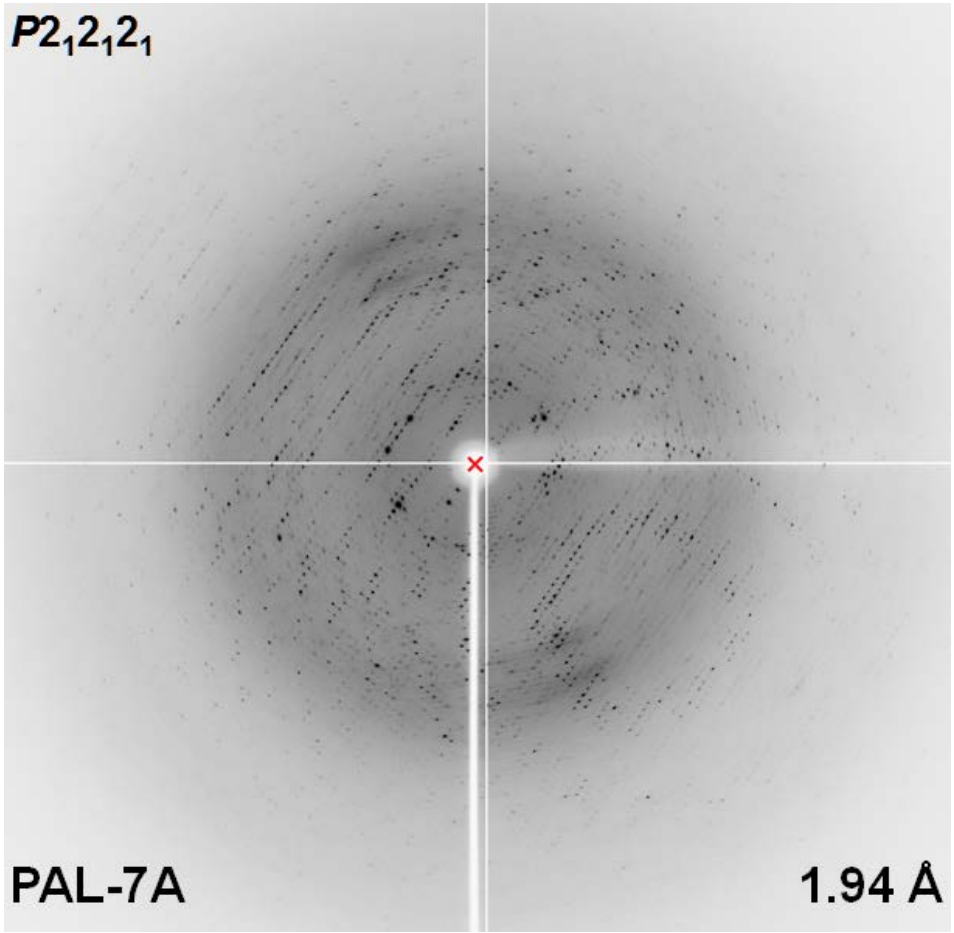

Figure 2-3. X-ray diffraction image from apo-TaTPI

X-ray diffraction data for apo-TaTPI crystals were collected at BL-7A synchrotron beamline at the Pohang Light Source, Korea.

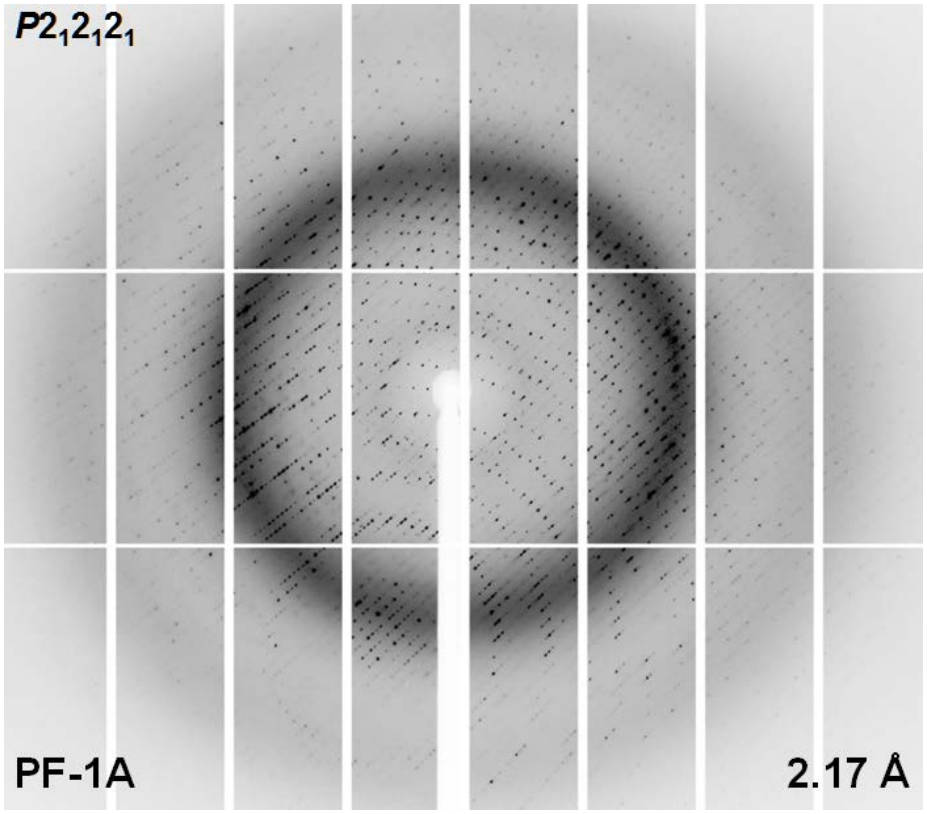

Figure 2-4. X-ray diffraction image from G3P-bound TaTPI

X-ray diffraction data for G3P-bound complex TaTPI crystals were collected at BL-1A synchrotron beamline at the Photon Factory, Japan.

Table 2-1. Statistics for data collection

Data collection[a]	**TaTPI**	**G3P-bound TaTPI**
Space group	$P2_12_12_1$	$P2_12_12_1$
Cell dimensions		
a, b, c (Å)	75.49, 113.96, 114.80	72.63, 84.08, 143.54
α, β, γ (°)	90, 90, 90	90, 90, 90
Data set		
X-ray wavelength (Å)	1.0000	1.1000
Resolution (Å)[b]	50.00–1.94	50.00-2.17
Total / unique reflections	521,936 / 73,921	294,576 / 47,245
Mean *I/sigma(I)*	32.4 (3.3)	20.9 (3.0)
Multiplicity	7.1 (5.6)	6.2 (5.6)
Completeness (%)	99.0 (83.5)	99.9 (99.9)
R_{merge} (%)[c]	9.1 (62.5)	13.4 (59.0)

Footnotes to Table 2-1

[a]Data collected at the synchrotron BL-7A at the Pohang Light Source and BL-1A at the Photon Factory.

[b]Numbers in parentheses indicate the highest resolution shell.

[c]$R_{merge} = \Sigma_h \Sigma_i |I(h)_i - \langle I(h) \rangle| / \Sigma_h \Sigma_i I(h)_i$, where $I(h)$ is the observed intensity of reflection h, and $\langle I(h) \rangle$ is the average intensity obtained from multiple measurements.

Table 2-2. Refinement statistics

Refinement	TaTPI	G3P-bound TaTPI
Resolution (Å)	50.00–1.94	50.00–2.17
R_{work}[a] / R_{free}[b] (%)	18.0 / 21.5	18.3 / 22.5
No. of non-hydrogen atoms / mean B-factor (Å^2)		
Protein	6,996 / 32.9	6,640 / 34.2
Water	561 / 39.8	401 / 34.4
Other atoms	28 / 40.1	44 / 22.9
Poor rotamers (%)[c]	0.1	0.3
Ramachandran plot analysis (%)		
Most favored regions	98.0	96.1
Additional allowed regions	2.0	3.4
Disallowed regions	0	0.5
R.m.s.d. from ideal geometry		
Bond lengths (Å)	0.019	0.015
Bond angles (°)	1.648	1.550

Footnotes to Table 2-2

[a]$R_{work} = \Sigma \mid |F_o| - |F_c| \mid / \Sigma |F_o|$, where $|F_o|$ is the observed structure factor amplitude and $|F_c|$ is the calculated structure factor amplitude.

[b]R_{free} = R-factor based on 5.0% of the data excluded from refinement.

[c]Values obtained using MolProbity.

2.4. Analytical ultracentrifugation (AUC)

Equilibrium sedimentation studies were performed using Beckman ProteomeLab XL-A analytical ultracentrifuge in 20 m*M* Tris-HCl buffer, pH 7.5, and 200 m*M* NaCl at 20 ℃. Sedimentation data were collected at 280 nm using a six-sector cell at rotor speeds of 20,000 and 26,000 rpms with three different protein concentrations: 12.6 u*M* (0.31 mg ml^{-1}), 16.8 u*M* (0.41 mg ml^{-1}), and 21.0 u*M* (0.52 mg ml^{-1}). All measured data fit well to a homogeneous dimer model and representative results measured at 26,000 rpm using 16.8 u*M* protein concentration are presented. TaTPI concentrations were calculated using e_{280nm} = 11,920 $M^{-1}cm^{-1}$ and molecular weight of 24,671 daltons. Time required for the attainment of equilibrium was established by running at given rotor speed until scans were invariant for 4 hours: this was achieved at most by 36 hours in six-sector cells using 130 ul of samples. Partial specific volume of TaTPI protein and buffer density were calculated using Sednterp (Laue, 1995, Methods Enzymol, 45). The calculated partial specific volume at 20 ℃ was 0.7417 $cm^3 g^{-1}$ and the buffer density was 1.00704 g cm^{-3}. For data analysis by mathematical modeling using non-linear least-squares curve fitting, following functions were used for homogeneous (Eqn. 1) and interactive (Eqn. 2) models.

$$C_r = C_b \exp[A_p M_p(r^2 - r_b^2)] + \varepsilon \quad \text{(Eqn. 1)}$$

$$C_r = C_b \exp[A_p M_p(r^2 - r_b^2)] + C_b^n \exp[Ink + nA_p M_p(r^2 - r_b^2)] + \varepsilon \quad \text{(Eqn. 2)}$$

$$A_p = (1 - v\rho)\omega^2/2RT$$

where C_r is the total concentration at the radial position r, C_b is the concentration of protein at the cell bottom, M_p is the molecular weight of protein monomer, ε is a baseline error term, v and ρ are the partial specific volume and the solution density, respectively, and ω is the rotor angular velocity. The *In*k value is a natural log for equilibrium constants for reversible models (1x-nx, where n is 2 & 3) on an absorbance scale. Selection of the best model was made by examining numbers of weighted sum of square and root mean square error values. Further data manipulation and data analysis by mathematical modeling were performed using MLAB (Knott, 1979, Comput Programs Biomed, 46).

2.5. Circular dichroism (CD)

Temperature of maximum heat capacity (or half-denaturation temperature, Td) of TaTPI was measured by CD spectroscopy. Experimental sample was prepared following purification and concentration of TaTPI proteins to 0.4 mg ml^{-1} containing 50 m*M* HEPES, pH 7.5. CD traces of TaTPI were obtained at 222 nm using the J-1500 CD spectrometer (JASCO) at a scanning rate of 1℃ min^{-1}. The denaturation curve of TaTPI was analyzed by Kaleidagraph (Synergy Software) based on John and Weeks's protocol (John and Weeks, 2000, Protein science : a publication of the Protein Society, 47).Effect of pH variation on the secondary structure of TaTPI was also monitored by CD spectroscopy. The pH of protein solutions containing 20 m*M* Tris-HCl and 200 m*M* NaCl were adjusted to desired values between pH 1.0 and pH 7.0 with HCl for CD measurements. The baseline signal was measured with a buffer containing 20 m*M* Tris-HCl, pH 7.5, and 200 m*M* NaCl. CD spectra of pH-titrated TaTPI were recorded and averaged over two scans between 200 to 260 nm using J-1500 CD spectrometer (JASCO). The secondary structure contents of TaTPI were calculated by Multivariate SSE Program (JASCO).

2.6. Analytical size-exclusion chromatography

Analytical size-exclusion chromatography of TaTPI was performed with Superdex 200 10/300 GL column (GE Healthcare) following equilibration with 20 m*M* Tris-HCl, pH 7.5, and 200 m*M* NaCl. The applied protein were at concentrations of 0.9 and 4.5 mg ml^{-1}. Standard proteins from Gel Filtration Standard (BIO-RAD) were applied to the column for calibration. The standard protein mixture contained thyroglobulin (M.W. 670 kDa), γ-globulin (M.W. 158 kDa), ovalbumin (M.W. 44 kDa), myoglobin (M.W. 17 kDa), and vitamin B_{12} (M.W. 1.35 kDa).

2.7. Differential scanning calorimetry (DSC)

Maximum temperature of heat capacity of MjTPI was measured with VP-DSC differential scanning microcalorimeter (Malvern). Experimental sample was prepared following purification and concentration of MjTPI proteins to 1.6 mg ml^{-1} (65 u*M*). Sample buffer containing 50 m*M* HEPES, pH 7.5, was loaded into the DSC cell after degassing in an evacuated chamber for 5 minutes and reference data were measured with scan rate of 0.5 ℃ min^{-1}. Experimental temperature was increased in the range from 50 to 120 ℃. After sample buffer scan reached equilibrium, MjTPI proteins were carefully loaded into the cell following degassing and experiments were performed under the same condition as for the reference. Heat capacity curve was plotted using the Origin software (Malvern).

2.8. Data deposition

The structure coordinates and structure factors for apo- and G3P-bound TaTPI have been deposited in PDB under the accession code **5CSR** and **5CSS**, respectively.

3. Results and discussion

3.1. Overall structures of apo- and glycerol-3-phosphate-bound TaTPI

The crystal structures of apo-TaTPI and its complex with glycerol-3-phosphate (G3P), an analogue of the substrate glyceraldehyde-3-phosphate, have been determined at 1.94 and 2.17 Å resolution, respectively. R_{work}/R_{free} values for the final models of apo- and G3P-bound TaTPI were 18.0%/21.5% and 18.3%/22.5%, respectively. Crystal structures of apo- and G3P-bound TaTPI contain four copies of TaTPI monomer in the asymmetric unit, comprising two homodimers. The overall structure of TaTPI protomer confirms to the canonical TIM-barrel fold with eight α-helices and eight parallel β-strands from 216 amino acid residues (Figure 2-5A). The crystal structure of G3P-bound TaTPI reveals that G3P is well positioned at the active site of TaTPI with functionally conserved residues Lys9, His89, and Glu137 (Figure 2-5B). Glu137 is clearly demonstrated as a catalytic base, with its position being within 3 Å from O1 and O2 of G3P. An oxyanion hole, which contributes to the stabilization of transition state, is formed by NZ nitrogen of Lys9 and NE2 nitrogen of His89 with O2 oxygen of G3P. The phosphate group of G3P is perfectly coordinated through hydrogen bonds with backbone nitrogen atoms of Gly143, Gly175,

Ala196, and Ser197 residues, including adjacent water molecules (Figure 2-6).

Overall structures of apo- and G3P-bound TaTPI were similar with r.m.s.d. of 0.69 Å for 216 C_α positions, except G3P-bound area. The conformational changes in the loop 6 of ligand bound-TPIs have been reported in previously determined structures of TPIs from many species, including *Trypanosoma brucei*, *Gallus gallus*, *Geobacillus stearothermophilus*, *Leishmania mexicana*, and *Vibrio marinus* (Delboni, et al., 1995, Protein science : a publication of the Protein Society, 41; Zhang, et al., 1994, Biochemistry, 48; Alvarez, et al., 1998, The Journal of biological chemistry, 49; Williams, et al., 1999, Protein engineering, 50; Noble, et al., 1993, Proteins, 51; Wierenga, et al., 2010, Cellular and molecular life sciences : CMLS, 52). Likewise, loop 6 located between β-strand 6 and helix 6 and loop 7 located between β-strand 7 and helix 7 showed remarkable conformational changes when G3P binds to apo-TaTPI. When compared with apo-TaTPI structure, Gly143 located in loop 6 and Gly175 located in loop 7 moved toward G3P by 8.3 and 3.8 Å, respectively (Figure 2-5B). Consequently, residue Ala174 is pushed to a disallowed region of the Ramachandran plot in the G3P-bound form, an amino acid residue within loop 7 that is displaced by the ligand binding. G3P binding triggers the conformational change and induces the transformation of TaTPI from

open to closed form, securing the catalytic site from bulk solvent to maintain efficient catalytic activity. In addition, water molecules around the active site of apo-TaTPI are expelled from the active site and would be replaced with substrate upon substrate binding.

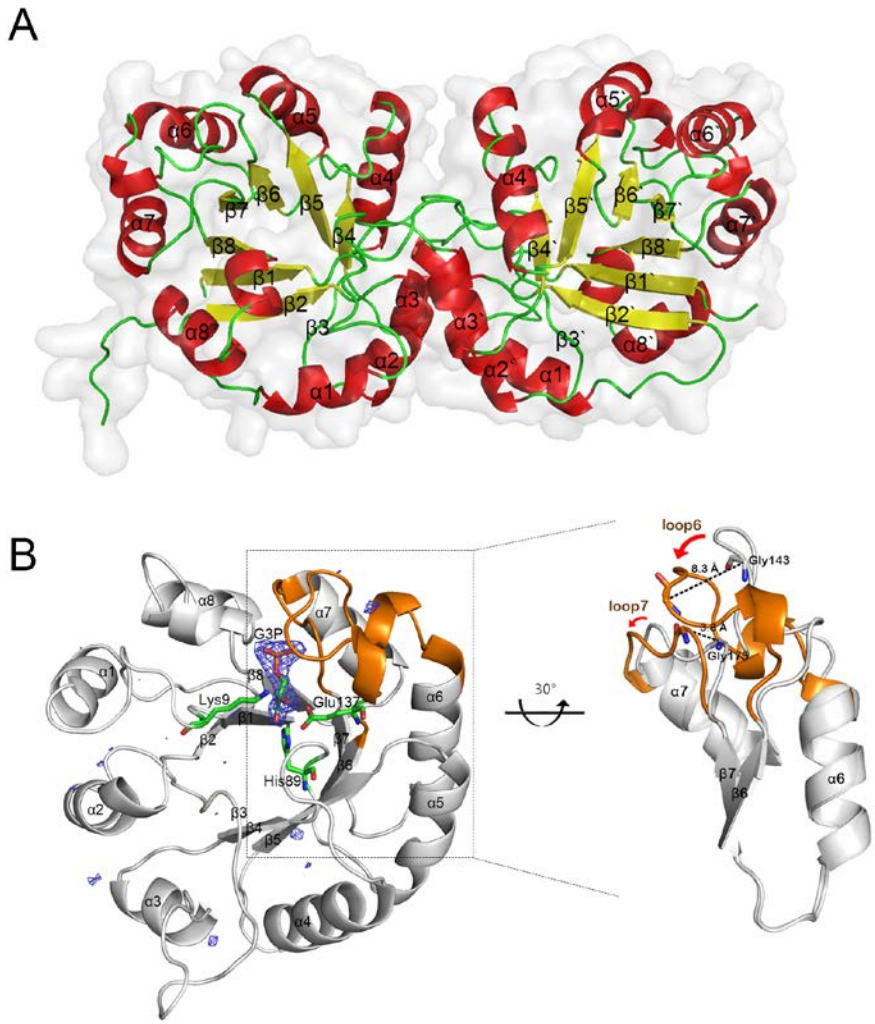

Figure 2-5. Overall structures of apo- and G3P-bound TaTPI

(A) Homodimer of apo-TaTPI is shown in carton representation, where α-helix, β-strand, and loop are colored in red, yellow, and green, respectively. (B) G3P-bound TaTPI. Only monomer of homodimeric G3P-bound TaTPI is demonstrated to emphasize a conformational change compared with apo-TaTPI. Extra positive electron density in F_o-F_c omit map contoured at 3.0 δ is shown as a blue mesh, which is

modelled as G3P later. Amino acid residues interacting with G3P in catalytic site and G3P are shown as stick model; carbon, oxygen, phosphorus, and nitrogen atoms are colored in green, red, orange, and, blue, respectively. Loop 6 and loop 7 regions, which show a distinctive conformational change upon binding of G3P, are represented in orange and magnified for clarity.

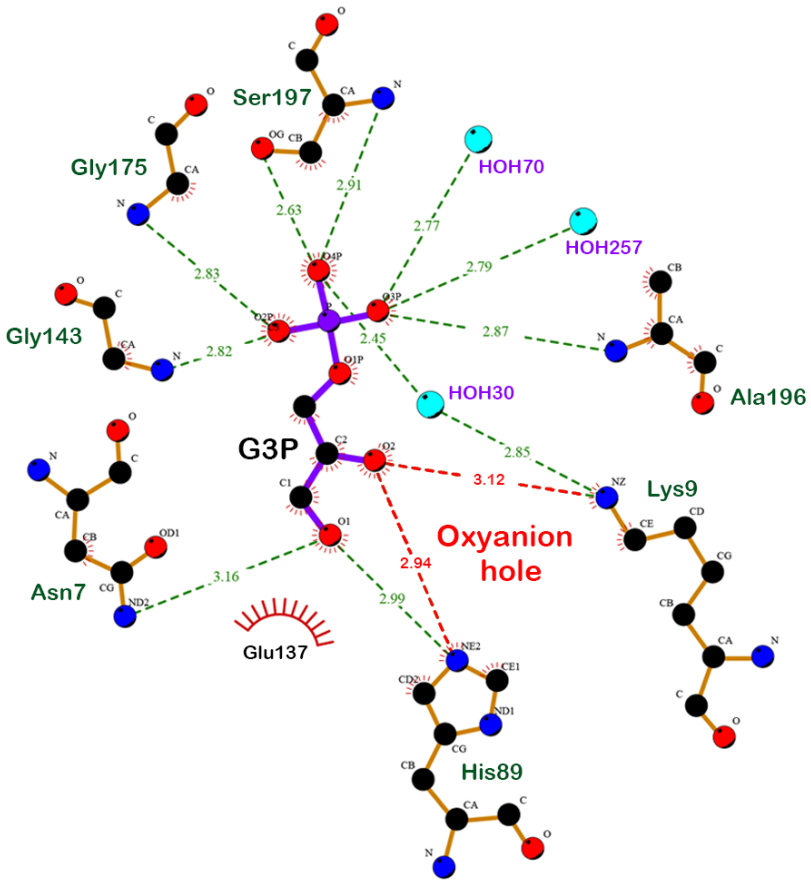

Figure 2-6. Binding modes of G3P with key amino acid residues of TaTPI

LIGPLOT diagram is used for representation of active site in the G3P-bound TaTPI. Carbon, nitrogen, oxygen, and phosphorus atoms are shown in black, blue, red, and magenta, respectively. Hydrogen bonds and oxyanion hole between G3P and TaTPI are shown as green and red dotted line, respectively.

3.2. Unique dimeric conformation of TaTPI

T. acidophilum belongs to thermoacidophilic euryarchaeota and TaTPI also shares high amino acid sequence similarity to other thermostable TPIs from *P. woesei*, *T. tenax*, and *M. jannaschii*, all of which adopt tetrameric conformation that renders them stable at high temperatures (Walden, et al., 2001, Journal of molecular biology, 43; Walden, et al., 2004, Journal of molecular biology, 53; Gayathri, et al., 2007, Acta Crystallogr D Biol Crystallogr, 54). Helix 4 and helix 5 of thermostable TPIs have been known to play important roles in the tetramer formation via hydrophobic interactions (Walden, et al., 2001, Journal of molecular biology, 43). However, crystal structures of apo- and G3P-bound TaTPI form a dimer and reveal a remarkable difference in helix 5 of TaTPI from other thermostable TPIs. Helix 5 of TaTPI is mainly composed of charged-amino acid residues (AEEAKYFREY) instead of hydrophobic residues found in other thermostable tetrameric TPIs. Structure-based sequence alignment of TaTPI with other TPIs shows that TaTPI resembles bacterial dimeric TPIs rather than tetrameric TPIs from thermostable archaea (Figure 2-7).

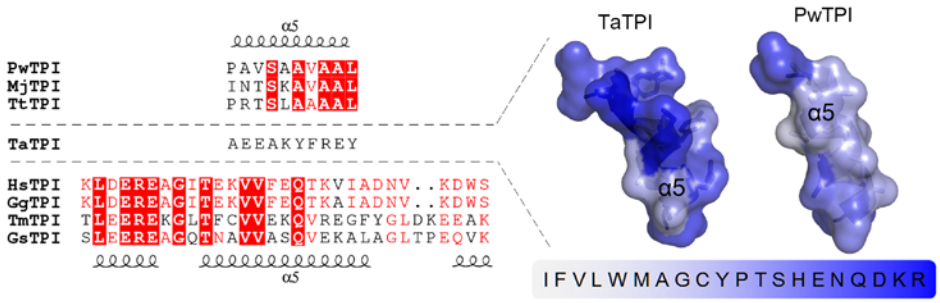

Figure 2-7. Structure-based sequence alignment of helix 5 region among TPIs

Structure-based sequence alignment of helix 5 region among TPIs from *Thermoplasma acidophilum* (TaTPI), *Pyrococcus woesei* (PwTPI), *Methanocaldococcus jannaschii* (MjTPI), *Thermoproteus tenax* (TtTPI), *Homo sapiens* (HsTPI), *Gallus gallus* (GgTPI), *Thermotoga maritima* (TmTPI), and *Geobacillus stearothermophilus* (GsTPI). Strictly conserved amino acid residues are highlighted in red shaded boxes and moderately conserved amino acid residues are colored in red. Helix 5 regions of TPIs from *Thermoplasma acidophilum* (PDB ID: 5CSR) and *Pyrococcus woesei* (PDB ID: 1HG3) are shown as cartoon representation with transparent surfaces, where amino acid residues are colored according to normalized consensus hydrophobicity scale (Eisenberg, et al., 1984, Journal of molecular biology, 55).

Structural differences between TaTPI and other tetrameric archaeal TPIs are observed not only in helix 5 but also in adjacent α-helices. In tetrameric archaeal TPIs, the N-terminus of helix 4 and the C-terminus of helix 6 play important roles in tetrameric interaction via hydrophobic effects and hydrogen bonds (Walden, et al., 2001, Journal of molecular biology, 43). The N-terminus of helix 4 of tetrameric archaeal TPIs contains conserved Leu (Leu103 in PwTPI numbering) that contributes to hydrophobic effects and hydrogen bonds with the other side of helix 4 and helix 5 for its tetrameric assembly. In the case of TaTPI, Leu in the N-terminus of helix 4 of tetrameric archaeal TPIs is replaced with Arg96, which deprives the hydrophobic effects for tetramer formation. Furthermore, TaTPI has shorter helix 6 than that of tetrameric archaeal TPIs, resulting in dissipated hydrophobic effects between two C-termini from each helix 6 of its accompanying dimeric partner, Val173 in PwTPI (Figure 2-8). Consequently, changes in amino acid composition of helix 5, thus in electrostatic surface, and slight modification of secondary structures in helix 4 and helix 6 seem to play subtle roles in dimer formation.

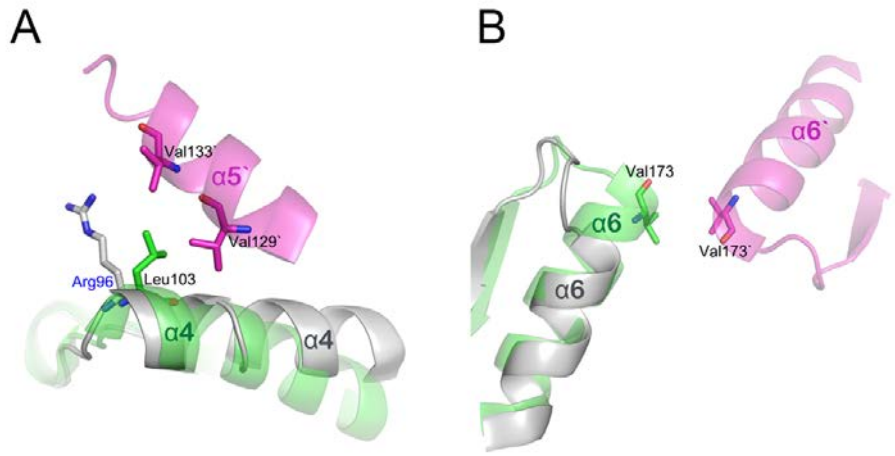

Figure 2-8. Structural comparison of helix 4 and helix 6 in TaTPI and PwTPI

(A) and (B) Structural comparison of helix 4 and helix 6 in TaTPI (gray) and PwTPI (green and magenta, each from different monomers). The important amino acid residues in tetrameric interface are shown as stick model.

3.3. Analytic ultracentrifugation analysis of TaTPI

In the crystal structure of apo-TaTPI, Cys50 in helix 2 of each homodimer drew this attention since it interacts with the other Cys50 from adjacent TaTPI homodimer via sulfur-containing hydrogen bonds, not disulfide bonds. Thus, I needed to re-confirm the oligomeric status of apo-TaTPI to make it sure whether the interaction of Cys-Cys is physiologically relevant or crystallographic artefact. To verify the oligomeric state of apo-TaTPI in solution, analytic ultracentrifugation analysis (AUC) was performed. Oligomeric state of apo-TaTPI in solution was investigated by equilibrium sedimentation technique at two speeds and three concentrations. Figure 2-9 shows the data and fits analyzed by using Eqn. 1 for homogeneous 1x, 2x, and 4x models at ultracentrifugal speed of 26,000 rpm. The weighted root-mean-square errors (RMS) for the 1x and 4x fits were 5.01×10^{-2} and 6.90×10^{-2}, respectively. In contrast to these models, dimer (2x) model gave much improved RMS value of 7.93×10^{-3}. Residual distribution plot (Figure 2-9 inset) also supports that the apo-TaTPI forms dimer in solution. Analysis at 20,000 rpm (data not shown) also gave a better RMS value of 5.76×10^{-3} for 2x model than those for 1x (3.90×10^{-2}) and 4x (5.42×10^{-2}) models. Mixture or reversible models were also investigated but there was no indication of the possibility. Data analysis using the reversible model (Eqn. 2) gave large negative *In*k values for monomer-

dimer (1x-2x) and monomer-trimer (1x-3x) models and much higher RMS values (~10^{-2}), so the reversible models for monomer-dimer (1x-2x) and monomer-trimer (1x-3x) equilibrium would not be the case for TaTPI. These results strongly indicate that apo-TaTPI exits as homogeneous dimer in solution. In addition, analytical size-exclusion chromatography results of apo-TaTPI, which were confirmed at two different TaTPI protein concentrations (0.9 and 4.5 mg ml^{-1}), also supported the dimeric conformation in solution (Figure 2-10).

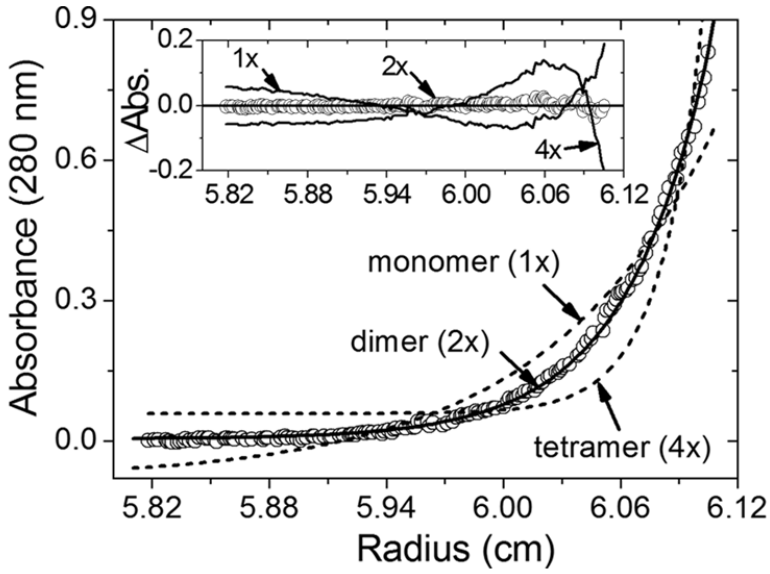

Figure 2-9. Analytical ultracentrifugation experiment of TaTPI

Sedimentation equilibrium distribution (circle) of TaTPI at 26,000 rpm and 20 ℃ is plotted as circle. Concentration of TaTPI was 16.8 u*M* (0.41 mg ml^{-1}) in 20 m*M* Tris-HCl, pH 7.5, and 0.2 *M* NaCl. Solid line is a fitting line for a homogeneous dimer (2x) model and dotted lines are fitting lines for homogeneous monomer (1x) and tetramer (4x) models. Calculated molecular weight for TaTPI monomer from its amino acid compositions is 24,671 daltons. Inset graph shows distributions of the residuals for homogeneous 1x, 4x (solid lines), and 2x (circle) models, respectively. The random distribution of the residuals for the 2x model indicates that TaTPI exists as homogeneous dimers in solution.

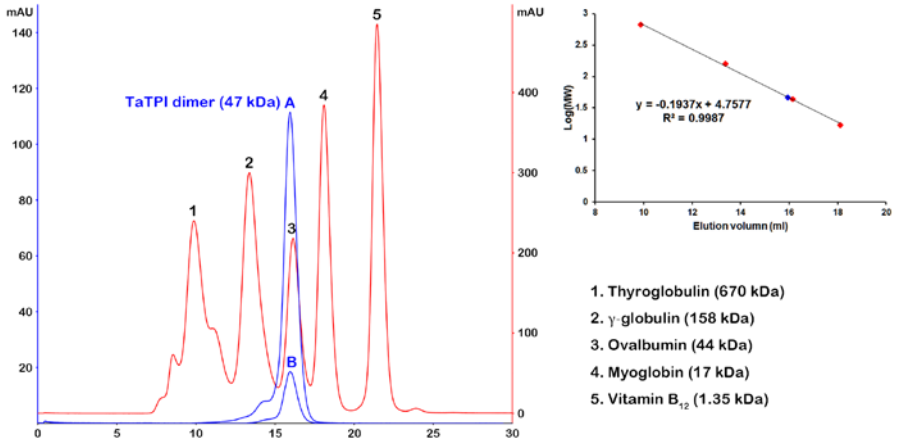

Figure 2-10. Analytical size-exclusion chromatography of TaTPI

TaTPI protein samples at two different concentrations (A: 4.5 mg ml^{-1}, B: 0.9 mg ml^{-1}) were applied to Superdex200 10/300 GL column. Chromatograms of TaTPI and gel filtration standard were shown as blue and red lines, respectively.

3.4. Structural stability of TaTPI under extreme acidic condition

T. acidophilum thrives in harsh environments such as high temperature and extremely acidic condition. TaTPI is also expected to function correctly at high temperature or in very low pH condition when physiological barriers are affected by various stresses. To elucidate the structural stability of TaTPI in extremely acidic condition and at high temperature, I carried out circular dichroism (CD) spectroscopy experiments.

As for the structural stability of TaTPI in extremely acidic condition, secondary structure changes of pH-titrated TaTPI were monitored using CD spectroscopy. Normally, intracellular environment is well kept from extracellular stresses such as abrupt pH change. So, most of intracellular proteins experience normal physiological conditions and function accordingly. TaTPI maintained its folded structure under extremely acidic condition (pH 1–2) as in neutral pH range. In the case of TaTPI, secondary structure contents under extremely acidic condition seem to change slightly with sustained folded structure. The content of α-helix in the TaTPI tends to increase with decreasing pH, whereas the content of β-strand decreases (Figure 2-11). These results suggest that TaTPI is designed to function normally even in cases of unexpected pH drop.

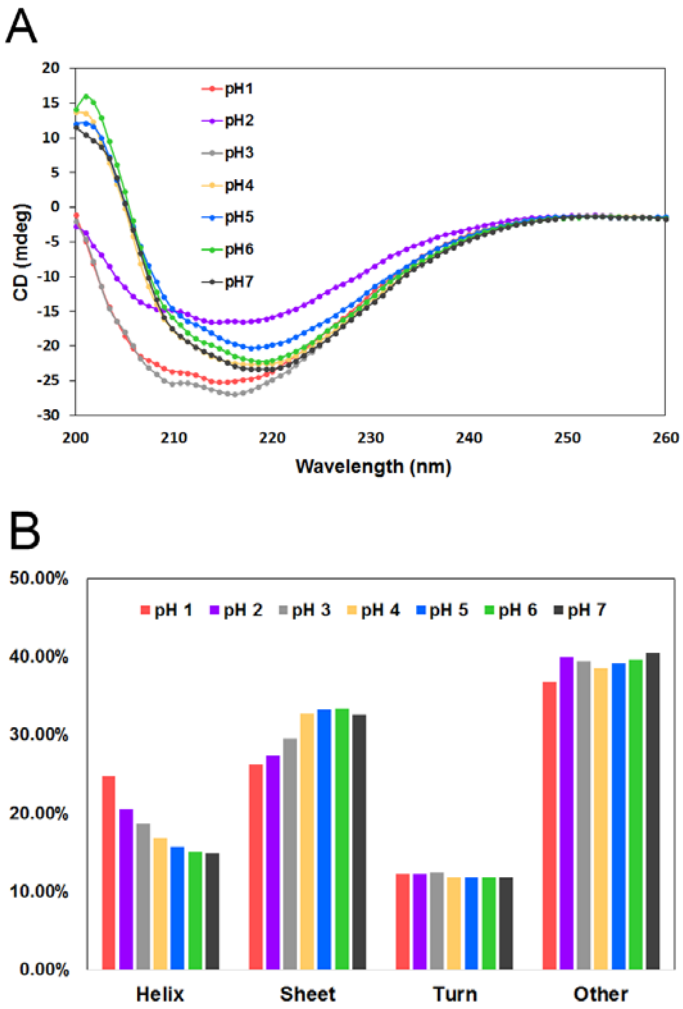

Figure 2-11. Circular dichroism spectra for TaTPI at variable pH conditions

(A) CD spectra of pH-titrated TaTPI (pH 1.0 – 7.0) were measured from 200 to 260 nm. (B) The secondary structure contents of pH-titrated TaTPI were calculated from Multivariate SSE Program (JASCO).

3.5. Structural stability of TaTPI at the high temperature

The temperature of maximum heat capacity (or half-denaturation temperature, Td) of TaTPI was measured by CD spectroscopy. The denaturation curve of TaTPI was analyzed by Kaleidagraph (Synergy Software) based on John and Weeks's protocol (John and Weeks, 2000, Protein science : a publication of the Protein Society, 47). The Td value for TaTPI is 74.6 ℃ (Figure 2-12), which is comparable with that of TPI from *Geobacillus stearothermophilus* (GsTPI), a biological indicator for the validation of sterilization processes, (T_d: 76 ℃) (Alvarez, et al., 1999, The Journal of biological chemistry, 56). In the case of GsTPI, a large number of prolines (5.2%), replacement of asparagine by histidine within the active site to prevent deamidation, the smallest cavity number and volume, and a large buried hydrophobic surface have been shown to contribute for the thermostability (Delboni, et al., 1995, Protein science : a publication of the Protein Society, 41). *Thermotoga maritima*, a hyperthermophilic bacterium, has been known to have TPI with the highest T_d value of 102 ℃ (Alvarez, et al., 1999, The Journal of biological chemistry, 56), resulting from a large number of salt bridges and extensive hydrophobic patches from tetramer conformation (Maes, et al., 1999, Proteins, 37). Using DSC, I found the Td app value of MjTPI to be 107.1 ℃ and it is the highest Td value among reported TPIs so far (Figure 2-13; Table 2-3). When compared

with TPIs mentioned above, TaTPI has smaller number of prolines (4.2%), larger cavity volume, and less buried hydrophobic surface than GsTPI, nor does it adopt tetrameric conformation.

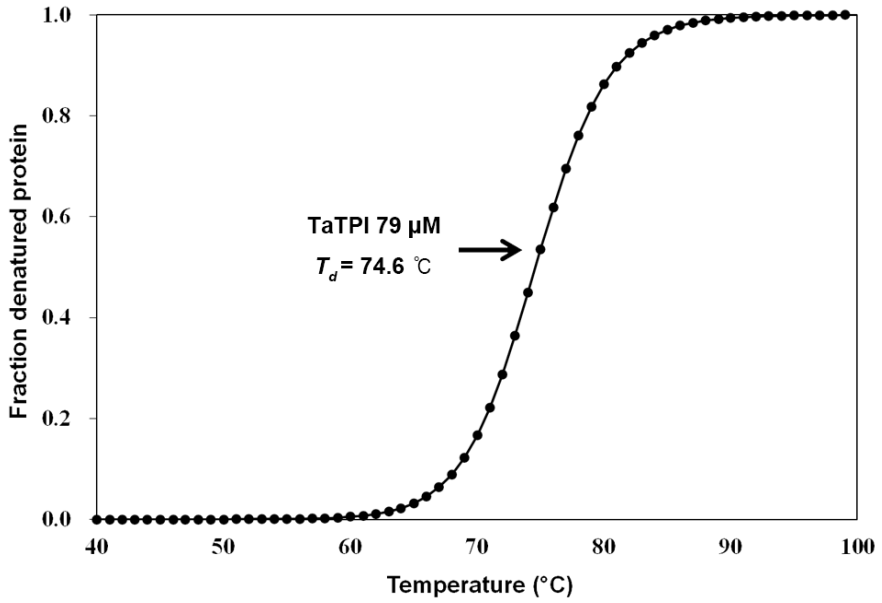

Figure 2-12. Thermal denaturation curve of TaTPI

Thermal denaturation curve of TaTPI was measured by CD spectroscopy.

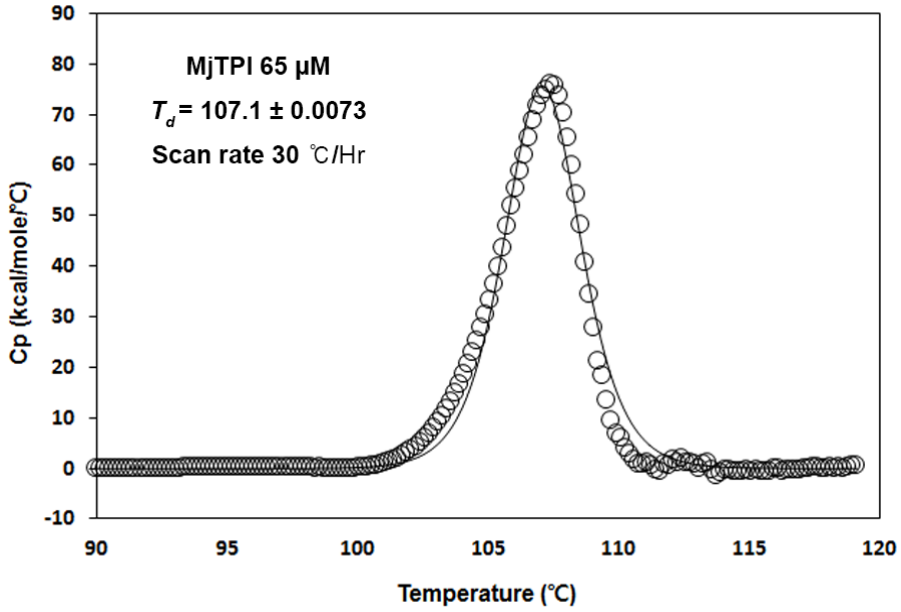

Figure 2-13. DSC thermogram of MjTPI

The black circle represents baseline-subtracted and normalized raw data. The black line indicates the best fits of the raw data. The maximum temperature of heat capacity (T_d) was calculated based on the best fits of the raw data.

Table 2-3. Half-denaturation temperatures of TPIs.

	The half-denaturation temperature ($T_{d,}$ ℃)	Reference
TaTPI	74 ℃	This manuscript
MjTPI	107 ℃	This manuscript
TmTPI	102 ℃	Alvarez et al., 1999
GsTPI	76 ℃	Alvarez et al., 1999
PfTPI	65 ℃	Gopal et al., 1999
HsTPI	55 ℃	Mainfroid et al., 1996
TbTPI	44 ℃	Borchert et al., 1993

Footnotes to Table 2-3

Ta, *Thermoplasma acidophilum*; Mj, *Methanocaldococcus jannaschii*; Tm, *Thermotoga maritima*; Gs, *Geobacillus stearothermophilus*; Pf, *Plasmodium falciparum*; Hs, *Homo sapience*; Tb, *Trypanosoma brucei*.

3.6. Proposal of TPI stabilization patches

TaTPI is composed of 216 amino acid residues and approximately 10% shorter in length than other TPIs from bacterial and eukaryotic species, which is a common feature in archaeal TPIs. According to the results of the structure-based sequence alignment for TPIs, helix 4, helix 5, and helix 6 are regions that mainly account for variation in amino acid composition, structural stability, and the oligomeric status of TPIs. To systematically validate the stabilization factors of TaTPI, I name regions of distinctive differences as TPI stabilization patches (TSPs) (Figure 2-14A). TSP1 is helix 4 region and TaTPI lacks a short helical N-terminus in this patch. Consequently, TaTPI forms a more compact structure. TSP2 exhibits a major structural discrepancy in that 18 amino acid residues are missing in helix 5 region of TaTPI, compared with other dimeric TPIs. In TSP2 area, truncated helix 5 (TSP2C) and lack of a short helix in its N-terminus (TSP2N) also make TaTPI tighter in their overall structure. Lastly, TSP3 arises from helix 6 region and helix 6 is trimmed along with a short α-helix in its C-terminus (Figure 2-14B). All the TSPs of TaTPI contribute to the formation of more compact dimeric structure.

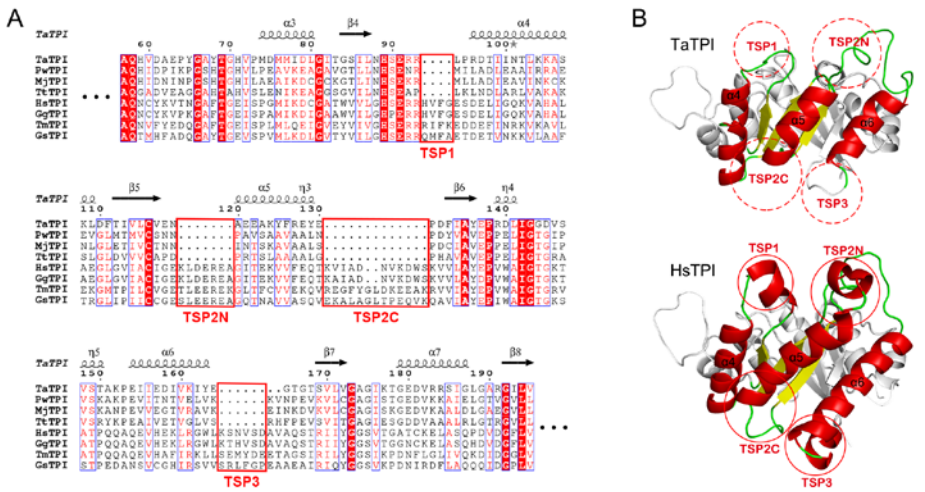

Figure 2-14. TPI stabilization patches (TSPs)

(A) Structure-based sequence alignment of TaTPI with other TPIs from *Pyrococcus woesei* (PwTPI), *Methanocaldococcus jannaschii* (MjTPI), *Thermoproteus tenax* (TtTPI), *Homo sapiens* (HsTPI), *Gallus gallus* (GgTPI), *Thermotoga maritima* (TmTPI), and *Geobacillus stearothermophilus* (GsTPI). Strictly conserved amino acid residues are highlighted in red shaded boxes and moderately conserved amino acid residues are colored in red. Conserved residues are enclosed in blue boxes and TSP regions are enclosed in red boxes. The alignment figure was prepared using *ESPript* program (Robert and Gouet, 2014, Nucleic acids research, 25). (B) Structural comparison of TaTPI and HsTPI. The red dotted and solid circles represent TSP regions in TaTPI and HsTPI, respectively.

The TSPs are not exclusive of TaTPI. Other tetrameric archaeal TPIs also have the TSPs. I speculated that other tetrameric archaeal TPIs could be more thermostable than TaTPI since they adopt tetrameric conformation and contains TSPs. To validate this speculation, I cloned and purified *M. jannaschii* TPI (MjTPI), a tetrameric archaeal TPI, and measured the Td app value of MjTPI. The Td app value of MjTPI was 107.1 ℃, which is the highest Td app value among reported TPIs so far. The result suggest that both higher oligomerization status and the TSPs could be important factors for thermostability of TPIs. TaTPI would keep its structural and functional integrity at high temperature through a compact dimeric conformation from contributing TSPs. Crystal structures of apo- and G3P-bound TaTPI and defined stability determining factors of TPIs would provide clear insights on engineering more stable TIM-barrel fold proteins which make up a large protein family and play pivotal role in metabolic pathways.

Reference

1. Normanly J, Abelson J. tRNA identity. Annual review of biochemistry 1989;58:1029-1049.
2. Eriani G, Delarue M, Poch O, Gangloff J, Moras D. Partition of tRNA synthetases into two classes based on mutually exclusive sets of sequence motifs. Nature 1990;347(6289):203-206.
3. Scheper GC, van der Klok T, van Andel RJ, van Berkel CG, Sissler M, Smet J, Muravina TI, Serkov SV, Uziel G, Bugiani M, Schiffmann R, Krageloh-Mann I, Smeitink JA, Florentz C, Van Coster R, Pronk JC, van der Knaap MS. Mitochondrial aspartyl-tRNA synthetase deficiency causes leukoencephalopathy with brain stem and spinal cord involvement and lactate elevation. Nature genetics 2007;39(4):534-539.
4. Neuenfeldt A, Lorber B, Ennifar E, Gaudry A, Sauter C, Sissler M, Florentz C. Thermodynamic properties distinguish human mitochondrial aspartyl-tRNA synthetase from bacterial homolog with same 3D architecture. Nucleic acids research 2012.
5. Deutscher MP. The eucaryotic aminoacyl-tRNA synthetase complex: suggestions for its structure and function. The Journal of cell biology 1984;99(2):373-377.

6. Lo WS, Gardiner E, Xu Z, Lau CF, Wang F, Zhou JJ, Mendlein JD, Nangle LA, Chiang KP, Yang XL, Au KF, Wong WH, Guo M, Zhang M, Schimmel P. Human tRNA synthetase catalytic nulls with diverse functions. Science 2014;345(6194):328-332.

7. Ray PS, Arif A, Fox PL. Macromolecular complexes as depots for releasable regulatory proteins. Trends Biochem Sci 2007;32(4):158-164.

8. Park SG, Ewalt KL, Kim S. Functional expansion of aminoacyl-tRNA synthetases and their interacting factors: new perspectives on housekeepers. Trends Biochem Sci 2005;30(10):569-574.

9. Robinson JC, Kerjan P, Mirande M. Macromolecular assemblage of aminoacyl-tRNA synthetases: quantitative analysis of protein-protein interactions and mechanism of complex assembly. J Mol Biol 2000;304(5):983-994.

10. Kaminska M, Havrylenko S, Decottignies P, Gillet S, Le Marechal P, Negrutskii B, Mirande M. Dissection of the structural organization of the aminoacyl-tRNA synthetase complex. J Biol Chem 2009;284(10):6053-6060.

11. Guzzo CM, Yang DC. Lysyl-tRNA synthetase interacts with EF1alpha, aspartyl-tRNA synthetase and p38 in vitro.

Biochemical and biophysical research communications 2008;365(4):718-723.

12. Woese CR, Olsen GJ, Ibba M, Soll D. Aminoacyl-tRNA synthetases, the genetic code, and the evolutionary process. Microbiology and molecular biology reviews : MMBR 2000;64(1):202-236.

13. Reed VS, Yang DC. Characterization of a novel N-terminal peptide in human aspartyl-tRNA synthetase. Roles in the transfer of aminoacyl-tRNA from aminoacyl-tRNA synthetase to the elongation factor 1 alpha. J Biol Chem 1994;269(52):32937-32941.

14. Reed VS, Wastney ME, Yang DC. Mechanisms of the transfer of aminoacyl-tRNA from aminoacyl-tRNA synthetase to the elongation factor 1 alpha. J Biol Chem 1994;269(52):32932-32936.

15. Cheong HK, Park JY, Kim EH, Lee C, Kim S, Kim Y, Choi BS, Cheong C. Structure of the N-terminal extension of human aspartyl-tRNA synthetase: implications for its biological function. The international journal of biochemistry & cell biology 2003;35(11):1548-1557.

16. Guo M, Schimmel P. Essential nontranslational functions of tRNA synthetases. Nature chemical biology 2013;9(3):145-153.

17. Cavarelli J, Eriani G, Rees B, Ruff M, Boeglin M, Mitschler A, Martin F, Gangloff J, Thierry JC, Moras D. The active site of yeast aspartyl-tRNA synthetase: structural and functional aspects of the aminoacylation reaction. The EMBO journal 1994;13(2):327-337.

18. Vagin A, Teplyakov A. Molecular replacement with MOLREP. Acta Crystallogr D Biol Crystallogr 2010;66(Pt 1):22-25.

19. Emsley P, Lohkamp B, Scott WG, Cowtan K. Features and development of Coot. Acta Crystallogr D Biol Crystallogr 2010;66(Pt 4):486-501.

20. Murshudov GN, Vagin AA, Dodson EJ. Refinement of macromolecular structures by the maximum-likelihood method. Acta Crystallogr D Biol Crystallogr 1997;53(Pt 3):240-255.

21. Lovell SC, Davis IW, Arendall WB, 3rd, de Bakker PI, Word JM, Prisant MG, Richardson JS, Richardson DC. Structure validation by Calpha geometry: phi,psi and Cbeta deviation. Proteins 2003;50(3):437-450.

22. Krissinel E, Henrick K. Inference of macromolecular assemblies from crystalline state. Journal of molecular biology 2007;372(3):774-797.

23. Sauter C, Lorber B, Cavarelli J, Moras D, Giege R. The free yeast aspartyl-tRNA synthetase differs from the tRNA(Asp)-

complexed enzyme by structural changes in the catalytic site, hinge region, and anticodon-binding domain. J Mol Biol 2000;299(5):1313-1324.

24. Messmer M, Blais SP, Balg C, Chenevert R, Grenier L, Lague P, Sauter C, Sissler M, Giege R, Lapointe J, Florentz C. Peculiar inhibition of human mitochondrial aspartyl-tRNA synthetase by adenylate analogs. Biochimie 2009;91(5):596-603.

25. Robert X, Gouet P. Deciphering key features in protein structures with the new ENDscript server. Nucleic acids research 2014;42(Web Server issue):W320-324.

26. Guo M, Yang XL, Schimmel P. New functions of aminoacyl-tRNA synthetases beyond translation. Nature reviews Molecular cell biology 2010;11(9):668-674.

27. Ofir-Birin Y, Fang P, Bennett SP, Zhang HM, Wang J, Rachmin I, Shapiro R, Song J, Dagan A, Pozo J, Kim S, Marshall AG, Schimmel P, Yang XL, Nechushtan H, Razin E, Guo M. Structural Switch of Lysyl-tRNA Synthetase between Translation and Transcription. Molecular cell 2012.

28. Olsen JV, Vermeulen M, Santamaria A, Kumar C, Miller ML, Jensen LJ, Gnad F, Cox J, Jensen TS, Nigg EA, Brunak S, Mann M. Quantitative phosphoproteomics reveals widespread

full phosphorylation site occupancy during mitosis. Science signaling 2010;3(104):ra3.

29. Schneider AS. Triosephosphate isomerase deficiency: historical perspectives and molecular aspects. Bailliere's best practice & research Clinical haematology 2000;13(1):119-140.

30. Celotto AM, Frank AC, Seigle JL, Palladino MJ. Drosophila model of human inherited triosephosphate isomerase deficiency glycolytic enzymopathy. Genetics 2006;174(3):1237-1246.

31. Arya R, Lalloz MR, Bellingham AJ, Layton DM. Evidence for founder effect of the Glu104Asp substitution and identification of new mutations in triosephosphate isomerase deficiency. Hum Mutat 1997;10(4):290-294.

32. Hollan S, Fujii H, Hirono A, Hirono K, Karro H, Miwa S, Harsanyi V, Gyodi E, Inselt-Kovacs M. Hereditary triosephosphate isomerase (TPI) deficiency: two severely affected brothers one with and one without neurological symptoms. Hum Genet 1993;92(5):486-490.

33. Daar IO, Artymiuk PJ, Phillips DC, Maquat LE. Human triose-phosphate isomerase deficiency: a single amino acid substitution results in a thermolabile enzyme. Proc Natl Acad Sci U S A 1986;83(20):7903-7907.

34. Jogl G, Rozovsky S, McDermott AE, Tong L. Optimal alignment for enzymatic proton transfer: structure of the Michaelis complex of triosephosphate isomerase at 1.2-A resolution. Proceedings of the National Academy of Sciences of the United States of America 2003;100(1):50-55.

35. Ruepp A, Graml W, Santos-Martinez ML, Koretke KK, Volker C, Mewes HW, Frishman D, Stocker S, Lupas AN, Baumeister W. The genome sequence of the thermoacidophilic scavenger Thermoplasma acidophilum. Nature 2000;407(6803):508-513.

36. Wierenga RK. The TIM-barrel fold: a versatile framework for efficient enzymes. FEBS Lett 2001;492(3):193-198.

37. Maes D, Zeelen JP, Thanki N, Beaucamp N, Alvarez M, Thi MH, Backmann J, Martial JA, Wyns L, Jaenicke R, Wierenga RK. The crystal structure of triosephosphate isomerase (TIM) from Thermotoga maritima: a comparative thermostability structural analysis of ten different TIM structures. Proteins 1999;37(3):441-453.

38. Xiao L, Honig B. Electrostatic contributions to the stability of hyperthermophilic proteins. Journal of molecular biology 1999;289(5):1435-1444.

39. Dams T, Auerbach G, Bader G, Jacob U, Ploom T, Huber R, Jaenicke R. The crystal structure of dihydrofolate reductase

from Thermotoga maritima: molecular features of thermostability. Journal of molecular biology 2000;297(3):659-672.

40. Szilagyi A, Zavodszky P. Structural differences between mesophilic, moderately thermophilic and extremely thermophilic protein subunits: results of a comprehensive survey. Structure 2000;8(5):493-504.

41. Delboni LF, Mande SC, Rentier-Delrue F, Mainfroid V, Turley S, Vellieux FM, Martial JA, Hol WG. Crystal structure of recombinant triosephosphate isomerase from Bacillus stearothermophilus. An analysis of potential thermostability factors in six isomerases with known three-dimensional structures points to the importance of hydrophobic interactions. Protein science : a publication of the Protein Society 1995;4(12):2594-2604.

42. Romero-Romero S, Costas M, Rodriguez-Romero A, Alejandro Fernandez-Velasco D. Reversibility and two state behaviour in the thermal unfolding of oligomeric TIM barrel proteins. Physical chemistry chemical physics : PCCP 2015;17(32):20699-20714.

43. Walden H, Bell GS, Russell RJ, Siebers B, Hensel R, Taylor GL. Tiny TIM: a small, tetrameric, hyperthermostable

triosephosphate isomerase. Journal of molecular biology 2001;306(4):745-757.

44. Otwinowski Z, Minor W. Processing of X-ray diffraction data collected in oscillation mode. Methods Enzymol 1997;276:307-326.

45. Laue TM. Sedimentation equilibrium as thermodynamic tool. Methods Enzymol 1995;259:427-452.

46. Knott GD. Mlab--a mathematical modeling tool. Comput Programs Biomed 1979;10(3):271-280.

47. John DM, Weeks KM. van't Hoff enthalpies without baselines. Protein science : a publication of the Protein Society 2000;9(7):1416-1419.

48. Zhang Z, Sugio S, Komives EA, Liu KD, Knowles JR, Petsko GA, Ringe D. Crystal structure of recombinant chicken triosephosphate isomerase-phosphoglycolohydroxamate complex at 1.8-A resolution. Biochemistry 1994;33(10):2830-2837.

49. Alvarez M, Zeelen JP, Mainfroid V, Rentier-Delrue F, Martial JA, Wyns L, Wierenga RK, Maes D. Triose-phosphate isomerase (TIM) of the psychrophilic bacterium Vibrio marinus. Kinetic and structural properties. The Journal of biological chemistry 1998;273(4):2199-2206.

50. Williams JC, Zeelen JP, Neubauer G, Vriend G, Backmann J, Michels PA, Lambeir AM, Wierenga RK. Structural and mutagenesis studies of leishmania triosephosphate isomerase: a point mutation can convert a mesophilic enzyme into a superstable enzyme without losing catalytic power. Protein engineering 1999;12(3):243-250.

51. Noble ME, Zeelen JP, Wierenga RK. Structures of the "open" and "closed" state of trypanosomal triosephosphate isomerase, as observed in a new crystal form: implications for the reaction mechanism. Proteins 1993;16(4):311-326.

52. Wierenga RK, Kapetaniou EG, Venkatesan R. Triosephosphate isomerase: a highly evolved biocatalyst. Cellular and molecular life sciences : CMLS 2010;67(23):3961-3982.

53. Walden H, Taylor GL, Lorentzen E, Pohl E, Lilie H, Schramm A, Knura T, Stubbe K, Tjaden B, Hensel R. Structure and function of a regulated archaeal triosephosphate isomerase adapted to high temperature. Journal of molecular biology 2004;342(3):861-875.

54. Gayathri P, Banerjee M, Vijayalakshmi A, Azeez S, Balaram H, Balaram P, Murthy MR. Structure of triosephosphate isomerase (TIM) from Methanocaldococcus jannaschii. Acta Crystallogr D Biol Crystallogr 2007;63(Pt 2):206-220.

55. Eisenberg D, Schwarz E, Komaromy M, Wall R. Analysis of membrane and surface protein sequences with the hydrophobic moment plot. Journal of molecular biology 1984;179(1):125-142.

56. Alvarez M, Wouters J, Maes D, Mainfroid V, Rentier-Delrue F, Wyns L, Depiereux E, Martial JA. Lys13 plays a crucial role in the functional adaptation of the thermophilic triose-phosphate isomerase from Bacillus stearothermophilus to high temperatures. The Journal of biological chemistry 1999;274(27):19181-19187.

국문초록

Structural and Biophysical Analyses of Aspartyl-tRNA Synthetase from *Homo sapiens* and Triosephosphate Isomerase from *Thermoplasma acidophilum*

Aspartyl-tRNA synthetase 와 triosephosphate isomerase 의 구조 및 생물학적 분석

Asaparty-tRNA synthetase (DRS) 단백질은 aspartic acid와 이를 인식하는 특정 tRNA을 연결시켜주는 효소이며, 또한 multi-tRNA synthetase complex (MSC)의 구성 단백질이다. MSC는 9가지 다른 aminoacyl-tRNA synthetase (AARSs)와 3개의 aminoacyl tRNA synthetase complex-interacting multifunctional protein (AIMP)로 구성된 단백질 복합체로, AARSs 단백질의 canonical과 non-canonical 기능을 조절하는 것으로 추정되나, 아직 확실한 기능은 밝혀져 있지 않다. 본 연구자는 DRS 단백질의 삼차원적 구조를 규명하였으며, 이를 바탕으로 DRS의 N말단의 유연구조부분을 예측하여 DRS와 $tRNA^{Asp}$사이의 상호작용을 예상하였다. 또한 번역후변형 (post-translational modification) 패턴을 분석하여 새로운 번역후변형 위치들을 발견하였다. 이 번역후변형들은 DRS와 $tRNA^{Asp}$의 계면에 위치하는 것으로 나타났으며, 둘의 결합에 영향을 줄 수 있을 것으로 보인다. 또한

DRS의 dimeric interface에 위치한 serine의 인산화로 인하여 DRS의 구조적 변화를 초래 할 것으로 예상되며, 이는 lysyl-tRNA synthetase (KRS)에서도 나타나는 방식이다. 전술한 특성들을 토대로 DRS의 알려지지 않은 non-canonical한 기능이 존재함을 추측할 수 있다.

*Thermoplasma acidophilum*은 호열성 고세균으로 당 (glucose) 분해를 위해 non-phosphorylative Entner-Doudoroff (ED) 과정과 Embden-Meyerhof-Parnas (EMP) 과정을 모두 이용할 수 있을 것으로 알려져 있다. 그 중 triosephosphate isomeraes (TPI) 단백질은 당분해 효소 중에 하나로 잘 알려져 있으나, *T.acidophilum*에서는 EMP 과정에서만 중요하게 사용 될 것으로 고려된다. 본 연구자는 *T.acidophilm*의 TPI (TaTPI) 단백질 및 glycerol-3-phosphate (G3P)의 결합구조들을 규명하였다. TaTPI 단백질은 다른 호열성 고세균 유래의 오솔로그들과 30% 정도의 서열 유사성을 지니지만, 다른 유형의 oligomerization을 통해 효소 활성을 유지한다. 즉, 지금까지 알려진 다른 호열성 고세균 유래의 TPI는 tetrameic 형태를 통해 가혹한 환경 속에서 효소의 안정성을 도모하지만, TaTPI의 경우 dimeric 형태로도 단백질의 안정성을 달성한다. 본 연구자는 초원심분리 및 크기배제크로마토그래피 분석을 통해 TaTPI 단백질이 dimeric 형태를 확증하였다. 이는 호열성 tetrameric TPI 단백질들의 경우 4, 5번째 α-helix들이 소수성 상호작용을 통해 oligomerization을 이루는데 반해, TaTPI 단백질의 경우 4, 5번째 α-helix들이 전하극성아미노산으로 이루어져 dimeric 형태로 존재하게 되는 것이다. TaTPI 단백질의 독특한 특성은 높은 온도뿐만 아니라, 매우

강한 산성 조건 (pH 1-2)에서도 단백질의 구조를 유지 하는 것에 일조한다. 이는 TaTPI의 구조·생물리학적 분석에 기초하여 볼 때, 다른 TPI보다 조밀한 구조가 *T.acidophilum* TPI에 내열·내산성을 부여한다고 볼 수 있다.

주요어: Aspartyl-tRNA synthetase, multi-tRNA synthetase complex, triosephosphate isomerase, glycolysis, crystal structure

학번: 2010-21682

Appendix：Printouts of first author publications

Acta Crystallographica Section F
Structural Biology and Crystallization Communications
ISSN 1744-3091

Overexpression, crystallization and preliminary X-ray crystallographic analysis of the C-terminal cytosolic domain of mouse anoctamin 1

Sang Ho Park,[a]‡ Ho Kyung Chung,[a]‡ Do Jin Kim,[b] Mi Ra Han,[a] Mi Seul Park,[a] Uhtaek Oh,[a] Hyun-Jung Kim[c]* and Byung Woo Han[a]*

[a]Research Institute of Pharmaceutical Sciences, College of Pharmacy, Seoul National University, Seoul 151-742, Republic of Korea, [b]Department of Chemistry, College of Natural Sciences, Seoul National University, Seoul 151-742, Republic of Korea, and [c]College of Pharmacy, Chung-Ang University, Seoul 156-756, Republic of Korea

‡ These authors contributed equally to this work.

Correspondence e-mail: hyunjungkim@cau.ac.kr, bwhan@snu.ac.kr

Received 23 May 2011
Accepted 12 July 2011

Transmembrane protein 16A (TMEM16A, also known as anoctamin 1; ANO1) is a bona fide Ca^{2+}-activated chloride channel that is activated by intracellular Ca^{2+}- and Ca^{2+}-mobilizing stimuli and plays important roles in a variety of physiological functions. To elucidate the structural features of ANO1, structural analysis of the C-terminal cytosolic domain of mouse ANO1 (mANO1-CTD) was initiated. mANO1-CTD was overexpressed in *Escherichia coli* and was crystallized at 297 K using a reservoir solution consisting of 0.2 *M* sodium acetate trihydrate, 0.1 *M* Tris–HCl pH 8.5 and 30%(*w*/*v*) PEG 4000. X-ray diffraction data were collected to 2.3 Å resolution. The crystals belonged to the orthorhombic space group $P2_12_12_1$, with unit-cell parameters a = 73.96, b = 103.73, c = 114.71 Å. If it is assumed that eight copies of a monomer molecule are present in the crystallographic asymmetric unit, the crystal volume per protein mass (V_M) is 2.38 Å^3 Da^{-1} and the solvent content is 48.38%. Attempts to solve the structure of mANO1-CTD by the MAD method using selenomethionine-labelled mANO1-CTD or heavy-atom-derivatized crystals are in progress.

1. Introduction

Ca^{2+}-activated chloride channels (CaCCs) play essential roles in many physiological processes, including transepithelial secretion, cardiac and neuronal excitation, sensory transduction, smooth muscle contraction and fertilization (Eggermont, 2004; Frings *et al.*, 2000; Hartzell *et al.*, 2005; Large & Wang, 1996). Anoctamin 1 (ANO1) is a recently discovered member of the CaCCs which is highly expressed in secretory epithelial tissues, including ductal glands, superficial epithelia of the airway, and oviduct, where it has been implicated to play a key role in calcium-dependent chloride secretion (Caputo *et al.*, 2008; Schroeder *et al.*, 2008; Yang *et al.*, 2008).

ANO1 is one of the members of the anoctamin (ANO, also known as transmembrane protein 16; TMEM16) family of membrane proteins, which consists of ten members (ANO1–10) in mammals. ANO1 consists of 26 exons and has been predicted to code for a variety of proteins (Caputo *et al.*, 2008). It belongs to a protein family with eight transmembrane helices and N- and C-terminal domains that face the cytoplasm (Galindo & Vacquier, 2005). ANO1 is essential for Ca^{2+}-dependent Cl^- currents in airways, the large intestine, salivary glands, pancreatic glands and hepatocytes (Ousingsawat *et al.*, 2009; Rock *et al.*, 2009; Romanenko *et al.*, 2010). Severe transport defects have been detected in epithelial tissues of ANO1-knockout mice, leading to reduced saliva production and attenuated mucociliary clearance of the airways (Lee & Foskett, 2010; Ousingsawat *et al.*, 2009; Rock *et al.*, 2009). Disruption of mouse ANO1 caused abnormal development of the trachea, indicating that the gene is a regulator of epithelial and smooth muscle cell organization in murine development (Rock *et al.*, 2009).

In addition to these results, recent studies have suggested the possibility that ANO1 proteins participate in tumourigenesis (Lee & Foskett, 2010; Yang *et al.*, 2008). The relationship between ANO1 and tumourigenesis has not been explained clearly, but a secretory environment might be important for tumour-cell proliferation. Thus, analysis of the ANO1 expression pattern in tumours could be used for the prediction or treatment of cancer.

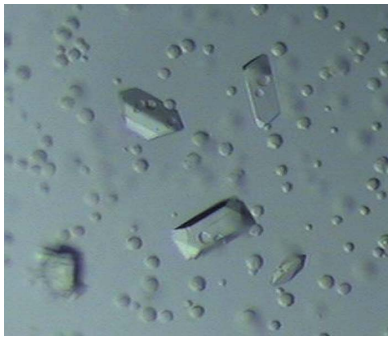

To facilitate the structural characterization of ANO1, we initiated structural study of the C-terminal cytosolic domain of mouse ANO1 (mANO1-CTD; residues 883–960; Fig. 1). In this report, we describe the overexpression, purification, crystallization and preliminary X-ray crystallographic analysis of recombinant mANO1-CTD.

2. Methods and results

2.1. Protein expression and purification

mANO1-CTD was cloned into the expression vector pET-15b(+) (Novagen), adding a hexahistidine-containing 20-residue tag to the N-terminus. The recombinant protein was overexpressed in *Escherichia coli* Rosetta2(DE3)pLysS cells using Luria broth culture medium. Protein expression was induced by 0.5 m*M* isopropyl β-D-1-thiogalactopyranoside and the cells were incubated for 16 h at 293 K following growth to mid-log phase at 310 K. The cells were lysed by sonication in lysis buffer (20 m*M* Tris–HCl pH 7.5, 500 m*M* NaCl, 35 m*M* imidazole and 1 m*M* phenylmethanesulfonylfluoride). The supernatant was applied onto a HiTrap Chelating HP column (GE Healthcare) which was previously equilibrated with buffer *A* (20 m*M* Tris–HCl pH 7.5, 500 m*M* NaCl and 35 m*M* imidazole). The protein was eluted with a linear gradient of 0.035–1.0 *M* imidazole in buffer *A*. The eluted sample was further purified by gel filtration on a HiLoad 16/60 Superdex 200 prep-grade column (GE Healthcare) which was equilibrated with 20 m*M* Tris–HCl pH 7.5 and 200 m*M* NaCl. The buffer of the fractions containing mANO1-CTD was gradually changed to buffer *B* (20 m*M* Tris–HCl pH 7.5 and 50 m*M* NaCl) using a Amicon Ultra-15 centrifugal filter device (Millipore). The sample was applied onto a HiTrap SP ion-exchange column (GE Healthcare) which was previously equilibrated with buffer *B*. The protein was eluted with a linear gradient of 0.05−1.0 *M* NaCl in buffer *B*. The homogeneity of the purified protein was assessed by SDS–PAGE. The buffer of the fractions containing mANO1-CTD was changed to 20 m*M* Tris–HCl pH 7.5 and 100 m*M* NaCl to reduce the concentration of NaCl and purified mANO1-CTD was concentrated to a final concentration of 9 mg ml^{-1} using an Amicon Ultra-15 centrifugal filter device (Millipore).

2.2. Crystallization and X-ray data collection

Crystals were grown by the sitting-drop vapour-diffusion method at 297 K by mixing equal volumes (1 µl each) of protein solution and reservoir solution. Crystals appeared after three weeks using a reservoir solution consisting of 0.1 *M* Tris–HCl pH 8.5, 0.2 *M* sodium acetate trihydrate and 30%(*v*/*v*) PEG 4000 with approximate dimensions of 0.1 × 0.1 × 0.3 mm (Fig. 2).

For diffraction data collection, the crystals were directly soaked in a cryoprotectant solution composed of 30%(*v*/*v*) glycerol added to the reservoir solution. X-ray diffraction data were collected at 100 K on a Quantum 4R CCD detector (Area Detector Systems Corporation, Poway, California, USA) at the BL-6C experimental station of Pohang Light Source, Republic of Korea (Fig. 3). For each image the crystal was rotated by 1° and the raw data were processed using the *HKL*-2000 program suite (Otwinowski & Minor, 1997). A total of 280 647 measured reflections were merged into 40 051 unique reflections with an $R_{\rm merge}$ of 12.7% and a completeness of 99.9%. The space group was determined to be $P2_12_12_1$ on the basis of systematic absences and symmetry of diffraction intensities using the *POINTLESS* program from *CCP*4 (Winn *et al.*, 2011). The unit-cell parameters are a = 73.96, b = 103.73, c = 114.71 Å. Table 1 summarizes the statistics of data collection. If it is assumed that eight copies of a

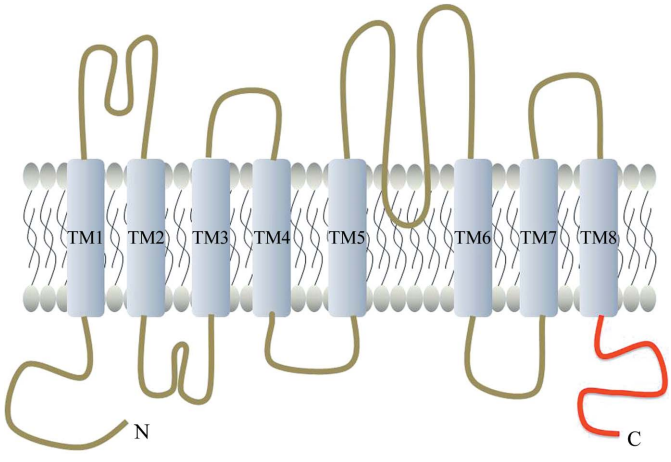

Figure 1
Predicted topology of mANO1. The cytosolic C-terminal domain of mANO1 is coloured red.

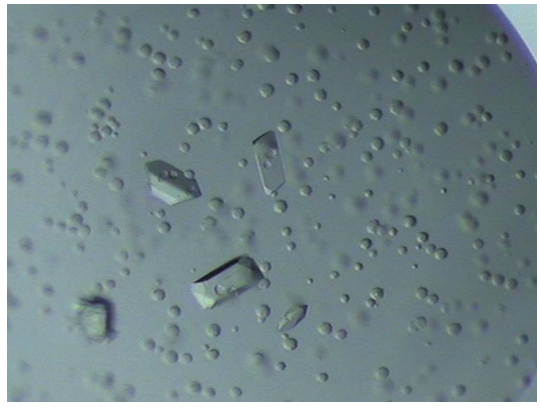

Figure 2
Native crystals of mANO1-CTD. The crystal dimensions are approximately 0.1 × 0.1 × 0.3 mm.

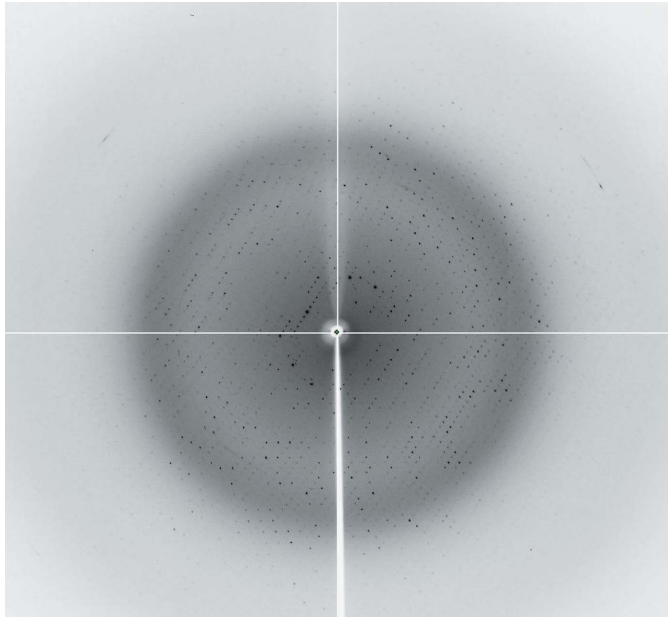

Figure 3
X-ray diffraction image from an mANO1-CTD crystal. The edge of the detector corresponds to a resolution of 2.0 Å.

Table 1
Data-collection statistics.

Values in parentheses are for the highest resolution shell.

X-ray source	Pohang Light Source beamline BL-6C
X-ray wavelength (Å)	1.23985
Temperature (K)	100
Space group	$P2_12_12_1$
Unit-cell parameters (Å)	a = 73.96, b = 103.73, c = 114.71
Resolution range (Å)	20–2.30 (2.34–2.30)
Total/unique reflections	280647/40051
$R_{\rm merge}$† (%)	12.7 (45.9)
Data completeness (%)	100.0 (99.9)
Multiplicity	7.0 (6.5)
Average $I/\sigma(I)$	18.8 (3.8)

† $R_{\rm merge} = \sum_{hkl}\sum_i |I_i(hkl) - \langle I(hkl)\rangle| / \sum_{hkl}\sum_i I_i(hkl)$, where $I_i(hkl)$ is the intensity of the ith measurement of reflection hkl and $\langle I(hkl)\rangle$ is the mean value of $I_i(hkl)$ for all i measurements.

monomer molecule are present in the crystallographic asymmetric unit, the crystal volume per protein mass ($V_{\rm M}$) is 2.38 Å^3 Da^{-1} and the solvent content is 48.38%. Attempts to solve the structure of mANO1-CTD by the MAD method using selenomethionine-labelled mANO1-CTD or heavy-atom-derivatized crystals are in progress.

We thank the staff at beamline BL-6C of Pohang Light Source for assistance during X-ray experiments. This research was supported by the Basic Science Research Program (2010-0028257 and 2011-0004305) and the Global Frontier (NRF-M1AXA002-2010-0029770) through the National Research Foundation of Korea (NRF) funded by the Ministry of Education, Science and Technology and by a grant from the Korea Healthcare Technology R&D Project, Ministry of Health and Welfare, Republic of Korea (A092006).

References

Caputo, A., Caci, E., Ferrera, L., Pedemonte, N., Barsanti, C., Sondo, E., Pfeffer, U., Ravazzolo, R., Zegarra-Moran, O. & Galietta, L. J. (2008). *Science*, **322**, 590–594.
Eggermont, J. (2004). *Proc. Am. Thorac. Soc.* **1**, 22–27.
Frings, S., Reuter, D. & Kleene, S. J. (2000). *Prog. Neurobiol.* **60**, 247–289.
Galindo, B. E. & Vacquier, V. D. (2005). *Int. J. Mol. Med.* **16**, 919–924.
Hartzell, C., Putzier, I. & Arreola, J. (2005). *Annu. Rev. Physiol.* **67**, 719–758.
Large, W. A. & Wang, Q. (1996). *Am. J. Physiol.* **271**, C435–C454.
Lee, R. J. & Foskett, J. K. (2010). *Am. J. Physiol. Lung Cell. Mol. Physiol.* **298**, L210–L231.
Otwinowski, Z. & Minor, W. (1997). *Methods Enzymol.* **276**, 307–326.
Ousingsawat, J., Martins, J. R., Schreiber, R., Rock, J. R., Harfe, B. D. & Kunzelmann, K. (2009). *J. Biol. Chem.* **284**, 28698–28703.
Rock, J. R., O'Neal, W. K., Gabriel, S. E., Randell, S. H., Harfe, B. D., Boucher, R. C. & Grubb, B. R. (2009). *J. Biol. Chem.* **284**, 14875–14880.
Romanenko, V. G., Catalán, M. A., Brown, D. A., Putzier, I., Hartzell, H. C., Marmorstein, A. D., Gonzalez-Begne, M., Rock, J. R., Harfe, B. D. & Melvin, J. E. (2010). *J. Biol. Chem.* **285**, 12990–13001.
Schroeder, B. C., Cheng, T., Jan, Y. N. & Jan, L. Y. (2008). *Cell*, **134**, 1019–1029.
Winn, M. D. *et al.* (2011). *Acta Cryst.* D**67**, 235–242.
Yang, Y. D., Cho, H., Koo, J. Y., Tak, M. H., Cho, Y., Shim, W.-S., Park, S. P., Lee, J., Lee, B., Kim, B.-M., Raouf, R., Shin, Y. K. & Oh, U. (2008). *Nature (London)*, **455**, 1210–1215.

PROTEINS
STRUCTURE ■ FUNCTION ■ BIOINFORMATICS

STRUCTURE NOTE

Crystal structure of human cytosolic aspartyl-tRNA synthetase, a component of multi-tRNA synthetase complex

Kyung Rok Kim,[1†] Sang Ho Park,[1†] Hyoun Sook Kim,[1] Kyung Hee Rhee,[1] Byung-Gyu Kim,[2] Dae Gyu Kim,[2] Mi Seul Park,[1] Hyun-Jung Kim,[3] Sunghoon Kim,[2] and Byung Woo Han[1*]

[1] Research Institute of Pharmaceutical Sciences, Department of Pharmacy, College of Pharmacy, Seoul National University, Seoul 151-742, Korea

[2] Medicinal Bioconvergence Research Center, Seoul National University, Seoul 151-742, Korea

[3] Department of Pharmacy, College of Pharmacy, Chung-Ang University, Seoul 156-756, Korea

Human cytosolic aspartyl-tRNA synthetase (DRS) catalyzes the attachment of the amino acid aspartic acid to its cognate tRNA and it is a component of the multi-tRNA synthetase complex (MSC) which has been known to be involved in unexpected signaling pathways. Here, we report the crystal structure of DRS at a resolution of 2.25 Å. DRS is a homodimer with a dimer interface of 3750.5 Å^2 which comprises 16.6% of the monomeric surface area. Our structure reveals the C-terminal end of the N-helix which is considered as a unique addition in DRS, and its conformation further supports the switching model of the N-helix for the transfer of tRNA^{Asp} to elongation factor 1α. From our analyses of the crystal structure and post-translational modification of DRS, we suggest that the phosphorylation of Ser146 provokes the separation of DRS from the MSC and provides the binding site for an interaction partner with unforeseen functions.

Proteins 2013; 81:1840–1846.

Key words: aspartyl-tRNA synthetase; multi-tRNA synthetase complex; N-helix; crystal structure.

INTRODUCTION

Aminoacyl-tRNA synthetases (AARSs) catalyze the attachment of respective amino acid substrate to its cognate tRNA through a two-step reaction.[1] An intermediate adenylate is formed from amino acid and ATP in the first step, and the amino acid is charged to the ribose of the terminal adenine of tRNA in the second step. Although AARSs catalyze the same type of reaction, they differ in amino acid sequence, size, three-dimensional structure, and oligomeric state. AARSs can be classified into two major classes; Classes I and II synthetase.[2] The Class I synthetase contains the representative Rossmann fold that binds ATP and the Class II synthetase adopts a core antiparallel β-sheet surrounded by α-helices and

Additional Supporting Information may be found in the online version of this article.

Abbreviations: AARS, aminoacyl-tRNA synthetase; AIMP, aminoacyl-tRNA synthetase-interacting multifunctional protein; DRS, aspartyl-tRNA synthetase; DRS2, mitochondrial aspartyl-tRNA synthetase; EF-1α, elongation factor 1α; KRS, lysyl-tRNA synthetase; MSC, multi-tRNA synthetase complex; NMR, nuclear magnetic resonance; NRS, asparaginyl-tRNA synthetase; PTM, post-translational modification.

Grant sponsor: Ministry of Education, Science and Technology (MEST), Republic of Korea; Grant number: 2012-054237 (Global Frontier Project funded through the National Research Foundation); Grant sponsor: National Cancer Center, Republic of Korea; Grant number: 1120170 (National R&D Program for Cancer Control).

[†]Kyung Rok Kim and Sang Ho Park contributed equally to this work.

*Correspondence to: Byung Woo Han, College of Pharmacy, Seoul National University, Seoul 151-742, Korea. E-mail: bwhan@snu.ac.kr

Received 5 February 2013; Revised 3 April 2013; Accepted 8 April 2013
Published online 23 April 2013 in Wiley Online Library (wileyonlinelibrary.com).
DOI: 10.1002/prot.24306

three unique conserved motifs namely Motifs 1, 2, and 3.[2]

For protein synthesis, AARSs play a basic cellular role not only in cytosol but also in mitochondria and most AARSs function distinctively in either location, and thus there are cytosolic or mitochondrial AARSs. In human, there are cytosolic and mitochondrial aspartyl-tRNA synthetases (DRS and DRS2), which share only 22.9% sequence identity. It has been known that DRS2 is associated with leukoencephalopathy with brain stem and spinal cord involvement and high lactate (LBSL)[3] and its structure revealed the function of the additional motif in the catalytic domain.[4] In the case of DRS, it is one of the components that forms the multi-tRNA synthetase complex (MSC) in higher eukaryotes.[5]

The MSC has been regarded as a reservoir for almost half of the cytosolic tRNA synthetases and it has been known to switch the canonical translational function and additional functions which are often observed in higher eukaryotes.[6,7] In the MSC, DRS is known to interact with the AARS-interacting multifunctional protein 2 (aminoacyl-tRNA synthetase-interacting multifunctional protein AIMP2/p38)[8,9] and the lysyl-tRNA synthetase (KRS).[10] The N-terminal extension of DRS, KRS, and asparaginyl-tRNA synthetase (NRS) is unique in the Class II synthetases and further classifies them into the subclass IIb.[11] The nuclear magnetic resonance (NMR) structure of the 21-residue N-terminal extension in DRS revealed that the N-terminal flexible β-turn followed by the amphipathic C-terminal helix induces the nonspecific tRNA binding and gives a force to transfer its charged tRNA to elongation factor 1α (EF-1α).[12–14]

In this study, we present the crystal structure of human cytosolic DRS at 2.25 Å. We show that DRS forms a homodimer with the N-terminal extension, anticodon-binding domain, hinge region, and catalytic domain. Analyses of our crystal structure and post-translational modification (PTM) shed lights on the molecular basis of the association and dissociation of DRS with the MSC.

MATERIALS AND METHODS

Cloning, protein expression, and purification

Human cytosolic full-length DRS (501 amino acids) was cloned into the pET-28a(+) vector containing the N-terminal His_6-tag (Novagen). The recombinant protein was transformed into *Escherichia coli* Rosetta2(DE3)pLysS strain. DRS was induced by 0.5 m*M* isopropyl 1-thio-β-D-galactopyranoside and incubated for 6 h at 310 K using Luria Broth culture medium. The harvested cell was sonicated with lysis buffer containing 20 m*M* of Tris-HCl (pH 7.5), 500 m*M* of NaCl, 35 m*M* of imidazole, and 1 m*M* of phenylmethanesulfonyl fluoride. The lysates were centrifuged at 35,000*g* for 50 min to remove the cell debris and denatured proteins. The supernatant was loaded onto a HiTrap Chelating HP column (GE Healthcare) and eluted with linear gradient 50–500 m*M* of imidazole following equilibration with 50 m*M* of imidazole. The protein was diluted with a buffer containing 50 m*M* of 4-(2-hydroxyethyl)-1-piperazineethanesulfonic acid (HEPES)–NaOH (pH 7.0), 50 m*M* of NaCl, 1 m*M* of dithiothreitol, and 5% of glycerol, and further purified using the ion exchange chromatography with a HiTrap Q HP column (GE Healthcare). The final purification step was the size-exclusion chromatography with a HiLoad 16/600 Superdex 200 prep grade column (GE Healthcare) equilibrated with 50 m*M* of HEPES–NaOH (pH 7.0), 200 m*M* of NaCl, 5% of glycerol, and 1 m*M* of dithiothreitol. For crystallization, the purified protein was concentrated to 11.1 mg mL^{-1}.

Crystallization, data collection, and structure determination

DRS crystals were grown by the sitting-drop vapor-diffusion method at 295 K by mixing equal volumes of the purified protein and the reservoir solution containing 8% v/v tacsimate (pH 8.0), and 20% w/v polyethylene glycol 3350. For diffraction data collection, crystals were soaked in the cryoprotectant solution containing 20% v/v glycerol added to the reservoir solution. X-ray diffraction data of the crystal were collected at the synchrotron BL-5A at the Photon Factory, Japan. The structure was solved by molecular replacement method with the structure of *Saccharomyces cerevisiae* DRS containing the anticodon-binding domain, hinge region, and catalytic domain (PDB ID: 1ASZ)[15] as a phasing model using *MOLREP*.[16] The structure was completed using alternate cycles of manual building in *WinCoot*[17] and refinement in *REFMAC*.[18] All refinement steps were monitored using an R_{free} value based on 5.0% of the independent reflections. The stereochemical quality of the final model was assessed using *MolProbity*.[19] The data collection and refinement statistics are summarized in Table I.

PTM analysis

Purified N-terminal OneSTrEP-tagged DRS and coeluted interaction partners of that, overexpressed and purified from HEK293T cells, were digested with sequencing grade gold-trypsin (Promega) after 1D-SDS PAGE/Coomassie blue staining. Tryptic peptides were analyzed with the LTQ Velos Orbitrap mass spectrometer equipped with an electron transfer dissociation source after an online reversed-phase chromatography. To improve sequencing coverage, we applied a data-dependent decision tree to select for collision-induced dissociation or electron-transfer dissociation fragmentation depending on the charged states, respectively. Protein identification was accomplished using the Sorcerer™-

Table I
Statistics for Data Collection, Phasing, and Model Refinement

Data collection[a]	Human cytosolic DRS
Space group	$P2_1$
Cell dimensions	
a, *b*, *c* (Å)	54.89, 141.92, 68.50
α, β, γ (°)	90, 102.19, 90
Data set	
X-ray wavelength (Å)	1.0000
Resolution (Å)[b]	50.00–2.25 (2.29–2.25)
Total/unique reflections	177,246/48,428
Completeness (%)	99.3 (95.4)
R_{merge} (%)[c]	11.0 (50.2)
Refinement	
Resolution (Å)	50.00–2.24
R_{work}[d]/R_{free}[e] (%)	19.7/22.8
No. of nonhydrogen atoms/mean B-factor (Å^2)	
Protein	6968/33.7
Water	354/40.2
Glycerol	48/52.5
Poor rotamers (%)[f]	3.1
Ramachandran plot analysis (%)	
Most favored regions	96.9
Additional allowed regions	3.1
Disallowed regions	0
R.m.s.d. from ideal geometry	
Bond lengths (Å)	0.010
Bond angles (°)	1.290

[a]Data collected at the synchrotron BL-5A at the Photon Factory, Japan.
[b]Numbers in parentheses indicate the highest resolution shell.
[c]$R_{merge} = \Sigma_h \Sigma_i |I(h)_i - <I(h)>| / \Sigma_h \Sigma_i I(h)_i$, where $I(h)$ is the observed intensity of reflection h, and $<I(h)>$ is the average intensity obtained from multiple measurements.
[d]$R_{work} = \Sigma ||F_o| - |F_c|| / \Sigma |F_o|$, where $|F_o|$ is the observed structure factor amplitude and $|F_c|$ is the calculated structure factor amplitude.
[e]R_{free} = *R*-factor based on 5.0% of the data excluded from refinement.
[f]Values obtained using *MolProbity*.

SEQUEST® (Sage-N Research), and searches were performed against the IPI human DB v3.87 fasta. The carbamidomethylation (+57.021 Da) of Cys is set as a static modification, and the following variable modification were allowed: GlyGly/+114.043 Da (Lys), Acetyl/+42.011 Da (Lys), HexNAc/+203.079 Da (Asn, Ser, Thr), Phospho/+79.966 Da (Ser, Thr, Tyr), Oxidation/+15.995 Da (Met), deamidated/+0.984 Da (Asn, Gln).

Data deposition

The coordinate and structure factors for human cytosolic DRS have been deposited in the RCSB Protein Data Bank, accession code 4J15.

RESULTS AND DISCUSSION

Overall structure and oligomeric state of DRS

The crystal structure of human cytosolic DRS was determined at a resolution of 2.25 Å by molecule replacement method with the structure of *S. cerevisiae* DRS containing the anticodon-binding domain, hinge region, and catalytic domain (PDB ID: 1ASZ)[15] as a phasing model. DRS contains a homodimer in the asymmetric unit and the dimer interface area is 3750.5 Å^2 which comprises 16.6% of the monomeric surface area calculated from Protein Interfaces, Surfaces, and Assemblies service.[20] Our crystal structure includes all the Class II AARS domains: anticodon-binding domain, hinge region, and catalytic domain. In addition, the N-terminal extension, which is a distinct domain in mammalian DRS, could be partially modeled including the C-terminal three residues of the characteristic helix motif [Fig. 1(A)]. Structural analyses on this N-terminal extension will be further discussed with the previous NMR structure below.

The anticodon-binding domain of DRS (residues, 57–146) adopts the oligonucleotide binding-fold (OB-fold) that is composed of a five-stranded antiparallel β-sheet connected by helices and loops (β1–β5) to form a closed β-barrel. The catalytic domain (residues, 189–497) contains 13 α-helices (αH–αT) and 8 β-strands (β6–β13) which constitute all the three conventional Class II AARS motifs: Motifs 1, 2, and 3.[2] The hinge region (residues, 156–188) plays an essential role in the connection of the anticodon-binding domain and the catalytic domain. In the middle of the hinge region, residues 163–172 could not be modeled owing to the lack of the electron density and the disordered residues are considered as a part of binding region to the ribose-phosphate backbone in the D-stem of tRNA^{Asp}, compared with the known *S. cerevisiae* DRS–tRNA^{Asp} complex structure.[15] In addition, residues 224–247 in the flipping loop and residues 273–282 in the Motif 2 could not be observed in our crystal structure [Fig. 1(B)]. These regions are known to be dynamic without its cognate tRNA and recognize its tRNA in an induced-fit manner.[21]

When the anticodon-binding domain, hinge region, and catalytic domain in our structure were independently superimposed with those of the *S. cerevisiae* DRS–tRNA^{Asp} complex structure, then the three domains were structurally well conserved with the root mean square deviation (r.m.s.d.) values of 1.08, 1.80, and 0.97 Å, respectively. In the anticodon-binding domain, three β-strands (β1, β2, and β3) could bind to the anticodon loop of tRNA^{Asp} which is composed of GUC elements. In the hinge region, short helices containing Asp158 and Asn175 could interact with the D-stem (U11, U12) of tRNA^{Asp}. In the catalytic domain, the flipping loop and the Class II Motif 2 play a key role in the interaction of DRS with the 3′-end of tRNAAsp. Detailed representations of the superposition results are shown in Supporting Information Figure S1.

Recently, the crystal structure of human mitochondrial DRS (DRS2) was solved at a resolution of 3.7 Å (PDB ID: 4AH6).[4] Human DRS and DRS2 share only 22.9% sequence identity [Fig. 1(B)]. However, when our crystal structure of DRS was superposed with that of DRS2, two

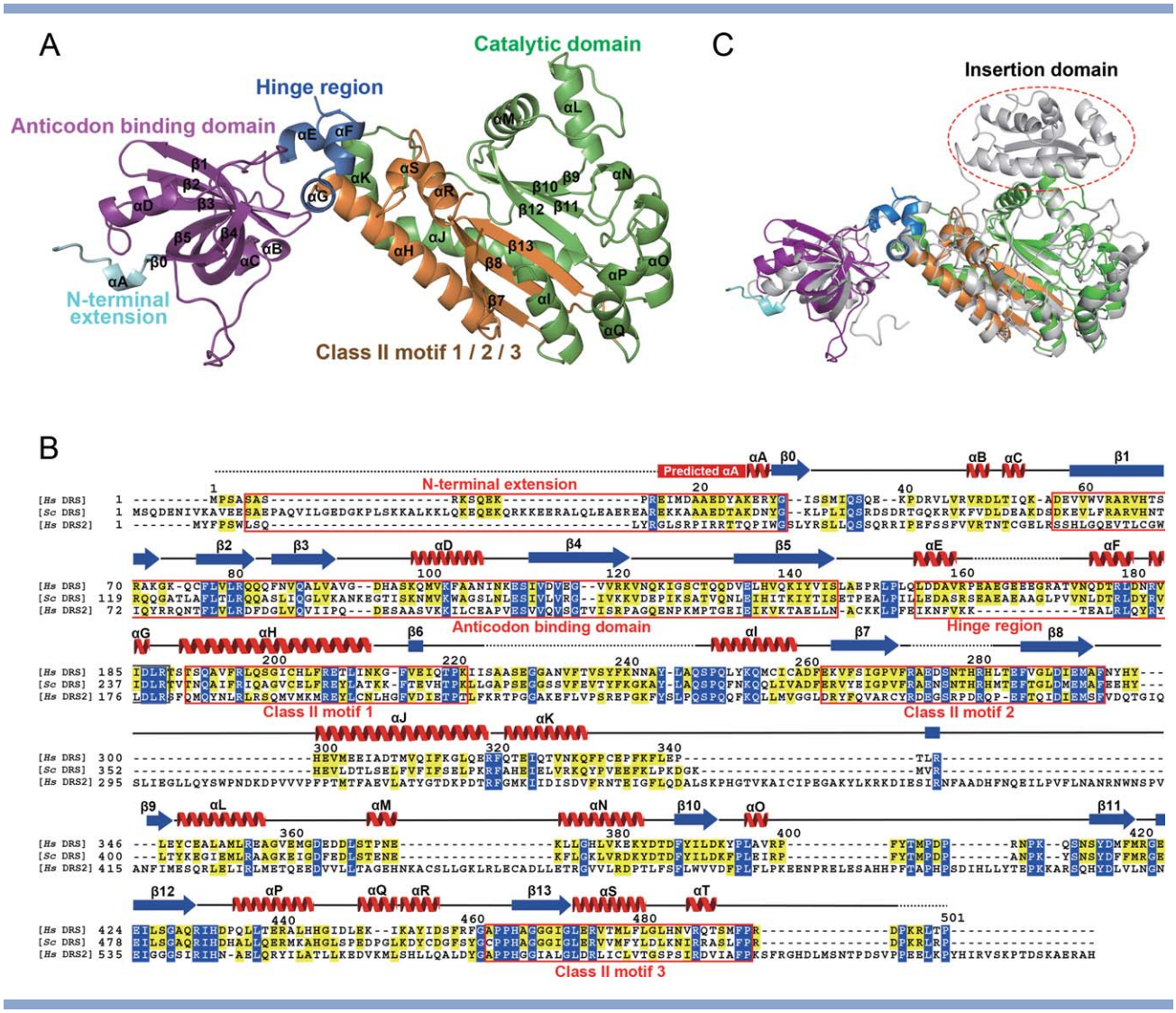

Figure 1

Overall structure of DRS. (**A**) DRS monomer. The N-terminal extension, anticodon-binding domain, hinge region, catalytic domain, and motifs are colored and labeled in cyan, magentas, blue, green, and orange, respectively. (**B**) Sequence alignment of human cytosolic DRS (*Hs* DRS) with *S. cerevisiae* DRS (*Sc* DRS) and human mitochondrial DRS (*Hs* DRS2). Strictly conserved residues are highlighted with blue-shaded boxes, and moderately conserved residues are shown as yellow-shaded boxes. The secondary structure of human DRS is shown on top of the sequence alignment. α-Helix, β-sheet, connecting region, and disordered region are represented by red spiral, blue arrow, black line, and dotted line, respectively. (**C**) Structural comparison of human cytosolic and mitochondrial DRSs. Human cytosolic DRS is shown as in (A) and mitochondrial DRS is colored in gray. The red dotted oval indicates the insertion domain of mitochondrial DRS.

structures are structurally similar to each other with the r.m.s.d. distance of 1.7 Å. The anticodon-binding domain, hinge region, and catalytic domain of DRS and DRS2 are structurally conserved, with the exception of an additional motif in the catalytic domain of DRS2 which is known as the insertion domain [Fig. 1(C)]. The insertion domain of DRS2 forms the enlarged catalytic groove with more electropositive surface potential, which enables an alternate interaction network at the subunit interface between tRNA and DRS2.[4] Interestingly, DRS2 showed a higher sensitivity than DRS for inhibitors with a nonhydrolysable adenylate moiety and its correlation with structural features has not been well understood.[22] Structural analyses of DRS and DRS2 in complex with same adenylate analogs would elucidate a subtle role of the domain difference with respect to substrate specificity and evolutionary advantages.

Flexible N-terminal extension of DRS

In higher eukaryotes, additional domains or motifs in a specific AARS result in new functions. In the case of DRS, KRS, and NRS, they contain the N-helix that is named after the helical conformation in part of their N-terminal extension region.[11,23] The previously determined NMR structure of the N-terminal extension of

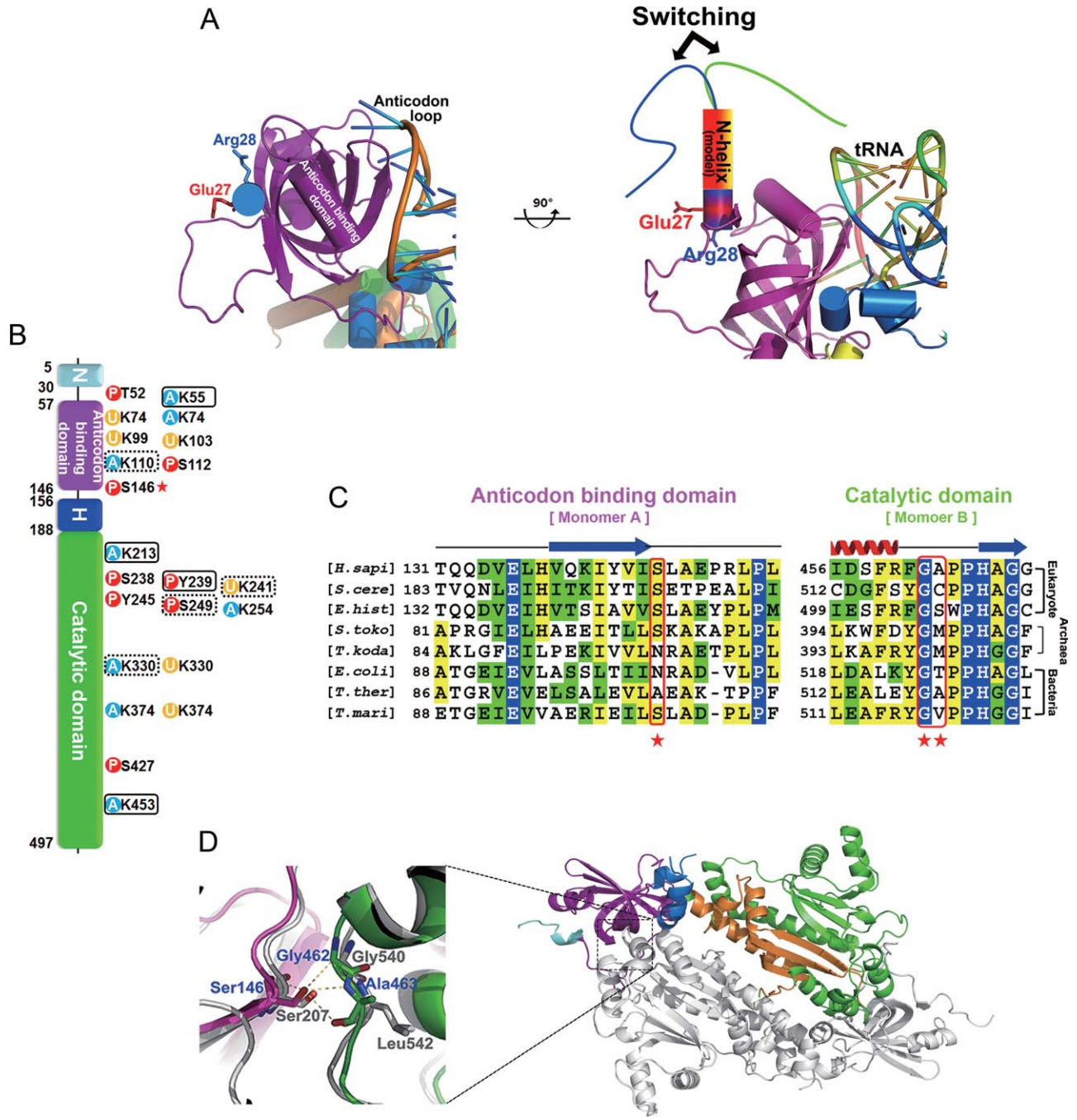

Figure 2

N-terminal extension, PTM, and key intermolecular interaction of DRS. (**A**) The switching model of the N-helix with our DRS structure. (**B**) PTM analyses. Acetylation, phosphorylation, and ubiquitination sites are shown as blue, red, and yellow circles, respectively. PTM sites uniquely observed in this study and residues observed both in the database and in our study are surrounded by black boxes and dotted boxes, respectively. Ser146, which is expected to play a key role in the organization of DRS, is marked with a red asterisk. (**C**) Sequence alignment of the interface residues of anticodon-binding domain and catalytic domain of DRSs from various organisms. Ser146, Gly462, and Ala463 of human DRS are marked with red asterisks. (**D**) Close-up view of Ser146 and the intermolecular interaction of DRS dimer. The structure of human DRS is superimposed with that of human KRS shown in a gray cartoon model.

DRS revealed the conformational flexibility caused by the β-turn followed by one α-helix and the N-terminal extension plays a crucial role in the interaction between $tRNA^{Asp}$ and EF-1α.[12–14] In our crystal structure, the C-terminal end of the α-helix in the N-terminal extension was observed, comprising Lys26, Glu27, and Arg28 although the N-terminal region was less-ordered. To get a glimpse of the whole N-helix structure, we superposed

the structurally well-resolved C-terminal end of the N-terminal extension residue Glu27 and Arg28 with the α-helix of the NMR structure, considering the helical wheel conformation (Supporting Information Fig. S2). The α-helix in the N-terminal extension is amphipathic and the hydrophilic face of the amphipathic helix could interact with positively charged residues Arg8 and Lys9 in the N-terminus by the conformational change on the flexible β-turn.[14] Our crystal structure further supports the structural switching model of the N-terminal extension of DRS in the aid of the direct transfer of $tRNA^{Asp}$ to EF-1α [Fig. 2(A)].

PTM of DRS and its implication on the MSC assembly

To speculate the organization of DRS as a main interacting component with AIMP2/p38 in the MSC assembly, we searched all the known PTM data and independently implemented the PTM analyses of DRS. Our liquid chromatography tandem mass spectrometry (MS) analysis revealed two phosphorylation sites (Tyr239 and Ser249) and six acetylation sites (Lys55, 110, 213, 241, 330, and 453), respectively. Among them, the phosphorylation of Tyr239 and the acetylation of Lys55, 213, and 453 were first identified. Our findings and other PTM site information of DRS from PhosphoSite Plus database (http://www.phosphosite.org) indicated that the residues 238–254 regions of the Class II AARS are dynamically regulated by various types of modifications such as phosphorylation, acetylation, and ubiquitination [Fig. 2(B)]. For instance, although Lys241 was identified with its acetylation modification in our analysis, collected six independent MS analysis data of ubiquitin branch motif (K-e-GG) immunoaffinity beads purification studies showed that Lys241 is also modified with ubiquitin. Thus, it seems that the phosphorylation status of Ser238, Tyr239, and/or Ser249 could affect the catalytic activity, stability, or partner-binding affinity of DRS through a competitive modification event between acetylation and ubiquitination of Lys241 and/or Lys254 though it should be clarified with further studies. PTM sites mapped on the surface representation of human DRS dimer modeled with $tRNA^{Asp}$ are shown in Supporting Information Figure S3.

In the MSC, AIMP2/p38 has been known to interact with two subcomplexes of the MSC (I: MRS, AIMP3/p18, EPRS, IRS, LRS; II: AIMP1/p43, QRS, RRS), KRS, and DRS, and the N-terminal domain of AIMP2/p38 interacts with the subcomplex II, KRS, and DRS.[9] The N-terminal Motifs 1 and 2 of AIMP2/p38 have been recently shown to interact with the bottom groove and the symmetric groove on the KRS dimer, respectively.[24] Based on the situational and structural similarity between KRS and DRS, we anticipated that two dimers of DRS would interact with AIMP2/p38 in the similar way of KRS regarding the association and dissociation from the MSC. In the case of KRS, Ser207 establishes the major intermolecular interaction of the KRS dimer through three hydrogen bonds between the hydroxyl group of Ser207 and the backbone of Gly540 and Leu541. Interestingly, a conformational change triggered by the phosphorylation of Ser207 switches the function of KRS from translation to transcription, provoking a new conformer and releasing KRS from the MSC.[24] To our surprise, DRS also contains the equivalent Ser146, Gly462, and Ala463, which are highly conserved in the amino acid sequence and three-dimensional structure in higher eukaryotes [Fig. 2(C–D)]. In addition, the PTM information of DRS from the PhosphoSite Plus database shows that the phosphorylation of Ser146 was already observed with the phosphoproteome analyses of the human cell cycle using the MS.[25] Thus, we suggest that the phosphorylation of Ser146 could initiate a conformation change of the DRS dimer and trigger an unpredicted function of DRS by releasing it from the MSC. Our structural study and PTM analyses extend the knowledge about the interaction of components in the MSC and provide fundamental information for human physiological signaling pathways related to the MSC.

ACKNOWLEDGMENTS

The authors thank the staff members of the BL-5A at the Photon Factory (Tsukuba, Japan) and the BL-7A at the Pohang Accelerator Laboratory (Pohang, Korea), Euiyoung Bae, Sojin Moon, and Dong Hyun Ka for data collection.

REFERENCES

1. Normanly J, Abelson J. tRNA identity. Annu Rev Biochem 1989;58:1029–1049.
2. Eriani G, Delarue M, Poch O, Gangloff J, Moras D. Partition of tRNA synthetases into two classes based on mutually exclusive sets of sequence motifs. Nature 1990;347:203–206.
3. Scheper GC, van der Klok T, van Andel RJ, van Berkel CG, Sissler M, Smet J, Muravina TI, Serkov SV, Uziel G, Bugiani M, Schiffmann R, Krageloh-Mann I, Smeitink JA, Florentz C, Van Coster R, Pronk JC, van der Knaap MS. Mitochondrial aspartyl-tRNA synthetase deficiency causes leukoencephalopathy with brain stem and spinal cord involvement and lactate elevation. Nature Genet 2007;39:534–539.
4. Neuenfeldt A, Lorber B, Ennifar E, Gaudry A, Sauter C, Sissler M, Florentz C. Thermodynamic properties distinguish human mitochondrial aspartyl-tRNA synthetase from bacterial homolog with same 3D architecture. Nucleic Acids Res 2012;41:2698–2708.
5. Deutscher MP. The eucaryotic aminoacyl-tRNA synthetase complex: suggestions for its structure and function. J Cell Biol 1984;99:373–377.
6. Ray PS, Arif A, Fox PL. Macromolecular complexes as depots for releasable regulatory proteins. Trends Biochem Sci 2007;32:158–164.
7. Park SG, Ewalt KL, Kim S. Functional expansion of aminoacyl-tRNA synthetases and their interacting factors: new perspectives on housekeepers. Trends Biochem Sci 2005;30:569–574.
8. Robinson JC, Kerjan P, Mirande M. Macromolecular assemblage of aminoacyl-tRNA synthetases: quantitative analysis of protein-protein interactions and mechanism of complex assembly. J Mol Biol 2000;304:983–994.

9. Kaminska M, Havrylenko S, Decottignies P, Gillet S, Le Marechal P, Negrutskii B, Mirande M. Dissection of the structural organization of the aminoacyl-tRNA synthetase complex. J Biol Chem 2009;284:6053–6060.
10. Guzzo CM, Yang DC. Lysyl-tRNA synthetase interacts with EF1alpha, aspartyl-tRNA synthetase and p38 in vitro. Biochem Biophys Res Commun 2008;365:718–723.
11. Woese CR, Olsen GJ, Ibba M, Soll D. Aminoacyl-tRNA synthetases, the genetic code, and the evolutionary process. Microbiol Mol Biol Rev 2000;64:202–236.
12. Reed VS, Yang DC. Characterization of a novel N-terminal peptide in human aspartyl-tRNA synthetase. Roles in the transfer of aminoacyl-tRNA from aminoacyl-tRNA synthetase to the elongation factor 1 alpha. J Biol Chem 1994;269:32937–32941.
13. Reed VS, Wastney ME, Yang DC. Mechanisms of the transfer of aminoacyl-tRNA from aminoacyl-tRNA synthetase to the elongation factor 1 alpha. J Biol Chem 1994;269:32932–32936.
14. Cheong HK, Park JY, Kim EH, Lee C, Kim S, Kim Y, Choi BS, Cheong C. Structure of the N-terminal extension of human aspartyl-tRNA synthetase: implications for its biological function. Int J Biochem Cell Biol 2003;35:1548–1557.
15. Cavarelli J, Eriani G, Rees B, Ruff M, Boeglin M, Mitschler A, Martin F, Gangloff J, Thierry JC, Moras D. The active site of yeast aspartyl-tRNA synthetase: structural and functional aspects of the aminoacylation reaction. EMBO J 1994;13:327–337.
16. Vagin A, Teplyakov A. Molecular replacement with MOLREP. Acta Crystallogr D Biol Crystallogr 2010;66:22–25.
17. Emsley P, Lohkamp B, Scott WG, Cowtan K. Features and development of Coot. Acta Crystallogr D Biol Crystallogr 2010;66:486–501.
18. Murshudov GN, Vagin AA, Dodson EJ. Refinement of macromolecular structures by the maximum-likelihood method. Acta Crystallogr D Biol Crystallogr 1997;53:240–255.
19. Lovell SC, Davis IW, Arendall WB, 3rd, de Bakker PI, Word JM, Prisant MG, Richardson JS, Richardson DC. Structure validation by Calpha geometry: phi,psi and Cbeta deviation. Proteins 2003;50:437–450.
20. Krissinel E, Henrick K. Inference of macromolecular assemblies from crystalline state. J Mol Biol 2007;372:774–797.
21. Sauter C, Lorber B, Cavarelli J, Moras D, Giege R. The free yeast aspartyl-tRNA synthetase differs from the tRNA(Asp)-complexed enzyme by structural changes in the catalytic site, hinge region, and anticodon-binding domain. J Mol Biol 2000;299:1313–1324.
22. Messmer M, Blais SP, Balg C, Chenevert R, Grenier L, Lague P, Sauter C, Sissler M, Giege R, Lapointe J, Florentz C. Peculiar inhibition of human mitochondrial aspartyl-tRNA synthetase by adenylate analogs. Biochimie 2009;91:596–603.
23. Guo M, Yang XL, Schimmel P. New functions of aminoacyl-tRNA synthetases beyond translation. Nat Rev Mol Cell Biol 2010;11:668–674.
24. Ofir-Birin Y, Fang P, Bennett SP, Zhang HM, Wang J, Rachmin I, Shapiro R, Song J, Dagan A, Pozo J, Kim S, Marshall AG, Schimmel P, Yang XL, Nechushtan H, Razin E, Guo M. Structural switch of Lysyl-tRNA synthetase between translation and transcription. Molr Cell 2012;49:30–42.
25. Olsen JV, Vermeulen M, Santamaria A, Kumar C, Miller ML, Jensen LJ, Gnad F, Cox J, Jensen TS, Nigg EA, Brunak S, Mann M. Quantitative phosphoproteomics reveals widespread full phosphorylation site occupancy during mitosis. Science Signal 2010;3:ra3.

PLOS | ONE

RESEARCH ARTICLE

Structure and Stability of the Dimeric Triosephosphate Isomerase from the Thermophilic Archaeon *Thermoplasma acidophilum*

Sang Ho Park[1], Hyoun Sook Kim[1], Mi Seul Park[1], Sojin Moon[2], Mi Kyung Song[1], Han Su Park[1], Hyunggu Hahn[1], Soon-Jong Kim[3], Euiyoung Bae[2], Hyun-Jung Kim[4], Byung Woo Han[1]*

1 Research Institute of Pharmaceutical Sciences, College of Pharmacy, Seoul National University, Seoul, Korea, **2** Department of Agricultural Biotechnology, Seoul National University, Seoul, Korea, **3** Department of Chemistry, Mokpo National University, Chonnam, Korea, **4** College of Pharmacy, Chung-Ang University, Seoul, Korea

* bwhan@snu.ac.kr

Citation: Park SH, Kim HS, Park MS, Moon S, Song MK, Park HS, et al. (2015) Structure and Stability of the Dimeric Triosephosphate Isomerase from the Thermophilic Archaeon *Thermoplasma acidophilum*. PLoS ONE 10(12): e0145331. doi:10.1371/journal.pone.0145331

Editor: Titus J. Boggon, Yale University School of Medicine, UNITED STATES

Received: August 14, 2015

Accepted: December 2, 2015

Published: December 28, 2015

Data Availability Statement: Atomic coordinates and structure factors are available from the Protein Data Bank database (accession number 5CSR and 5CSS, http://www.rcsb.org/pdb/search/structidSearch.do?structureId=5csr, http://www.rcsb.org/pd /search/structidSearch.do?structureId=5css).

Funding: This work was supported by Ministry of Science, ICT and Future Planning of Korea; Grant number: NRF-2011-0030001 and NRF-2013M-3A6A-4043695 (Tumor Microenvironment Global Core Research Center and Global Frontier Project funded through the National Research Foundation). The

Abstract

Thermoplasma acidophilum is a thermophilic archaeon that uses both non-phosphorylative Entner-Doudoroff (ED) pathway and Embden-Meyerhof-Parnas (EMP) pathway for glucose degradation. While triosephosphate isomerase (TPI), a well-known glycolytic enzyme, is not involved in the ED pathway in *T. acidophilum*, it has been considered to play an important role in the EMP pathway. Here, we report crystal structures of apo- and glycerol-3-phosphate-bound TPI from *T. acidophilum* (TaTPI). TaTPI adopts the canonical TIM-barrel fold with eight α-helices and parallel eight β-strands. Although TaTPI shares ~30% sequence identity to other TPIs from thermophilic species that adopt tetrameric conformation for enzymatic activity in their harsh physiological environments, TaTPI exists as a dimer in solution. We confirmed the dimeric conformation of TaTPI by analytical ultracentrifugation and size-exclusion chromatography. Helix 5 as well as helix 4 of thermostable tetrameric TPIs have been known to play crucial roles in oligomerization, forming a hydrophobic interface. However, TaTPI contains unique charged-amino acid residues in the helix 5 and adopts dimer conformation. TaTPI exhibits the apparent T_d value of 74.6°C and maintains its overall structure with some changes in the secondary structure contents at extremely acidic conditions (pH 1–2). Based on our structural and biophysical analyses of TaTPI, more compact structure of the protomer with reduced length of loops and certain patches on the surface could account for the robust nature of *Thermoplasma acidophilum* TPI.

funders had no role in study design, data collection and analysis, decision to publish, or preparation of the manuscript.

Competing Interests: The authors have declared that no competing interests exist.

Abbreviations: TaTPI, triosephosphate isomerase from *Thermoplasma acidophilum*; PDB, Protein Data Bank; G3P, glycerol-3-phosphate.

Introduction

Triosephosphate isomerase (TPI or TIM) is a functionally and structurally well-known enzyme that plays a crucial role in glycolytic and gluconeogenic metabolism. TPI accurately and efficiently interconverts dihydroxyacetone phosphate (DHAP) and glyceraldehyde-3-phosphate (GAP). Missense mutations of TPI genes result in TPI deficiency through loss-of-function [1]. TPI deficiency has been known to cause metabolic diseases, glycolytic enzymopathies, in which neurological pathogenesis is uniquely severe [2]. Pathogenic TPI deficiency mutations dramatically affect TPI activity owing to either catalytic interruption or oligomeric state alteration [3–5].

Thermoplasma acidophilum is one of the most acidophilic organisms among known thermophilic archaea. It optimally grows at 55–60°C and pH 0.5–2. For glucose degradation, *T. acidophilum* has been known to utilize not only non-phosphorylative Entner-Doudoroff (ED) pathway but also canonical glycolysis/gluconeogenesis pathway (Embden-Meyerhof-Parnas pathway) [6]. Although one of the glycolysis/gluconeogenesis pathway enzymes, phosphofructokinase, has not been identified in *T. acidophilum*, TPI has been considered to play a crucial role in the glycolysis/gluconeogenesis pathway in *T. acidophilum*.

TPI is a representative α/β protein with eight α-helices and eight β-strands connected by loops, forming a TIM-barrel fold [7]. The active site of TPI is highly conserved in all kingdoms and located inside of the TIM-barrel fold with three catalytic residues (Lys9, His89, and Glu137 in TaTPI numbering). Most TPIs are optimally active in their dimeric forms. In contrast, archaeal TPIs that withstand high temperatures are tetrameric in their active states [8]. Thermostable proteins have been known to adapt to high temperature in various ways: increased electrostatic interactions, hydrogen bonds, and hydrophobic effects, resulting in fortified subunit contacts, more compact packing, higher oligomerization state, and two-state equilibrium reversibility [9–13].

In the Protein Data Bank (PDB), structures of one bacterial TPI (*Thermotoga maritima;* Tm) and three archaeal TPIs (*Pyrococcus woesei;* Pw, *Thermoproteus tenax;* Tt, and *Methanocaldococcus jannaschii;* Mj) that have been deposited are in tetrameric form. *P. woesei*, *M. jannaschii*, and *T. acidophilum* belong to Euryarchaeota and *T. tenax* is affiliated to Crenarchaeota in phylogeny. Among tetrameric TPIs in PDB, tetrameric conformation of bacterial TmTPI is maintained by disulfide bonds between two classical TPI dimers [8]. In archaeal TPIs, helix 4 and helix 5 in the tetrameric interface are of key importance for their tetrameric forms. Especially, helix 5 in thermostable TPIs has been considered as a major contributor for tetramer formation via dominant hydrophobic effects [14].

In this work, we report crystal structures of apo- and glycerol-3-phosphate (G3P)-bound TaTPI, each representing open and closed form. Unlike other thermostable archaeal TPIs, TaTPI forms a stable dimer in solution, which we confirmed using analytical ultracentrifugation and size-exclusion chromatography. We also show the effect of pH on the secondary structure and temperature-induced unfolding of TaTPI. Through systematic comparison of TaTPI with available dimeric and tetrameric TPIs, we suggest that TPI stabilization patches can be targeted for the design of more stable TIM-barrel fold proteins.

Materials and Methods

Cloning, expression, and purification of TaTPI and MjTPI

Full-length sequence of *Thermoplasma acidophilum* TPI (TaTPI, 216 amino acid residues) and *Methanocaldococcus jannaschii* TPI (MjTPI, 219 amino acid residues) were amplified using PCR and cloned into pET-28a(+) vector (Novagen) containing C-terminal His_6-tag. Cloned plasmid were transformed into *Escherichia coli* Rosetta 2(DE3)pLysS strain. Recombinant

proteins were overexpressed by adding 0.5 m*M* IPTG (isopropyl 1-thio-ß-D-galactopyranoside) at $O.D._{600nm}$ 0.5 and cells were further incubated at 20°C overnight (16 h) using Luria Broth culture media. Harvested cells were lysed by cell sonicator (SONICS) in lysis buffer (20 m*M* Tris-HCl, pH 7.5, 500 m*M* NaCl, 35 m*M* imidazole, and 1 m*M* PMSF (phenylmethylsulfonyl fluoride)). After incubation of cell lysate at 60°C for 10 minutes, cell debris and denatured proteins were removed by centrifugation at 35,000 xg for 50 minutes. Supernatant was applied to HiTrap Chelating HP column (GE Healthcare) for affinity chromatography. Loaded sample was eluted with elution buffer (20 m*M* Tris-HCl, pH 7.5, 500 m*M* NaCl, and 500 m*M* imidazole) following equilibration with washing buffer (20 m*M* Tris-HCl, pH 7.5, 500 m*M* NaCl, and 50 m*M* imidazole). Eluted sample was further purified by size-exclusion chromatography with HiLoad 16/600 Superdex 200 prep grade column (GE Healthcare) equilibrated with 20 m*M* Tris-HCl, pH 7.5, and 200 m*M* NaCl. Fractions containing TPI proteins were further purified by anion exchange chromatography with HiTrap Q HP column (GE Healthcare) after 2 X dilution of the fractions with 20 m*M* Tris-HCl, pH 7.5, and 100 m*M* NaCl. Linear gradient of 0–500 m*M* NaCl in 20 m*M* Tris-HCl, pH 7.5, was applied for elution. For the final purification step, second size-exclusion chromatography was performed with HiLoad 16/600 Superdex 200 prep grade column (GE Healthcare) equilibrated with 20 m*M* Tris-HCl, pH 7.5, and 200 m*M* NaCl for TaTPI or 50 m*M* HEPES (4-(2-hydroxyethyl)-1-piperazineethanesulfonic acid), pH 7.5, for MjTPI. For crystallization, purified TaTPI proteins were concentrated to 30 mg ml^{-1}.

Crystallization and structure determination

Initial crystals of apo-TaTPI were grown at 22°C by sitting drop vapor diffusion method with crystallization solution containing 2 *M* NaCl and 10% (w/v) polyethylene glycol 6000. Apo-TaTPI crystals suitable for diffraction data collection were grown at 4°C using hanging-drop vapor diffusion method after mixing apo-TaTPI proteins with 2 times volume of crystallization solution containing 0.5 *M* NaCl, 10% (w/v) polyethylene glycol 6000, and 0.1 *M* Tris-HCl, pH 8.5. Crystals of TaTPI in complex with glycerol-3-phosphate (G3P) were obtained from crystallization solution with 0.6 *M* NaCl, 9% (w/v) polyethylene glycol 6000, and 0.1 *M* Tris-HCl, pH 8.5, after incubating purified apo-TaTPI proteins with 20 m*M* G3P for 4 h at 4°C. For diffraction data collection, crystals were frozen in liquid nitrogen following cryoprotection by soaking TaTPI crystals in crystallization solution supplemented with 20% glycerol. X-ray diffraction data for apo- and G3P-bound complex TaTPI crystals were collected at BL-7A synchrotron beamline at the Pohang Light Source, Korea, and at BL-1A synchrotron beamline at the Photon Factory, Japan, respectively. Collected data were processed using *HKL*2000 program suite [15]. The crystal structure of apo-TaTPI was solved by molecular replacement method using MOLREP program [16], with the crystal structure of *Pyrococcus woesei* TPI (PDB ID: 1HG3) as a phasing model [14]. The crystal structure of G3P-bound TaTPI was solved with the apo-TaTPI structure as a phasing model. The initial model building was carried out by *WinCoot* program [17] and further refined with *REFMAC*5 program [18]. All refinement steps were monitored using R_{free} value based on 5.0% of independently saved reflections. The final model was evaluated with *MolProbity* program [19]. Data collection and refinement statistics are summarized in Table 1.

Analytical ultracentrifugation (AUC)

Equilibrium sedimentation studies were performed using Beckman ProteomeLab XL-A analytical ultracentrifuge in 20 m*M* Tris-HCl buffer, pH 7.5, and 200 m*M* NaCl at 20°C. Sedimentation data were collected at 280 nm using a six-sector cell at rotor speeds of 20,000 and 26,000 rpms with three different protein concentrations: 12.6 u*M* (0.31 mg ml^{-1}), 16.8 u*M* (0.41 mg ml^{-1}), and

Table 1. Statistics for data collection, phasing, and model refinement.

Data collection[a]	TaTPI	G3P-bound TaTPI
Space group	$P2_12_12_1$	$P2_12_121$
Cell dimensions		
a, b, c (Å)	75.49, 113.96, 114.80	72.63, 84.08, 143.54
α, β, γ (°)	90, 90, 90	90, 90, 90
Data set		
X-ray wavelength (Å)	1.0000	1.1000
Resolution (Å)[b]	50.00–1.94 (1.97–1.94)	50.00–2.17 (2.21–2.17)
Total / unique reflections	521,936 / 73,921	294,576 / 47,245
Mean *I/sigma(I)*	32.4 (3.3)	20.9 (3.0)
Multiplicity	7.1 (5.6)	6.2 (5.6)
Completeness (%)	99.0 (83.5)	99.9 (99.9)
R_{merge} (%)[c]	9.1 (62.5)	13.4 (59.0)
Refinement		
Resolution (Å)	50.00–1.94	50.00–2.17
R_{work}[d] / R_{free}[e] (%)	18.0 / 21.5	18.3 / 22.5
No. of non-hydrogen atoms / mean B-factor (Å^2)		
Protein	6,996 / 32.9	6,640 / 34.2
Water	561 / 39.8	401 / 34.4
Other atoms	28 / 40.1	44 / 22.9
Poor rotamers (%)[f]	0.1	0.3
Ramachandran plot analysis (%)		
Most favored regions	98.0	96.1
Additional allowed regions	2.0	3.4
Disallowed regions	0	0.5
R.m.s.d. from ideal geometry		
Bond lengths (Å)	0.019	0.015
Bond angles (°)	1.648	1.550

[a]Data collected at the synchrotron BL-7A at the Pohang Light Source and BL-1 at the Photon Factory.
[b]Numbers in parentheses indicate the highest resolution shell.
[c]$R_{merge} = \Sigma_h \Sigma_i |I(h)_i - \langle I(h) \rangle| / \Sigma_h \Sigma_i I(h)_i$, where $I(h)$ is the observed intensity of reflection h, and $< I(h) >$ is the average intensity obtained from multiple measurements.
[d]$R_{work} = \Sigma \, | |F_o| - |F_c| \, | / \Sigma |F_o|$, where $|F_o|$ is the observed structure factor amplitude and $|F_c|$ is the calculated structure factor amplitude.
[e]R_{free} = R-factor based on 5.0% of the data excluded from refinement.
[f]Values obtained using MolProbity.

doi:10.1371/journal.pone.0145331.t001

21.0 u*M* (0.52 mg ml^{-1}). All measured data fit well to a homogeneous dimer model and representative results measured at 26,000 rpm using 16.8 u*M* protein concentration are presented. TaTPI concentrations were calculated using e_{280nm} = 11,920 M^{-1}cm^{-1} and molecular weight of 24,671 daltons. Time required for the attainment of equilibrium was established by running at given rotor speed until scans were invariant for 4 hours: this was achieved at most by 36 hours in six-sector cells using 130 ul of samples. Partial specific volume of TaTPI protein and buffer density were calculated using Sednterp [20]. The calculated partial specific volume at 20°C was 0.7417 cm^3 g^{-1} and the buffer density was 1.00704 g cm^{-3}. For data analysis by mathematical modeling using non-linear least-squares curve fitting, following functions were used for homogeneous

(Eq 1) and interactive (Eq 2) models.

$$C_r = C_b exp[A_p M_p (r^2 - r_b{}^2)] + \varepsilon \quad \text{(Eq.1)}$$

$$C_r = C_b exp[A_p M_p (r^2 - r_b{}^2)] + C_b{}^n exp[Ink + nA_p M_p (r^2 - r_b{}^2)] + \varepsilon \quad \text{(Eq.2)}$$

$$A_p = (1 - v\rho)\omega^2 \div 2RT$$

where C_r is the total concentration at the radial position r, C_b is the concentration of protein at the cell bottom, M_p is the molecular weight of protein monomer, ε is a baseline error term, v and ρ are the partial specific volume and the solution density, respectively, and ω is the rotor angular velocity. The *In*k value is a natural log for equilibrium constants for reversible models (1x-nx, where n is 2 & 3) on an absorbance scale. Selection of the best model was made by examining numbers of weighted sum of square and root mean square error values. Further data manipulation and data analysis by mathematical modeling were performed using MLAB [21].

Circular dichroism (CD)

Temperature of maximum heat capacity (or half-denaturation temperature, Td) of TaTPI was measured by CD spectroscopy. Experimental sample was prepared following purification and concentration of TaTPI proteins to 0.4 mg ml^{-1} containing 50 m*M* HEPES, pH 7.5. CD traces of TaTPI were obtained at 222 nm using the J-1500 CD spectrometer (JASCO) at a scanning rate of 1°C min^{-1}. The denaturation curve of TaTPI was analyzed by Kaleidagraph (Synergy Software) based on John and Weeks's protocol [22].

Effect of pH variation on the secondary structure of TaTPI was also monitored by CD spectroscopy. pH of protein solutions containing 20 m*M* Tris-HCl and 200 m*M* NaCl was adjusted to desired values between pH 1.0 and pH 7.0 with HCl for CD measurements. The baseline signal was measured with a buffer containing 20 m*M* Tris-HCl, pH 7.5, and 200 m*M* NaCl. CD spectra of pH-titrated TaTPI were recorded and averaged over two scans between 200 to 260 nm using J-1500 CD spectrometer (JASCO). The secondary structure contents of TaTPI were calculated by Multivariate SSE Program (JASCO).

Analytical size-exclusion chromatography

Analytical size-exclusion chromatography of TaTPI was performed with Superdex 200 10/300 GL column (GE Healthcare) following equilibration with 20 m*M* Tris-HCl, pH 7.5, and 200 m*M* NaCl. The applied protein were at concentrations of 0.9 and 4.5 mg ml^{-1}. Standard proteins from Gel Filtration Standard (BIO-RAD) were applied to the column for calibration. The standard protein mixture contained thyroglobulin (M.W. 670 kDa), γ-globulin (M.W. 158 kDa), ovalbumin (M.W. 44 kDa), myoglobin (M.W. 17 kDa), and vitamin B_{12} (M.W. 1.35 kDa).

Differential scanning calorimetry (DSC)

Maximum temperature of heat capacity of MjTPI was measured with VP-DSC differential scanning microcalorimeter (Malvern). Experimental sample was prepared following purification and concentration of MjTPI proteins to 1.6 mg ml^{-1} (65 u*M*). Sample buffer containing 50 m*M* HEPES, pH 7.5, was loaded into the DSC cell after degassing in an evacuated chamber for 5 minutes and reference data were measured with scan rate of 0.5°C min^{-1}. Experimental temperature was increased in the range from 50 to 120°C. After sample buffer scan reached equilibrium, MjTPI proteins were carefully loaded into the cell following degassing and

experiments were performed under the same condition as for the reference. Heat capacity curve was plotted using the Origin software (Malvern).

Accession numbers

The structure coordinates and structure factors for apo- and G3P-bound TaTPI have been deposited in PDB under the accession code 5CSR and 5CSS, respectively.

Results and Discussion

Overall structures of apo- and glycerol-3-phosphate-bound TaTPI

The crystal structures of apo-TaTPI and its complex with glycerol-3-phosphate (G3P), an analogue of the substrate glyceraldehyde-3-phosphate, have been determined at 1.94 and 2.17 Å resolution, respectively. R_{work}/R_{free} values for the final models of apo- and G3P-bound TaTPI were 18.0%/21.5% and 18.3%/22.5%, respectively (Table 1). Crystal structures of apo- and G3P-bound TaTPI contain four copies of TaTPI monomer in the asymmetric unit, comprising two homodimers. The overall structure of TaTPI protomer confirms to the canonical TIM-barrel fold with eight α-helices and eight parallel β-strands from 216 amino acid residues (Fig 1A). The crystal structure of G3P-bound TaTPI reveals that G3P is well positioned at the active site of TaTPI with functionally conserved residues Lys9, His89, and Glu137 (Fig 1B). Glu137 is clearly demonstrated as a catalytic base, with its position being within 3 Å from O1 and O2 of G3P. An oxyanion hole, which contributes to the stabilization of transition state, is formed by NZ nitrogen of Lys9 and NE2 nitrogen of His89 with O2 oxygen of G3P. The phosphate group of G3P is perfectly coordinated through hydrogen bonds with backbone nitrogen atoms of Gly143, Gly175, Ala196, and Ser197 residues, including adjacent water molecules (S1 Fig).

Overall structures of apo- and G3P-bound TaTPI were similar with r.m.s.d. of 0.69 Å for 216 C_α positions, except G3P-bound area. The conformational changes in the loop 6 of ligand bound-TPIs have been reported in previously determined structures of TPIs from many species, including *Trypanosoma brucei*, *Gallus gallus*, *Geobacillus stearothermophilus*, *Leishmania mexicana*, and *Vibrio marinus* [12, 23–27]. Likewise, loop 6 located between β-strand 6 and helix 6 and loop 7 located between β-strand 7 and helix 7 showed remarkable conformational changes when G3P binds to apo-TaTPI. When compared with apo-TaTPI structure, Gly143 located in loop 6 and Gly175 located in loop 7 moved toward G3P by 8.3 and 3.8 Å, respectively (Fig 1B). Consequently, residue Ala174 is pushed to a disallowed region of the Ramachandran plot in the G3P-bound form, an amino acid residue within loop 7 that is displaced by the ligand binding. G3P binding triggers the conformational change and induces the transformation of TaTPI from open to closed form, securing the catalytic site from bulk solvent to maintain efficient catalytic activity. In addition, water molecules around the active site of apo-TaTPI are expelled from the active site and would be replaced with substrate upon substrate binding.

Unique dimeric conformation of TaTPI

T. acidophilum belongs to thermoacidophilic euryarchaeota and TaTPI also shares high amino acid sequence similarity to other thermostable TPIs from *P. woesei*, *T. tenax*, and *M. jannaschii*, all of which adopt tetrameric conformation that renders them stable at high temperatures [14, 28, 29]. Helix 4 and helix 5 of thermostable TPIs have been known to play important roles in the tetramer formation via hydrophobic interactions [14]. However, crystal structures of apo- and G3P-bound TaTPI form a dimer and reveal a remarkable difference in helix 5 of TaTPI from other thermostable TPIs. Helix 5 of TaTPI is mainly composed of charged-amino acid residues (AEEAKYFREY) instead of hydrophobic residues found in other thermostable

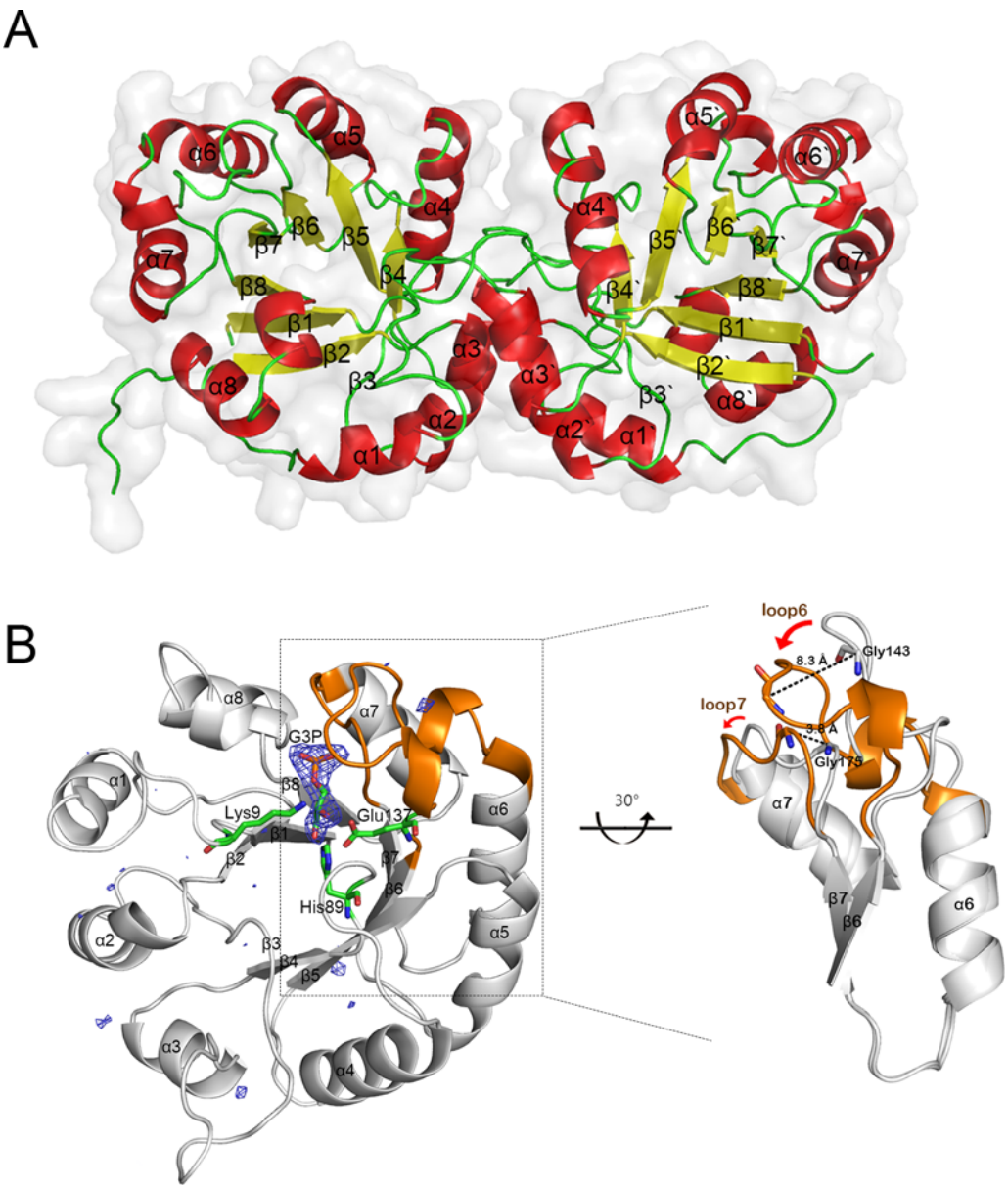

Fig 1. Overall structures of apo- and G3P-bound TaTPI. (A) Homodimer of apo-TaTPI is shown in carton representation, where α-helix, β-strand, and loop are colored in red, yellow, and green, respectively. (B) G3P-bound TaTPI. Only monomer of homodimeric G3P-bound TaTPI is demonstrated to emphasize a conformational change compared with apo-TaTPI. Extra positive electron density in F_o-F_c omit map contoured at 3.0 δ is shown as a blue mesh, which is modelled as G3P later. Amino acid residues interacting with G3P in catalytic site and G3P are shown as stick model; carbon, oxygen, phosphorus, and nitrogen atoms are colored in green, red, orange, and, blue, respectively. Loop 6 and loop 7 regions, which show a distinctive conformational change upon binding of G3P, are represented in orange and magnified for clarity.

doi:10.1371/journal.pone.0145331.g001

tetrameric TPIs. Structure-based sequence alignment of TaTPI with other TPIs shows that TaTPI resembles bacterial dimeric TPIs rather than tetrameric TPIs from thermostable archaea (Fig 2A).

Structural differences between TaTPI and other tetrameric archaeal TPIs are observed not only in helix 5 but also in adjacent α-helices. In tetrameric archaeal TPIs, the N-terminus of helix 4 and the C-terminus of helix 6 play important roles in tetrameric interaction via hydrophobic effects and hydrogen bonds [14]. The N-terminus of helix 4 of tetrameric archaeal TPIs

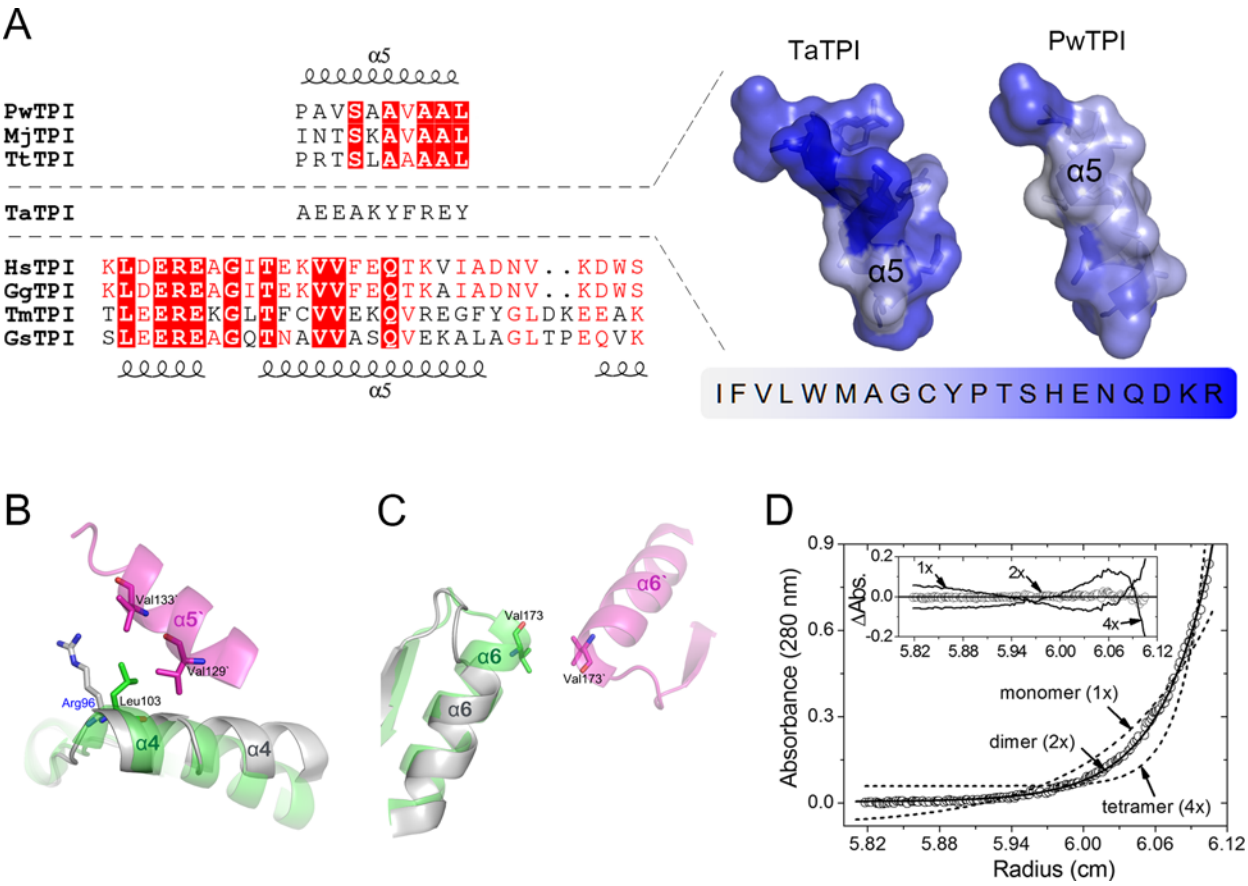

Fig 2. Dimeric conformation of TaTPI. (A) Structure-based sequence alignment of helix 5 region among TPIs from *Thermoplasma acidophilum* (TaTPI), *Pyrococcus woesei* (PwTPI), *Methanocaldococcus jannaschii* (MjTPI), *Thermoproteus tenax* (TtTPI), *Homo sapiens* (HsTPI), *Gallus gallus* (GgTPI), *Thermotoga maritima* (TmTPI), and *Geobacillus stearothermophilus* (GsTPI). Strictly conserved amino acid residues are highlighted in red shaded boxes and moderately conserved amino acid residues are colored in red. Helix 5 regions of TPIs from *Thermoplasma acidophilum* (PDB ID: 5CSR) and *Pyrococcus woesei* (PDB ID: 1HG3) are shown as cartoon representation with transparent surfaces, where amino acid residues are colored according to normalized consensus hydrophobicity scale [31]. (B) and (C) Structural comparison of helix 4 and helix 6 in TaTPI (gray) and PwTPI (green and magenta, each from different monomers). The important amino acid residues in tetrameric interface are shown as stick model. (D) Analytical ultracentrifugation experiment of TaTPI. Sedimentation equilibrium distribution (circle) of TaTPI at 26,000 rpm and 20°C is plotted as circle. Concentration of TaTPI was 16.8 u*M* (0.41 mg ml^{-1}) in 20 m*M* Tris-HCl, pH 7.5, and 0.2 *M* NaCl. Solid line is a fitting line for a homogeneous dimer (2x) model and dotted lines are fitting lines for homogeneous monomer (1x) and tetramer (4x) models. Calculated molecular weight for TaTPI monomer from its amino acid compositions is 24,671 daltons. Inset graph shows distributions of the residuals for homogeneous 1x, 4x (solid lines), and 2x (circle) models, respectively. The random distribution of the residuals for the 2x model indicates that TaTPI exists as homogeneous dimers in solution.

doi:10.1371/journal.pone.0145331.g002

contains conserved Leu (Leu103 in PwTPI numbering) that contributes to hydrophobic effects and hydrogen bonds with the other side of helix 4 and helix 5 for its tetrameric assembly. In the case of TaTPI, Leu in the N-terminus of helix 4 of tetrameric archaeal TPIs is replaced with Arg96, which deprives the hydrophobic effects for tetramer formation (Fig 2B). Furthermore, TaTPI has shorter helix 6 than that of tetrameric archaeal TPIs, resulting in dissipated hydrophobic effects between two C-termini from each helix 6 of its accompanying dimeric partner, Val173 in PwTPI (Fig 2C). Consequently, changes in amino acid composition of helix 5, thus in electrostatic surface, and slight modification of secondary structures in helix 4 and helix 6 seem to play subtle roles in dimer formation.

In the crystal structure of apo-TaTPI, Cys50 in helix 2 of each homodimer drew our attention since it interacts with the other Cys50 from adjacent TaTPI homodimer via sulfur-containing hydrogen bonds, not disulfide bonds. Thus, we needed to re-confirm the oligomeric

status of apo-TaTPI to make it sure whether the interaction of Cys-Cys is physiologically relevant or crystallographic artefact. To verify the oligomeric state of apo-TaTPI in solution, analytic ultracentrifugation analysis (AUC) was performed. Oligomeric state of apo-TaTPI in solution was investigated by equilibrium sedimentation technique at two speeds and three concentrations. Fig 2D shows the data and fits analyzed by using Eq. 1 for homogeneous 1x, 2x, and 4x models at ultracentrifugal speed of 26,000 rpm. The weighted root-mean-square errors (RMS) for the 1x and 4x fits were 5.01×10^{-2} and 6.90×10^{-2}, respectively. In contrast to these models, dimer (2x) model gave much improved RMS value of 7.93×10^{-3}. Residual distribution plot (Fig 2D inset) also supports that the apo-TaTPI forms dimer in solution. Analysis at 20,000 rpm (data not shown) also gave a better RMS value of 5.76×10^{-3} for 2x model than those for 1x (3.90×10^{-2}) and 4x (5.42×10^{-2}) models. Mixture or reversible models were also investigated but there was no indication of the possibility. Data analysis using the reversible model (Eq 2) gave large negative *In*k values for monomer-dimer (1x-2x) and monomer-trimer (1x-3x) models and much higher RMS values (~10^{-2}), so the reversible models for monomer-dimer (1x-2x) and monomer-trimer (1x-3x) equilibrium would not be the case for TaTPI. These results strongly indicate that apo-TaTPI exits as homogeneous dimer in solution. In addition, analytical size-exclusion chromatography results of apo-TaTPI, which were confirmed at two different TaTPI protein concentrations (0.9 and 4.5 mg ml^{-1}), also supported the dimeric conformation in solution (S2 Fig).

Structural stability of TaTPI under extreme condition

T. acidophilum thrives in harsh environments such as high temperature and extremely acidic condition. TaTPI is also expected to function correctly at high temperature or in very low pH condition when physiological barriers are affected by various stresses. To elucidate the structural stability of TaTPI in extremely acidic condition and at high temperature, we carried out circular dichroism (CD) spectroscopy experiments.

As for the structural stability of TaTPI in extremely acidic condition, secondary structure changes of pH-titrated TaTPI were monitored using CD spectroscopy. Normally, intracellular environment is well kept from extracellular stresses such as abrupt pH change. So, most of intracellular proteins experience normal physiological conditions and function accordingly. TaTPI maintained its folded structure under extremely acidic condition (pH 1–2) as in neutral pH range (S3 Fig). In the case of TaTPI, secondary structure contents under extremely acidic condition seem to change slightly with sustained folded structure. The content of α-helix in the TaTPI tends to increase with decreasing pH, whereas the content of β-strand decreases. These results suggest that TaTPI is designed to function normally even in cases of unexpected pH drop.

The temperature of maximum heat capacity (or half-denaturation temperature, Td) of TaTPI was measured by CD spectroscopy. The denaturation curve of TaTPI was analyzed by Kaleidagraph (Synergy Software) based on John and Weeks's protocol [22]. The Td value for TaTPI is 74.6°C (S4 Fig), which is comparable with that of TPI from *Geobacillus stearothermophilus* (GsTPI), a biological indicator for the validation of sterilization processes, (T_d: 76°C) [30]. In the case of GsTPI, a large number of prolines (5.2%), replacement of asparagine by histidine within the active site to prevent deamidation, the smallest cavity number and volume, and a large buried hydrophobic surface have been shown to contribute for the thermostability [12]. *Thermotoga maritima*, a hyperthermophilic bacterium, has been known to have TPI with the highest T_d value of 102°C [30], resulting from a large number of salt bridges and extensive hydrophobic patches from tetramer conformation [8]. Using DSC, we found the Td app value of MjTPI to be 107.1°C and it is the highest Td value among reported TPIs so far (Table 2; S5

Table 2. Half-denaturation temperatures of TPIs.

	The half-denaturation temperature (T_d,°C)	Reference
TaTPI	74°C	This manuscript
MjTPI	107°C	This manuscript
TmTPI	102°C	Alvarez et al., 1999 [30]
GsTPI	76°C	Alvarez et al., 1999 [30]
PfTPI	65°C	Gopal et al., 1999 [33]
HsTPI	55°C	Mainfroid et al., 1996 [34]
TbTPI	44°C	Borchert et al., 1993 [35]

Ta, *Thermoplasma acidophilum*; Mj, *Methanocaldococcus jannaschii*; Tm, *Thermotoga maritima*; Gs, *Geobacillus stearothermophilus*; Pf, *Plasmodium falciparum*; Hs, *Homo sapience*; Tb, *Trypanosoma brucei*.

doi:10.1371/journal.pone.0145331.t002

Fig). When compared with TPIs mentioned above, TaTPI has smaller number of prolines (4.2%), larger cavity volume, and less buried hydrophobic surface than GsTPI, nor does it adopt tetrameric conformation.

Proposal of TPI stabilization patches

TaTPI is composed of 216 amino acid residues and approximately 10% shorter in length than other TPIs from bacterial and eukaryotic species, which is a common feature in archaeal TPIs. According to the results of our structure-based sequence alignment for TPIs, helix 4, helix 5, and helix 6 are regions that mainly account for variation in amino acid composition, structural stability, and the oligomeric status of TPIs. To systematically validate the stabilization factors

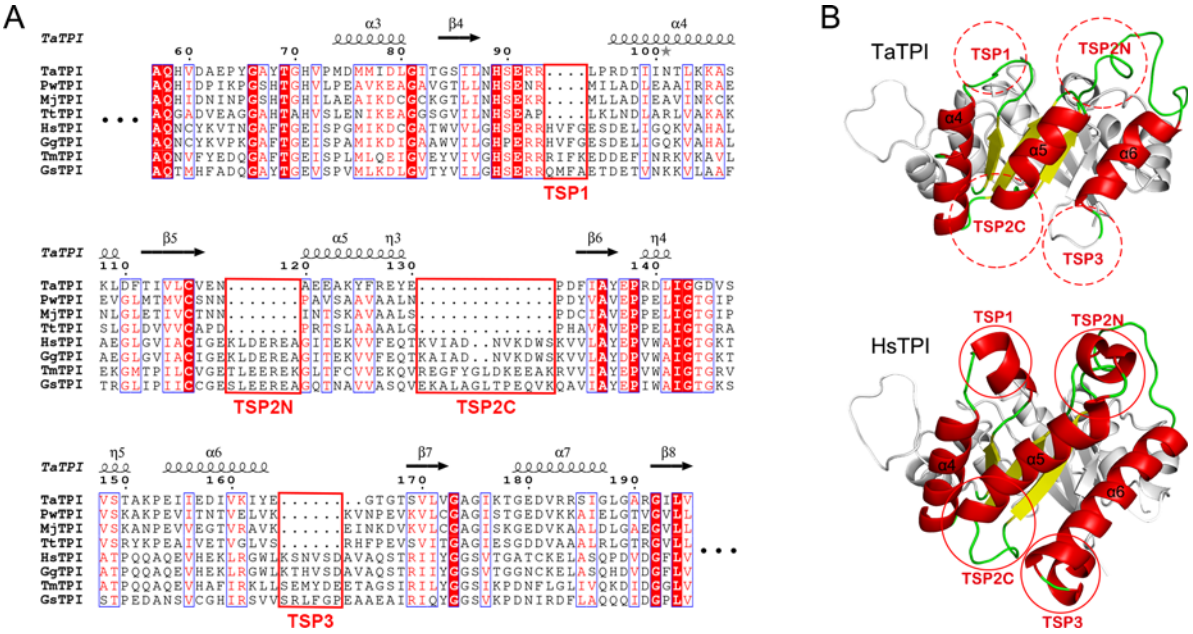

Fig 3. TPI stabilization patches (TSPs). (A) Structure-based sequence alignment of TaTPI with other TPIs from *Pyrococcus woesei* (PwTPI), *Methanocaldococcus jannaschii* (MjTPI), *Thermoproteus tenax* (TtTPI), *Homo sapiens* (HsTPI), *Gallus gallus* (GgTPI), *Thermotoga maritima* (TmTPI), and *Geobacillus stearothermophilus* (GsTPI). Strictly conserved amino acid residues are highlighted in red shaded boxes and moderately conserved amino acid residues are colored in red. Conserved residues are enclosed in blue boxes and TSP regions are enclosed in red boxes. The alignment figure was prepared using *ESPript* program [32]. (B) Structural comparison of TaTPI and HsTPI. The red dotted and solid circles represent TSP regions in TaTPI and HsTPI, respectively.

doi:10.1371/journal.pone.0145331.g003

of TaTPI, we name regions of distinctive differences as TPI stabilization patches (TSPs) (Fig 3A). TSP1 is helix 4 region and TaTPI lacks a short helical N-terminus in this patch. Consequently, TaTPI forms a more compact structure. TSP2 exhibits a major structural discrepancy in that 18 amino acid residues are missing in helix 5 region of TaTPI, compared with other dimeric TPIs. In TSP2 area, truncated helix 5 (TSP2C) and lack of a short helix in its N-terminus (TSP2N) also make TaTPI tighter in their overall structure. Lastly, TSP3 arises from helix 6 region and helix 6 is trimmed along with a short α-helix in its C-terminus (Fig 3B). All the TSPs of TaTPI contribute to the formation of more compact dimeric structure.

The TSPs are not exclusive of TaTPI. Other tetrameric archaeal TPIs also have the TSPs. We speculated that other tetrameric archaeal TPIs could be more thermostable than TaTPI since they adopt tetrameric conformation and contains TSPs. To validate our speculation, we cloned and purified *M. jannaschii* TPI (MjTPI), a tetrameric archaeal TPI, and measured the Td app value of MjTPI. The Td app value of MjTPI was 107.1°C, which is the highest Td app value among reported TPIs so far. The result suggest that both higher oligomerization status and the TSPs could be important factors for thermostability of TPIs. TaTPI would keep its structural and functional integrity at high temperature through a compact dimeric conformation from contributing TSPs. Crystal structures of apo- and G3P-bound TaTPI and defined stability determining factors of TPIs would provide clear insights on engineering more stable TIM-barrel fold proteins which make up a large protein family and play pivotal role in metabolic pathways.

Supporting Information

S1 Fig. Binding modes of G3P with key amino acid residues of TaTPI. LIGPLOT diagram is used for representation of active site in the G3P-bound TaTPI. Carbon, nitrogen, oxygen, and phosphorus atoms are shown in black, blue, red, and magenta, respectively. Hydrogen bonds and oxyanion hole between G3P and TaTPI are shown as green and red dotted line, respectively.
(TIF)

S2 Fig. Analytic size-exclusion chromatography of TaTPI. TaTPI protein samples at two different concentrations (A: 4.5 mg ml^{-1}, B: 0.9 mg ml^{-1}) were applied to Superdex200 10/300 GL column. Chromatograms of TaTPI and gel filtration standard were shown as blue and red lines, respectively.
(TIF)

S3 Fig. Circular dichroism spectra for TaTPI at variable pH conditions. (A) CD spectra of pH-titrated TaTPI (pH 1.0–7.0) were measured from 200 to 260 nm. (B) The secondary structure contents of pH-titrated TaTPI were calculated from Multivariate SSE Program (JASCO).
(TIF)

S4 Fig. Thermal denaturation curve of TaTPI. The black line represents baseline-subtracted and normalized raw data. The red line indicates the best fits of the raw data. The maximum temperature of heat capacity (T_d) was calculated according to the best fits of the raw data.
(TIF)

S5 Fig. DSC thermogram of MjTPI. The black circle represents baseline-subtracted and normalized raw data. The black line indicates the best fits of the raw data. The maximum temperature of heat capacity (T_d) was calculated based on the best fits of the raw data.
(TIF)

Acknowledgments

The authors thank the staff members of the BL-1A at the Photon Factory (Tsukuba, Japan) and the BL-7A at the Pohang Accelerator Laboratory (Pohang, Korea).

Author Contributions

Conceived and designed the experiments: SHP BWH. Performed the experiments: SHP MSP SM MKS HSP HH SJK EB. Analyzed the data: SHP HSK MSP SM MKS HSP HH SJK EB HJK BWH. Contributed reagents/materials/analysis tools: SHP MKS SJK BWH. Wrote the paper: SHP HH HJK BWH.

References

1. Schneider AS. Triosephosphate isomerase deficiency: historical perspectives and molecular aspects. Bailliere's best practice & research Clinical haematology. 2000; 13(1):119–40.
2. Celotto AM, Frank AC, Seigle JL, Palladino MJ. Drosophila model of human inherited triosephosphate isomerase deficiency glycolytic enzymopathy. Genetics. 2006; 174(3):1237–46. PMID: 16980388
3. Arya R, Lalloz MR, Bellingham AJ, Layton DM. Evidence for founder effect of the Glu104Asp substitution and identification of new mutations in triosephosphate isomerase deficiency. Hum Mutat. 1997; 10 (4):290–4. PMID: 9338582
4. Hollan S, Fujii H, Hirono A, Hirono K, Karro H, Miwa S, et al. Hereditary triosephosphate isomerase (TPI) deficiency: two severely affected brothers one with and one without neurological symptoms. Hum Genet. 1993; 92(5):486–90. PMID: 8244340
5. Daar IO, Artymiuk PJ, Phillips DC, Maquat LE. Human triose-phosphate isomerase deficiency: a single amino acid substitution results in a thermolabile enzyme. Proc Natl Acad Sci U S A. 1986; 83 (20):7903–7. PMID: 2876430
6. Ruepp A, Graml W, Santos-Martinez ML, Koretke KK, Volker C, Mewes HW, et al. The genome sequence of the thermoacidophilic scavenger Thermoplasma acidophilum. Nature. 2000; 407 (6803):508–13. PMID: 11029001
7. Wierenga RK. The TIM-barrel fold: a versatile framework for efficient enzymes. FEBS Lett. 2001; 492 (3):193–8. PMID: 11257493
8. Maes D, Zeelen JP, Thanki N, Beaucamp N, Alvarez M, Thi MH, et al. The crystal structure of triosephosphate isomerase (TIM) from Thermotoga maritima: a comparative thermostability structural analysis of ten different TIM structures. Proteins. 1999; 37(3):441–53. PMID: 10591103
9. Xiao L, Honig B. Electrostatic contributions to the stability of hyperthermophilic proteins. Journal of molecular biology. 1999; 289(5):1435–44. PMID: 10373377
10. Dams T, Auerbach G, Bader G, Jacob U, Ploom T, Huber R, et al. The crystal structure of dihydrofolate reductase from Thermotoga maritima: molecular features of thermostability. Journal of molecular biology. 2000; 297(3):659–72. PMID: 10731419
11. Szilagyi A, Zavodszky P. Structural differences between mesophilic, moderately thermophilic and extremely thermophilic protein subunits: results of a comprehensive survey. Structure. 2000; 8(5):493–504. PMID: 10801491
12. Delboni LF, Mande SC, Rentier-Delrue F, Mainfroid V, Turley S, Vellieux FM, et al. Crystal structure of recombinant triosephosphate isomerase from Bacillus stearothermophilus. An analysis of potential thermostability factors in six isomerases with known three-dimensional structures points to the importance of hydrophobic interactions. Protein science: a publication of the Protein Society. 1995; 4 (12):2594–604.
13. Romero-Romero S, Costas M, Rodriguez-Romero A, Alejandro Fernandez-Velasco D. Reversibility and two state behaviour in the thermal unfolding of oligomeric TIM barrel proteins. Physical chemistry chemical physics: PCCP. 2015; 17(32):20699–714. doi: 10.1039/c5cp01599e PMID: 26206330
14. Walden H, Bell GS, Russell RJ, Siebers B, Hensel R, Taylor GL. Tiny TIM: a small, tetrameric, hyperthermostable triosephosphate isomerase. Journal of molecular biology. 2001; 306(4):745–57. PMID: 11243785
15. Otwinowski Z, Minor W. Processing of X-ray diffraction data collected in oscillation mode. Methods Enzymol. 1997; 276:307–26.
16. Vagin A, Teplyakov A. Molecular replacement with MOLREP. Acta Crystallogr D Biol Crystallogr. 2010; 66(Pt 1):22–5. doi: 10.1107/S0907444909042589 PMID: 20057045

17. Emsley P, Lohkamp B, Scott WG, Cowtan K. Features and development of Coot. Acta Crystallogr D Biol Crystallogr. 2010; 66(Pt 4):486–501. doi: 10.1107/S0907444910007493 PMID: 20383002
18. Murshudov GN, Vagin AA, Dodson EJ. Refinement of macromolecular structures by the maximum-likelihood method. Acta Crystallogr D Biol Crystallogr. 1997; 53(Pt 3):240–55. PMID: 15299926
19. Lovell SC, Davis IW, Arendall WB 3rd, de Bakker PI, Word JM, Prisant MG, et al. Structure validation by Calpha geometry: phi,psi and Cbeta deviation. Proteins. 2003; 50(3):437–50. PMID: 12557186
20. Laue TM. Sedimentation equilibrium as thermodynamic tool. Methods Enzymol. 1995; 259:427–52. PMID: 8538465
21. Knott GD. Mlab—a mathematical modeling tool. Comput Programs Biomed. 1979; 10(3):271–80. PMID: 527325
22. John DM, Weeks KM. van't Hoff enthalpies without baselines. Protein science: a publication of the Protein Society. 2000; 9(7):1416–9.
23. Zhang Z, Sugio S, Komives EA, Liu KD, Knowles JR, Petsko GA, et al. Crystal structure of recombinant chicken triosephosphate isomerase-phosphoglycolohydroxamate complex at 1.8-A resolution. Biochemistry. 1994; 33(10):2830–7. PMID: 8130195
24. Alvarez M, Zeelen JP, Mainfroid V, Rentier-Delrue F, Martial JA, Wyns L, et al. Triose-phosphate isomerase (TIM) of the psychrophilic bacterium Vibrio marinus. Kinetic and structural properties. The Journal of biological chemistry. 1998; 273(4):2199–206. PMID: 9442062
25. Williams JC, Zeelen JP, Neubauer G, Vriend G, Backmann J, Michels PA, et al. Structural and mutagenesis studies of leishmania triosephosphate isomerase: a point mutation can convert a mesophilic enzyme into a superstable enzyme without losing catalytic power. Protein engineering. 1999; 12 (3):243–50. PMID: 10235625
26. Noble ME, Zeelen JP, Wierenga RK. Structures of the "open" and "closed" state of trypanosomal triosephosphate isomerase, as observed in a new crystal form: implications for the reaction mechanism. Proteins. 1993; 16(4):311–26. PMID: 8356028
27. Wierenga RK, Kapetaniou EG, Venkatesan R. Triosephosphate isomerase: a highly evolved biocatalyst. Cellular and molecular life sciences: CMLS. 2010; 67(23):3961–82. doi: 10.1007/s00018-010-0473-9 PMID: 20694739
28. Walden H, Taylor GL, Lorentzen E, Pohl E, Lilie H, Schramm A, et al. Structure and function of a regulated archaeal triosephosphate isomerase adapted to high temperature. Journal of molecular biology. 2004; 342(3):861–75. PMID: 15342242
29. Gayathri P, Banerjee M, Vijayalakshmi A, Azeez S, Balaram H, Balaram P, et al. Structure of triosephosphate isomerase (TIM) from Methanocaldococcus jannaschii. Acta Crystallogr D Biol Crystallogr. 2007; 63(Pt 2):206–20. PMID: 17242514
30. Alvarez M, Wouters J, Maes D, Mainfroid V, Rentier-Delrue F, Wyns L, et al. Lys13 plays a crucial role in the functional adaptation of the thermophilic triose-phosphate isomerase from Bacillus stearothermophilus to high temperatures. The Journal of biological chemistry. 1999; 274(27):19181–7. PMID: 10383424
31. Eisenberg D, Schwarz E, Komaromy M, Wall R. Analysis of membrane and surface protein sequences with the hydrophobic moment plot. Journal of molecular biology. 1984; 179(1):125–42. PMID: 6502707
32. Robert X, Gouet P. Deciphering key features in protein structures with the new ENDscript server. Nucleic acids research. 2014; 42(Web Server issue):W320–4. doi: 10.1093/nar/gku316 PMID: 24753421
33. Gopal B, Ray SS, Gokhale RS, Balaram H, Murthy MR, Balaram P. Cavity-creating mutation at the dimer interface of Plasmodium falciparum triosephosphate isomerase: restoration of stability by disulfide cross-linking of subunits. Biochemistry. 1999; 38(1):478–86. PMID: 9890931
34. Mainfroid V, Terpstra P, Beauregard M, Frere JM, Mande SC, Hol WG, et al. Three hTIM mutants that provide new insights on why TIM is a dimer. Journal of molecular biology. 1996; 257(2):441–56. PMID: 8609635
35. Borchert TV, Pratt K, Zeelen JP, Callens M, Noble ME, Opperdoes FR, et al. Overexpression of trypanosomal triosephosphate isomerase in Escherichia coli and characterisation of a dimer-interface mutant. European journal of biochemistry / FEBS. 1993; 211(3):703–10.

약학박사 학위논문

Structural and Biophysical Analyses of Aspartyl-tRNA Synthetase from *Homo sapiens* and Triosephosphate Isomerase from *Thermoplasma acidophilum*

Aspartyl-tRNA Synthetase와 Triosephosphate Isomerase의 구조 및 생물학적 분석

2016년 2월

서울대학교 대학원

약학과 의약생명과학전공

박 상 호

Structural and Biophysical Analyses of Aspartyl-tRNA Synthetase from *Homo sapiens* and Triosephosphate Isomerase from *Thermoplasma acidophilum*

Thesis by

Sang Ho Park

Professor: Byung Woo Han

A Thesis Submitted to the Graduate Faculty of Seoul National University in Partial Fulfillment of the Requirements for the Degree of Doctor of Philosophy

2016

Abstract

Structural and Biophysical Analyses of Aspartyl-tRNA Synthetase from *Homo sapiens* and Triosephosphate Isomerase from *Thermoplasma acidophilum*

Sang Ho Park
College of Pharmacy
The Graduate School
Seoul National University

Human cytosolic aspartyl-tRNA synthetase (DRS) catalyzes the attachment of the aspartic acid to its specific tRNA. DRS is a component of the multi-tRNA synthetase complex (MSC) which has been known to be involved in unanticipated signaling pathways. The crystal structure of DRS has been determined at 2.25 Å resolution containing the anticodon binding domain, hinge region, and catalytic domain. The structure also reveals the C-terminal end of the N-helix which is considered as a unique additional domain of DRS, and its conformation further supports the switching model of the N-helix for the transfer of $tRNA^{Asp}$ to elongation factor 1α. From the analyses of the crystal structure and post-translational modification of DRS, I suggest that the phosphorylation of Ser146 could initiate a conformational change of the DRS dimer and provokes the separation

of DRS from the MSC. This structural study provides the binding site for an interaction partner with unforeseen functions.

Thermoplasma acidophilum is one of the most acidophilic organisms that utilize not only non-phosphorylative Entner-Doudoroff (ED) pathway but also Embden-Meyerhof-Parnas (EMP) pathway for glucose degradation. Triosephosphate isomerase (TPI) is structurally and functionally well-known glycolytic enzyme that plays an important role in glycolytic and gluconeogenic metabolism. Crystal structures of apo- and glycerol-3-phosphate-bound TPI from *T. acidophilum* (TaTPI) have been determined at 1.94 and 2.17 Å resolution. TaTPI adopts the canonical TIM-barrel fold with eight α-helices and parallel eight β-strands. Although TaTPI shares ~30% sequence identity to other TPIs from thermophilic species that adopt tetrameric conformation for enzymatic activity in their harsh physiological environments, TaTPI exists as a dimer in solution. Dimeric conformation of TaTPI was further confirmed by analytical ultracentrifugation and size-exclusion chromatography. Helix 5 and helix 4 regions of thermostable tetrameric TPIs are key important tetrameric interface, forming a hydrophobic effects. However, TaTPI contains unique charged-amino acid residues in the helix 5 and adopts dimer conformation. TaTPI exhibits the apparent T_d value of 74.6 ℃ and maintains its overall structure with slight changes in the secondary structure contents under extremely

acidic conditions. Based on the structural and biophysical analyses of TaTPI, more compact structure of the protomer with reduced length of loops and certain patches on the surface could account for the robust nature of *Thermoplasma acidophilum* TPI.

Keywords: aspartyl-tRNA synthetase, multi-tRNA synthetase complex, triosephosphate isomerase, glycolysis, crystal structure

Student number: 2010-21682

Table of Contents

Abstract · · ·

Chapter 2

Structure and stability of the dimeric triosephosphate isomerase from *Thermoplasma acidophilum*

1. Introduction · · ·

References · 83

Abstract (in Korean) · 94

Acknowledgements · 97

Appendix: Printouts of first author publications · · · · · · · · · · · · · · 98

List of Tables

List of Figures

Chapter 1

Chapter 2

Figure 2-1. The isomerization reaction catalyzed by triosephosphate isomerase · · ·

Abbreviations

AARSs	aminoacyl-tRNA synthetases
DRS	aspartyl-tRNA synthetase
KRS	lysyl-tRNA synthetase
MSC	multi-tRNA synthetase complex
NMR	nuclear magnetic resonance
EF-1α	elongation factor 1α
OB-fold	oligonucleotide binding-fold
PTM	post-translational modification
TPI	triosephosphate isomerase
DHAP	dihydroxyacetone phosphate
GAP	glyceraldehyde-3-phosphate
PDB	protein data bank
HEPES	4-(2-hydroxyethyl)-1-piperazineethanesulfonic acid
G3P	glycerol-3-phosphate
CD	circular dichroism
DSC	differential scanning calorimetry
AUC	analytic ultracentrifugation
RMS	root-mean-square errors
T_d	half-denaturation temperature
TSPs	TPI stabilization patches

Chapter 1

Crystal structure of human cytosolic aspartyl-tRNA synthetase

[This chapter was published in PROTEINS.]

Kim KR, Park SH et al. (2013) Crystal Structure of Human cytosolic aspartyl-tRNA synthetase, a component of multi-tRNA synthetase complex.

PROTEINS 81(10):1840-1846

1. Introduction

Aminoacyl-tRNA synthetases (AARSs) catalyze the attachment of specific amino acid to its compatible cognate tRNAs through a two-step reaction.(Normanly and Abelson, 1989, Annual review of biochemistry, 1) In the first step, an intermediate adenylate is formed from amino acid and ATP, then the amino acid is charged to the ribose of the terminal adenine of tRNA (Figure 1-1). Even though AARSs catalyze the same type of reaction, they vary in amino acid sequence, size, three-dimensional structure, and oligomeric state.

This chapter was co-work with Kyung Rok Kim and he equally contributed to this work

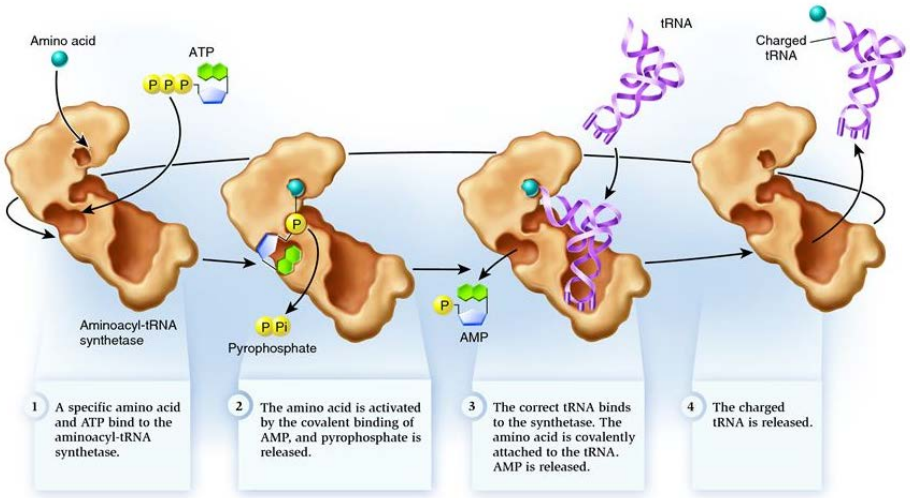

Figure 1-1. Aminoacyl-tRNA synthetase charging a tRNA (biology-forums.com)

AARSs can be classified into two major classes based on conseverd sequence motif; class I and II synthetase.(Eriani, et al., 1990, Nature, 2) Whereas the class I synthetase adopts the representative Rossmann fold that binds ATP, the class II synthetase contains a core antiparallel β-sheet surrounded by α-helices and three unique conserved motifs; motif 1, 2, and 3 (Figure 1-2).(Eriani, et al., 1990, Nature, 2)

There are cytosolic or mitochondrial AARSs that play an essential cellular role not only in cytosol but also in mitochondria and most AARSs function distinctively in either location for protein synthesis. In human, there are cytosolic and mitochondrial aspartyl-tRNA synthetases (DRS and DRS2), which share only 22.9% sequence identity. It has been known that DRS2 is associated with neurodegenerative disorder; leukoencephalopathy with brain stem and spinal cord involvement and high lactate (LBSL). (Scheper, et al., 2007, Nature genetics, 3) Structure of DRS2 revealed the function of the additional motif in the catalytic domain.(Neuenfeldt, et al., 2012, Nucleic acids research, 4) In the case of DRS, it has been known to the component of multi-tRNA synthetase complex (MSC) in higher eukaryotes.(Deutscher, 1984, The Journal of cell biology, 5)

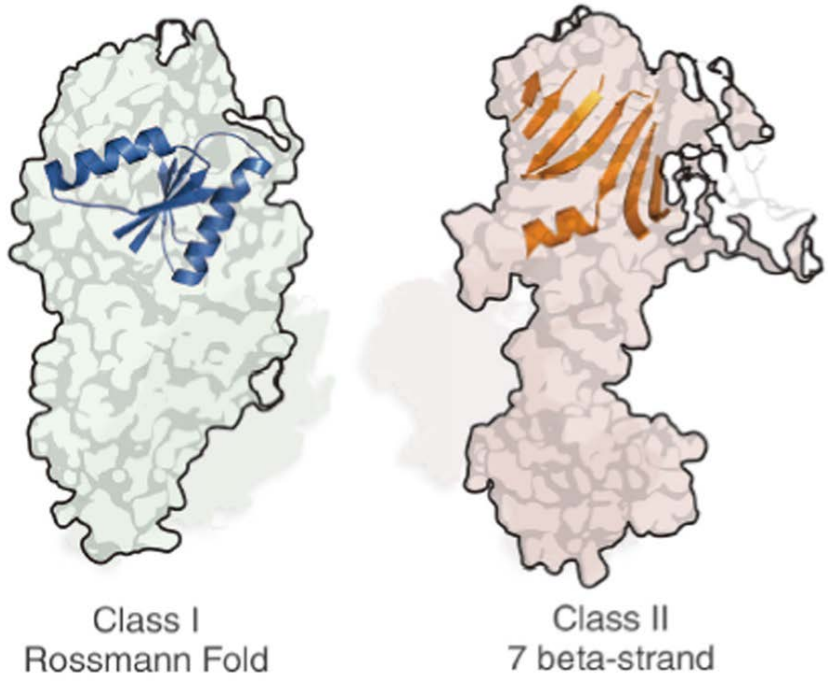

Figure 1-2. Architectures of the catalytic domains for aminoacylation – class I versus class II (Lo, et al., 2014, Science, 6)

The conserved core Rossmann fold is represented on the structure of MRS (PDB ID: 2CT8) in class I, and the conserved core 7 beta-strand with motif-3 helix is represented on the structure of KRS (PDB ID: 4DPG) in class II.

The MSC consists of nine cytosolic tRNA synthetases (DRS, KRS, MRS, RRS, QRS, IRS, LRS, and EPRS) with three auxillary proteins (AIMP1/p43, AIMP2/p38, and AIMP3/p18) and it has been known to switch the canonical translational function and additional functions which are often observed in higher eukaryotes (Figure 1-3).(Ray, et al., 2007, Trends Biochem Sci, 7; Park, et al., 2005, Trends Biochem Sci, 8) In the MSC, DRS is known to interact with the aminoacyl-tRNA synthetase-interacting multifunctional protein 2 (AIMP2/p38) (Robinson, et al., 2000, J Mol Biol, 9; Kaminska, et al., 2009, J Biol Chem, 10) and the lysyl-tRNA synthetase (KRS).(Guzzo and Yang, 2008, Biochemical and biophysical research communications, 11) The N-terminal extension of DRS, KRS, and asparaginyl-tRNA synthetase (NRS) is unique additional region in the class II synthetases and further classifies them into the subclass IIb.(Woese, et al., 2000, Microbiology and molecular biology reviews : MMBR, 12) The NMR structure of the N-terminal extension region in DRS revealed that the N-terminal flexible β-turn followed by the amphipathic C-terminal helix induces the nonspecific tRNA binding and gives a force to transfer its charged tRNA to elongation factor 1α (EF-1α).(Reed and Yang, 1994, J Biol Chem, 13; Reed, et al., 1994, J Biol Chem, 14; Cheong, et al., 2003, The international journal of biochemistry & cell biology, 15)

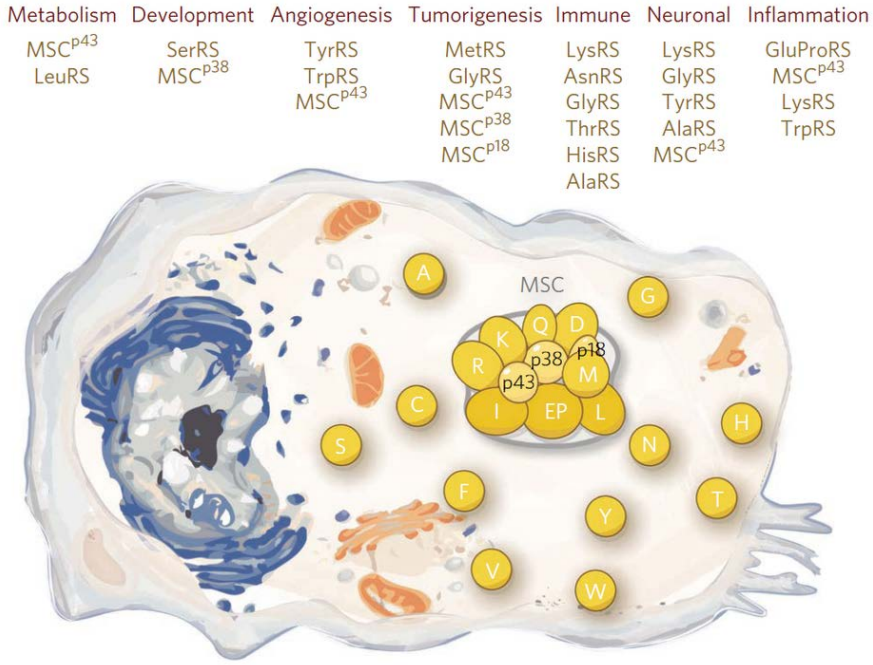

Figure 1-3. The nontranslational functions of AARs (Guo and Schimmel, 2013, Nature chemical biology, 16)

In this work, I present the crystal structure of human cytosolic DRS at 2.25 Å. I show that DRS forms a homodimer with the N-terminal extension, anticodon binding domain, and catalytic domain. Analyses of the crystal structure and post-translational modification shed lights on the molecular basis of the association and dissociation of DRS with the MSC.

2. Material and methods

2.1. Cloning, protein expression, and purification

Full-length sequence of human cytosolic DRS (501 amino acids) was amplified using PCR and cloned into the pET-28a(+) vector containing the N-terminal His_6-tag (Novagen). The recombinant protein was transformed into *Escherichia coli* Rosetta2(DE3)pLysS strain. DRS was induced by 0.5 m*M* isopropyl 1-thio-β-D-galactopyranoside and incubated for 6 hours at 310 K using Luria Broth culture medium. The harvested cells were lysed by cell sonicator (SONICS) in lysis buffer containing 20 m*M* Tris-HCl (pH 7.5), 500 m*M* NaCl, 35 m*M* imidazole, and 1 m*M* phenylmethanesulfonyl fluoride. The lysates were centrifuged at 35,000g for 50 min to remove the cell debris and denatured proteins. The supernatant was applied to a HiTrap Chelating HP column (GE Healthcare) for affinity chromatography and eluted with linear gradient 50-500 m*M* imidazole following equilibration with 50 m*M* imidazole. The eluted protein was diluted with a buffer containing 50 m*M* HEPES-NaOH (pH 7.0), 50 m*M* NaCl, 1 m*M* dithiothreitol, and 5% (v/v) glycerol, and further purified using the ion exchange chromatography with a HiTrap Q HP column (GE Healthcare). For the final purification step, size-exclusion chromatography was performed with a HiLoad 16/600 Superdex 200

prep grade column (GE Healthcare) equilibrated with 50 m*M* HEPES-NaOH (pH 7.0), 200 m*M* NaCl, 5% (v/v) glycerol, and 1 m*M* dithiothreitol. For crystallization, the purified DRS proteins were concentrated to 11.1 mg ml^{-1}.

2.2. Crystallization

Initial DRS crystals were searched using commercial screen solutions, Crystal screen I, II, PEG/Ion I, II (Hampton Research), and Wizard classic I, II, III, IV (Rigaku), by the sitting-drop vapor-diffusion method at 295 K. DRS crystals were grown by the sitting-drop vapor-diffusion method at 295 K by mixing equal volumes of the purified protein and the reservoir solution containing 8% (v/v) tacsimate (pH 8.0), and 20% (w/v) polyethylene glycol 3350 (Figure 1-4).

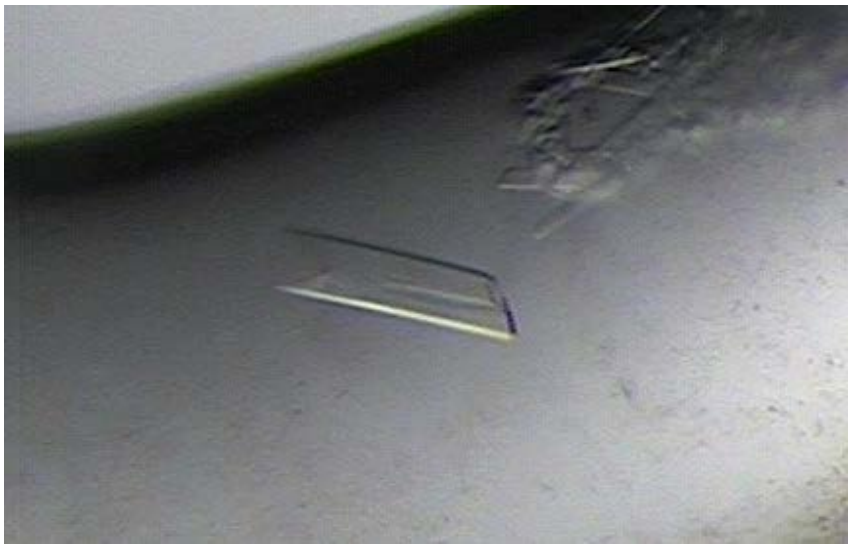

Figure 1-4. Crystals of human cytosolic DRS

Crystals of human cytosolic DRS with approximate dimensions of 0.3 mm × 0.1 mm × 0.05 mm.

2.3. X-ray data collection and structure determination

For X-ray diffraction data collection, crystals were soaked in the cryoprotectant solution containing 20% (v/v) glycerol added to the reservoir solution. X-ray diffraction data of the crystal were collected at the synchrotron BL-5A at the Photon Factory, Japan. The DRS crystals belong to the space group $P2_1$, with unit cell parameters of a = 54.89, b = 141.92, c= 98.50, $\alpha = \gamma = 90^{\circ}$, and $\beta = 102.19^{\circ}$. The structure was solved by molecular replacement method with the structure of *S. cerevisiae* DRS containing the anticodon binding domain, hinge region, and catalytic domain (PDB ID: 1ASZ)(Cavarelli, et al., 1994, The EMBO journal, 17) as a phasing model using *MOLREP*.(Vagin and Teplyakov, 2010, Acta Crystallogr D Biol Crystallogr, 18) The structure was completed using alternate cycles of manual building in *WinCoot*(Emsley, et al., 2010, Acta Crystallogr D Biol Crystallogr, 19) and refinement in *REFMAC*(Murshudov, et al., 1997, Acta Crystallogr D Biol Crystallogr, 20). All refinement steps were monitored using an R_{free} value based on 5.0% of the independent reflections. The stereochemical quality of the final model was assessed using *MolProbity*(Lovell, et al., 2003, Proteins, 21). The data collection and refinement statistics are summarized in Table1-1; 1-2.

Table 1-1. Statistics for data collection

Data collection[a]	**Human cytosolic DRS**
Space group	$P2_1$
Cell dimensions	
a, b, c (Å)	54.89, 141.92, 68.50
α, β, γ (°)	90, 102.19, 90
Data set	
X-ray wavelength (Å)	1.0000
Resolution (Å)[b]	50.00–2.25 (2.29–2.25)
Total / unique reflections	177,246 / 48,428
Completeness (%)	99.3 (95.4)
R_{merge} (%)[c]	11.0 (50.2)

Footnotes to Table 1-1

[a]Data collected at the synchrotron BL-5A at the Photon Factory.

[b]Numbers in parentheses indicate the highest resolution shell.

[c]$R_{merge} = \Sigma_h \Sigma_i |I(h)_i - \langle I(h) \rangle| / \Sigma_h \Sigma_i I(h)_i$, where $I(h)$ is the observed intensity of reflection h, and $\langle I(h) \rangle$ is the average intensity obtained from multiple measurements.

Table 1-2. Refinement statistics

Refinement	Human cytosolic DRS
Resolution (Å)	50.00–2.25
R_{work}[a] / R_{free}[b] (%)	19.7 / 22.8
No. of non-hydrogen atoms / mean B-factor (Å^2)	
Protein	6,968 / 33.7
Water	354 / 40.2
Glycerol	48 / 52.5
Poor rotamers (%)[c]	3.1
Ramachandran plot analysis (%)	
Most favored regions	96.9
Additional allowed regions	3.1
Disallowed regions	0
R.m.s.d. from ideal geometry	
Bond lengths (Å)	0.010
Bond angles (°)	1.290

Footnotes to Table 1-2

[a]$R_{work} = \Sigma \mid |F_o| - |F_c| \mid / \Sigma |F_o|$, where $|F_o|$ is the observed structure factor amplitude and $|F_c|$ is the calculated structure factor amplitude.

[b]R_{free} = R-factor based on 5.0% of the data excluded from refinement.

[c]Values obtained using MolProbity.

2.4. Post-translational modification analysis

Purified N-terminal OneSTrEP-tagged DRS and co-eluted interaction partners of that, overexpressed and purified from HEK293T cells, were digested with sequencing grade gold-trypsin (Promega) after 1D-SDS PAGE/Coomassie blue staining. Tryptic peptides were analyzed with the LTQ Velos Orbitrap mass spectrometer equipped with an electron transfer dissociation source after an online reversed-phase chromatography. To improve sequencing coverage, I applied a data dependent decision tree to select for collision induced dissociation or electron transfer dissociation fragmentation depending on the charged states, respectively. Protein identification was accomplished using the Sorcerer™-SEQUEST® (Sage-N Research), and searches were performed against the IPI human DB v3.87 fasta. The carbamidomethylation (+57.021 Da) of Cys is set as a static modification, and the following variable modification were allowed: GlyGly / +114.043 Da (Lys), Acetyl / +42.011 Da (Lys), HexNAc / +203.079 Da (Asn, Ser, Thr), Phospho / +79.966 Da (Ser, Thr, Tyr), Oxidation / +15.995 Da (Met), deamidated / +0.984 Da (Asn, Gln).

2.5. Data deposition

The coordinate and structure factors for human cytosolic DRS have been deposited in the RCSB Protein Data Bank, accession code **4J15**.

3. Results and discussion

3.1. Overall structure and oligomeric state of DRS

The crystal structure of human cytosolic DRS has been determined at 2.25 Å resolution by molecule replacement method with the structure of *S. cerevisiae* DRS containing the anticodon binding domain, hinge region, and catalytic domain (PDB ID: 1ASZ) (Cavarelli, et al., 1994, The EMBO journal, 17) as a phasing model. R_{work}/R_{free} values for the final models of DRS was 19.7%/22.8%. Crystal structure of DRS contains a homodimer in the asymmetric unit and the dimer interface area is 3,750.5 $Å^2$ which comprises of 16.6% of the monomeric surface area calculated from Protein Interfaces, Surfaces and Assemblies service.(Krissinel and Henrick, 2007, Journal of molecular biology, 22) The crystal structure of DRS contains anticodon binding domain, hinge region, and catalytic domain. In addition, the N-terminal extension region, which is a distinct domain in mammalian DRS, could be partially modeled including the C-terminal three residues of the characteristic helix motif (Figure 1-5). Structural analyses on this N-terminal extension region will be further discussed with the previous NMR structure below.

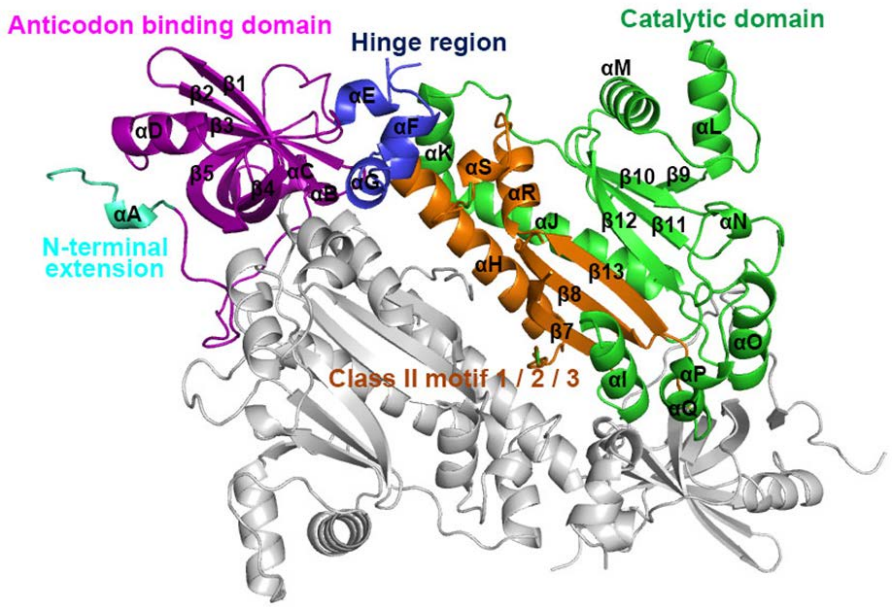

Figure 1-5. Crystal structure of DRS dimer

The N-terminal extension, anticodon binding domain, hinge region, catalytic domain, and motifs are colored and labeled in cyan, magentas, blue, green, and orange respectively.

The anticodon binding domain of DRS (residues 57-146) contains the oligonucleotide binding-fold (OB-fold) that is composed of a five-stranded antiparallel β-sheet connected by helices and loops (β1-β5) to form a closed β-barrel. The catalytic domain (residues 189-497) adopts thirteen α-helices (αH-αT) and eight β-strands (β6-β13) which comprise all the three conventional class II aminoacyl-tRNA synthetase motifs; motif 1, 2, and 3.(Eriani, et al., 1990, Nature, 2) The hinge region (residues 156-188) plays a fundamental role in the connection of the anticodon binding domain and the catalytic domain. In the middle of the hinge region, residues 163-172 could not be observed due to the lack of the electron density and the disordered residues are considered as a part of binding region to the ribose-phosphate backbone in the D-stem of $tRNA^{Asp}$, compared with the known *S. cerevisiae* DRS-$tRNA^{Asp}$ complex structure.(Cavarelli, et al., 1994, The EMBO journal, 17) In addition, residues 224-247 in the flipping loop and residues 273-282 in the motif 2 could not be modeled in the crystal structure of DRS. These regions are known to be dynamic without its cognate tRNA and recognize its tRNA in an induced-fit manner.(Sauter, et al., 2000, J Mol Biol, 23)

When the anticodon binding domain, hinge region, and catalytic domain in the structure were independently superimposed with those of the *S. cerevisiae* DRS-$tRNA^{Asp}$ complex structure, the three domains

were structurally well-conserved with the r.m.s.d. values of 1.08 Å, 1.80 Å, and 0.97 Å, respectively. In the anticodon binding domain, three β-strands (β1, β2, and β3) could bind to the anticodon loop of $tRNA^{Asp}$ which is composed of GUC elements. In the hinge region, short helices containing Asp158 and Asn175 could interact with the D-stem (U11, U12) of $tRNA^{Asp}$. In the catalytic domain, the flipping loop and the class II motif 2 play a key role in the interaction of DRS with the 3'-end of $tRNA^{Asp}$ (Figure 1-6).

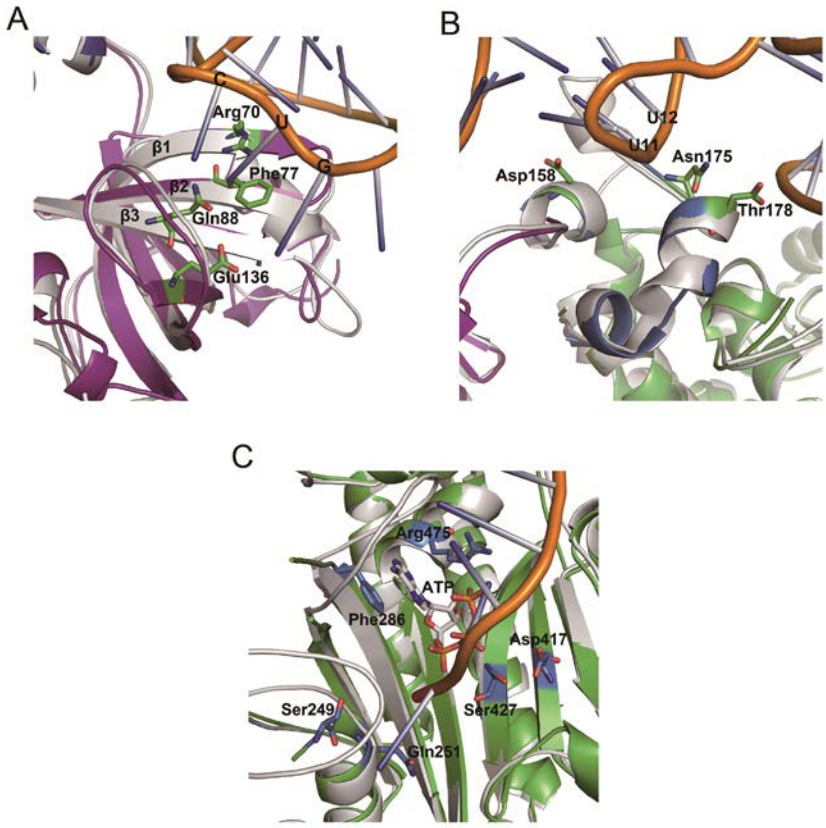

Figure 1-6. Superposition of human DRS with *S.cerevisiae* DRS-tRNA^{Asp}

The anticodon binding domain (**A**) and the hinge region (**B**) of human DRS are colored as in Figure 1-5 and the catalytic domain (**C**) of human DRS is represented in green. *S. cerevisiae* DRS is colored in gray and tRNA^{Asp} is shown in orange. Carbon, oxygen, nitrogen and phosphorus atoms of ATP are shown with stick model in gray, red, blue, and orange, respectively. The predicted interaction residues of human DRS with tRNA^{Asp} are labeled and shown in stick model.

3.2. Structural comparison of human cytosolic and mitochondrial DRSs

Recently, the crystal structure of human mitochondrial DRS (DRS2) has been determined at 3.7 Å resolution (PDB ID: 4AH6).(Neuenfeldt, et al., 2012, Nucleic acids research, 4) Even though human DRS and DRS2 share only 22.9% sequence identity (Figure 1-7), two structures are structurally similar to each other with the r.m.s.d. distance of 1.7 Å. The anticodon binding domain, hinge region, and catalytic domain of DRS and DRS2 are structurally well-conserved, with the exception of an additional motif in the catalytic domain of DRS2 which is known as the insertion domain (Figure 1-8). The insertion domain of DRS2 adopts the enlarged catalytic groove with more electropositive surface potential, which enables an alternate interaction network at the subunit interface between tRNA and DRS2.(Neuenfeldt, et al., 2012, Nucleic acids research, 4) Interestingly, DRS2 showed a higher sensitivity than DRS for inhibitors with a non-hydrolysable adenylate moiety and its correlation with structural features has not been well understood. (Messmer, et al., 2009, Biochimie, 24) Structural analyses of DRS and DRS2 in complex with same adenylate analogs would elucidate a subtle role of the domain difference with respect to substrate specificity and evolutionary advantages.

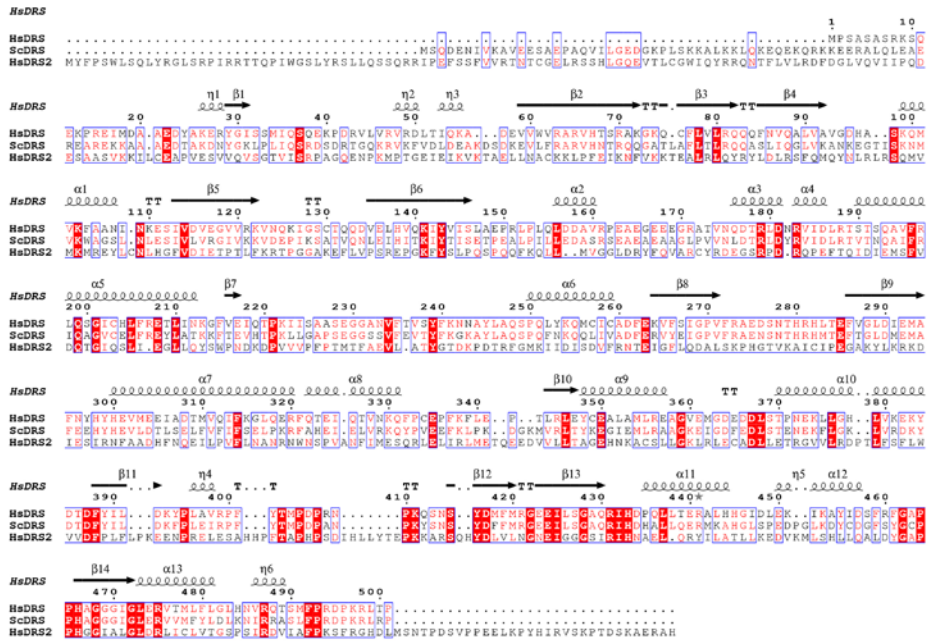

Figure 1-7. Sequence alignment of human cytosolic DRS with *S.cerevisiae* DRS and human mitochondrial DRS

Strictly conserved amino acid residues are highlighted in red shaded boxes and moderately conserved amino acid residues are colored in red. The alignment figure was prepared using *ESPript* program (Robert and Gouet, 2014, Nucleic acids research, 25).

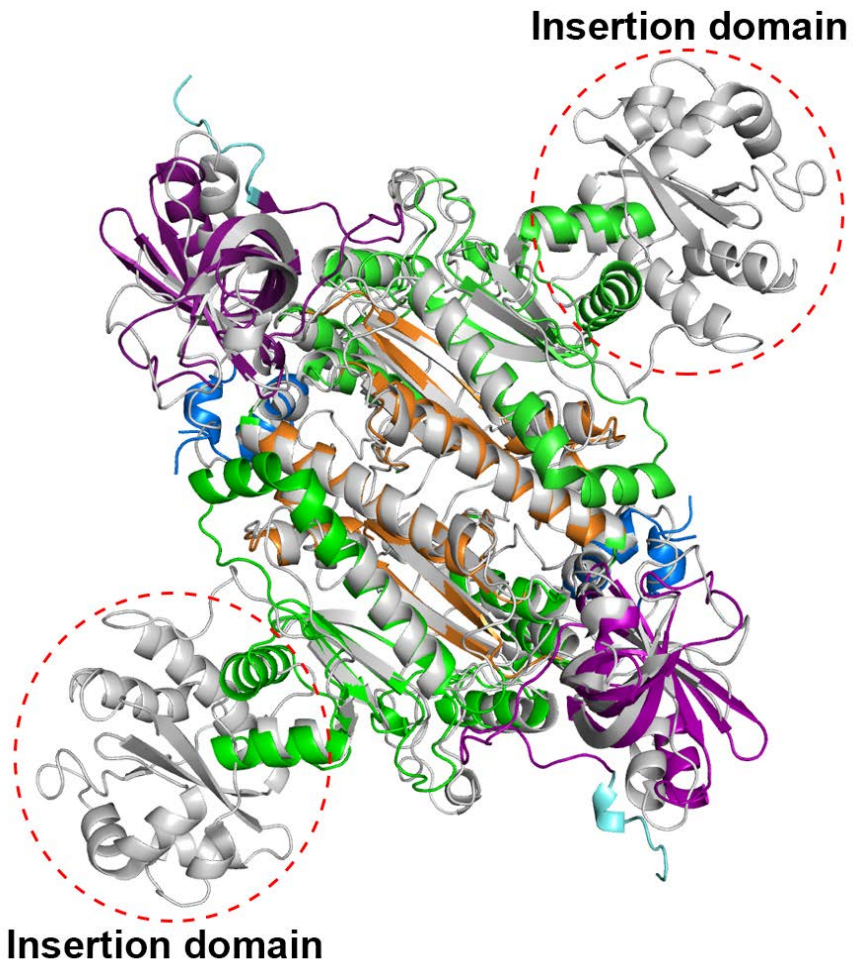

Figure 1-8. Structural comparison of human cytosolic DRS and mitochondrial DRS

Human cytosolic DRS is shown as in Figure 1-5 and mitochondrial DRS is colored in gray. The red dotted ovals indicate the insertion domain of mitochondrial DRS.

3.3. Flexible N-terminal extension of DRS

In higher eukaryotes, additional domains or motifs in a specific AARS result in additional functions. In the case of DRS, KRS, and NRS, they contain the N-helix that is named after the helical conformation in part of their N-terminal extension region.(Woese, et al., 2000, Microbiology and molecular biology reviews : MMBR, 12; Guo, et al., 2010, Nature reviews Molecular cell biology, 26) The previously determined NMR structure of the N-terminal extension of DRS revealed the conformational flexibility caused by the β-turn followed by one α-helix and the N-terminal extension plays a crucial role in the interaction between $tRNA^{Asp}$ and EF-1α.(Reed and Yang, 1994, J Biol Chem, 13; Reed, et al., 1994, J Biol Chem, 14; Cheong, et al., 2003, The international journal of biochemistry & cell biology, 15) In the crystal structure of DRS, the C-terminal end of the α-helix in the N-terminal extension was observed, comprising of Lys26, Glu27, and Arg28, even though the N-terminal region was less-ordered. To get a glimpse of the whole N-helix structure, the structurally well-resolved C-terminal end of the N-terminal extension residue Glu27 and Arg28 was superposed with the α-helix of the NMR structure, considering the helical wheel conformation (Figure 1-9). The α-helix in the N-terminal extension is amphipathic and the hydrophilic face of the amphipathic helix could interact with positively charged residues Arg8 and Lys9 in

the N-terminus by the conformational change on the flexible β-turn.(Cheong, et al., 2003, The international journal of biochemistry & cell biology, 15) Consequentially, the crystal structure further supports the structural switching model of the N-terminal extension of DRS in the aid of the direct transfer of $tRNA^{Asp}$ to EF-1α (Figure 1-10).

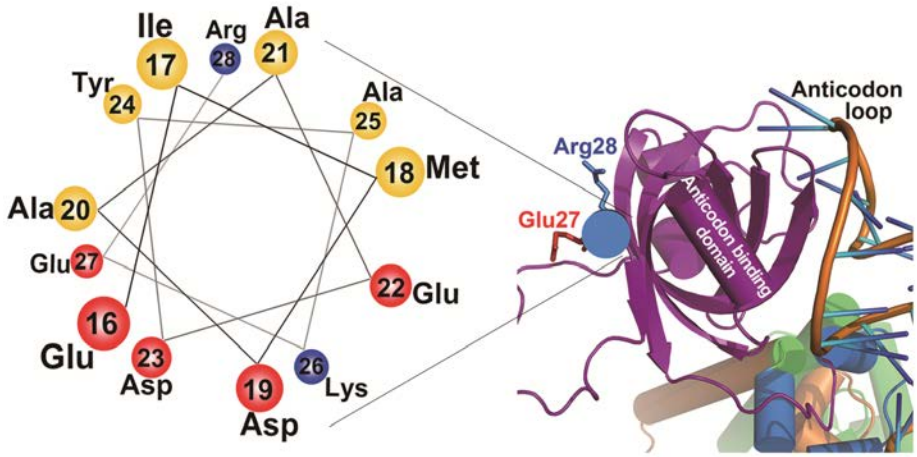

Figure 1-9. Helical wheel of the α-helix in the N-terminal extension

Helical wheel represent the α-helix in the N-terminal extension and the anticodon binding domain. The hydrophobic, negative-charged, and positive-charged residues in the helical wheel are colored yellow, red, and blue, respectively.

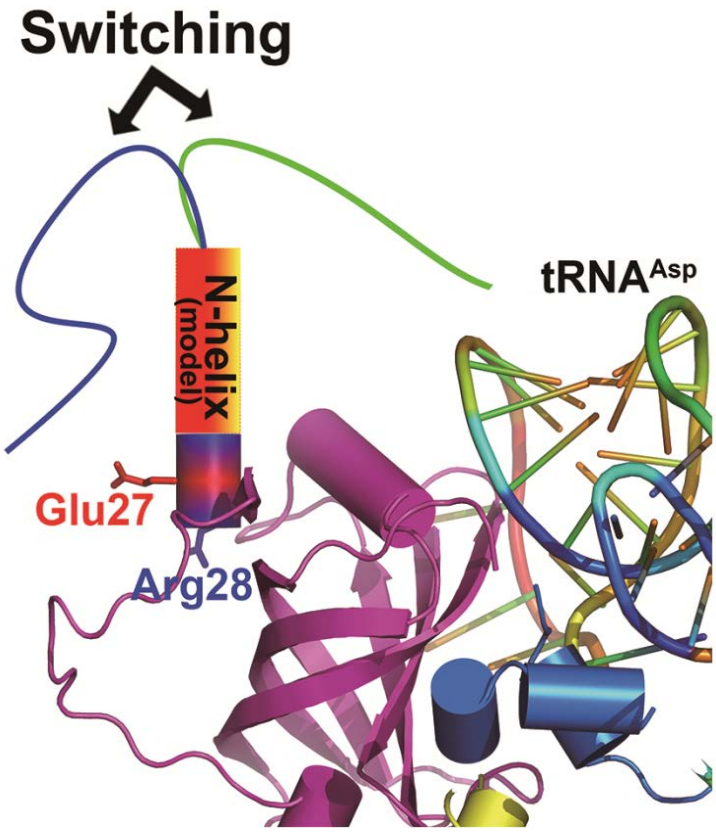

Figure 1-10. The switching model of the N-helix with DRS structure

From the helical wheel model, the switching model of the N-helix with the DRS structure is suggested.

3.4. Post-translational modification of DRS

To speculate the organization of DRS as a main interacting component with AIMP2/p38 in the MSC assembly, all the known post-translational modification (PTM) data was searched and independently implemented the PTM analyses of DRS. The liquid chromatography tandem mass spectrometry analysis was performed and two phosphorylation sites (Tyr239 and Ser249) and six acetylation sites (Lys55, 110, 213, 241, 330 and 453) were identified. Among the results, the phosphorylation of Tyr239 and the acetylation of Lys55, 213 and 453 were firstly identified. These findings and other PTM sites information of DRS from PhosphoSite Plus database (http://www.phosphosite.org) indicated that the residues 238-254 region of the class II aminoacyl-tRNA synthetase are dynamically regulated by various types of modifications such as phosphorylation, acetylation and ubiquitination (Figure 1-11). For instance, while Lys241 was identified with its acetylation modification in the analysis, collected six independent MS-analysis data of ubiquitin branch motif (K-e-GG) immunoaffinity beads purification studies showed that Lys241 is also modified with ubiquitin. Thus it seems that the phosphorylation status of Ser238, Tyr239 and/or Ser249 could affect the catalytic activity, stability or partner binding affinity of DRS through a competitive modification event between acetylation and

ubiquitination of Lys241 and/or Lys254, though it should be clarified with further studies. PTM sites mapped on the surface representation of human DRS dimer modeled with $tRNA^{Asp}$ are shown in Figure 1-12. A large numer of PTM sites locate in tRNA interaction region, or surface of DRS. These results suggest that the PTM sites could affect on interaction between DRS and tRNA.

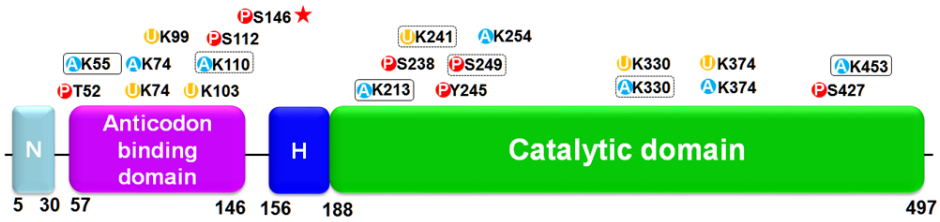

Figure 1-11. PTM analyses

Acetylation, phosphorylation, and ubiquitination sites are shown as blue, red, and yellow circles, respectively. PTM sites uniquely observed in this study and residues observed both in the database and in this study are surrounded by black boxes and dotted boxes, respectively. Ser146, which is expected to play a key role in the organization of DRS, is marked with a red asterisk.

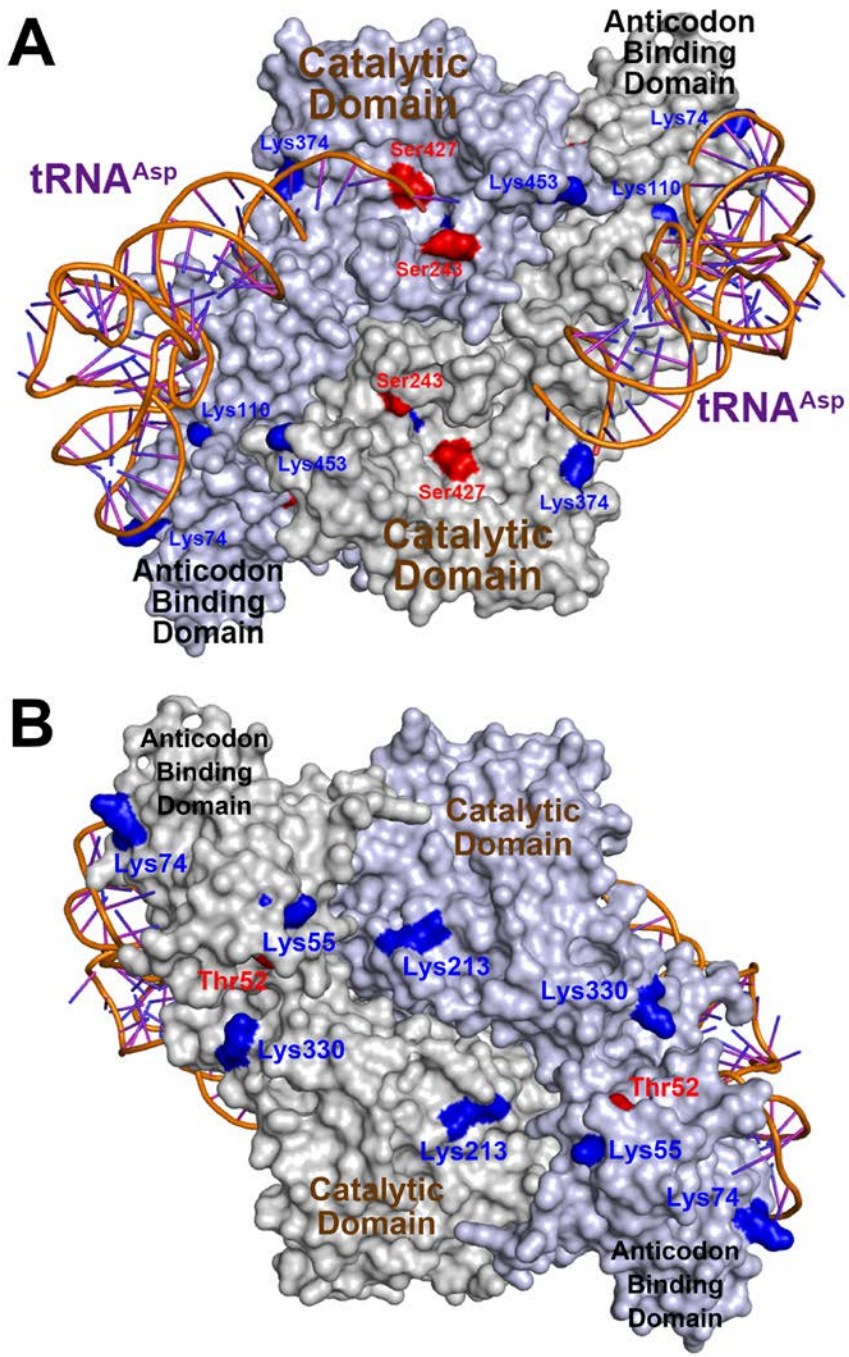

Figure 1-12. PTM sites mapped on the surface representation of human DRS dimer modeled with tRNA^{Asp}

The crystal structure of human DRS dimer was superposed with that of *S. cerevisiae* DRS dimer in complex with $tRNA^{Asp}$ and human DRS is shown as surface representation. (**A**) tRNA binding face of DRS dimer. (**B**) Bottom and symmetric groove of the DRS dimer. Acetylation and phosphorylation sites are colored in blue and red, respectively.

3.5. Implication on the MSC assembly

In the MSC, AIMP2/p38 has been known to interact with two subcomplexes of the MSC (I: MRS, AIMP3/p18, EPRS, IRS, LRS; II: AIMP1/p43, QRS, RRS, DRS, and KRS), and the N-terminal domain of AIMP2/p38 interacts with the subcomplex II, DRS, and KRS.(Kaminska, et al., 2009, J Biol Chem, 10) The N-terminal motif 1 and 2 of AIMP2/p38 have been recently shown to interact with the bottom groove and the symmetric groove on the KRS dimer, respectively.(Ofir-Birin, et al., 2012, Molecular cell, 27) Based on the situational and structural similarity between KRS and DRS, two dimers of DRS would interact with AIMP2/p38 in the similar manner of KRS regarding the association and dissociation from the MSC. In the case of KRS, Ser207 establishes the major intermolecular interaction of the KRS dimer through three hydrogen bonds between the hydroxyl group of Ser207 and the backbone of Gly540 and Leu541. Interestingly, a conformational change triggered by the phosphorylation of Ser207 switches the function of KRS from translation to transcription, provoking a new conformer and releasing KRS from the MSC.(Ofir-Birin, et al., 2012, Molecular cell, 27) To this surprise, DRS also contains the equivalent Ser146, Gly462, and Ala463, which are highly conserved in the amino acid sequence and three-dimensional structure in higher eukaryotes (Figure 1-13). In addition, the PTM information of

DRS from the PhosphoSite Plus database shows that the phosphorylation of Ser146 was already observed with the phosphoproteome analyses of the human cell cycle using the mass spectrometry.(Olsen, et al., 2010, Science signaling, 28) Thus, the phosphorylation of Ser146 could initiate a conformation change of the DRS dimer and trigger an unpredicted function of DRS by releasing it from the MSC. The structural study and PTM analyses of DRS extend the knowledge about the interaction of components in the MSC and provide fundamental information for human physiological signaling pathways related to the MSC.

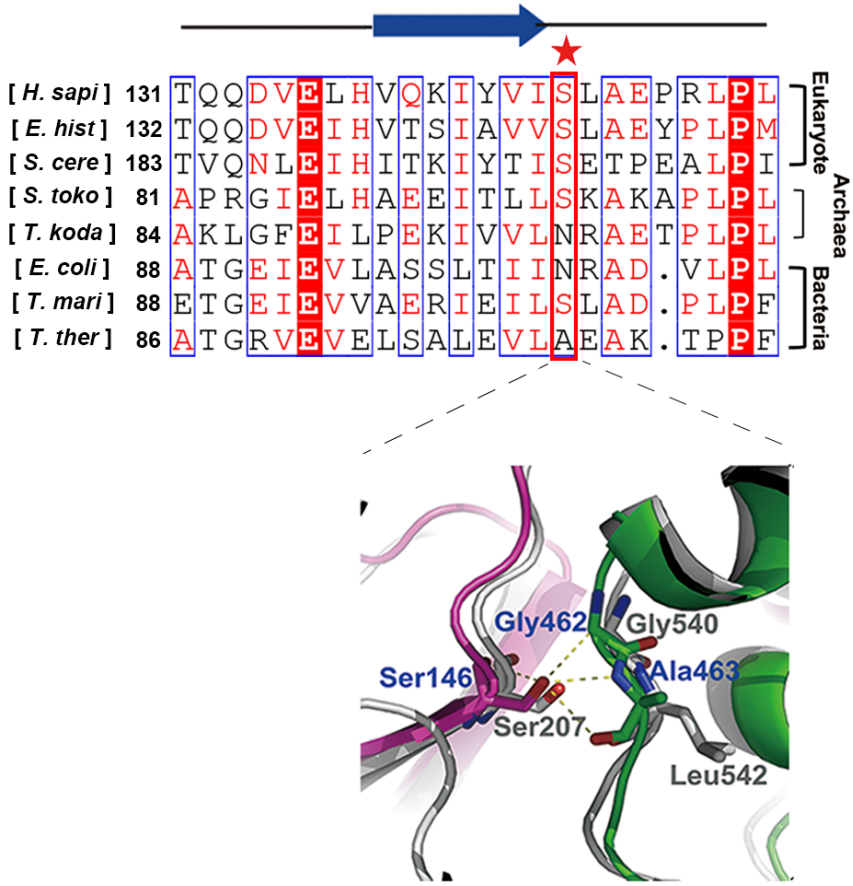

Figure 1-13. Key intermolecular interaction of DRS

Sequence alignment of the interface residues of anticodon binding domain and catalytic domain of DRSs from various organisms. Ser146 of human DRS are marked with red asterisks. Close-up view of Ser146 and the intermolecular interaction of DRS dimer. The structure of human DRS is superimposed with that of human KRS shown in a gray cartoon model.

Chapter 2

Structure and stability of the dimeric triosephosphate isomerase from *Thermoplasma acidophilum*

[This chapter was published in *PLoS One*.]

Park SH et al. (2015) Structure and Stability of the Dimeric Triosephosphate Isomerase from the Thermophilic Archaeon *Thermoplasma acidophilum*. *PLoS One* 10(12):e0145331. doi: 10.1371/journal.pone.

1. Introduction

Triosephosphate isomerase (TPI or TIM) is a functionally and structurally well-known enzyme that plays a crucial role in glycolytic and gluconeogenic metabolism. TPI accurately and efficiently interconverts dihydroxyacetone phosphate (DHAP) and glyceraldehyde-3-phosphate (GAP) (Figure 2-1). Missense mutations of TPI genes result in TPI deficiency through loss-of-function (Schneider, 2000, Bailliere's best practice & research Clinical haematology, 29). TPI deficiency has been known to cause metabolic diseases, glycolytic enzymopathies, in which neurological pathogenesis is uniquely severe (Celotto, et al., 2006, Genetics, 30). Pathogenic TPI

deficiency mutations dramatically affect TPI activity owing to either catalytic interruption or oligomeric state alteration (Arya, et al., 1997, Hum Mutat, 31; Hollan, et al., 1993, Hum Genet, 32; Daar, et al., 1986, Proc Natl Acad Sci U S A, 33).

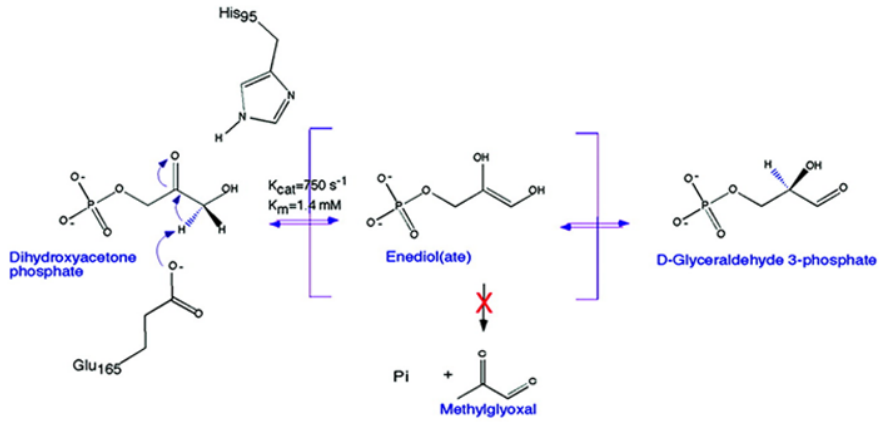

Figure 2-1. The isomerization reaction catalyzed by triosephosphate isomerase (Jogl, et al., 2003, Proceedings of the National Academy of Sciences of the United States of America, 34)

The reaction pathway from DHAP to GAP, including the putative reaction intermediate, an enediol.

Thermoplasma acidophilum is one of the most acidophilic organisms among known thermophilic archaea. It optimally grows at 55 – 60 ℃ and pH 0.5 – 2.0. For glucose degradation, *T. acidophilum* has been known to utilize not only non-phosphorylative Entner-Doudoroff (ED) pathway but also canonical glycolysis/gluconeogenesis pathway (Embden-Meyerhof-Parnas pathway) (Ruepp, et al., 2000, Nature, 35). Although one of the glycolysis/gluconeogenesis pathway enzymes, phosphofructokinase, has not been identified in *T. acidophilum*, TPI has been considered to play a crucial role in the glycolysis/gluconeogenesis pathway in *T. acidophilum*.

TPI is a representative α/β protein with eight α-helices and eight β-strands connected by loops, forming a TIM-barrel fold (Wierenga, 2001, FEBS Lett, 36). The active site of TPI is highly conserved in all kingdoms and located inside of the TIM-barrel fold with three catalytic residues (Lys9, His89, and Glu137 in TaTPI numbering). Most TPIs are optimally active in their dimeric forms. In contrast, archaeal TPIs that withstand high temperatures are tetrameric in their active states (Maes, et al., 1999, Proteins, 37). Thermostable proteins have been known to adapt to high temperature in various ways: increased electrostatic interactions, hydrogen bonds, and hydrophobic effects, resulting in fortified subunit contacts, more compact packing, higher oligomerization state, and two-state equilibrium reversibility (Xiao and

Honig, 1999, Journal of molecular biology, 38; Dams, et al., 2000, Journal of molecular biology, 39; Szilagyi and Zavodszky, 2000, Structure, 40; Delboni, et al., 1995, Protein science : a publication of the Protein Society, 41; Romero-Romero, et al., 2015, Physical chemistry chemical physics : PCCP, 42).

In the Protein Data Bank (PDB), structures of one bacterial TPI (*Thermotoga maritima;* Tm) and three archaeal TPIs (*Pyrococcus woesei;* Pw, *Thermoproteus tenax;* Tt, and *Methanocaldococcus jannaschii;* Mj) that have been deposited are in tetrameric form. *P. woesei*, *M. jannaschii*, and *T. acidophilum* belong to Euryarchaeota and *T. tenax* is affiliated to Crenarchaeota in phylogeny. Among tetrameric TPIs in PDB, tetrameric conformation of bacterial TmTPI is maintained by disulfide bonds between two classical TPI dimers (Maes, et al., 1999, Proteins, 37). In archaeal TPIs, helix 4 and helix 5 in the tetrameric interface are of key importance for their tetrameric forms. Especially, helix 5 in thermostable TPIs has been considered as a major contributor for tetramer formation via dominant hydrophobic effects (Walden, et al., 2001, Journal of molecular biology, 43).

In this work, I report crystal structures of apo- and glycerol-3-phosphate (G3P)-bound TaTPI, each representing open and closed form. Unlike other thermostable archaeal TPIs, TaTPI forms a stable dimer in solution, which I confirmed using analytical ultracentrifugation and

size-exclusion chromatography. I also show the effect of pH on the secondary structure and temperature-induced unfolding of TaTPI. Through systematic comparison of TaTPI with available dimeric and tetrameric TPIs, I suggest that TPI stabilization patches can be targeted for the design of more stable TIM-barrel fold proteins.

2. Material and methods

2.1. Cloning, expression, and purification of TaTPI and MjTPI

Full-length sequences of *Thermoplasma acidophilum* TPI (TaTPI, 216 amino acid residues) and *Methanocaldococcus jannaschii* TPI (MjTPI, 219 amino acid residues) were amplified using PCR and cloned into pET-28a(+) vector (Novagen) containing C-terminal His_6-tag. Cloned plasmids were transformed into *Escherichia coli* Rosetta2(DE3)pLysS strain. Recombinant proteins were overexpressed by adding 0.5 m*M* isopropyl 1-thio-ß-D-galactopyranoside at $O.D._{600nm}$ 0.5 and cells were further incubated at 20 ℃ overnight (16 h) using Luria Broth culture media. Harvested cells were lysed by cell sonicator (SONICS) in lysis buffer (20 m*M* Tris-HCl, pH 7.5, 500 m*M* NaCl, 35 m*M* imidazole, and 1 m*M* phenylmethylsulfonyl fluoride). After incubation of cell lysate at 60 ℃ for 10 minutes, cell debris and denatured proteins were removed by centrifugation at 35,000 xg for 50 minutes. Supernatant was applied to HiTrap Chelating HP column (GE Healthcare) for affinity chromatography. Loaded sample was eluted with elution buffer (20 m*M* Tris-HCl, pH 7.5, 500 m*M* NaCl, and 500 m*M* imidazole) following equilibration with washing buffer (20 m*M* Tris-HCl, pH 7.5, 500 m*M* NaCl, and 50 m*M* imidazole). Eluted sample was further purified by size-exclusion chromatography with

HiLoad 16/600 Superdex 200 prep grade column (GE Healthcare) equilibrated with 20 m*M* Tris-HCl, pH 7.5, and 200 m*M* NaCl. Fractions containing TPI proteins were further purified by anion exchange chromatography with HiTrap Q HP column (GE Healthcare) after 2 X dilution of the fractions with 20 m*M* Tris-HCl, pH 7.5, and 100 m*M* NaCl. Linear gradient of 0-500 m*M* NaCl in 20 m*M* Tris-HCl, pH 7.5, was applied for elution. For the final purification step, second size-exclusion chromatography was performed with HiLoad 16/600 Superdex 200 prep grade column (GE Healthcare) equilibrated with 20 m*M* Tris-HCl, pH 7.5, and 200 m*M* NaCl for TaTPI or 50 m*M* HEPES (4-(2-hydroxyethyl)-1-piperazineethanesulfonic acid), pH 7.5, for MjTPI. For crystallization, purified TaTPI proteins were concentrated to 30 mg ml^{-1}.

2.2. Crystallization

Initial crystals of apo-TaTPI were grown at 22 ℃ by sitting drop vapor diffusion method with crystallization solution containing 2 *M* NaCl and 10% (w/v) polyethylene glycol 6000. Apo-TaTPI crystals suitable for diffraction data collection were grown at 4 ℃ using hanging-drop vapor diffusion method after mixing apo-TaTPI proteins with 2 times volume of crystallization solution containing 0.5 *M* NaCl, 10% (w/v) polyethylene glycol 6000, and 0.1 *M* Tris-HCl, pH 8.5. Crystals of TaTPI in complex with glycerol-3-phosphate (G3P) were obtained from crystallization solution with 0.6 *M* NaCl, 9% (w/v) polyethylene glycol 6000, and 0.1 *M* Tris-HCl, pH 8.5, after incubating purified apo-TaTPI proteins with 20 m*M* G3P for 4 h at 4 ℃ (Figure 2-2).

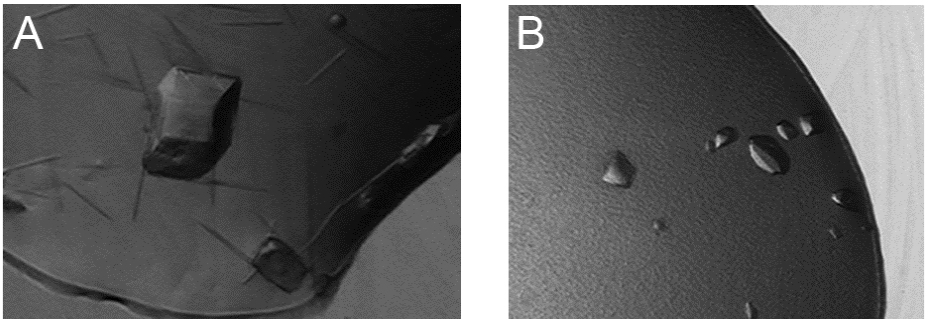

Figure 2-2. Crystals of TaTPI from *T.acidophilum*

(A) Crystals of the apo-TaTPI. (B) Crystals of the TaTPI in complex with glycerol-3-phosphate (G3P).

2.3. X-ray data collection and structure determination

For X-ray diffraction data collection, crystals were frozen in liquid nitrogen following cryoprotection by soaking TaTPI crystals in crystallization solution supplemented with 20% (v/v) glycerol. X-ray diffraction data for apo- and G3P-bound complex TaTPI crystals were collected at BL-7A synchrotron beamline at the Pohang Light Source, Korea, and at BL-1A synchrotron beamline at the Photon Factory, Japan, respectively. Collected data were processed using *HKL*2000 program suite (Otwinowski and Minor, 1997, Methods Enzymol, 44). The apo- and G3P-bound TaTPI crystals belong to the space group $P2_12_12_1$, with unit cell parameters of a = 75.49, b = 113.96, c= 114.80, and a = 72.63, b = 84.08, c = 143.54, respectively (Figure 2-3; 2-4). The crystal structure of apo-TaTPI was solved by molecular replacement method using MOLREP program (Vagin and Teplyakov, 2010, Acta Crystallogr D Biol Crystallogr, 18), with the crystal structure of *Pyrococcus woesei* TPI (PDB ID: 1HG3) as a phasing model (Walden, et al., 2001, Journal of molecular biology, 43). The crystal structure of G3P-bound TaTPI was solved with the apo-TaTPI structure as a phasing model. The initial models building were carried out by *WinCoot* program (Emsley, et al., 2010, Acta Crystallogr D Biol Crystallogr, 19) and further refined with *REFMAC*5 program (Murshudov, et al., 1997, Acta Crystallogr D Biol Crystallogr, 20). All

refinement steps were monitored using R_{free} value based on 5.0% of independently saved reflections. The final models were evaluated with *MolProbity* program (Lovell, et al., 2003, Proteins, 21). Data collection and refinement statistics are summarized in Table 2-1; 2-2.

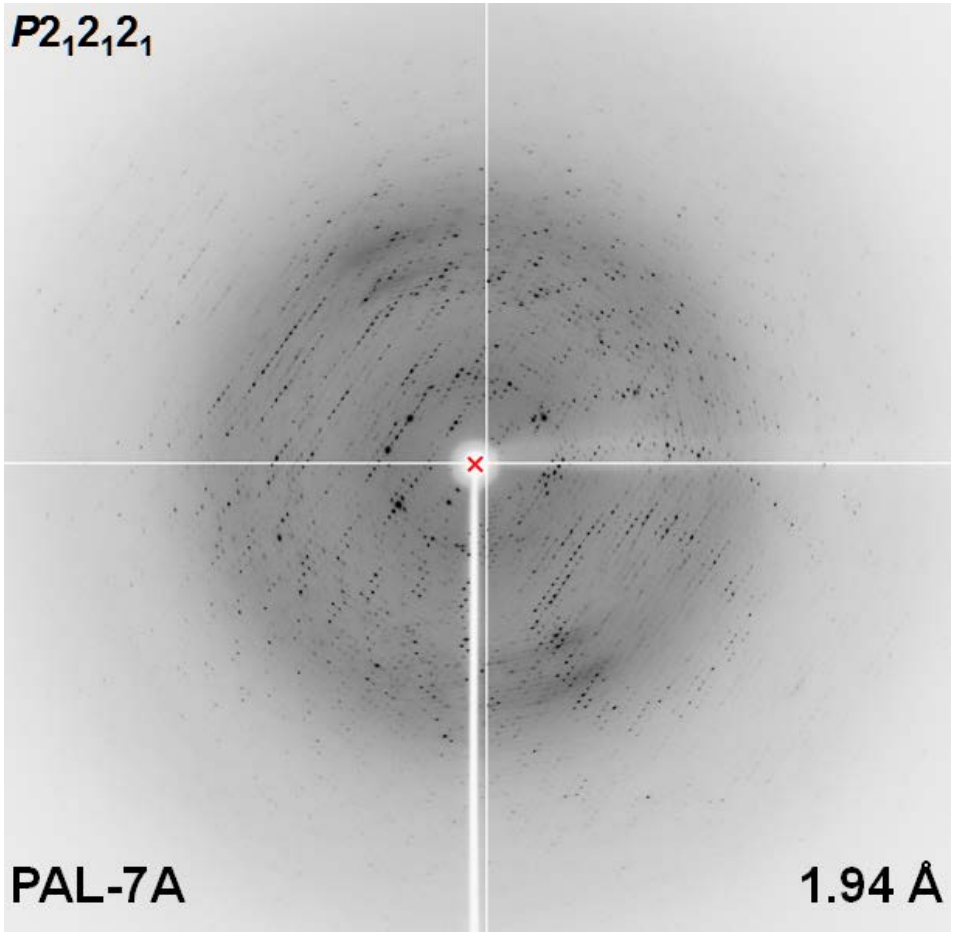

Figure 2-3. X-ray diffraction image from apo-TaTPI

X-ray diffraction data for apo-TaTPI crystals were collected at BL-7A synchrotron beamline at the Pohang Light Source, Korea.

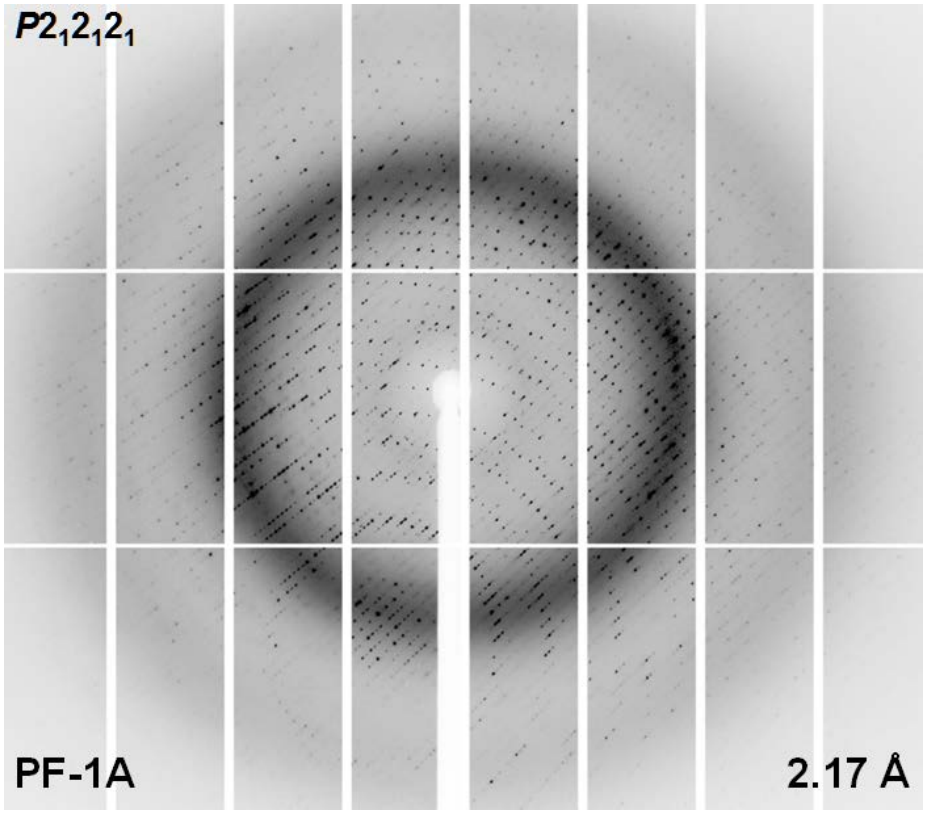

Figure 2-4. X-ray diffraction image from G3P-bound TaTPI

X-ray diffraction data for G3P-bound complex TaTPI crystals were collected at BL-1A synchrotron beamline at the Photon Factory, Japan.

Table 2-1. Statistics for data collection

Data collection[a]	**TaTPI**	**G3P-bound TaTPI**
Space group	$P2_12_12_1$	$P2_12_12_1$
Cell dimensions		
a, b, c (Å)	75.49, 113.96, 114.80	72.63, 84.08, 143.54
α, β, γ (°)	90, 90, 90	90, 90, 90
Data set		
X-ray wavelength (Å)	1.0000	1.1000
Resolution (Å)[b]	50.00–1.94	50.00-2.17
Total / unique reflections	521,936 / 73,921	294,576 / 47,245
Mean *I/sigma(I)*	32.4 (3.3)	20.9 (3.0)
Multiplicity	7.1 (5.6)	6.2 (5.6)
Completeness (%)	99.0 (83.5)	99.9 (99.9)
R_{merge} (%)[c]	9.1 (62.5)	13.4 (59.0)

Footnotes to Table 2-1

[a]Data collected at the synchrotron BL-7A at the Pohang Light Source and BL-1A at the Photon Factory.

[b]Numbers in parentheses indicate the highest resolution shell.

[c]$R_{merge} = \Sigma_h \Sigma_i |I(h)_i - \langle I(h) \rangle| / \Sigma_h \Sigma_i I(h)_i$, where $I(h)$ is the observed intensity of reflection h, and $\langle I(h) \rangle$ is the average intensity obtained from multiple measurements.

Table 2-2. Refinement statistics

Refinement	TaTPI	G3P-bound TaTPI
Resolution (Å)	50.00–1.94	50.00–2.17
R_{work}[a] / R_{free}[b] (%)	18.0 / 21.5	18.3 / 22.5
No. of non-hydrogen atoms / mean B-factor (Å^2)		
Protein	6,996 / 32.9	6,640 / 34.2
Water	561 / 39.8	401 / 34.4
Other atoms	28 / 40.1	44 / 22.9
Poor rotamers (%)[c]	0.1	0.3
Ramachandran plot analysis (%)		
Most favored regions	98.0	96.1
Additional allowed regions	2.0	3.4
Disallowed regions	0	0.5
R.m.s.d. from ideal geometry		
Bond lengths (Å)	0.019	0.015
Bond angles (°)	1.648	1.550

Footnotes to Table 2-2

[a]$R_{work} = \Sigma \mid |F_o| - |F_c| \mid / \Sigma |F_o|$, where $|F_o|$ is the observed structure factor amplitude and $|F_c|$ is the calculated structure factor amplitude.

[b]R_{free} = R-factor based on 5.0% of the data excluded from refinement.

[c]Values obtained using MolProbity.

2.4. Analytical ultracentrifugation (AUC)

Equilibrium sedimentation studies were performed using Beckman ProteomeLab XL-A analytical ultracentrifuge in 20 m*M* Tris-HCl buffer, pH 7.5, and 200 m*M* NaCl at 20 ℃. Sedimentation data were collected at 280 nm using a six-sector cell at rotor speeds of 20,000 and 26,000 rpms with three different protein concentrations: 12.6 u*M* (0.31 mg ml^{-1}), 16.8 u*M* (0.41 mg ml^{-1}), and 21.0 u*M* (0.52 mg ml^{-1}). All measured data fit well to a homogeneous dimer model and representative results measured at 26,000 rpm using 16.8 u*M* protein concentration are presented. TaTPI concentrations were calculated using e_{280nm} = 11,920 $M^{-1}cm^{-1}$ and molecular weight of 24,671 daltons. Time required for the attainment of equilibrium was established by running at given rotor speed until scans were invariant for 4 hours: this was achieved at most by 36 hours in six-sector cells using 130 ul of samples. Partial specific volume of TaTPI protein and buffer density were calculated using Sednterp (Laue, 1995, Methods Enzymol, 45). The calculated partial specific volume at 20 ℃ was 0.7417 $cm^3 g^{-1}$ and the buffer density was 1.00704 g cm^{-3}. For data analysis by mathematical modeling using non-linear least-squares curve fitting, following functions were used for homogeneous (Eqn. 1) and interactive (Eqn. 2) models.

$$C_r = C_b \exp[A_p M_p(r^2 - r_b^2)] + \varepsilon \quad \text{(Eqn. 1)}$$

$$C_r = C_b \exp[A_p M_p(r^2 - r_b^2)] + C_b^n \exp[Ink + nA_p M_p(r^2 - r_b^2)] + \varepsilon \quad \text{(Eqn. 2)}$$

$$A_p = (1 - v\rho)\omega^2/2RT$$

where C_r is the total concentration at the radial position r, C_b is the concentration of protein at the cell bottom, M_p is the molecular weight of protein monomer, ε is a baseline error term, v and ρ are the partial specific volume and the solution density, respectively, and ω is the rotor angular velocity. The *In*k value is a natural log for equilibrium constants for reversible models (1x-nx, where n is 2 & 3) on an absorbance scale. Selection of the best model was made by examining numbers of weighted sum of square and root mean square error values. Further data manipulation and data analysis by mathematical modeling were performed using MLAB (Knott, 1979, Comput Programs Biomed, 46).

2.5. Circular dichroism (CD)

Temperature of maximum heat capacity (or half-denaturation temperature, Td) of TaTPI was measured by CD spectroscopy. Experimental sample was prepared following purification and concentration of TaTPI proteins to 0.4 mg ml^{-1} containing 50 m*M* HEPES, pH 7.5. CD traces of TaTPI were obtained at 222 nm using the J-1500 CD spectrometer (JASCO) at a scanning rate of 1℃ min^{-1}. The denaturation curve of TaTPI was analyzed by Kaleidagraph (Synergy Software) based on John and Weeks's protocol (John and Weeks, 2000, Protein science : a publication of the Protein Society, 47).Effect of pH variation on the secondary structure of TaTPI was also monitored by CD spectroscopy. The pH of protein solutions containing 20 m*M* Tris-HCl and 200 m*M* NaCl were adjusted to desired values between pH 1.0 and pH 7.0 with HCl for CD measurements. The baseline signal was measured with a buffer containing 20 m*M* Tris-HCl, pH 7.5, and 200 m*M* NaCl. CD spectra of pH-titrated TaTPI were recorded and averaged over two scans between 200 to 260 nm using J-1500 CD spectrometer (JASCO). The secondary structure contents of TaTPI were calculated by Multivariate SSE Program (JASCO).

2.6. Analytical size-exclusion chromatography

Analytical size-exclusion chromatography of TaTPI was performed with Superdex 200 10/300 GL column (GE Healthcare) following equilibration with 20 m*M* Tris-HCl, pH 7.5, and 200 m*M* NaCl. The applied protein were at concentrations of 0.9 and 4.5 mg ml^{-1}. Standard proteins from Gel Filtration Standard (BIO-RAD) were applied to the column for calibration. The standard protein mixture contained thyroglobulin (M.W. 670 kDa), γ-globulin (M.W. 158 kDa), ovalbumin (M.W. 44 kDa), myoglobin (M.W. 17 kDa), and vitamin B_{12} (M.W. 1.35 kDa).

2.7. Differential scanning calorimetry (DSC)

Maximum temperature of heat capacity of MjTPI was measured with VP-DSC differential scanning microcalorimeter (Malvern). Experimental sample was prepared following purification and concentration of MjTPI proteins to 1.6 mg ml^{-1} (65 u*M*). Sample buffer containing 50 m*M* HEPES, pH 7.5, was loaded into the DSC cell after degassing in an evacuated chamber for 5 minutes and reference data were measured with scan rate of 0.5 ℃ min^{-1}. Experimental temperature was increased in the range from 50 to 120 ℃. After sample buffer scan reached equilibrium, MjTPI proteins were carefully loaded into the cell following degassing and experiments were performed under the same condition as for the reference. Heat capacity curve was plotted using the Origin software (Malvern).

2.8. Data deposition

The structure coordinates and structure factors for apo- and G3P-bound TaTPI have been deposited in PDB under the accession code **5CSR** and **5CSS**, respectively.

3. Results and discussion

3.1. Overall structures of apo- and glycerol-3-phosphate-bound TaTPI

The crystal structures of apo-TaTPI and its complex with glycerol-3-phosphate (G3P), an analogue of the substrate glyceraldehyde-3-phosphate, have been determined at 1.94 and 2.17 Å resolution, respectively. R_{work}/R_{free} values for the final models of apo- and G3P-bound TaTPI were 18.0%/21.5% and 18.3%/22.5%, respectively. Crystal structures of apo- and G3P-bound TaTPI contain four copies of TaTPI monomer in the asymmetric unit, comprising two homodimers. The overall structure of TaTPI protomer confirms to the canonical TIM-barrel fold with eight α-helices and eight parallel β-strands from 216 amino acid residues (Figure 2-5A). The crystal structure of G3P-bound TaTPI reveals that G3P is well positioned at the active site of TaTPI with functionally conserved residues Lys9, His89, and Glu137 (Figure 2-5B). Glu137 is clearly demonstrated as a catalytic base, with its position being within 3 Å from O1 and O2 of G3P. An oxyanion hole, which contributes to the stabilization of transition state, is formed by NZ nitrogen of Lys9 and NE2 nitrogen of His89 with O2 oxygen of G3P. The phosphate group of G3P is perfectly coordinated through hydrogen bonds with backbone nitrogen atoms of Gly143, Gly175,

Ala196, and Ser197 residues, including adjacent water molecules (Figure 2-6).

Overall structures of apo- and G3P-bound TaTPI were similar with r.m.s.d. of 0.69 Å for 216 C_α positions, except G3P-bound area. The conformational changes in the loop 6 of ligand bound-TPIs have been reported in previously determined structures of TPIs from many species, including *Trypanosoma brucei*, *Gallus gallus*, *Geobacillus stearothermophilus*, *Leishmania mexicana*, and *Vibrio marinus* (Delboni, et al., 1995, Protein science : a publication of the Protein Society, 41; Zhang, et al., 1994, Biochemistry, 48; Alvarez, et al., 1998, The Journal of biological chemistry, 49; Williams, et al., 1999, Protein engineering, 50; Noble, et al., 1993, Proteins, 51; Wierenga, et al., 2010, Cellular and molecular life sciences : CMLS, 52). Likewise, loop 6 located between β-strand 6 and helix 6 and loop 7 located between β-strand 7 and helix 7 showed remarkable conformational changes when G3P binds to apo-TaTPI. When compared with apo-TaTPI structure, Gly143 located in loop 6 and Gly175 located in loop 7 moved toward G3P by 8.3 and 3.8 Å, respectively (Figure 2-5B). Consequently, residue Ala174 is pushed to a disallowed region of the Ramachandran plot in the G3P-bound form, an amino acid residue within loop 7 that is displaced by the ligand binding. G3P binding triggers the conformational change and induces the transformation of TaTPI from

open to closed form, securing the catalytic site from bulk solvent to maintain efficient catalytic activity. In addition, water molecules around the active site of apo-TaTPI are expelled from the active site and would be replaced with substrate upon substrate binding.

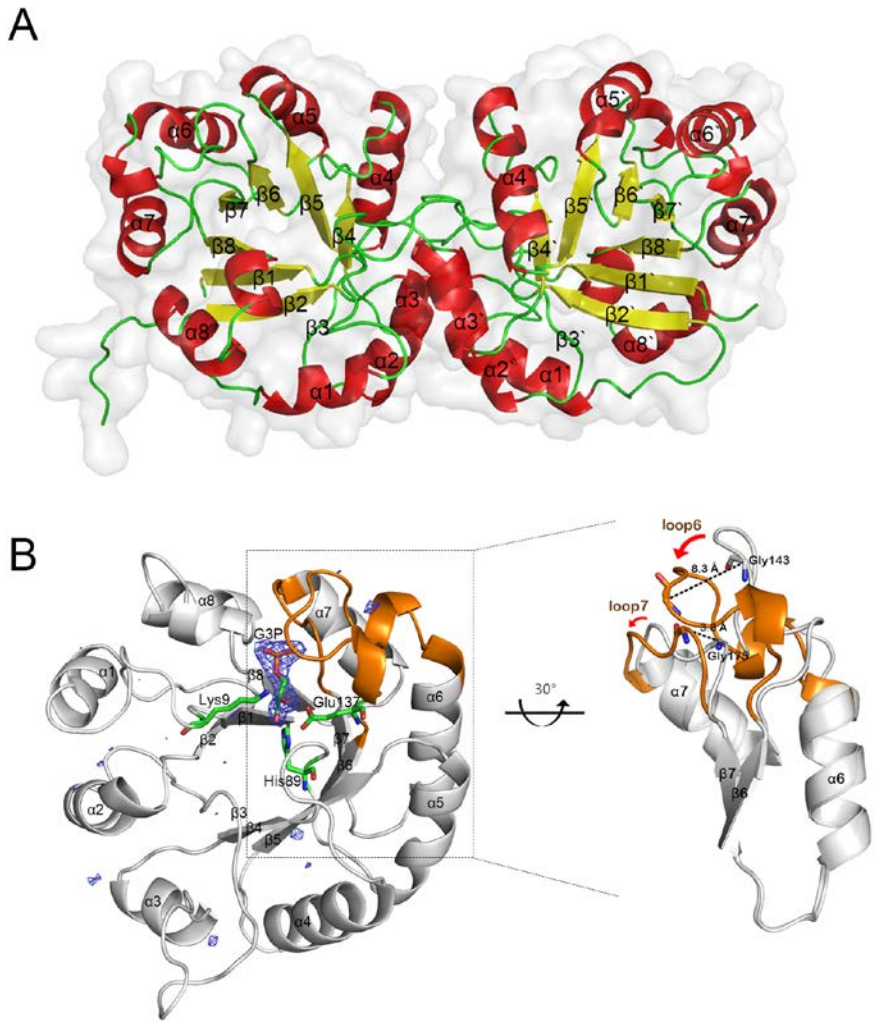

Figure 2-5. Overall structures of apo- and G3P-bound TaTPI

(A) Homodimer of apo-TaTPI is shown in carton representation, where α-helix, β-strand, and loop are colored in red, yellow, and green, respectively. (B) G3P-bound TaTPI. Only monomer of homodimeric G3P-bound TaTPI is demonstrated to emphasize a conformational change compared with apo-TaTPI. Extra positive electron density in F_o-F_c omit map contoured at 3.0 δ is shown as a blue mesh, which is

modelled as G3P later. Amino acid residues interacting with G3P in catalytic site and G3P are shown as stick model; carbon, oxygen, phosphorus, and nitrogen atoms are colored in green, red, orange, and, blue, respectively. Loop 6 and loop 7 regions, which show a distinctive conformational change upon binding of G3P, are represented in orange and magnified for clarity.

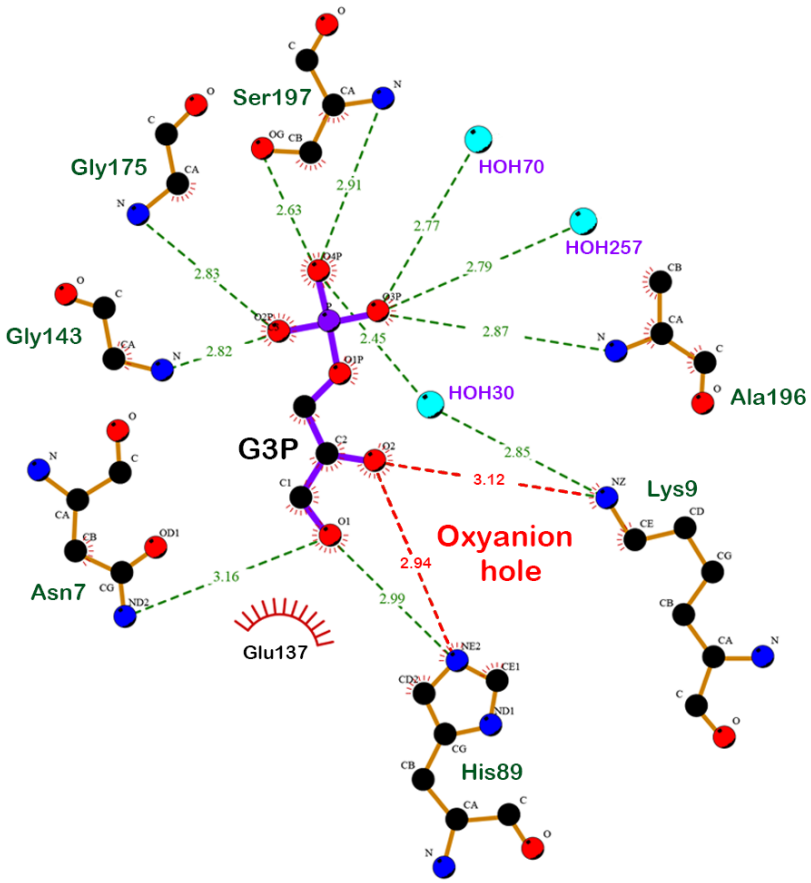

Figure 2-6. Binding modes of G3P with key amino acid residues of TaTPI

LIGPLOT diagram is used for representation of active site in the G3P-bound TaTPI. Carbon, nitrogen, oxygen, and phosphorus atoms are shown in black, blue, red, and magenta, respectively. Hydrogen bonds and oxyanion hole between G3P and TaTPI are shown as green and red dotted line, respectively.

3.2. Unique dimeric conformation of TaTPI

T. acidophilum belongs to thermoacidophilic euryarchaeota and TaTPI also shares high amino acid sequence similarity to other thermostable TPIs from *P. woesei*, *T. tenax*, and *M. jannaschii*, all of which adopt tetrameric conformation that renders them stable at high temperatures (Walden, et al., 2001, Journal of molecular biology, 43; Walden, et al., 2004, Journal of molecular biology, 53; Gayathri, et al., 2007, Acta Crystallogr D Biol Crystallogr, 54). Helix 4 and helix 5 of thermostable TPIs have been known to play important roles in the tetramer formation via hydrophobic interactions (Walden, et al., 2001, Journal of molecular biology, 43). However, crystal structures of apo- and G3P-bound TaTPI form a dimer and reveal a remarkable difference in helix 5 of TaTPI from other thermostable TPIs. Helix 5 of TaTPI is mainly composed of charged-amino acid residues (AEEAKYFREY) instead of hydrophobic residues found in other thermostable tetrameric TPIs. Structure-based sequence alignment of TaTPI with other TPIs shows that TaTPI resembles bacterial dimeric TPIs rather than tetrameric TPIs from thermostable archaea (Figure 2-7).

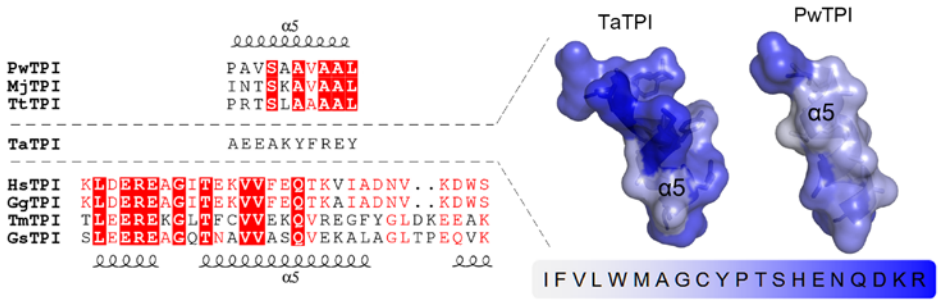

Figure 2-7. Structure-based sequence alignment of helix 5 region among TPIs

Structure-based sequence alignment of helix 5 region among TPIs from *Thermoplasma acidophilum* (TaTPI), *Pyrococcus woesei* (PwTPI), *Methanocaldococcus jannaschii* (MjTPI), *Thermoproteus tenax* (TtTPI), *Homo sapiens* (HsTPI), *Gallus gallus* (GgTPI), *Thermotoga maritima* (TmTPI), and *Geobacillus stearothermophilus* (GsTPI). Strictly conserved amino acid residues are highlighted in red shaded boxes and moderately conserved amino acid residues are colored in red. Helix 5 regions of TPIs from *Thermoplasma acidophilum* (PDB ID: 5CSR) and *Pyrococcus woesei* (PDB ID: 1HG3) are shown as cartoon representation with transparent surfaces, where amino acid residues are colored according to normalized consensus hydrophobicity scale (Eisenberg, et al., 1984, Journal of molecular biology, 55).

Structural differences between TaTPI and other tetrameric archaeal TPIs are observed not only in helix 5 but also in adjacent α-helices. In tetrameric archaeal TPIs, the N-terminus of helix 4 and the C-terminus of helix 6 play important roles in tetrameric interaction via hydrophobic effects and hydrogen bonds (Walden, et al., 2001, Journal of molecular biology, 43). The N-terminus of helix 4 of tetrameric archaeal TPIs contains conserved Leu (Leu103 in PwTPI numbering) that contributes to hydrophobic effects and hydrogen bonds with the other side of helix 4 and helix 5 for its tetrameric assembly. In the case of TaTPI, Leu in the N-terminus of helix 4 of tetrameric archaeal TPIs is replaced with Arg96, which deprives the hydrophobic effects for tetramer formation. Furthermore, TaTPI has shorter helix 6 than that of tetrameric archaeal TPIs, resulting in dissipated hydrophobic effects between two C-termini from each helix 6 of its accompanying dimeric partner, Val173 in PwTPI (Figure 2-8). Consequently, changes in amino acid composition of helix 5, thus in electrostatic surface, and slight modification of secondary structures in helix 4 and helix 6 seem to play subtle roles in dimer formation.

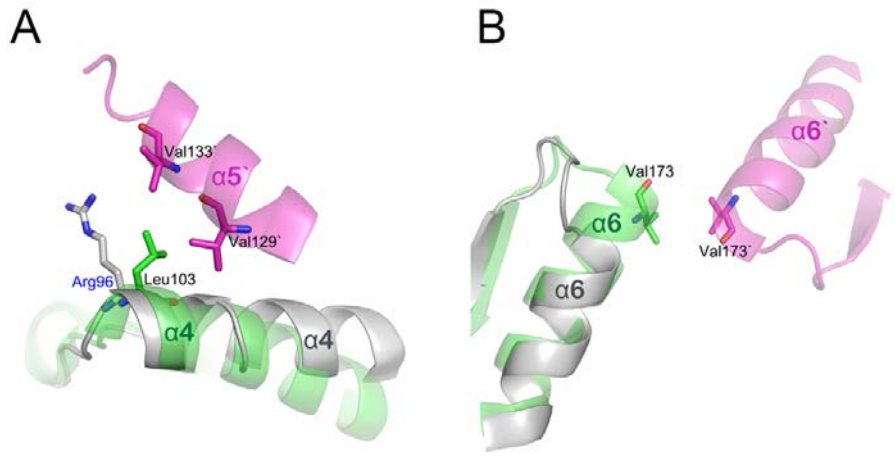

Figure 2-8. Structural comparison of helix 4 and helix 6 in TaTPI and PwTPI

(A) and (B) Structural comparison of helix 4 and helix 6 in TaTPI (gray) and PwTPI (green and magenta, each from different monomers). The important amino acid residues in tetrameric interface are shown as stick model.

3.3. Analytic ultracentrifugation analysis of TaTPI

In the crystal structure of apo-TaTPI, Cys50 in helix 2 of each homodimer drew this attention since it interacts with the other Cys50 from adjacent TaTPI homodimer via sulfur-containing hydrogen bonds, not disulfide bonds. Thus, I needed to re-confirm the oligomeric status of apo-TaTPI to make it sure whether the interaction of Cys-Cys is physiologically relevant or crystallographic artefact. To verify the oligomeric state of apo-TaTPI in solution, analytic ultracentrifugation analysis (AUC) was performed. Oligomeric state of apo-TaTPI in solution was investigated by equilibrium sedimentation technique at two speeds and three concentrations. Figure 2-9 shows the data and fits analyzed by using Eqn. 1 for homogeneous 1x, 2x, and 4x models at ultracentrifugal speed of 26,000 rpm. The weighted root-mean-square errors (RMS) for the 1x and 4x fits were 5.01×10^{-2} and 6.90×10^{-2}, respectively. In contrast to these models, dimer (2x) model gave much improved RMS value of 7.93×10^{-3}. Residual distribution plot (Figure 2-9 inset) also supports that the apo-TaTPI forms dimer in solution. Analysis at 20,000 rpm (data not shown) also gave a better RMS value of 5.76×10^{-3} for 2x model than those for 1x (3.90×10^{-2}) and 4x (5.42×10^{-2}) models. Mixture or reversible models were also investigated but there was no indication of the possibility. Data analysis using the reversible model (Eqn. 2) gave large negative *In*k values for monomer-

dimer (1x-2x) and monomer-trimer (1x-3x) models and much higher RMS values (~10^{-2}), so the reversible models for monomer-dimer (1x-2x) and monomer-trimer (1x-3x) equilibrium would not be the case for TaTPI. These results strongly indicate that apo-TaTPI exits as homogeneous dimer in solution. In addition, analytical size-exclusion chromatography results of apo-TaTPI, which were confirmed at two different TaTPI protein concentrations (0.9 and 4.5 mg ml^{-1}), also supported the dimeric conformation in solution (Figure 2-10).

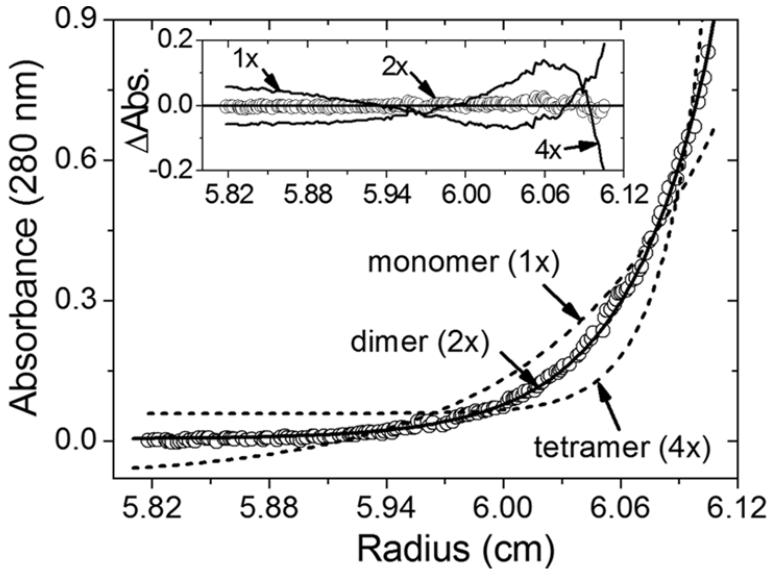

Figure 2-9. Analytical ultracentrifugation experiment of TaTPI

Sedimentation equilibrium distribution (circle) of TaTPI at 26,000 rpm and 20 ℃ is plotted as circle. Concentration of TaTPI was 16.8 u*M* (0.41 mg ml^{-1}) in 20 m*M* Tris-HCl, pH 7.5, and 0.2 *M* NaCl. Solid line is a fitting line for a homogeneous dimer (2x) model and dotted lines are fitting lines for homogeneous monomer (1x) and tetramer (4x) models. Calculated molecular weight for TaTPI monomer from its amino acid compositions is 24,671 daltons. Inset graph shows distributions of the residuals for homogeneous 1x, 4x (solid lines), and 2x (circle) models, respectively. The random distribution of the residuals for the 2x model indicates that TaTPI exists as homogeneous dimers in solution.

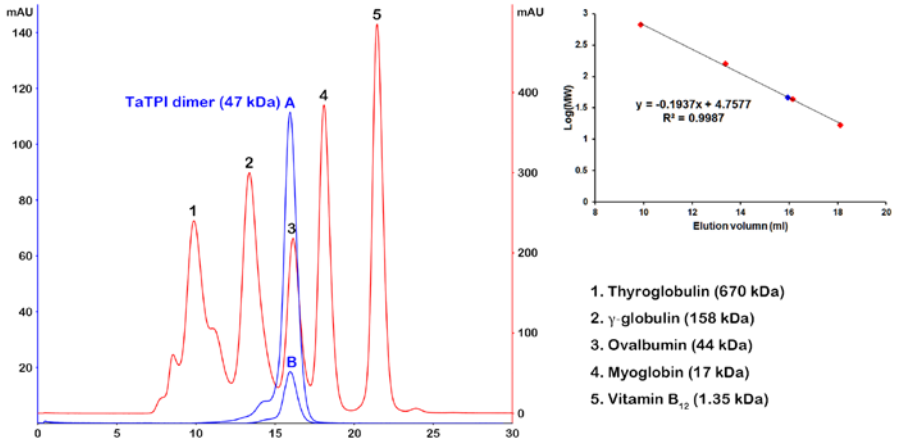

Figure 2-10. Analytical size-exclusion chromatography of TaTPI

TaTPI protein samples at two different concentrations (A: 4.5 mg ml^{-1}, B: 0.9 mg ml^{-1}) were applied to Superdex200 10/300 GL column. Chromatograms of TaTPI and gel filtration standard were shown as blue and red lines, respectively.

3.4. Structural stability of TaTPI under extreme acidic condition

T. acidophilum thrives in harsh environments such as high temperature and extremely acidic condition. TaTPI is also expected to function correctly at high temperature or in very low pH condition when physiological barriers are affected by various stresses. To elucidate the structural stability of TaTPI in extremely acidic condition and at high temperature, I carried out circular dichroism (CD) spectroscopy experiments.

As for the structural stability of TaTPI in extremely acidic condition, secondary structure changes of pH-titrated TaTPI were monitored using CD spectroscopy. Normally, intracellular environment is well kept from extracellular stresses such as abrupt pH change. So, most of intracellular proteins experience normal physiological conditions and function accordingly. TaTPI maintained its folded structure under extremely acidic condition (pH 1–2) as in neutral pH range. In the case of TaTPI, secondary structure contents under extremely acidic condition seem to change slightly with sustained folded structure. The content of α-helix in the TaTPI tends to increase with decreasing pH, whereas the content of β-strand decreases (Figure 2-11). These results suggest that TaTPI is designed to function normally even in cases of unexpected pH drop.

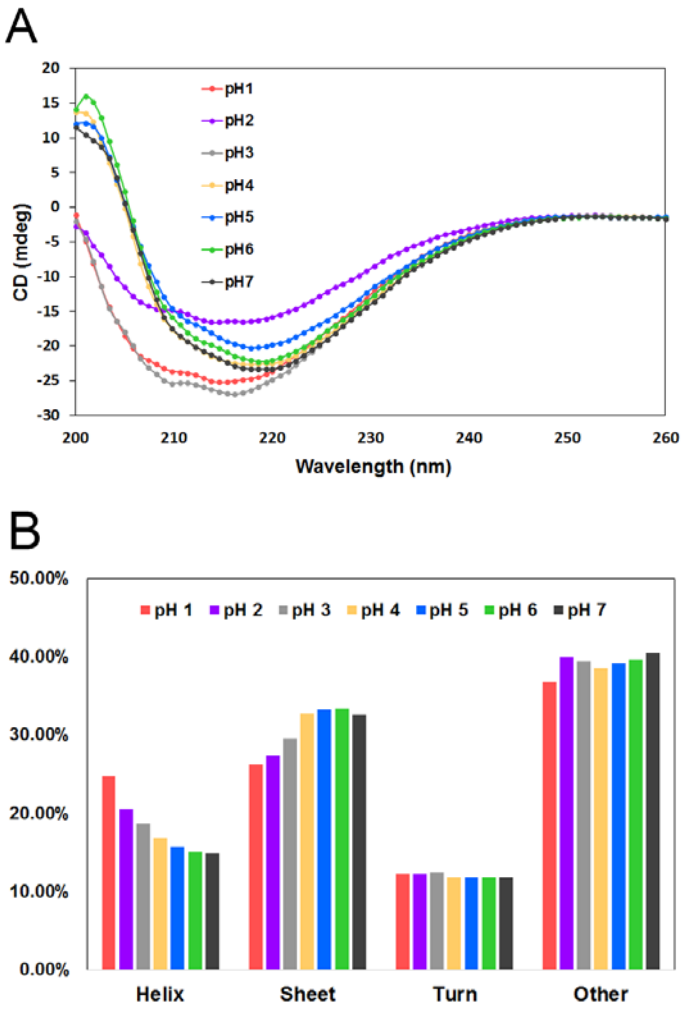

Figure 2-11. Circular dichroism spectra for TaTPI at variable pH conditions

(A) CD spectra of pH-titrated TaTPI (pH 1.0 – 7.0) were measured from 200 to 260 nm. (B) The secondary structure contents of pH-titrated TaTPI were calculated from Multivariate SSE Program (JASCO).

3.5. Structural stability of TaTPI at the high temperature

The temperature of maximum heat capacity (or half-denaturation temperature, Td) of TaTPI was measured by CD spectroscopy. The denaturation curve of TaTPI was analyzed by Kaleidagraph (Synergy Software) based on John and Weeks's protocol (John and Weeks, 2000, Protein science : a publication of the Protein Society, 47). The Td value for TaTPI is 74.6 ℃ (Figure 2-12), which is comparable with that of TPI from *Geobacillus stearothermophilus* (GsTPI), a biological indicator for the validation of sterilization processes, (T_d: 76 ℃) (Alvarez, et al., 1999, The Journal of biological chemistry, 56). In the case of GsTPI, a large number of prolines (5.2%), replacement of asparagine by histidine within the active site to prevent deamidation, the smallest cavity number and volume, and a large buried hydrophobic surface have been shown to contribute for the thermostability (Delboni, et al., 1995, Protein science : a publication of the Protein Society, 41). *Thermotoga maritima*, a hyperthermophilic bacterium, has been known to have TPI with the highest T_d value of 102 ℃ (Alvarez, et al., 1999, The Journal of biological chemistry, 56), resulting from a large number of salt bridges and extensive hydrophobic patches from tetramer conformation (Maes, et al., 1999, Proteins, 37). Using DSC, I found the Td app value of MjTPI to be 107.1 ℃ and it is the highest Td value among reported TPIs so far (Figure 2-13; Table 2-3). When compared

with TPIs mentioned above, TaTPI has smaller number of prolines (4.2%), larger cavity volume, and less buried hydrophobic surface than GsTPI, nor does it adopt tetrameric conformation.

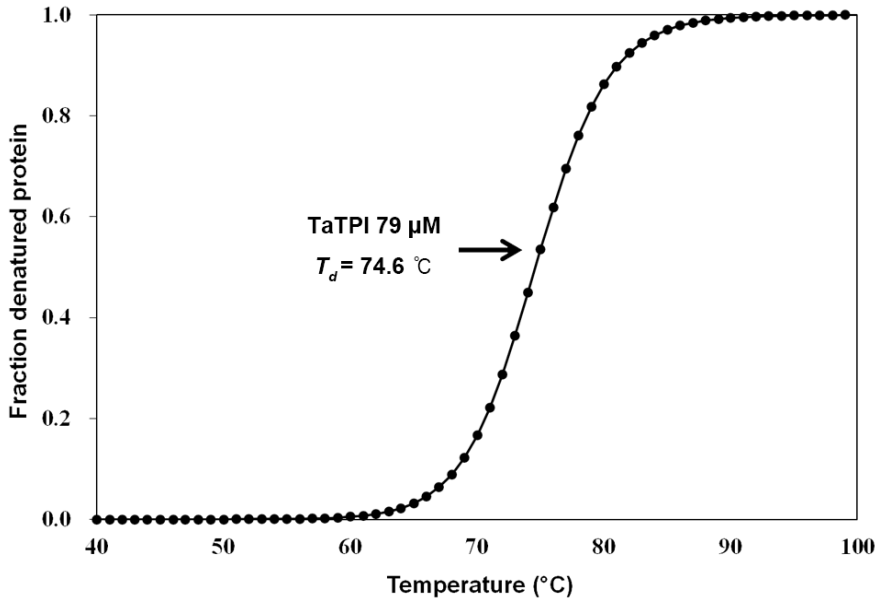

Figure 2-12. Thermal denaturation curve of TaTPI

Thermal denaturation curve of TaTPI was measured by CD spectroscopy.

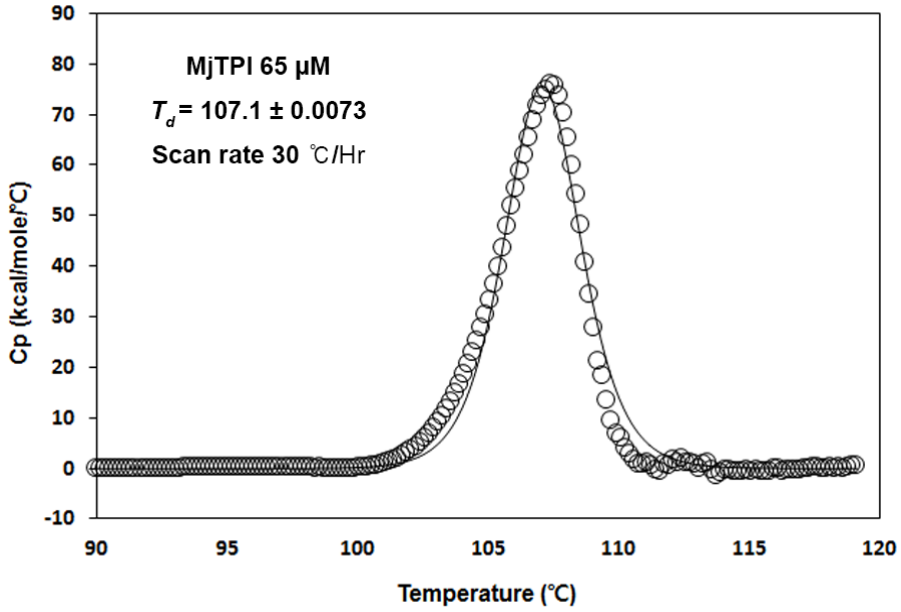

Figure 2-13. DSC thermogram of MjTPI

The black circle represents baseline-subtracted and normalized raw data. The black line indicates the best fits of the raw data. The maximum temperature of heat capacity (T_d) was calculated based on the best fits of the raw data.

Table 2-3. Half-denaturation temperatures of TPIs.

	The half-denaturation temperature ($T_{d,}$ ℃)	Reference
TaTPI	74 ℃	This manuscript
MjTPI	107 ℃	This manuscript
TmTPI	102 ℃	Alvarez et al., 1999
GsTPI	76 ℃	Alvarez et al., 1999
PfTPI	65 ℃	Gopal et al., 1999
HsTPI	55 ℃	Mainfroid et al., 1996
TbTPI	44 ℃	Borchert et al., 1993

Footnotes to Table 2-3

Ta, *Thermoplasma acidophilum*; Mj, *Methanocaldococcus jannaschii*; Tm, *Thermotoga maritima*; Gs, *Geobacillus stearothermophilus*; Pf, *Plasmodium falciparum*; Hs, *Homo sapience*; Tb, *Trypanosoma brucei*.

3.6. Proposal of TPI stabilization patches

TaTPI is composed of 216 amino acid residues and approximately 10% shorter in length than other TPIs from bacterial and eukaryotic species, which is a common feature in archaeal TPIs. According to the results of the structure-based sequence alignment for TPIs, helix 4, helix 5, and helix 6 are regions that mainly account for variation in amino acid composition, structural stability, and the oligomeric status of TPIs. To systematically validate the stabilization factors of TaTPI, I name regions of distinctive differences as TPI stabilization patches (TSPs) (Figure 2-14A). TSP1 is helix 4 region and TaTPI lacks a short helical N-terminus in this patch. Consequently, TaTPI forms a more compact structure. TSP2 exhibits a major structural discrepancy in that 18 amino acid residues are missing in helix 5 region of TaTPI, compared with other dimeric TPIs. In TSP2 area, truncated helix 5 (TSP2C) and lack of a short helix in its N-terminus (TSP2N) also make TaTPI tighter in their overall structure. Lastly, TSP3 arises from helix 6 region and helix 6 is trimmed along with a short α-helix in its C-terminus (Figure 2-14B). All the TSPs of TaTPI contribute to the formation of more compact dimeric structure.

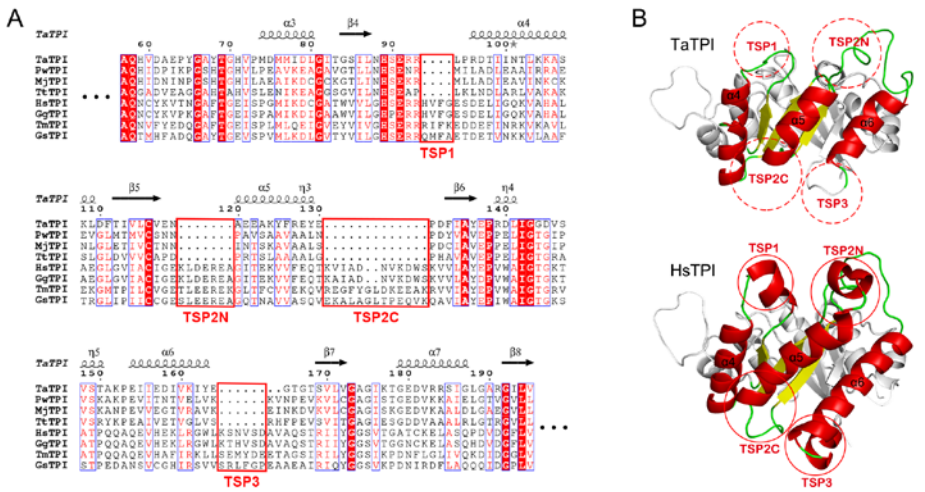

Figure 2-14. TPI stabilization patches (TSPs)

(A) Structure-based sequence alignment of TaTPI with other TPIs from *Pyrococcus woesei* (PwTPI), *Methanocaldococcus jannaschii* (MjTPI), *Thermoproteus tenax* (TtTPI), *Homo sapiens* (HsTPI), *Gallus gallus* (GgTPI), *Thermotoga maritima* (TmTPI), and *Geobacillus stearothermophilus* (GsTPI). Strictly conserved amino acid residues are highlighted in red shaded boxes and moderately conserved amino acid residues are colored in red. Conserved residues are enclosed in blue boxes and TSP regions are enclosed in red boxes. The alignment figure was prepared using *ESPript* program (Robert and Gouet, 2014, Nucleic acids research, 25). (B) Structural comparison of TaTPI and HsTPI. The red dotted and solid circles represent TSP regions in TaTPI and HsTPI, respectively.

The TSPs are not exclusive of TaTPI. Other tetrameric archaeal TPIs also have the TSPs. I speculated that other tetrameric archaeal TPIs could be more thermostable than TaTPI since they adopt tetrameric conformation and contains TSPs. To validate this speculation, I cloned and purified *M. jannaschii* TPI (MjTPI), a tetrameric archaeal TPI, and measured the Td app value of MjTPI. The Td app value of MjTPI was 107.1 ℃, which is the highest Td app value among reported TPIs so far. The result suggest that both higher oligomerization status and the TSPs could be important factors for thermostability of TPIs. TaTPI would keep its structural and functional integrity at high temperature through a compact dimeric conformation from contributing TSPs. Crystal structures of apo- and G3P-bound TaTPI and defined stability determining factors of TPIs would provide clear insights on engineering more stable TIM-barrel fold proteins which make up a large protein family and play pivotal role in metabolic pathways.

Reference

1. Normanly J, Abelson J. tRNA identity. Annual review of biochemistry 1989;58:1029-1049.
2. Eriani G, Delarue M, Poch O, Gangloff J, Moras D. Partition of tRNA synthetases into two classes based on mutually exclusive sets of sequence motifs. Nature 1990;347(6289):203-206.
3. Scheper GC, van der Klok T, van Andel RJ, van Berkel CG, Sissler M, Smet J, Muravina TI, Serkov SV, Uziel G, Bugiani M, Schiffmann R, Krageloh-Mann I, Smeitink JA, Florentz C, Van Coster R, Pronk JC, van der Knaap MS. Mitochondrial aspartyl-tRNA synthetase deficiency causes leukoencephalopathy with brain stem and spinal cord involvement and lactate elevation. Nature genetics 2007;39(4):534-539.
4. Neuenfeldt A, Lorber B, Ennifar E, Gaudry A, Sauter C, Sissler M, Florentz C. Thermodynamic properties distinguish human mitochondrial aspartyl-tRNA synthetase from bacterial homolog with same 3D architecture. Nucleic acids research 2012.
5. Deutscher MP. The eucaryotic aminoacyl-tRNA synthetase complex: suggestions for its structure and function. The Journal of cell biology 1984;99(2):373-377.

6. Lo WS, Gardiner E, Xu Z, Lau CF, Wang F, Zhou JJ, Mendlein JD, Nangle LA, Chiang KP, Yang XL, Au KF, Wong WH, Guo M, Zhang M, Schimmel P. Human tRNA synthetase catalytic nulls with diverse functions. Science 2014;345(6194):328-332.

7. Ray PS, Arif A, Fox PL. Macromolecular complexes as depots for releasable regulatory proteins. Trends Biochem Sci 2007;32(4):158-164.

8. Park SG, Ewalt KL, Kim S. Functional expansion of aminoacyl-tRNA synthetases and their interacting factors: new perspectives on housekeepers. Trends Biochem Sci 2005;30(10):569-574.

9. Robinson JC, Kerjan P, Mirande M. Macromolecular assemblage of aminoacyl-tRNA synthetases: quantitative analysis of protein-protein interactions and mechanism of complex assembly. J Mol Biol 2000;304(5):983-994.

10. Kaminska M, Havrylenko S, Decottignies P, Gillet S, Le Marechal P, Negrutskii B, Mirande M. Dissection of the structural organization of the aminoacyl-tRNA synthetase complex. J Biol Chem 2009;284(10):6053-6060.

11. Guzzo CM, Yang DC. Lysyl-tRNA synthetase interacts with EF1alpha, aspartyl-tRNA synthetase and p38 in vitro.

Biochemical and biophysical research communications 2008;365(4):718-723.

12. Woese CR, Olsen GJ, Ibba M, Soll D. Aminoacyl-tRNA synthetases, the genetic code, and the evolutionary process. Microbiology and molecular biology reviews : MMBR 2000;64(1):202-236.

13. Reed VS, Yang DC. Characterization of a novel N-terminal peptide in human aspartyl-tRNA synthetase. Roles in the transfer of aminoacyl-tRNA from aminoacyl-tRNA synthetase to the elongation factor 1 alpha. J Biol Chem 1994;269(52):32937-32941.

14. Reed VS, Wastney ME, Yang DC. Mechanisms of the transfer of aminoacyl-tRNA from aminoacyl-tRNA synthetase to the elongation factor 1 alpha. J Biol Chem 1994;269(52):32932-32936.

15. Cheong HK, Park JY, Kim EH, Lee C, Kim S, Kim Y, Choi BS, Cheong C. Structure of the N-terminal extension of human aspartyl-tRNA synthetase: implications for its biological function. The international journal of biochemistry & cell biology 2003;35(11):1548-1557.

16. Guo M, Schimmel P. Essential nontranslational functions of tRNA synthetases. Nature chemical biology 2013;9(3):145-153.

17. Cavarelli J, Eriani G, Rees B, Ruff M, Boeglin M, Mitschler A, Martin F, Gangloff J, Thierry JC, Moras D. The active site of yeast aspartyl-tRNA synthetase: structural and functional aspects of the aminoacylation reaction. The EMBO journal 1994;13(2):327-337.

18. Vagin A, Teplyakov A. Molecular replacement with MOLREP. Acta Crystallogr D Biol Crystallogr 2010;66(Pt 1):22-25.

19. Emsley P, Lohkamp B, Scott WG, Cowtan K. Features and development of Coot. Acta Crystallogr D Biol Crystallogr 2010;66(Pt 4):486-501.

20. Murshudov GN, Vagin AA, Dodson EJ. Refinement of macromolecular structures by the maximum-likelihood method. Acta Crystallogr D Biol Crystallogr 1997;53(Pt 3):240-255.

21. Lovell SC, Davis IW, Arendall WB, 3rd, de Bakker PI, Word JM, Prisant MG, Richardson JS, Richardson DC. Structure validation by Calpha geometry: phi,psi and Cbeta deviation. Proteins 2003;50(3):437-450.

22. Krissinel E, Henrick K. Inference of macromolecular assemblies from crystalline state. Journal of molecular biology 2007;372(3):774-797.

23. Sauter C, Lorber B, Cavarelli J, Moras D, Giege R. The free yeast aspartyl-tRNA synthetase differs from the tRNA(Asp)-

complexed enzyme by structural changes in the catalytic site, hinge region, and anticodon-binding domain. J Mol Biol 2000;299(5):1313-1324.

24. Messmer M, Blais SP, Balg C, Chenevert R, Grenier L, Lague P, Sauter C, Sissler M, Giege R, Lapointe J, Florentz C. Peculiar inhibition of human mitochondrial aspartyl-tRNA synthetase by adenylate analogs. Biochimie 2009;91(5):596-603.

25. Robert X, Gouet P. Deciphering key features in protein structures with the new ENDscript server. Nucleic acids research 2014;42(Web Server issue):W320-324.

26. Guo M, Yang XL, Schimmel P. New functions of aminoacyl-tRNA synthetases beyond translation. Nature reviews Molecular cell biology 2010;11(9):668-674.

27. Ofir-Birin Y, Fang P, Bennett SP, Zhang HM, Wang J, Rachmin I, Shapiro R, Song J, Dagan A, Pozo J, Kim S, Marshall AG, Schimmel P, Yang XL, Nechushtan H, Razin E, Guo M. Structural Switch of Lysyl-tRNA Synthetase between Translation and Transcription. Molecular cell 2012.

28. Olsen JV, Vermeulen M, Santamaria A, Kumar C, Miller ML, Jensen LJ, Gnad F, Cox J, Jensen TS, Nigg EA, Brunak S, Mann M. Quantitative phosphoproteomics reveals widespread

full phosphorylation site occupancy during mitosis. Science signaling 2010;3(104):ra3.

29. Schneider AS. Triosephosphate isomerase deficiency: historical perspectives and molecular aspects. Bailliere's best practice & research Clinical haematology 2000;13(1):119-140.

30. Celotto AM, Frank AC, Seigle JL, Palladino MJ. Drosophila model of human inherited triosephosphate isomerase deficiency glycolytic enzymopathy. Genetics 2006;174(3):1237-1246.

31. Arya R, Lalloz MR, Bellingham AJ, Layton DM. Evidence for founder effect of the Glu104Asp substitution and identification of new mutations in triosephosphate isomerase deficiency. Hum Mutat 1997;10(4):290-294.

32. Hollan S, Fujii H, Hirono A, Hirono K, Karro H, Miwa S, Harsanyi V, Gyodi E, Inselt-Kovacs M. Hereditary triosephosphate isomerase (TPI) deficiency: two severely affected brothers one with and one without neurological symptoms. Hum Genet 1993;92(5):486-490.

33. Daar IO, Artymiuk PJ, Phillips DC, Maquat LE. Human triose-phosphate isomerase deficiency: a single amino acid substitution results in a thermolabile enzyme. Proc Natl Acad Sci U S A 1986;83(20):7903-7907.

34. Jogl G, Rozovsky S, McDermott AE, Tong L. Optimal alignment for enzymatic proton transfer: structure of the Michaelis complex of triosephosphate isomerase at 1.2-A resolution. Proceedings of the National Academy of Sciences of the United States of America 2003;100(1):50-55.

35. Ruepp A, Graml W, Santos-Martinez ML, Koretke KK, Volker C, Mewes HW, Frishman D, Stocker S, Lupas AN, Baumeister W. The genome sequence of the thermoacidophilic scavenger Thermoplasma acidophilum. Nature 2000;407(6803):508-513.

36. Wierenga RK. The TIM-barrel fold: a versatile framework for efficient enzymes. FEBS Lett 2001;492(3):193-198.

37. Maes D, Zeelen JP, Thanki N, Beaucamp N, Alvarez M, Thi MH, Backmann J, Martial JA, Wyns L, Jaenicke R, Wierenga RK. The crystal structure of triosephosphate isomerase (TIM) from Thermotoga maritima: a comparative thermostability structural analysis of ten different TIM structures. Proteins 1999;37(3):441-453.

38. Xiao L, Honig B. Electrostatic contributions to the stability of hyperthermophilic proteins. Journal of molecular biology 1999;289(5):1435-1444.

39. Dams T, Auerbach G, Bader G, Jacob U, Ploom T, Huber R, Jaenicke R. The crystal structure of dihydrofolate reductase

from Thermotoga maritima: molecular features of thermostability. Journal of molecular biology 2000;297(3):659-672.

40. Szilagyi A, Zavodszky P. Structural differences between mesophilic, moderately thermophilic and extremely thermophilic protein subunits: results of a comprehensive survey. Structure 2000;8(5):493-504.

41. Delboni LF, Mande SC, Rentier-Delrue F, Mainfroid V, Turley S, Vellieux FM, Martial JA, Hol WG. Crystal structure of recombinant triosephosphate isomerase from Bacillus stearothermophilus. An analysis of potential thermostability factors in six isomerases with known three-dimensional structures points to the importance of hydrophobic interactions. Protein science : a publication of the Protein Society 1995;4(12):2594-2604.

42. Romero-Romero S, Costas M, Rodriguez-Romero A, Alejandro Fernandez-Velasco D. Reversibility and two state behaviour in the thermal unfolding of oligomeric TIM barrel proteins. Physical chemistry chemical physics : PCCP 2015;17(32):20699-20714.

43. Walden H, Bell GS, Russell RJ, Siebers B, Hensel R, Taylor GL. Tiny TIM: a small, tetrameric, hyperthermostable

triosephosphate isomerase. Journal of molecular biology 2001;306(4):745-757.

44. Otwinowski Z, Minor W. Processing of X-ray diffraction data collected in oscillation mode. Methods Enzymol 1997;276:307-326.

45. Laue TM. Sedimentation equilibrium as thermodynamic tool. Methods Enzymol 1995;259:427-452.

46. Knott GD. Mlab--a mathematical modeling tool. Comput Programs Biomed 1979;10(3):271-280.

47. John DM, Weeks KM. van't Hoff enthalpies without baselines. Protein science : a publication of the Protein Society 2000;9(7):1416-1419.

48. Zhang Z, Sugio S, Komives EA, Liu KD, Knowles JR, Petsko GA, Ringe D. Crystal structure of recombinant chicken triosephosphate isomerase-phosphoglycolohydroxamate complex at 1.8-A resolution. Biochemistry 1994;33(10):2830-2837.

49. Alvarez M, Zeelen JP, Mainfroid V, Rentier-Delrue F, Martial JA, Wyns L, Wierenga RK, Maes D. Triose-phosphate isomerase (TIM) of the psychrophilic bacterium Vibrio marinus. Kinetic and structural properties. The Journal of biological chemistry 1998;273(4):2199-2206.

50. Williams JC, Zeelen JP, Neubauer G, Vriend G, Backmann J, Michels PA, Lambeir AM, Wierenga RK. Structural and mutagenesis studies of leishmania triosephosphate isomerase: a point mutation can convert a mesophilic enzyme into a superstable enzyme without losing catalytic power. Protein engineering 1999;12(3):243-250.

51. Noble ME, Zeelen JP, Wierenga RK. Structures of the "open" and "closed" state of trypanosomal triosephosphate isomerase, as observed in a new crystal form: implications for the reaction mechanism. Proteins 1993;16(4):311-326.

52. Wierenga RK, Kapetaniou EG, Venkatesan R. Triosephosphate isomerase: a highly evolved biocatalyst. Cellular and molecular life sciences : CMLS 2010;67(23):3961-3982.

53. Walden H, Taylor GL, Lorentzen E, Pohl E, Lilie H, Schramm A, Knura T, Stubbe K, Tjaden B, Hensel R. Structure and function of a regulated archaeal triosephosphate isomerase adapted to high temperature. Journal of molecular biology 2004;342(3):861-875.

54. Gayathri P, Banerjee M, Vijayalakshmi A, Azeez S, Balaram H, Balaram P, Murthy MR. Structure of triosephosphate isomerase (TIM) from Methanocaldococcus jannaschii. Acta Crystallogr D Biol Crystallogr 2007;63(Pt 2):206-220.

55. Eisenberg D, Schwarz E, Komaromy M, Wall R. Analysis of membrane and surface protein sequences with the hydrophobic moment plot. Journal of molecular biology 1984;179(1):125-142.

56. Alvarez M, Wouters J, Maes D, Mainfroid V, Rentier-Delrue F, Wyns L, Depiereux E, Martial JA. Lys13 plays a crucial role in the functional adaptation of the thermophilic triose-phosphate isomerase from Bacillus stearothermophilus to high temperatures. The Journal of biological chemistry 1999;274(27):19181-19187.

국문초록

Structural and Biophysical Analyses of Aspartyl-tRNA Synthetase from *Homo sapiens* and Triosephosphate Isomerase from *Thermoplasma acidophilum*

Aspartyl-tRNA synthetase 와 triosephosphate isomerase 의 구조 및 생물학적 분석

Asaparty-tRNA synthetase (DRS) 단백질은 aspartic acid와 이를 인식하는 특정 tRNA을 연결시켜주는 효소이며, 또한 multi-tRNA synthetase complex (MSC)의 구성 단백질이다. MSC는 9가지 다른 aminoacyl-tRNA synthetase (AARSs)와 3개의 aminoacyl tRNA synthetase complex-interacting multifunctional protein (AIMP)로 구성된 단백질 복합체로, AARSs 단백질의 canonical과 non-canonical 기능을 조절하는 것으로 추정되나, 아직 확실한 기능은 밝혀져 있지 않다. 본 연구자는 DRS 단백질의 삼차원적 구조를 규명하였으며, 이를 바탕으로 DRS의 N말단의 유연구조부분을 예측하여 DRS와 $tRNA^{Asp}$사이의 상호작용을 예상하였다. 또한 번역후변형 (post-translational modification) 패턴을 분석하여 새로운 번역후변형 위치들을 발견하였다. 이 번역후변형들은 DRS와 $tRNA^{Asp}$의 계면에 위치하는 것으로 나타났으며, 둘의 결합에 영향을 줄 수 있을 것으로 보인다. 또한

DRS의 dimeric interface에 위치한 serine의 인산화로 인하여 DRS의 구조적 변화를 초래 할 것으로 예상되며, 이는 lysyl-tRNA synthetase (KRS)에서도 나타나는 방식이다. 전술한 특성들을 토대로 DRS의 알려지지 않은 non-canonical한 기능이 존재함을 추측할 수 있다.

*Thermoplasma acidophilum*은 호열성 고세균으로 당 (glucose) 분해를 위해 non-phosphorylative Entner-Doudoroff (ED) 과정과 Embden-Meyerhof-Parnas (EMP) 과정을 모두 이용할 수 있을 것으로 알려져 있다. 그 중 triosephosphate isomeraes (TPI) 단백질은 당분해 효소 중에 하나로 잘 알려져 있으나, *T.acidophilum*에서는 EMP 과정에서만 중요하게 사용 될 것으로 고려된다. 본 연구자는 *T.acidophilm*의 TPI (TaTPI) 단백질 및 glycerol-3-phosphate (G3P)의 결합구조들을 규명하였다. TaTPI 단백질은 다른 호열성 고세균 유래의 오솔로그들과 30% 정도의 서열 유사성을 지니지만, 다른 유형의 oligomerization을 통해 효소 활성을 유지한다. 즉, 지금까지 알려진 다른 호열성 고세균 유래의 TPI는 tetrameic 형태를 통해 가혹한 환경 속에서 효소의 안정성을 도모하지만, TaTPI의 경우 dimeric 형태로도 단백질의 안정성을 달성한다. 본 연구자는 초원심분리 및 크기배제크로마토그래피 분석을 통해 TaTPI 단백질이 dimeric 형태를 확증하였다. 이는 호열성 tetrameric TPI 단백질들의 경우 4, 5번째 α-helix들이 소수성 상호작용을 통해 oligomerization을 이루는데 반해, TaTPI 단백질의 경우 4, 5번째 α-helix들이 전하극성아미노산으로 이루어져 dimeric 형태로 존재하게 되는 것이다. TaTPI 단백질의 독특한 특성은 높은 온도뿐만 아니라, 매우

강한 산성 조건 (pH 1-2)에서도 단백질의 구조를 유지 하는 것에 일조한다. 이는 TaTPI의 구조·생물리학적 분석에 기초하여 볼 때, 다른 TPI보다 조밀한 구조가 *T.acidophilum* TPI에 내열·내산성을 부여한다고 볼 수 있다.

주요어: Aspartyl-tRNA synthetase, multi-tRNA synthetase complex, triosephosphate isomerase, glycolysis, crystal structure

학번: 2010-21682

Appendix：Printouts of first author publications

Acta Crystallographica Section F
Structural Biology and Crystallization Communications
ISSN 1744-3091

Overexpression, crystallization and preliminary X-ray crystallographic analysis of the C-terminal cytosolic domain of mouse anoctamin 1

Sang Ho Park,[a]‡ Ho Kyung Chung,[a]‡ Do Jin Kim,[b] Mi Ra Han,[a] Mi Seul Park,[a] Uhtaek Oh,[a] Hyun-Jung Kim[c]* and Byung Woo Han[a]*

[a]Research Institute of Pharmaceutical Sciences, College of Pharmacy, Seoul National University, Seoul 151-742, Republic of Korea, [b]Department of Chemistry, College of Natural Sciences, Seoul National University, Seoul 151-742, Republic of Korea, and [c]College of Pharmacy, Chung-Ang University, Seoul 156-756, Republic of Korea

‡ These authors contributed equally to this work.

Correspondence e-mail: hyunjungkim@cau.ac.kr, bwhan@snu.ac.kr

Received 23 May 2011
Accepted 12 July 2011

Transmembrane protein 16A (TMEM16A, also known as anoctamin 1; ANO1) is a bona fide Ca^{2+}-activated chloride channel that is activated by intracellular Ca^{2+}- and Ca^{2+}-mobilizing stimuli and plays important roles in a variety of physiological functions. To elucidate the structural features of ANO1, structural analysis of the C-terminal cytosolic domain of mouse ANO1 (mANO1-CTD) was initiated. mANO1-CTD was overexpressed in *Escherichia coli* and was crystallized at 297 K using a reservoir solution consisting of 0.2 *M* sodium acetate trihydrate, 0.1 *M* Tris–HCl pH 8.5 and 30%(*w*/*v*) PEG 4000. X-ray diffraction data were collected to 2.3 Å resolution. The crystals belonged to the orthorhombic space group $P2_12_12_1$, with unit-cell parameters a = 73.96, b = 103.73, c = 114.71 Å. If it is assumed that eight copies of a monomer molecule are present in the crystallographic asymmetric unit, the crystal volume per protein mass (V_M) is 2.38 Å^3 Da^{-1} and the solvent content is 48.38%. Attempts to solve the structure of mANO1-CTD by the MAD method using selenomethionine-labelled mANO1-CTD or heavy-atom-derivatized crystals are in progress.

1. Introduction

Ca^{2+}-activated chloride channels (CaCCs) play essential roles in many physiological processes, including transepithelial secretion, cardiac and neuronal excitation, sensory transduction, smooth muscle contraction and fertilization (Eggermont, 2004; Frings *et al.*, 2000; Hartzell *et al.*, 2005; Large & Wang, 1996). Anoctamin 1 (ANO1) is a recently discovered member of the CaCCs which is highly expressed in secretory epithelial tissues, including ductal glands, superficial epithelia of the airway, and oviduct, where it has been implicated to play a key role in calcium-dependent chloride secretion (Caputo *et al.*, 2008; Schroeder *et al.*, 2008; Yang *et al.*, 2008).

ANO1 is one of the members of the anoctamin (ANO, also known as transmembrane protein 16; TMEM16) family of membrane proteins, which consists of ten members (ANO1–10) in mammals. ANO1 consists of 26 exons and has been predicted to code for a variety of proteins (Caputo *et al.*, 2008). It belongs to a protein family with eight transmembrane helices and N- and C-terminal domains that face the cytoplasm (Galindo & Vacquier, 2005). ANO1 is essential for Ca^{2+}-dependent Cl^- currents in airways, the large intestine, salivary glands, pancreatic glands and hepatocytes (Ousingsawat *et al.*, 2009; Rock *et al.*, 2009; Romanenko *et al.*, 2010). Severe transport defects have been detected in epithelial tissues of ANO1-knockout mice, leading to reduced saliva production and attenuated mucociliary clearance of the airways (Lee & Foskett, 2010; Ousingsawat *et al.*, 2009; Rock *et al.*, 2009). Disruption of mouse ANO1 caused abnormal development of the trachea, indicating that the gene is a regulator of epithelial and smooth muscle cell organization in murine development (Rock *et al.*, 2009).

In addition to these results, recent studies have suggested the possibility that ANO1 proteins participate in tumourigenesis (Lee & Foskett, 2010; Yang *et al.*, 2008). The relationship between ANO1 and tumourigenesis has not been explained clearly, but a secretory environment might be important for tumour-cell proliferation. Thus, analysis of the ANO1 expression pattern in tumours could be used for the prediction or treatment of cancer.

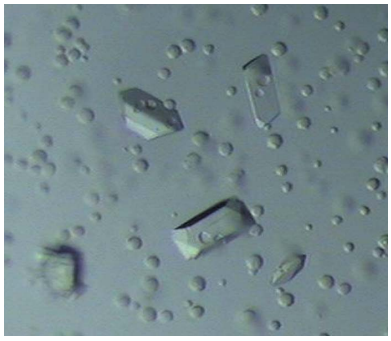

To facilitate the structural characterization of ANO1, we initiated structural study of the C-terminal cytosolic domain of mouse ANO1 (mANO1-CTD; residues 883–960; Fig. 1). In this report, we describe the overexpression, purification, crystallization and preliminary X-ray crystallographic analysis of recombinant mANO1-CTD.

2. Methods and results

2.1. Protein expression and purification

mANO1-CTD was cloned into the expression vector pET-15b(+) (Novagen), adding a hexahistidine-containing 20-residue tag to the N-terminus. The recombinant protein was overexpressed in *Escherichia coli* Rosetta2(DE3)pLysS cells using Luria broth culture medium. Protein expression was induced by 0.5 m*M* isopropyl β-D-1-thiogalactopyranoside and the cells were incubated for 16 h at 293 K following growth to mid-log phase at 310 K. The cells were lysed by sonication in lysis buffer (20 m*M* Tris–HCl pH 7.5, 500 m*M* NaCl, 35 m*M* imidazole and 1 m*M* phenylmethanesulfonylfluoride). The supernatant was applied onto a HiTrap Chelating HP column (GE Healthcare) which was previously equilibrated with buffer *A* (20 m*M* Tris–HCl pH 7.5, 500 m*M* NaCl and 35 m*M* imidazole). The protein was eluted with a linear gradient of 0.035–1.0 *M* imidazole in buffer *A*. The eluted sample was further purified by gel filtration on a HiLoad 16/60 Superdex 200 prep-grade column (GE Healthcare) which was equilibrated with 20 m*M* Tris–HCl pH 7.5 and 200 m*M* NaCl. The buffer of the fractions containing mANO1-CTD was gradually changed to buffer *B* (20 m*M* Tris–HCl pH 7.5 and 50 m*M* NaCl) using a Amicon Ultra-15 centrifugal filter device (Millipore). The sample was applied onto a HiTrap SP ion-exchange column (GE Healthcare) which was previously equilibrated with buffer *B*. The protein was eluted with a linear gradient of 0.05−1.0 *M* NaCl in buffer *B*. The homogeneity of the purified protein was assessed by SDS–PAGE. The buffer of the fractions containing mANO1-CTD was changed to 20 m*M* Tris–HCl pH 7.5 and 100 m*M* NaCl to reduce the concentration of NaCl and purified mANO1-CTD was concentrated to a final concentration of 9 mg ml^{-1} using an Amicon Ultra-15 centrifugal filter device (Millipore).

2.2. Crystallization and X-ray data collection

Crystals were grown by the sitting-drop vapour-diffusion method at 297 K by mixing equal volumes (1 µl each) of protein solution and reservoir solution. Crystals appeared after three weeks using a reservoir solution consisting of 0.1 *M* Tris–HCl pH 8.5, 0.2 *M* sodium acetate trihydrate and 30%(*v*/*v*) PEG 4000 with approximate dimensions of 0.1 × 0.1 × 0.3 mm (Fig. 2).

For diffraction data collection, the crystals were directly soaked in a cryoprotectant solution composed of 30%(*v*/*v*) glycerol added to the reservoir solution. X-ray diffraction data were collected at 100 K on a Quantum 4R CCD detector (Area Detector Systems Corporation, Poway, California, USA) at the BL-6C experimental station of Pohang Light Source, Republic of Korea (Fig. 3). For each image the crystal was rotated by 1° and the raw data were processed using the *HKL*-2000 program suite (Otwinowski & Minor, 1997). A total of 280 647 measured reflections were merged into 40 051 unique reflections with an $R_{\rm merge}$ of 12.7% and a completeness of 99.9%. The space group was determined to be $P2_12_12_1$ on the basis of systematic absences and symmetry of diffraction intensities using the *POINTLESS* program from *CCP*4 (Winn *et al.*, 2011). The unit-cell parameters are a = 73.96, b = 103.73, c = 114.71 Å. Table 1 summarizes the statistics of data collection. If it is assumed that eight copies of a

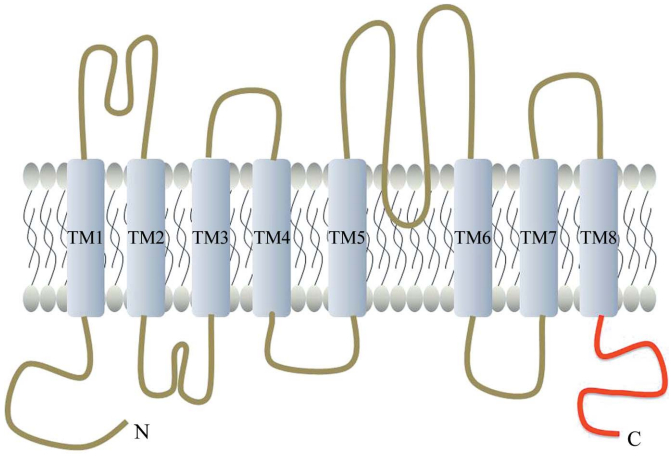

Figure 1
Predicted topology of mANO1. The cytosolic C-terminal domain of mANO1 is coloured red.

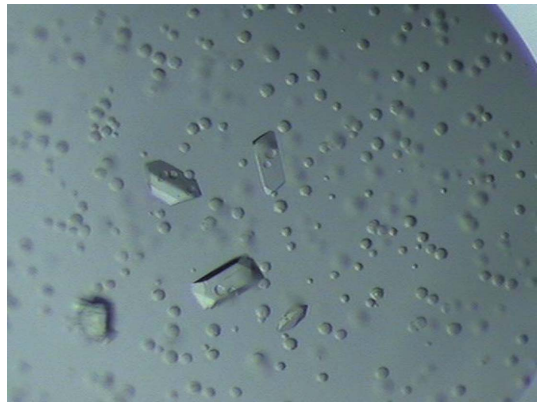

Figure 2
Native crystals of mANO1-CTD. The crystal dimensions are approximately 0.1 × 0.1 × 0.3 mm.

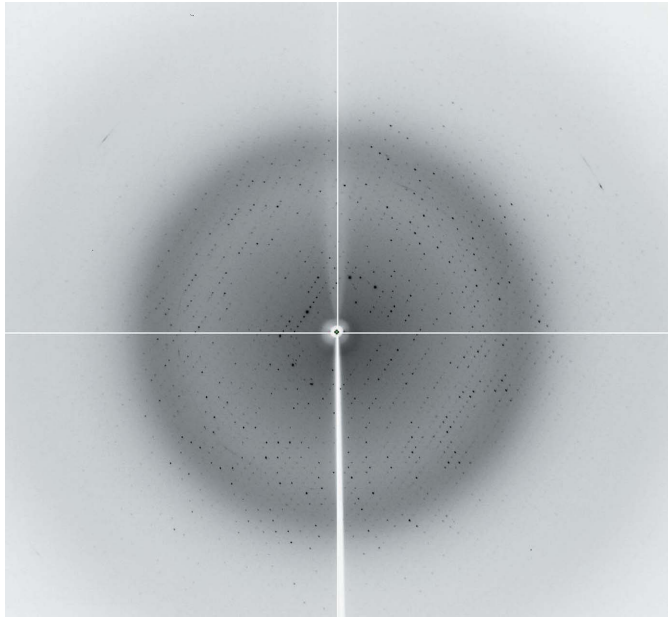

Figure 3
X-ray diffraction image from an mANO1-CTD crystal. The edge of the detector corresponds to a resolution of 2.0 Å.

Table 1
Data-collection statistics.

Values in parentheses are for the highest resolution shell.

X-ray source	Pohang Light Source beamline BL-6C
X-ray wavelength (Å)	1.23985
Temperature (K)	100
Space group	$P2_12_12_1$
Unit-cell parameters (Å)	a = 73.96, b = 103.73, c = 114.71
Resolution range (Å)	20–2.30 (2.34–2.30)
Total/unique reflections	280647/40051
$R_{\rm merge}$† (%)	12.7 (45.9)
Data completeness (%)	100.0 (99.9)
Multiplicity	7.0 (6.5)
Average $I/\sigma(I)$	18.8 (3.8)

† $R_{\rm merge} = \sum_{hkl}\sum_i |I_i(hkl) - \langle I(hkl)\rangle| / \sum_{hkl}\sum_i I_i(hkl)$, where $I_i(hkl)$ is the intensity of the ith measurement of reflection hkl and $\langle I(hkl)\rangle$ is the mean value of $I_i(hkl)$ for all i measurements.

monomer molecule are present in the crystallographic asymmetric unit, the crystal volume per protein mass ($V_{\rm M}$) is 2.38 Å^3 Da^{-1} and the solvent content is 48.38%. Attempts to solve the structure of mANO1-CTD by the MAD method using selenomethionine-labelled mANO1-CTD or heavy-atom-derivatized crystals are in progress.

We thank the staff at beamline BL-6C of Pohang Light Source for assistance during X-ray experiments. This research was supported by the Basic Science Research Program (2010-0028257 and 2011-0004305) and the Global Frontier (NRF-M1AXA002-2010-0029770) through the National Research Foundation of Korea (NRF) funded by the Ministry of Education, Science and Technology and by a grant from the Korea Healthcare Technology R&D Project, Ministry of Health and Welfare, Republic of Korea (A092006).

References

Caputo, A., Caci, E., Ferrera, L., Pedemonte, N., Barsanti, C., Sondo, E., Pfeffer, U., Ravazzolo, R., Zegarra-Moran, O. & Galietta, L. J. (2008). *Science*, **322**, 590–594.
Eggermont, J. (2004). *Proc. Am. Thorac. Soc.* **1**, 22–27.
Frings, S., Reuter, D. & Kleene, S. J. (2000). *Prog. Neurobiol.* **60**, 247–289.
Galindo, B. E. & Vacquier, V. D. (2005). *Int. J. Mol. Med.* **16**, 919–924.
Hartzell, C., Putzier, I. & Arreola, J. (2005). *Annu. Rev. Physiol.* **67**, 719–758.
Large, W. A. & Wang, Q. (1996). *Am. J. Physiol.* **271**, C435–C454.
Lee, R. J. & Foskett, J. K. (2010). *Am. J. Physiol. Lung Cell. Mol. Physiol.* **298**, L210–L231.
Otwinowski, Z. & Minor, W. (1997). *Methods Enzymol.* **276**, 307–326.
Ousingsawat, J., Martins, J. R., Schreiber, R., Rock, J. R., Harfe, B. D. & Kunzelmann, K. (2009). *J. Biol. Chem.* **284**, 28698–28703.
Rock, J. R., O'Neal, W. K., Gabriel, S. E., Randell, S. H., Harfe, B. D., Boucher, R. C. & Grubb, B. R. (2009). *J. Biol. Chem.* **284**, 14875–14880.
Romanenko, V. G., Catalán, M. A., Brown, D. A., Putzier, I., Hartzell, H. C., Marmorstein, A. D., Gonzalez-Begne, M., Rock, J. R., Harfe, B. D. & Melvin, J. E. (2010). *J. Biol. Chem.* **285**, 12990–13001.
Schroeder, B. C., Cheng, T., Jan, Y. N. & Jan, L. Y. (2008). *Cell*, **134**, 1019–1029.
Winn, M. D. *et al.* (2011). *Acta Cryst.* D**67**, 235–242.
Yang, Y. D., Cho, H., Koo, J. Y., Tak, M. H., Cho, Y., Shim, W.-S., Park, S. P., Lee, J., Lee, B., Kim, B.-M., Raouf, R., Shin, Y. K. & Oh, U. (2008). *Nature (London)*, **455**, 1210–1215.

PROTEINS
STRUCTURE ■ FUNCTION ■ BIOINFORMATICS

STRUCTURE NOTE

Crystal structure of human cytosolic aspartyl-tRNA synthetase, a component of multi-tRNA synthetase complex

Kyung Rok Kim,[1†] Sang Ho Park,[1†] Hyoun Sook Kim,[1] Kyung Hee Rhee,[1] Byung-Gyu Kim,[2] Dae Gyu Kim,[2] Mi Seul Park,[1] Hyun-Jung Kim,[3] Sunghoon Kim,[2] and Byung Woo Han[1*]

[1] Research Institute of Pharmaceutical Sciences, Department of Pharmacy, College of Pharmacy, Seoul National University, Seoul 151-742, Korea

[2] Medicinal Bioconvergence Research Center, Seoul National University, Seoul 151-742, Korea

[3] Department of Pharmacy, College of Pharmacy, Chung-Ang University, Seoul 156-756, Korea

Human cytosolic aspartyl-tRNA synthetase (DRS) catalyzes the attachment of the amino acid aspartic acid to its cognate tRNA and it is a component of the multi-tRNA synthetase complex (MSC) which has been known to be involved in unexpected signaling pathways. Here, we report the crystal structure of DRS at a resolution of 2.25 Å. DRS is a homodimer with a dimer interface of 3750.5 Å^2 which comprises 16.6% of the monomeric surface area. Our structure reveals the C-terminal end of the N-helix which is considered as a unique addition in DRS, and its conformation further supports the switching model of the N-helix for the transfer of tRNA^{Asp} to elongation factor 1α. From our analyses of the crystal structure and post-translational modification of DRS, we suggest that the phosphorylation of Ser146 provokes the separation of DRS from the MSC and provides the binding site for an interaction partner with unforeseen functions.

Proteins 2013; 81:1840–1846.

Key words: aspartyl-tRNA synthetase; multi-tRNA synthetase complex; N-helix; crystal structure.

INTRODUCTION

Aminoacyl-tRNA synthetases (AARSs) catalyze the attachment of respective amino acid substrate to its cognate tRNA through a two-step reaction.[1] An intermediate adenylate is formed from amino acid and ATP in the first step, and the amino acid is charged to the ribose of the terminal adenine of tRNA in the second step. Although AARSs catalyze the same type of reaction, they differ in amino acid sequence, size, three-dimensional structure, and oligomeric state. AARSs can be classified into two major classes; Classes I and II synthetase.[2] The Class I synthetase contains the representative Rossmann fold that binds ATP and the Class II synthetase adopts a core antiparallel β-sheet surrounded by α-helices and

Additional Supporting Information may be found in the online version of this article.

Abbreviations: AARS, aminoacyl-tRNA synthetase; AIMP, aminoacyl-tRNA synthetase-interacting multifunctional protein; DRS, aspartyl-tRNA synthetase; DRS2, mitochondrial aspartyl-tRNA synthetase; EF-1α, elongation factor 1α; KRS, lysyl-tRNA synthetase; MSC, multi-tRNA synthetase complex; NMR, nuclear magnetic resonance; NRS, asparaginyl-tRNA synthetase; PTM, post-translational modification.

Grant sponsor: Ministry of Education, Science and Technology (MEST), Republic of Korea; Grant number: 2012-054237 (Global Frontier Project funded through the National Research Foundation); Grant sponsor: National Cancer Center, Republic of Korea; Grant number: 1120170 (National R&D Program for Cancer Control).

[†]Kyung Rok Kim and Sang Ho Park contributed equally to this work.

*Correspondence to: Byung Woo Han, College of Pharmacy, Seoul National University, Seoul 151-742, Korea. E-mail: bwhan@snu.ac.kr

Received 5 February 2013; Revised 3 April 2013; Accepted 8 April 2013
Published online 23 April 2013 in Wiley Online Library (wileyonlinelibrary.com).
DOI: 10.1002/prot.24306

three unique conserved motifs namely Motifs 1, 2, and 3.[2]

For protein synthesis, AARSs play a basic cellular role not only in cytosol but also in mitochondria and most AARSs function distinctively in either location, and thus there are cytosolic or mitochondrial AARSs. In human, there are cytosolic and mitochondrial aspartyl-tRNA synthetases (DRS and DRS2), which share only 22.9% sequence identity. It has been known that DRS2 is associated with leukoencephalopathy with brain stem and spinal cord involvement and high lactate (LBSL)[3] and its structure revealed the function of the additional motif in the catalytic domain.[4] In the case of DRS, it is one of the components that forms the multi-tRNA synthetase complex (MSC) in higher eukaryotes.[5]

The MSC has been regarded as a reservoir for almost half of the cytosolic tRNA synthetases and it has been known to switch the canonical translational function and additional functions which are often observed in higher eukaryotes.[6,7] In the MSC, DRS is known to interact with the AARS-interacting multifunctional protein 2 (aminoacyl-tRNA synthetase-interacting multifunctional protein AIMP2/p38)[8,9] and the lysyl-tRNA synthetase (KRS).[10] The N-terminal extension of DRS, KRS, and asparaginyl-tRNA synthetase (NRS) is unique in the Class II synthetases and further classifies them into the subclass IIb.[11] The nuclear magnetic resonance (NMR) structure of the 21-residue N-terminal extension in DRS revealed that the N-terminal flexible β-turn followed by the amphipathic C-terminal helix induces the nonspecific tRNA binding and gives a force to transfer its charged tRNA to elongation factor 1α (EF-1α).[12–14]

In this study, we present the crystal structure of human cytosolic DRS at 2.25 Å. We show that DRS forms a homodimer with the N-terminal extension, anticodon-binding domain, hinge region, and catalytic domain. Analyses of our crystal structure and post-translational modification (PTM) shed lights on the molecular basis of the association and dissociation of DRS with the MSC.

MATERIALS AND METHODS

Cloning, protein expression, and purification

Human cytosolic full-length DRS (501 amino acids) was cloned into the pET-28a(+) vector containing the N-terminal His_6-tag (Novagen). The recombinant protein was transformed into *Escherichia coli* Rosetta2(DE3)pLysS strain. DRS was induced by 0.5 m*M* isopropyl 1-thio-β-D-galactopyranoside and incubated for 6 h at 310 K using Luria Broth culture medium. The harvested cell was sonicated with lysis buffer containing 20 m*M* of Tris-HCl (pH 7.5), 500 m*M* of NaCl, 35 m*M* of imidazole, and 1 m*M* of phenylmethanesulfonyl fluoride. The lysates were centrifuged at 35,000*g* for 50 min to remove the cell debris and denatured proteins. The supernatant was loaded onto a HiTrap Chelating HP column (GE Healthcare) and eluted with linear gradient 50–500 m*M* of imidazole following equilibration with 50 m*M* of imidazole. The protein was diluted with a buffer containing 50 m*M* of 4-(2-hydroxyethyl)-1-piperazineethanesulfonic acid (HEPES)–NaOH (pH 7.0), 50 m*M* of NaCl, 1 m*M* of dithiothreitol, and 5% of glycerol, and further purified using the ion exchange chromatography with a HiTrap Q HP column (GE Healthcare). The final purification step was the size-exclusion chromatography with a HiLoad 16/600 Superdex 200 prep grade column (GE Healthcare) equilibrated with 50 m*M* of HEPES–NaOH (pH 7.0), 200 m*M* of NaCl, 5% of glycerol, and 1 m*M* of dithiothreitol. For crystallization, the purified protein was concentrated to 11.1 mg mL^{-1}.

Crystallization, data collection, and structure determination

DRS crystals were grown by the sitting-drop vapor-diffusion method at 295 K by mixing equal volumes of the purified protein and the reservoir solution containing 8% v/v tacsimate (pH 8.0), and 20% w/v polyethylene glycol 3350. For diffraction data collection, crystals were soaked in the cryoprotectant solution containing 20% v/v glycerol added to the reservoir solution. X-ray diffraction data of the crystal were collected at the synchrotron BL-5A at the Photon Factory, Japan. The structure was solved by molecular replacement method with the structure of *Saccharomyces cerevisiae* DRS containing the anticodon-binding domain, hinge region, and catalytic domain (PDB ID: 1ASZ)[15] as a phasing model using *MOLREP*.[16] The structure was completed using alternate cycles of manual building in *WinCoot*[17] and refinement in *REFMAC*.[18] All refinement steps were monitored using an R_{free} value based on 5.0% of the independent reflections. The stereochemical quality of the final model was assessed using *MolProbity*.[19] The data collection and refinement statistics are summarized in Table I.

PTM analysis

Purified N-terminal OneSTrEP-tagged DRS and coeluted interaction partners of that, overexpressed and purified from HEK293T cells, were digested with sequencing grade gold-trypsin (Promega) after 1D-SDS PAGE/Coomassie blue staining. Tryptic peptides were analyzed with the LTQ Velos Orbitrap mass spectrometer equipped with an electron transfer dissociation source after an online reversed-phase chromatography. To improve sequencing coverage, we applied a data-dependent decision tree to select for collision-induced dissociation or electron-transfer dissociation fragmentation depending on the charged states, respectively. Protein identification was accomplished using the Sorcerer™-

Table I
Statistics for Data Collection, Phasing, and Model Refinement

Data collection[a]	Human cytosolic DRS
Space group	$P2_1$
Cell dimensions	
a, *b*, *c* (Å)	54.89, 141.92, 68.50
α, β, γ (°)	90, 102.19, 90
Data set	
X-ray wavelength (Å)	1.0000
Resolution (Å)[b]	50.00–2.25 (2.29–2.25)
Total/unique reflections	177,246/48,428
Completeness (%)	99.3 (95.4)
R_{merge} (%)[c]	11.0 (50.2)
Refinement	
Resolution (Å)	50.00–2.24
R_{work}[d]/R_{free}[e] (%)	19.7/22.8
No. of nonhydrogen atoms/mean B-factor (Å^2)	
Protein	6968/33.7
Water	354/40.2
Glycerol	48/52.5
Poor rotamers (%)[f]	3.1
Ramachandran plot analysis (%)	
Most favored regions	96.9
Additional allowed regions	3.1
Disallowed regions	0
R.m.s.d. from ideal geometry	
Bond lengths (Å)	0.010
Bond angles (°)	1.290

[a]Data collected at the synchrotron BL-5A at the Photon Factory, Japan.
[b]Numbers in parentheses indicate the highest resolution shell.
[c]$R_{merge} = \Sigma_h \Sigma_i |I(h)_i - <I(h)>| / \Sigma_h \Sigma_i I(h)_i$, where $I(h)$ is the observed intensity of reflection h, and $<I(h)>$ is the average intensity obtained from multiple measurements.
[d]$R_{work} = \Sigma ||F_o| - |F_c|| / \Sigma |F_o|$, where $|F_o|$ is the observed structure factor amplitude and $|F_c|$ is the calculated structure factor amplitude.
[e]R_{free} = *R*-factor based on 5.0% of the data excluded from refinement.
[f]Values obtained using *MolProbity*.

SEQUEST® (Sage-N Research), and searches were performed against the IPI human DB v3.87 fasta. The carbamidomethylation (+57.021 Da) of Cys is set as a static modification, and the following variable modification were allowed: GlyGly/+114.043 Da (Lys), Acetyl/+42.011 Da (Lys), HexNAc/+203.079 Da (Asn, Ser, Thr), Phospho/+79.966 Da (Ser, Thr, Tyr), Oxidation/+15.995 Da (Met), deamidated/+0.984 Da (Asn, Gln).

Data deposition

The coordinate and structure factors for human cytosolic DRS have been deposited in the RCSB Protein Data Bank, accession code 4J15.

RESULTS AND DISCUSSION

Overall structure and oligomeric state of DRS

The crystal structure of human cytosolic DRS was determined at a resolution of 2.25 Å by molecule replacement method with the structure of *S. cerevisiae* DRS containing the anticodon-binding domain, hinge region, and catalytic domain (PDB ID: 1ASZ)[15] as a phasing model. DRS contains a homodimer in the asymmetric unit and the dimer interface area is 3750.5 Å^2 which comprises 16.6% of the monomeric surface area calculated from Protein Interfaces, Surfaces, and Assemblies service.[20] Our crystal structure includes all the Class II AARS domains: anticodon-binding domain, hinge region, and catalytic domain. In addition, the N-terminal extension, which is a distinct domain in mammalian DRS, could be partially modeled including the C-terminal three residues of the characteristic helix motif [Fig. 1(A)]. Structural analyses on this N-terminal extension will be further discussed with the previous NMR structure below.

The anticodon-binding domain of DRS (residues, 57–146) adopts the oligonucleotide binding-fold (OB-fold) that is composed of a five-stranded antiparallel β-sheet connected by helices and loops (β1–β5) to form a closed β-barrel. The catalytic domain (residues, 189–497) contains 13 α-helices (αH–αT) and 8 β-strands (β6–β13) which constitute all the three conventional Class II AARS motifs: Motifs 1, 2, and 3.[2] The hinge region (residues, 156–188) plays an essential role in the connection of the anticodon-binding domain and the catalytic domain. In the middle of the hinge region, residues 163–172 could not be modeled owing to the lack of the electron density and the disordered residues are considered as a part of binding region to the ribose-phosphate backbone in the D-stem of tRNA^{Asp}, compared with the known *S. cerevisiae* DRS–tRNA^{Asp} complex structure.[15] In addition, residues 224–247 in the flipping loop and residues 273–282 in the Motif 2 could not be observed in our crystal structure [Fig. 1(B)]. These regions are known to be dynamic without its cognate tRNA and recognize its tRNA in an induced-fit manner.[21]

When the anticodon-binding domain, hinge region, and catalytic domain in our structure were independently superimposed with those of the *S. cerevisiae* DRS–tRNA^{Asp} complex structure, then the three domains were structurally well conserved with the root mean square deviation (r.m.s.d.) values of 1.08, 1.80, and 0.97 Å, respectively. In the anticodon-binding domain, three β-strands (β1, β2, and β3) could bind to the anticodon loop of tRNA^{Asp} which is composed of GUC elements. In the hinge region, short helices containing Asp158 and Asn175 could interact with the D-stem (U11, U12) of tRNA^{Asp}. In the catalytic domain, the flipping loop and the Class II Motif 2 play a key role in the interaction of DRS with the 3′-end of tRNAAsp. Detailed representations of the superposition results are shown in Supporting Information Figure S1.

Recently, the crystal structure of human mitochondrial DRS (DRS2) was solved at a resolution of 3.7 Å (PDB ID: 4AH6).[4] Human DRS and DRS2 share only 22.9% sequence identity [Fig. 1(B)]. However, when our crystal structure of DRS was superposed with that of DRS2, two

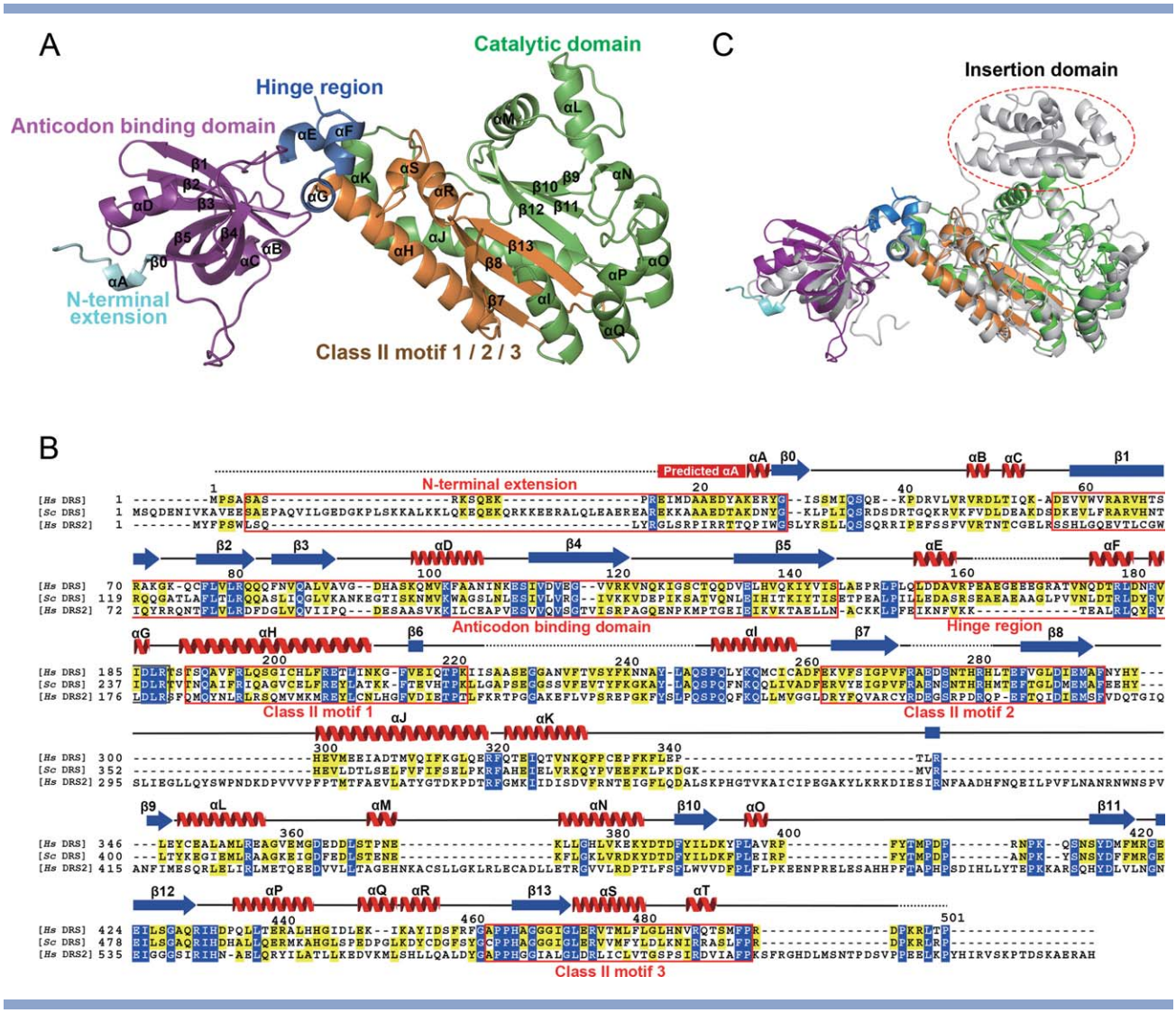

Figure 1

Overall structure of DRS. (**A**) DRS monomer. The N-terminal extension, anticodon-binding domain, hinge region, catalytic domain, and motifs are colored and labeled in cyan, magentas, blue, green, and orange, respectively. (**B**) Sequence alignment of human cytosolic DRS (*Hs* DRS) with *S. cerevisiae* DRS (*Sc* DRS) and human mitochondrial DRS (*Hs* DRS2). Strictly conserved residues are highlighted with blue-shaded boxes, and moderately conserved residues are shown as yellow-shaded boxes. The secondary structure of human DRS is shown on top of the sequence alignment. α-Helix, β-sheet, connecting region, and disordered region are represented by red spiral, blue arrow, black line, and dotted line, respectively. (**C**) Structural comparison of human cytosolic and mitochondrial DRSs. Human cytosolic DRS is shown as in (A) and mitochondrial DRS is colored in gray. The red dotted oval indicates the insertion domain of mitochondrial DRS.

structures are structurally similar to each other with the r.m.s.d. distance of 1.7 Å. The anticodon-binding domain, hinge region, and catalytic domain of DRS and DRS2 are structurally conserved, with the exception of an additional motif in the catalytic domain of DRS2 which is known as the insertion domain [Fig. 1(C)]. The insertion domain of DRS2 forms the enlarged catalytic groove with more electropositive surface potential, which enables an alternate interaction network at the subunit interface between tRNA and DRS2.[4] Interestingly, DRS2 showed a higher sensitivity than DRS for inhibitors with a nonhydrolysable adenylate moiety and its correlation with structural features has not been well understood.[22] Structural analyses of DRS and DRS2 in complex with same adenylate analogs would elucidate a subtle role of the domain difference with respect to substrate specificity and evolutionary advantages.

Flexible N-terminal extension of DRS

In higher eukaryotes, additional domains or motifs in a specific AARS result in new functions. In the case of DRS, KRS, and NRS, they contain the N-helix that is named after the helical conformation in part of their N-terminal extension region.[11,23] The previously determined NMR structure of the N-terminal extension of

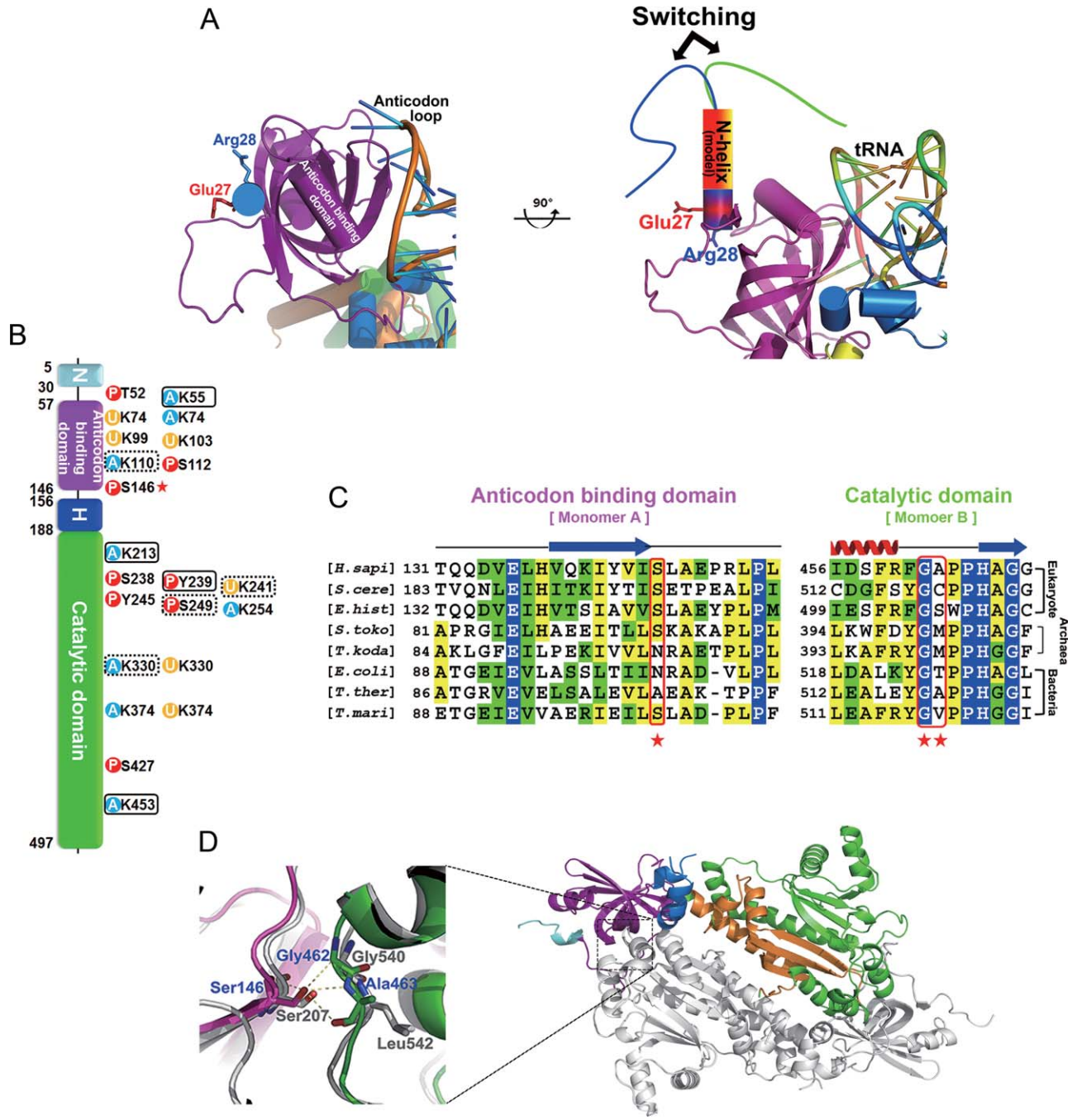

Figure 2

N-terminal extension, PTM, and key intermolecular interaction of DRS. (**A**) The switching model of the N-helix with our DRS structure. (**B**) PTM analyses. Acetylation, phosphorylation, and ubiquitination sites are shown as blue, red, and yellow circles, respectively. PTM sites uniquely observed in this study and residues observed both in the database and in our study are surrounded by black boxes and dotted boxes, respectively. Ser146, which is expected to play a key role in the organization of DRS, is marked with a red asterisk. (**C**) Sequence alignment of the interface residues of anticodon-binding domain and catalytic domain of DRSs from various organisms. Ser146, Gly462, and Ala463 of human DRS are marked with red asterisks. (**D**) Close-up view of Ser146 and the intermolecular interaction of DRS dimer. The structure of human DRS is superimposed with that of human KRS shown in a gray cartoon model.

DRS revealed the conformational flexibility caused by the β-turn followed by one α-helix and the N-terminal extension plays a crucial role in the interaction between $tRNA^{Asp}$ and EF-1α.[12–14] In our crystal structure, the C-terminal end of the α-helix in the N-terminal extension was observed, comprising Lys26, Glu27, and Arg28 although the N-terminal region was less-ordered. To get a glimpse of the whole N-helix structure, we superposed

the structurally well-resolved C-terminal end of the N-terminal extension residue Glu27 and Arg28 with the α-helix of the NMR structure, considering the helical wheel conformation (Supporting Information Fig. S2). The α-helix in the N-terminal extension is amphipathic and the hydrophilic face of the amphipathic helix could interact with positively charged residues Arg8 and Lys9 in the N-terminus by the conformational change on the flexible β-turn.[14] Our crystal structure further supports the structural switching model of the N-terminal extension of DRS in the aid of the direct transfer of $tRNA^{Asp}$ to EF-1α [Fig. 2(A)].

PTM of DRS and its implication on the MSC assembly

To speculate the organization of DRS as a main interacting component with AIMP2/p38 in the MSC assembly, we searched all the known PTM data and independently implemented the PTM analyses of DRS. Our liquid chromatography tandem mass spectrometry (MS) analysis revealed two phosphorylation sites (Tyr239 and Ser249) and six acetylation sites (Lys55, 110, 213, 241, 330, and 453), respectively. Among them, the phosphorylation of Tyr239 and the acetylation of Lys55, 213, and 453 were first identified. Our findings and other PTM site information of DRS from PhosphoSite Plus database (http://www.phosphosite.org) indicated that the residues 238–254 regions of the Class II AARS are dynamically regulated by various types of modifications such as phosphorylation, acetylation, and ubiquitination [Fig. 2(B)]. For instance, although Lys241 was identified with its acetylation modification in our analysis, collected six independent MS analysis data of ubiquitin branch motif (K-e-GG) immunoaffinity beads purification studies showed that Lys241 is also modified with ubiquitin. Thus, it seems that the phosphorylation status of Ser238, Tyr239, and/or Ser249 could affect the catalytic activity, stability, or partner-binding affinity of DRS through a competitive modification event between acetylation and ubiquitination of Lys241 and/or Lys254 though it should be clarified with further studies. PTM sites mapped on the surface representation of human DRS dimer modeled with $tRNA^{Asp}$ are shown in Supporting Information Figure S3.

In the MSC, AIMP2/p38 has been known to interact with two subcomplexes of the MSC (I: MRS, AIMP3/p18, EPRS, IRS, LRS; II: AIMP1/p43, QRS, RRS), KRS, and DRS, and the N-terminal domain of AIMP2/p38 interacts with the subcomplex II, KRS, and DRS.[9] The N-terminal Motifs 1 and 2 of AIMP2/p38 have been recently shown to interact with the bottom groove and the symmetric groove on the KRS dimer, respectively.[24] Based on the situational and structural similarity between KRS and DRS, we anticipated that two dimers of DRS would interact with AIMP2/p38 in the similar way of KRS regarding the association and dissociation from the MSC. In the case of KRS, Ser207 establishes the major intermolecular interaction of the KRS dimer through three hydrogen bonds between the hydroxyl group of Ser207 and the backbone of Gly540 and Leu541. Interestingly, a conformational change triggered by the phosphorylation of Ser207 switches the function of KRS from translation to transcription, provoking a new conformer and releasing KRS from the MSC.[24] To our surprise, DRS also contains the equivalent Ser146, Gly462, and Ala463, which are highly conserved in the amino acid sequence and three-dimensional structure in higher eukaryotes [Fig. 2(C–D)]. In addition, the PTM information of DRS from the PhosphoSite Plus database shows that the phosphorylation of Ser146 was already observed with the phosphoproteome analyses of the human cell cycle using the MS.[25] Thus, we suggest that the phosphorylation of Ser146 could initiate a conformation change of the DRS dimer and trigger an unpredicted function of DRS by releasing it from the MSC. Our structural study and PTM analyses extend the knowledge about the interaction of components in the MSC and provide fundamental information for human physiological signaling pathways related to the MSC.

ACKNOWLEDGMENTS

The authors thank the staff members of the BL-5A at the Photon Factory (Tsukuba, Japan) and the BL-7A at the Pohang Accelerator Laboratory (Pohang, Korea), Euiyoung Bae, Sojin Moon, and Dong Hyun Ka for data collection.

REFERENCES

1. Normanly J, Abelson J. tRNA identity. Annu Rev Biochem 1989;58:1029–1049.
2. Eriani G, Delarue M, Poch O, Gangloff J, Moras D. Partition of tRNA synthetases into two classes based on mutually exclusive sets of sequence motifs. Nature 1990;347:203–206.
3. Scheper GC, van der Klok T, van Andel RJ, van Berkel CG, Sissler M, Smet J, Muravina TI, Serkov SV, Uziel G, Bugiani M, Schiffmann R, Krageloh-Mann I, Smeitink JA, Florentz C, Van Coster R, Pronk JC, van der Knaap MS. Mitochondrial aspartyl-tRNA synthetase deficiency causes leukoencephalopathy with brain stem and spinal cord involvement and lactate elevation. Nature Genet 2007;39:534–539.
4. Neuenfeldt A, Lorber B, Ennifar E, Gaudry A, Sauter C, Sissler M, Florentz C. Thermodynamic properties distinguish human mitochondrial aspartyl-tRNA synthetase from bacterial homolog with same 3D architecture. Nucleic Acids Res 2012;41:2698–2708.
5. Deutscher MP. The eucaryotic aminoacyl-tRNA synthetase complex: suggestions for its structure and function. J Cell Biol 1984;99:373–377.
6. Ray PS, Arif A, Fox PL. Macromolecular complexes as depots for releasable regulatory proteins. Trends Biochem Sci 2007;32:158–164.
7. Park SG, Ewalt KL, Kim S. Functional expansion of aminoacyl-tRNA synthetases and their interacting factors: new perspectives on housekeepers. Trends Biochem Sci 2005;30:569–574.
8. Robinson JC, Kerjan P, Mirande M. Macromolecular assemblage of aminoacyl-tRNA synthetases: quantitative analysis of protein-protein interactions and mechanism of complex assembly. J Mol Biol 2000;304:983–994.

9. Kaminska M, Havrylenko S, Decottignies P, Gillet S, Le Marechal P, Negrutskii B, Mirande M. Dissection of the structural organization of the aminoacyl-tRNA synthetase complex. J Biol Chem 2009;284:6053–6060.
10. Guzzo CM, Yang DC. Lysyl-tRNA synthetase interacts with EF1alpha, aspartyl-tRNA synthetase and p38 in vitro. Biochem Biophys Res Commun 2008;365:718–723.
11. Woese CR, Olsen GJ, Ibba M, Soll D. Aminoacyl-tRNA synthetases, the genetic code, and the evolutionary process. Microbiol Mol Biol Rev 2000;64:202–236.
12. Reed VS, Yang DC. Characterization of a novel N-terminal peptide in human aspartyl-tRNA synthetase. Roles in the transfer of aminoacyl-tRNA from aminoacyl-tRNA synthetase to the elongation factor 1 alpha. J Biol Chem 1994;269:32937–32941.
13. Reed VS, Wastney ME, Yang DC. Mechanisms of the transfer of aminoacyl-tRNA from aminoacyl-tRNA synthetase to the elongation factor 1 alpha. J Biol Chem 1994;269:32932–32936.
14. Cheong HK, Park JY, Kim EH, Lee C, Kim S, Kim Y, Choi BS, Cheong C. Structure of the N-terminal extension of human aspartyl-tRNA synthetase: implications for its biological function. Int J Biochem Cell Biol 2003;35:1548–1557.
15. Cavarelli J, Eriani G, Rees B, Ruff M, Boeglin M, Mitschler A, Martin F, Gangloff J, Thierry JC, Moras D. The active site of yeast aspartyl-tRNA synthetase: structural and functional aspects of the aminoacylation reaction. EMBO J 1994;13:327–337.
16. Vagin A, Teplyakov A. Molecular replacement with MOLREP. Acta Crystallogr D Biol Crystallogr 2010;66:22–25.
17. Emsley P, Lohkamp B, Scott WG, Cowtan K. Features and development of Coot. Acta Crystallogr D Biol Crystallogr 2010;66:486–501.
18. Murshudov GN, Vagin AA, Dodson EJ. Refinement of macromolecular structures by the maximum-likelihood method. Acta Crystallogr D Biol Crystallogr 1997;53:240–255.
19. Lovell SC, Davis IW, Arendall WB, 3rd, de Bakker PI, Word JM, Prisant MG, Richardson JS, Richardson DC. Structure validation by Calpha geometry: phi,psi and Cbeta deviation. Proteins 2003;50:437–450.
20. Krissinel E, Henrick K. Inference of macromolecular assemblies from crystalline state. J Mol Biol 2007;372:774–797.
21. Sauter C, Lorber B, Cavarelli J, Moras D, Giege R. The free yeast aspartyl-tRNA synthetase differs from the tRNA(Asp)-complexed enzyme by structural changes in the catalytic site, hinge region, and anticodon-binding domain. J Mol Biol 2000;299:1313–1324.
22. Messmer M, Blais SP, Balg C, Chenevert R, Grenier L, Lague P, Sauter C, Sissler M, Giege R, Lapointe J, Florentz C. Peculiar inhibition of human mitochondrial aspartyl-tRNA synthetase by adenylate analogs. Biochimie 2009;91:596–603.
23. Guo M, Yang XL, Schimmel P. New functions of aminoacyl-tRNA synthetases beyond translation. Nat Rev Mol Cell Biol 2010;11:668–674.
24. Ofir-Birin Y, Fang P, Bennett SP, Zhang HM, Wang J, Rachmin I, Shapiro R, Song J, Dagan A, Pozo J, Kim S, Marshall AG, Schimmel P, Yang XL, Nechushtan H, Razin E, Guo M. Structural switch of Lysyl-tRNA synthetase between translation and transcription. Molr Cell 2012;49:30–42.
25. Olsen JV, Vermeulen M, Santamaria A, Kumar C, Miller ML, Jensen LJ, Gnad F, Cox J, Jensen TS, Nigg EA, Brunak S, Mann M. Quantitative phosphoproteomics reveals widespread full phosphorylation site occupancy during mitosis. Science Signal 2010;3:ra3.

PLOS | ONE

RESEARCH ARTICLE

Structure and Stability of the Dimeric Triosephosphate Isomerase from the Thermophilic Archaeon *Thermoplasma acidophilum*

Sang Ho Park[1], Hyoun Sook Kim[1], Mi Seul Park[1], Sojin Moon[2], Mi Kyung Song[1], Han Su Park[1], Hyunggu Hahn[1], Soon-Jong Kim[3], Euiyoung Bae[2], Hyun-Jung Kim[4], Byung Woo Han[1]*

1 Research Institute of Pharmaceutical Sciences, College of Pharmacy, Seoul National University, Seoul, Korea, **2** Department of Agricultural Biotechnology, Seoul National University, Seoul, Korea, **3** Department of Chemistry, Mokpo National University, Chonnam, Korea, **4** College of Pharmacy, Chung-Ang University, Seoul, Korea

* bwhan@snu.ac.kr

Citation: Park SH, Kim HS, Park MS, Moon S, Song MK, Park HS, et al. (2015) Structure and Stability of the Dimeric Triosephosphate Isomerase from the Thermophilic Archaeon *Thermoplasma acidophilum*. PLoS ONE 10(12): e0145331. doi:10.1371/journal.pone.0145331

Editor: Titus J. Boggon, Yale University School of Medicine, UNITED STATES

Received: August 14, 2015

Accepted: December 2, 2015

Published: December 28, 2015

Data Availability Statement: Atomic coordinates and structure factors are available from the Protein Data Bank database (accession number 5CSR and 5CSS, http://www.rcsb.org/pdb/search/structidSearch.do?structureId=5csr, http://www.rcsb.org/pd /search/structidSearch.do?structureId=5css).

Funding: This work was supported by Ministry of Science, ICT and Future Planning of Korea; Grant number: NRF-2011-0030001 and NRF-2013M-3A6A-4043695 (Tumor Microenvironment Global Core Research Center and Global Frontier Project funded through the National Research Foundation). The

Abstract

Thermoplasma acidophilum is a thermophilic archaeon that uses both non-phosphorylative Entner-Doudoroff (ED) pathway and Embden-Meyerhof-Parnas (EMP) pathway for glucose degradation. While triosephosphate isomerase (TPI), a well-known glycolytic enzyme, is not involved in the ED pathway in *T. acidophilum*, it has been considered to play an important role in the EMP pathway. Here, we report crystal structures of apo- and glycerol-3-phosphate-bound TPI from *T. acidophilum* (TaTPI). TaTPI adopts the canonical TIM-barrel fold with eight α-helices and parallel eight β-strands. Although TaTPI shares ~30% sequence identity to other TPIs from thermophilic species that adopt tetrameric conformation for enzymatic activity in their harsh physiological environments, TaTPI exists as a dimer in solution. We confirmed the dimeric conformation of TaTPI by analytical ultracentrifugation and size-exclusion chromatography. Helix 5 as well as helix 4 of thermostable tetrameric TPIs have been known to play crucial roles in oligomerization, forming a hydrophobic interface. However, TaTPI contains unique charged-amino acid residues in the helix 5 and adopts dimer conformation. TaTPI exhibits the apparent T_d value of 74.6°C and maintains its overall structure with some changes in the secondary structure contents at extremely acidic conditions (pH 1–2). Based on our structural and biophysical analyses of TaTPI, more compact structure of the protomer with reduced length of loops and certain patches on the surface could account for the robust nature of *Thermoplasma acidophilum* TPI.

funders had no role in study design, data collection and analysis, decision to publish, or preparation of the manuscript.

Competing Interests: The authors have declared that no competing interests exist.

Abbreviations: TaTPI, triosephosphate isomerase from *Thermoplasma acidophilum*; PDB, Protein Data Bank; G3P, glycerol-3-phosphate.

Introduction

Triosephosphate isomerase (TPI or TIM) is a functionally and structurally well-known enzyme that plays a crucial role in glycolytic and gluconeogenic metabolism. TPI accurately and efficiently interconverts dihydroxyacetone phosphate (DHAP) and glyceraldehyde-3-phosphate (GAP). Missense mutations of TPI genes result in TPI deficiency through loss-of-function [1]. TPI deficiency has been known to cause metabolic diseases, glycolytic enzymopathies, in which neurological pathogenesis is uniquely severe [2]. Pathogenic TPI deficiency mutations dramatically affect TPI activity owing to either catalytic interruption or oligomeric state alteration [3–5].

Thermoplasma acidophilum is one of the most acidophilic organisms among known thermophilic archaea. It optimally grows at 55–60°C and pH 0.5–2. For glucose degradation, *T. acidophilum* has been known to utilize not only non-phosphorylative Entner-Doudoroff (ED) pathway but also canonical glycolysis/gluconeogenesis pathway (Embden-Meyerhof-Parnas pathway) [6]. Although one of the glycolysis/gluconeogenesis pathway enzymes, phosphofructokinase, has not been identified in *T. acidophilum*, TPI has been considered to play a crucial role in the glycolysis/gluconeogenesis pathway in *T. acidophilum*.

TPI is a representative α/β protein with eight α-helices and eight β-strands connected by loops, forming a TIM-barrel fold [7]. The active site of TPI is highly conserved in all kingdoms and located inside of the TIM-barrel fold with three catalytic residues (Lys9, His89, and Glu137 in TaTPI numbering). Most TPIs are optimally active in their dimeric forms. In contrast, archaeal TPIs that withstand high temperatures are tetrameric in their active states [8]. Thermostable proteins have been known to adapt to high temperature in various ways: increased electrostatic interactions, hydrogen bonds, and hydrophobic effects, resulting in fortified subunit contacts, more compact packing, higher oligomerization state, and two-state equilibrium reversibility [9–13].

In the Protein Data Bank (PDB), structures of one bacterial TPI (*Thermotoga maritima;* Tm) and three archaeal TPIs (*Pyrococcus woesei;* Pw, *Thermoproteus tenax;* Tt, and *Methanocaldococcus jannaschii;* Mj) that have been deposited are in tetrameric form. *P. woesei*, *M. jannaschii*, and *T. acidophilum* belong to Euryarchaeota and *T. tenax* is affiliated to Crenarchaeota in phylogeny. Among tetrameric TPIs in PDB, tetrameric conformation of bacterial TmTPI is maintained by disulfide bonds between two classical TPI dimers [8]. In archaeal TPIs, helix 4 and helix 5 in the tetrameric interface are of key importance for their tetrameric forms. Especially, helix 5 in thermostable TPIs has been considered as a major contributor for tetramer formation via dominant hydrophobic effects [14].

In this work, we report crystal structures of apo- and glycerol-3-phosphate (G3P)-bound TaTPI, each representing open and closed form. Unlike other thermostable archaeal TPIs, TaTPI forms a stable dimer in solution, which we confirmed using analytical ultracentrifugation and size-exclusion chromatography. We also show the effect of pH on the secondary structure and temperature-induced unfolding of TaTPI. Through systematic comparison of TaTPI with available dimeric and tetrameric TPIs, we suggest that TPI stabilization patches can be targeted for the design of more stable TIM-barrel fold proteins.

Materials and Methods

Cloning, expression, and purification of TaTPI and MjTPI

Full-length sequence of *Thermoplasma acidophilum* TPI (TaTPI, 216 amino acid residues) and *Methanocaldococcus jannaschii* TPI (MjTPI, 219 amino acid residues) were amplified using PCR and cloned into pET-28a(+) vector (Novagen) containing C-terminal His_6-tag. Cloned plasmid were transformed into *Escherichia coli* Rosetta 2(DE3)pLysS strain. Recombinant

proteins were overexpressed by adding 0.5 m*M* IPTG (isopropyl 1-thio-ß-D-galactopyranoside) at $O.D._{600nm}$ 0.5 and cells were further incubated at 20°C overnight (16 h) using Luria Broth culture media. Harvested cells were lysed by cell sonicator (SONICS) in lysis buffer (20 m*M* Tris-HCl, pH 7.5, 500 m*M* NaCl, 35 m*M* imidazole, and 1 m*M* PMSF (phenylmethylsulfonyl fluoride)). After incubation of cell lysate at 60°C for 10 minutes, cell debris and denatured proteins were removed by centrifugation at 35,000 xg for 50 minutes. Supernatant was applied to HiTrap Chelating HP column (GE Healthcare) for affinity chromatography. Loaded sample was eluted with elution buffer (20 m*M* Tris-HCl, pH 7.5, 500 m*M* NaCl, and 500 m*M* imidazole) following equilibration with washing buffer (20 m*M* Tris-HCl, pH 7.5, 500 m*M* NaCl, and 50 m*M* imidazole). Eluted sample was further purified by size-exclusion chromatography with HiLoad 16/600 Superdex 200 prep grade column (GE Healthcare) equilibrated with 20 m*M* Tris-HCl, pH 7.5, and 200 m*M* NaCl. Fractions containing TPI proteins were further purified by anion exchange chromatography with HiTrap Q HP column (GE Healthcare) after 2 X dilution of the fractions with 20 m*M* Tris-HCl, pH 7.5, and 100 m*M* NaCl. Linear gradient of 0–500 m*M* NaCl in 20 m*M* Tris-HCl, pH 7.5, was applied for elution. For the final purification step, second size-exclusion chromatography was performed with HiLoad 16/600 Superdex 200 prep grade column (GE Healthcare) equilibrated with 20 m*M* Tris-HCl, pH 7.5, and 200 m*M* NaCl for TaTPI or 50 m*M* HEPES (4-(2-hydroxyethyl)-1-piperazineethanesulfonic acid), pH 7.5, for MjTPI. For crystallization, purified TaTPI proteins were concentrated to 30 mg ml^{-1}.

Crystallization and structure determination

Initial crystals of apo-TaTPI were grown at 22°C by sitting drop vapor diffusion method with crystallization solution containing 2 *M* NaCl and 10% (w/v) polyethylene glycol 6000. Apo-TaTPI crystals suitable for diffraction data collection were grown at 4°C using hanging-drop vapor diffusion method after mixing apo-TaTPI proteins with 2 times volume of crystallization solution containing 0.5 *M* NaCl, 10% (w/v) polyethylene glycol 6000, and 0.1 *M* Tris-HCl, pH 8.5. Crystals of TaTPI in complex with glycerol-3-phosphate (G3P) were obtained from crystallization solution with 0.6 *M* NaCl, 9% (w/v) polyethylene glycol 6000, and 0.1 *M* Tris-HCl, pH 8.5, after incubating purified apo-TaTPI proteins with 20 m*M* G3P for 4 h at 4°C. For diffraction data collection, crystals were frozen in liquid nitrogen following cryoprotection by soaking TaTPI crystals in crystallization solution supplemented with 20% glycerol. X-ray diffraction data for apo- and G3P-bound complex TaTPI crystals were collected at BL-7A synchrotron beamline at the Pohang Light Source, Korea, and at BL-1A synchrotron beamline at the Photon Factory, Japan, respectively. Collected data were processed using *HKL*2000 program suite [15]. The crystal structure of apo-TaTPI was solved by molecular replacement method using MOLREP program [16], with the crystal structure of *Pyrococcus woesei* TPI (PDB ID: 1HG3) as a phasing model [14]. The crystal structure of G3P-bound TaTPI was solved with the apo-TaTPI structure as a phasing model. The initial model building was carried out by *WinCoot* program [17] and further refined with *REFMAC*5 program [18]. All refinement steps were monitored using R_{free} value based on 5.0% of independently saved reflections. The final model was evaluated with *MolProbity* program [19]. Data collection and refinement statistics are summarized in Table 1.

Analytical ultracentrifugation (AUC)

Equilibrium sedimentation studies were performed using Beckman ProteomeLab XL-A analytical ultracentrifuge in 20 m*M* Tris-HCl buffer, pH 7.5, and 200 m*M* NaCl at 20°C. Sedimentation data were collected at 280 nm using a six-sector cell at rotor speeds of 20,000 and 26,000 rpms with three different protein concentrations: 12.6 u*M* (0.31 mg ml^{-1}), 16.8 u*M* (0.41 mg ml^{-1}), and

Table 1. Statistics for data collection, phasing, and model refinement.

Data collection[a]	TaTPI	G3P-bound TaTPI
Space group	$P2_12_12_1$	$P2_12_121$
Cell dimensions		
a, b, c (Å)	75.49, 113.96, 114.80	72.63, 84.08, 143.54
α, β, γ (°)	90, 90, 90	90, 90, 90
Data set		
X-ray wavelength (Å)	1.0000	1.1000
Resolution (Å)[b]	50.00–1.94 (1.97–1.94)	50.00–2.17 (2.21–2.17)
Total / unique reflections	521,936 / 73,921	294,576 / 47,245
Mean *I/sigma(I)*	32.4 (3.3)	20.9 (3.0)
Multiplicity	7.1 (5.6)	6.2 (5.6)
Completeness (%)	99.0 (83.5)	99.9 (99.9)
R_{merge} (%)[c]	9.1 (62.5)	13.4 (59.0)
Refinement		
Resolution (Å)	50.00–1.94	50.00–2.17
R_{work}[d] / R_{free}[e] (%)	18.0 / 21.5	18.3 / 22.5
No. of non-hydrogen atoms / mean B-factor (Å^2)		
Protein	6,996 / 32.9	6,640 / 34.2
Water	561 / 39.8	401 / 34.4
Other atoms	28 / 40.1	44 / 22.9
Poor rotamers (%)[f]	0.1	0.3
Ramachandran plot analysis (%)		
Most favored regions	98.0	96.1
Additional allowed regions	2.0	3.4
Disallowed regions	0	0.5
R.m.s.d. from ideal geometry		
Bond lengths (Å)	0.019	0.015
Bond angles (°)	1.648	1.550

[a]Data collected at the synchrotron BL-7A at the Pohang Light Source and BL-1 at the Photon Factory.
[b]Numbers in parentheses indicate the highest resolution shell.
[c]$R_{merge} = \Sigma_h \Sigma_i |I(h)_i - \langle I(h) \rangle| / \Sigma_h \Sigma_i I(h)_i$, where $I(h)$ is the observed intensity of reflection h, and $< I(h) >$ is the average intensity obtained from multiple measurements.
[d]$R_{work} = \Sigma \, | |F_o| - |F_c| \, | / \Sigma |F_o|$, where $|F_o|$ is the observed structure factor amplitude and $|F_c|$ is the calculated structure factor amplitude.
[e]R_{free} = R-factor based on 5.0% of the data excluded from refinement.
[f]Values obtained using MolProbity.

doi:10.1371/journal.pone.0145331.t001

21.0 u*M* (0.52 mg ml^{-1}). All measured data fit well to a homogeneous dimer model and representative results measured at 26,000 rpm using 16.8 u*M* protein concentration are presented. TaTPI concentrations were calculated using e_{280nm} = 11,920 M^{-1}cm^{-1} and molecular weight of 24,671 daltons. Time required for the attainment of equilibrium was established by running at given rotor speed until scans were invariant for 4 hours: this was achieved at most by 36 hours in six-sector cells using 130 ul of samples. Partial specific volume of TaTPI protein and buffer density were calculated using Sednterp [20]. The calculated partial specific volume at 20°C was 0.7417 cm^3 g^{-1} and the buffer density was 1.00704 g cm^{-3}. For data analysis by mathematical modeling using non-linear least-squares curve fitting, following functions were used for homogeneous

(Eq 1) and interactive (Eq 2) models.

$$C_r = C_b exp[A_p M_p (r^2 - r_b{}^2)] + \varepsilon \quad \text{(Eq.1)}$$

$$C_r = C_b exp[A_p M_p (r^2 - r_b{}^2)] + C_b{}^n exp[Ink + nA_p M_p (r^2 - r_b{}^2)] + \varepsilon \quad \text{(Eq.2)}$$

$$A_p = (1 - v\rho)\omega^2 \div 2RT$$

where C_r is the total concentration at the radial position r, C_b is the concentration of protein at the cell bottom, M_p is the molecular weight of protein monomer, ε is a baseline error term, v and ρ are the partial specific volume and the solution density, respectively, and ω is the rotor angular velocity. The *In*k value is a natural log for equilibrium constants for reversible models (1x-nx, where n is 2 & 3) on an absorbance scale. Selection of the best model was made by examining numbers of weighted sum of square and root mean square error values. Further data manipulation and data analysis by mathematical modeling were performed using MLAB [21].

Circular dichroism (CD)

Temperature of maximum heat capacity (or half-denaturation temperature, Td) of TaTPI was measured by CD spectroscopy. Experimental sample was prepared following purification and concentration of TaTPI proteins to 0.4 mg ml^{-1} containing 50 m*M* HEPES, pH 7.5. CD traces of TaTPI were obtained at 222 nm using the J-1500 CD spectrometer (JASCO) at a scanning rate of 1°C min^{-1}. The denaturation curve of TaTPI was analyzed by Kaleidagraph (Synergy Software) based on John and Weeks's protocol [22].

Effect of pH variation on the secondary structure of TaTPI was also monitored by CD spectroscopy. pH of protein solutions containing 20 m*M* Tris-HCl and 200 m*M* NaCl was adjusted to desired values between pH 1.0 and pH 7.0 with HCl for CD measurements. The baseline signal was measured with a buffer containing 20 m*M* Tris-HCl, pH 7.5, and 200 m*M* NaCl. CD spectra of pH-titrated TaTPI were recorded and averaged over two scans between 200 to 260 nm using J-1500 CD spectrometer (JASCO). The secondary structure contents of TaTPI were calculated by Multivariate SSE Program (JASCO).

Analytical size-exclusion chromatography

Analytical size-exclusion chromatography of TaTPI was performed with Superdex 200 10/300 GL column (GE Healthcare) following equilibration with 20 m*M* Tris-HCl, pH 7.5, and 200 m*M* NaCl. The applied protein were at concentrations of 0.9 and 4.5 mg ml^{-1}. Standard proteins from Gel Filtration Standard (BIO-RAD) were applied to the column for calibration. The standard protein mixture contained thyroglobulin (M.W. 670 kDa), γ-globulin (M.W. 158 kDa), ovalbumin (M.W. 44 kDa), myoglobin (M.W. 17 kDa), and vitamin B_{12} (M.W. 1.35 kDa).

Differential scanning calorimetry (DSC)

Maximum temperature of heat capacity of MjTPI was measured with VP-DSC differential scanning microcalorimeter (Malvern). Experimental sample was prepared following purification and concentration of MjTPI proteins to 1.6 mg ml^{-1} (65 u*M*). Sample buffer containing 50 m*M* HEPES, pH 7.5, was loaded into the DSC cell after degassing in an evacuated chamber for 5 minutes and reference data were measured with scan rate of 0.5°C min^{-1}. Experimental temperature was increased in the range from 50 to 120°C. After sample buffer scan reached equilibrium, MjTPI proteins were carefully loaded into the cell following degassing and

experiments were performed under the same condition as for the reference. Heat capacity curve was plotted using the Origin software (Malvern).

Accession numbers

The structure coordinates and structure factors for apo- and G3P-bound TaTPI have been deposited in PDB under the accession code 5CSR and 5CSS, respectively.

Results and Discussion

Overall structures of apo- and glycerol-3-phosphate-bound TaTPI

The crystal structures of apo-TaTPI and its complex with glycerol-3-phosphate (G3P), an analogue of the substrate glyceraldehyde-3-phosphate, have been determined at 1.94 and 2.17 Å resolution, respectively. R_{work}/R_{free} values for the final models of apo- and G3P-bound TaTPI were 18.0%/21.5% and 18.3%/22.5%, respectively (Table 1). Crystal structures of apo- and G3P-bound TaTPI contain four copies of TaTPI monomer in the asymmetric unit, comprising two homodimers. The overall structure of TaTPI protomer confirms to the canonical TIM-barrel fold with eight α-helices and eight parallel β-strands from 216 amino acid residues (Fig 1A). The crystal structure of G3P-bound TaTPI reveals that G3P is well positioned at the active site of TaTPI with functionally conserved residues Lys9, His89, and Glu137 (Fig 1B). Glu137 is clearly demonstrated as a catalytic base, with its position being within 3 Å from O1 and O2 of G3P. An oxyanion hole, which contributes to the stabilization of transition state, is formed by NZ nitrogen of Lys9 and NE2 nitrogen of His89 with O2 oxygen of G3P. The phosphate group of G3P is perfectly coordinated through hydrogen bonds with backbone nitrogen atoms of Gly143, Gly175, Ala196, and Ser197 residues, including adjacent water molecules (S1 Fig).

Overall structures of apo- and G3P-bound TaTPI were similar with r.m.s.d. of 0.69 Å for 216 C_α positions, except G3P-bound area. The conformational changes in the loop 6 of ligand bound-TPIs have been reported in previously determined structures of TPIs from many species, including *Trypanosoma brucei*, *Gallus gallus*, *Geobacillus stearothermophilus*, *Leishmania mexicana*, and *Vibrio marinus* [12, 23–27]. Likewise, loop 6 located between β-strand 6 and helix 6 and loop 7 located between β-strand 7 and helix 7 showed remarkable conformational changes when G3P binds to apo-TaTPI. When compared with apo-TaTPI structure, Gly143 located in loop 6 and Gly175 located in loop 7 moved toward G3P by 8.3 and 3.8 Å, respectively (Fig 1B). Consequently, residue Ala174 is pushed to a disallowed region of the Ramachandran plot in the G3P-bound form, an amino acid residue within loop 7 that is displaced by the ligand binding. G3P binding triggers the conformational change and induces the transformation of TaTPI from open to closed form, securing the catalytic site from bulk solvent to maintain efficient catalytic activity. In addition, water molecules around the active site of apo-TaTPI are expelled from the active site and would be replaced with substrate upon substrate binding.

Unique dimeric conformation of TaTPI

T. acidophilum belongs to thermoacidophilic euryarchaeota and TaTPI also shares high amino acid sequence similarity to other thermostable TPIs from *P. woesei*, *T. tenax*, and *M. jannaschii*, all of which adopt tetrameric conformation that renders them stable at high temperatures [14, 28, 29]. Helix 4 and helix 5 of thermostable TPIs have been known to play important roles in the tetramer formation via hydrophobic interactions [14]. However, crystal structures of apo- and G3P-bound TaTPI form a dimer and reveal a remarkable difference in helix 5 of TaTPI from other thermostable TPIs. Helix 5 of TaTPI is mainly composed of charged-amino acid residues (AEEAKYFREY) instead of hydrophobic residues found in other thermostable

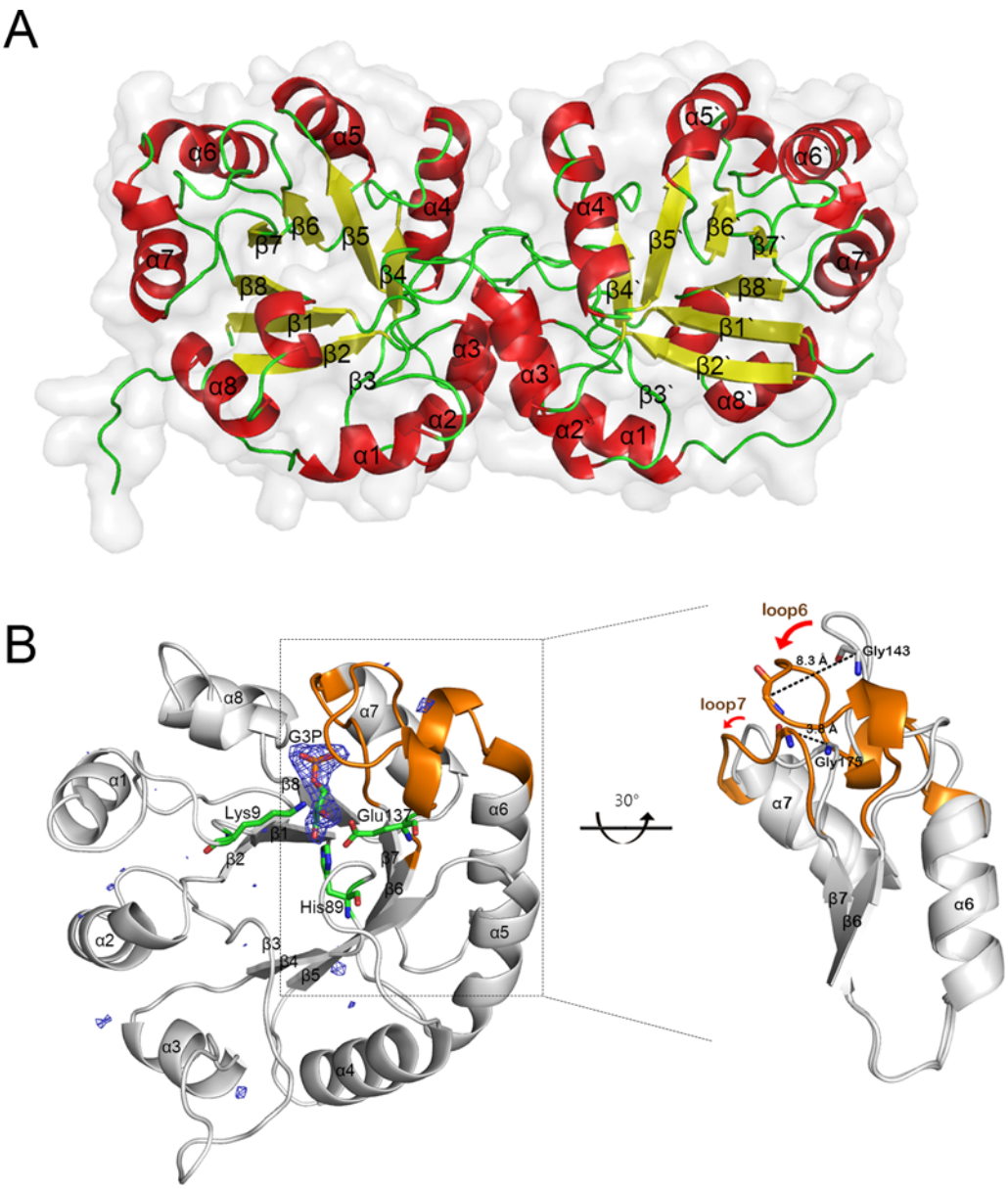

Fig 1. Overall structures of apo- and G3P-bound TaTPI. (A) Homodimer of apo-TaTPI is shown in carton representation, where α-helix, β-strand, and loop are colored in red, yellow, and green, respectively. (B) G3P-bound TaTPI. Only monomer of homodimeric G3P-bound TaTPI is demonstrated to emphasize a conformational change compared with apo-TaTPI. Extra positive electron density in F_o-F_c omit map contoured at 3.0 δ is shown as a blue mesh, which is modelled as G3P later. Amino acid residues interacting with G3P in catalytic site and G3P are shown as stick model; carbon, oxygen, phosphorus, and nitrogen atoms are colored in green, red, orange, and, blue, respectively. Loop 6 and loop 7 regions, which show a distinctive conformational change upon binding of G3P, are represented in orange and magnified for clarity.

doi:10.1371/journal.pone.0145331.g001

tetrameric TPIs. Structure-based sequence alignment of TaTPI with other TPIs shows that TaTPI resembles bacterial dimeric TPIs rather than tetrameric TPIs from thermostable archaea (Fig 2A).

Structural differences between TaTPI and other tetrameric archaeal TPIs are observed not only in helix 5 but also in adjacent α-helices. In tetrameric archaeal TPIs, the N-terminus of helix 4 and the C-terminus of helix 6 play important roles in tetrameric interaction via hydrophobic effects and hydrogen bonds [14]. The N-terminus of helix 4 of tetrameric archaeal TPIs

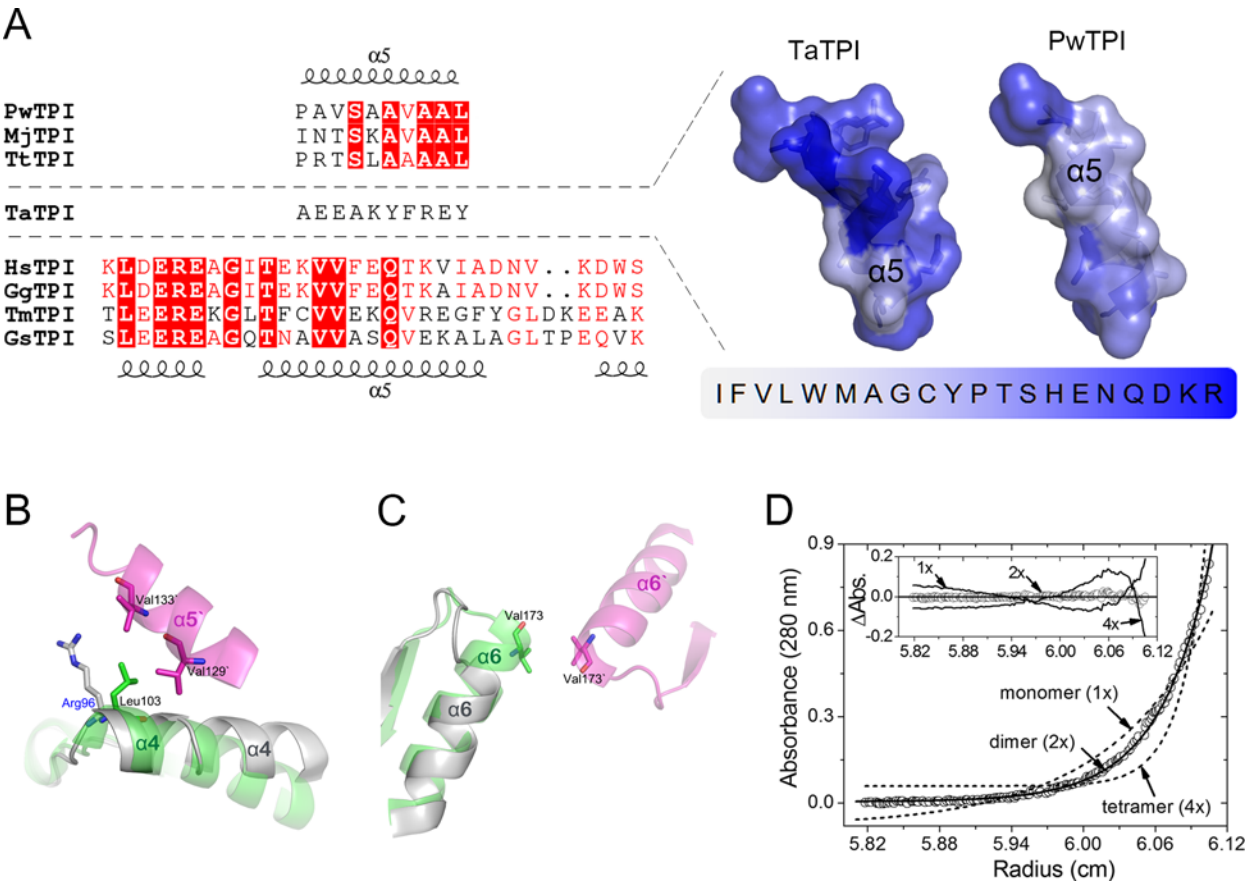

Fig 2. Dimeric conformation of TaTPI. (A) Structure-based sequence alignment of helix 5 region among TPIs from *Thermoplasma acidophilum* (TaTPI), *Pyrococcus woesei* (PwTPI), *Methanocaldococcus jannaschii* (MjTPI), *Thermoproteus tenax* (TtTPI), *Homo sapiens* (HsTPI), *Gallus gallus* (GgTPI), *Thermotoga maritima* (TmTPI), and *Geobacillus stearothermophilus* (GsTPI). Strictly conserved amino acid residues are highlighted in red shaded boxes and moderately conserved amino acid residues are colored in red. Helix 5 regions of TPIs from *Thermoplasma acidophilum* (PDB ID: 5CSR) and *Pyrococcus woesei* (PDB ID: 1HG3) are shown as cartoon representation with transparent surfaces, where amino acid residues are colored according to normalized consensus hydrophobicity scale [31]. (B) and (C) Structural comparison of helix 4 and helix 6 in TaTPI (gray) and PwTPI (green and magenta, each from different monomers). The important amino acid residues in tetrameric interface are shown as stick model. (D) Analytical ultracentrifugation experiment of TaTPI. Sedimentation equilibrium distribution (circle) of TaTPI at 26,000 rpm and 20°C is plotted as circle. Concentration of TaTPI was 16.8 u*M* (0.41 mg ml^{-1}) in 20 m*M* Tris-HCl, pH 7.5, and 0.2 *M* NaCl. Solid line is a fitting line for a homogeneous dimer (2x) model and dotted lines are fitting lines for homogeneous monomer (1x) and tetramer (4x) models. Calculated molecular weight for TaTPI monomer from its amino acid compositions is 24,671 daltons. Inset graph shows distributions of the residuals for homogeneous 1x, 4x (solid lines), and 2x (circle) models, respectively. The random distribution of the residuals for the 2x model indicates that TaTPI exists as homogeneous dimers in solution.

doi:10.1371/journal.pone.0145331.g002

contains conserved Leu (Leu103 in PwTPI numbering) that contributes to hydrophobic effects and hydrogen bonds with the other side of helix 4 and helix 5 for its tetrameric assembly. In the case of TaTPI, Leu in the N-terminus of helix 4 of tetrameric archaeal TPIs is replaced with Arg96, which deprives the hydrophobic effects for tetramer formation (Fig 2B). Furthermore, TaTPI has shorter helix 6 than that of tetrameric archaeal TPIs, resulting in dissipated hydrophobic effects between two C-termini from each helix 6 of its accompanying dimeric partner, Val173 in PwTPI (Fig 2C). Consequently, changes in amino acid composition of helix 5, thus in electrostatic surface, and slight modification of secondary structures in helix 4 and helix 6 seem to play subtle roles in dimer formation.

In the crystal structure of apo-TaTPI, Cys50 in helix 2 of each homodimer drew our attention since it interacts with the other Cys50 from adjacent TaTPI homodimer via sulfur-containing hydrogen bonds, not disulfide bonds. Thus, we needed to re-confirm the oligomeric

status of apo-TaTPI to make it sure whether the interaction of Cys-Cys is physiologically relevant or crystallographic artefact. To verify the oligomeric state of apo-TaTPI in solution, analytic ultracentrifugation analysis (AUC) was performed. Oligomeric state of apo-TaTPI in solution was investigated by equilibrium sedimentation technique at two speeds and three concentrations. Fig 2D shows the data and fits analyzed by using Eq. 1 for homogeneous 1x, 2x, and 4x models at ultracentrifugal speed of 26,000 rpm. The weighted root-mean-square errors (RMS) for the 1x and 4x fits were 5.01×10^{-2} and 6.90×10^{-2}, respectively. In contrast to these models, dimer (2x) model gave much improved RMS value of 7.93×10^{-3}. Residual distribution plot (Fig 2D inset) also supports that the apo-TaTPI forms dimer in solution. Analysis at 20,000 rpm (data not shown) also gave a better RMS value of 5.76×10^{-3} for 2x model than those for 1x (3.90×10^{-2}) and 4x (5.42×10^{-2}) models. Mixture or reversible models were also investigated but there was no indication of the possibility. Data analysis using the reversible model (Eq 2) gave large negative *In*k values for monomer-dimer (1x-2x) and monomer-trimer (1x-3x) models and much higher RMS values (~10^{-2}), so the reversible models for monomer-dimer (1x-2x) and monomer-trimer (1x-3x) equilibrium would not be the case for TaTPI. These results strongly indicate that apo-TaTPI exits as homogeneous dimer in solution. In addition, analytical size-exclusion chromatography results of apo-TaTPI, which were confirmed at two different TaTPI protein concentrations (0.9 and 4.5 mg ml^{-1}), also supported the dimeric conformation in solution (S2 Fig).

Structural stability of TaTPI under extreme condition

T. acidophilum thrives in harsh environments such as high temperature and extremely acidic condition. TaTPI is also expected to function correctly at high temperature or in very low pH condition when physiological barriers are affected by various stresses. To elucidate the structural stability of TaTPI in extremely acidic condition and at high temperature, we carried out circular dichroism (CD) spectroscopy experiments.

As for the structural stability of TaTPI in extremely acidic condition, secondary structure changes of pH-titrated TaTPI were monitored using CD spectroscopy. Normally, intracellular environment is well kept from extracellular stresses such as abrupt pH change. So, most of intracellular proteins experience normal physiological conditions and function accordingly. TaTPI maintained its folded structure under extremely acidic condition (pH 1–2) as in neutral pH range (S3 Fig). In the case of TaTPI, secondary structure contents under extremely acidic condition seem to change slightly with sustained folded structure. The content of α-helix in the TaTPI tends to increase with decreasing pH, whereas the content of β-strand decreases. These results suggest that TaTPI is designed to function normally even in cases of unexpected pH drop.

The temperature of maximum heat capacity (or half-denaturation temperature, Td) of TaTPI was measured by CD spectroscopy. The denaturation curve of TaTPI was analyzed by Kaleidagraph (Synergy Software) based on John and Weeks's protocol [22]. The Td value for TaTPI is 74.6°C (S4 Fig), which is comparable with that of TPI from *Geobacillus stearothermophilus* (GsTPI), a biological indicator for the validation of sterilization processes, (T_d: 76°C) [30]. In the case of GsTPI, a large number of prolines (5.2%), replacement of asparagine by histidine within the active site to prevent deamidation, the smallest cavity number and volume, and a large buried hydrophobic surface have been shown to contribute for the thermostability [12]. *Thermotoga maritima*, a hyperthermophilic bacterium, has been known to have TPI with the highest T_d value of 102°C [30], resulting from a large number of salt bridges and extensive hydrophobic patches from tetramer conformation [8]. Using DSC, we found the Td app value of MjTPI to be 107.1°C and it is the highest Td value among reported TPIs so far (Table 2; S5

Table 2. Half-denaturation temperatures of TPIs.

	The half-denaturation temperature (T_d,°C)	Reference
TaTPI	74°C	This manuscript
MjTPI	107°C	This manuscript
TmTPI	102°C	Alvarez et al., 1999 [30]
GsTPI	76°C	Alvarez et al., 1999 [30]
PfTPI	65°C	Gopal et al., 1999 [33]
HsTPI	55°C	Mainfroid et al., 1996 [34]
TbTPI	44°C	Borchert et al., 1993 [35]

Ta, *Thermoplasma acidophilum*; Mj, *Methanocaldococcus jannaschii*; Tm, *Thermotoga maritima*; Gs, *Geobacillus stearothermophilus*; Pf, *Plasmodium falciparum*; Hs, *Homo sapience*; Tb, *Trypanosoma brucei*.

doi:10.1371/journal.pone.0145331.t002

Fig). When compared with TPIs mentioned above, TaTPI has smaller number of prolines (4.2%), larger cavity volume, and less buried hydrophobic surface than GsTPI, nor does it adopt tetrameric conformation.

Proposal of TPI stabilization patches

TaTPI is composed of 216 amino acid residues and approximately 10% shorter in length than other TPIs from bacterial and eukaryotic species, which is a common feature in archaeal TPIs. According to the results of our structure-based sequence alignment for TPIs, helix 4, helix 5, and helix 6 are regions that mainly account for variation in amino acid composition, structural stability, and the oligomeric status of TPIs. To systematically validate the stabilization factors

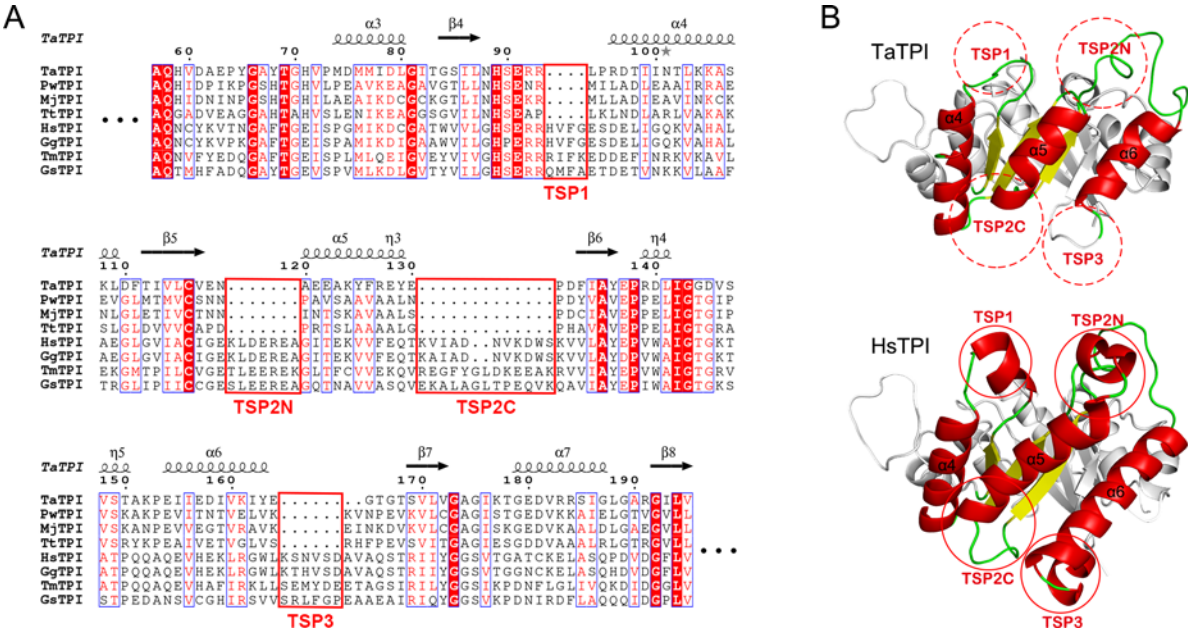

Fig 3. TPI stabilization patches (TSPs). (A) Structure-based sequence alignment of TaTPI with other TPIs from *Pyrococcus woesei* (PwTPI), *Methanocaldococcus jannaschii* (MjTPI), *Thermoproteus tenax* (TtTPI), *Homo sapiens* (HsTPI), *Gallus gallus* (GgTPI), *Thermotoga maritima* (TmTPI), and *Geobacillus stearothermophilus* (GsTPI). Strictly conserved amino acid residues are highlighted in red shaded boxes and moderately conserved amino acid residues are colored in red. Conserved residues are enclosed in blue boxes and TSP regions are enclosed in red boxes. The alignment figure was prepared using *ESPript* program [32]. (B) Structural comparison of TaTPI and HsTPI. The red dotted and solid circles represent TSP regions in TaTPI and HsTPI, respectively.

doi:10.1371/journal.pone.0145331.g003

of TaTPI, we name regions of distinctive differences as TPI stabilization patches (TSPs) (Fig 3A). TSP1 is helix 4 region and TaTPI lacks a short helical N-terminus in this patch. Consequently, TaTPI forms a more compact structure. TSP2 exhibits a major structural discrepancy in that 18 amino acid residues are missing in helix 5 region of TaTPI, compared with other dimeric TPIs. In TSP2 area, truncated helix 5 (TSP2C) and lack of a short helix in its N-terminus (TSP2N) also make TaTPI tighter in their overall structure. Lastly, TSP3 arises from helix 6 region and helix 6 is trimmed along with a short α-helix in its C-terminus (Fig 3B). All the TSPs of TaTPI contribute to the formation of more compact dimeric structure.

The TSPs are not exclusive of TaTPI. Other tetrameric archaeal TPIs also have the TSPs. We speculated that other tetrameric archaeal TPIs could be more thermostable than TaTPI since they adopt tetrameric conformation and contains TSPs. To validate our speculation, we cloned and purified *M. jannaschii* TPI (MjTPI), a tetrameric archaeal TPI, and measured the Td app value of MjTPI. The Td app value of MjTPI was 107.1°C, which is the highest Td app value among reported TPIs so far. The result suggest that both higher oligomerization status and the TSPs could be important factors for thermostability of TPIs. TaTPI would keep its structural and functional integrity at high temperature through a compact dimeric conformation from contributing TSPs. Crystal structures of apo- and G3P-bound TaTPI and defined stability determining factors of TPIs would provide clear insights on engineering more stable TIM-barrel fold proteins which make up a large protein family and play pivotal role in metabolic pathways.

Supporting Information

S1 Fig. Binding modes of G3P with key amino acid residues of TaTPI. LIGPLOT diagram is used for representation of active site in the G3P-bound TaTPI. Carbon, nitrogen, oxygen, and phosphorus atoms are shown in black, blue, red, and magenta, respectively. Hydrogen bonds and oxyanion hole between G3P and TaTPI are shown as green and red dotted line, respectively.
(TIF)

S2 Fig. Analytic size-exclusion chromatography of TaTPI. TaTPI protein samples at two different concentrations (A: 4.5 mg ml^{-1}, B: 0.9 mg ml^{-1}) were applied to Superdex200 10/300 GL column. Chromatograms of TaTPI and gel filtration standard were shown as blue and red lines, respectively.
(TIF)

S3 Fig. Circular dichroism spectra for TaTPI at variable pH conditions. (A) CD spectra of pH-titrated TaTPI (pH 1.0–7.0) were measured from 200 to 260 nm. (B) The secondary structure contents of pH-titrated TaTPI were calculated from Multivariate SSE Program (JASCO).
(TIF)

S4 Fig. Thermal denaturation curve of TaTPI. The black line represents baseline-subtracted and normalized raw data. The red line indicates the best fits of the raw data. The maximum temperature of heat capacity (T_d) was calculated according to the best fits of the raw data.
(TIF)

S5 Fig. DSC thermogram of MjTPI. The black circle represents baseline-subtracted and normalized raw data. The black line indicates the best fits of the raw data. The maximum temperature of heat capacity (T_d) was calculated based on the best fits of the raw data.
(TIF)

Acknowledgments

The authors thank the staff members of the BL-1A at the Photon Factory (Tsukuba, Japan) and the BL-7A at the Pohang Accelerator Laboratory (Pohang, Korea).

Author Contributions

Conceived and designed the experiments: SHP BWH. Performed the experiments: SHP MSP SM MKS HSP HH SJK EB. Analyzed the data: SHP HSK MSP SM MKS HSP HH SJK EB HJK BWH. Contributed reagents/materials/analysis tools: SHP MKS SJK BWH. Wrote the paper: SHP HH HJK BWH.

References

1. Schneider AS. Triosephosphate isomerase deficiency: historical perspectives and molecular aspects. Bailliere's best practice & research Clinical haematology. 2000; 13(1):119–40.
2. Celotto AM, Frank AC, Seigle JL, Palladino MJ. Drosophila model of human inherited triosephosphate isomerase deficiency glycolytic enzymopathy. Genetics. 2006; 174(3):1237–46. PMID: 16980388
3. Arya R, Lalloz MR, Bellingham AJ, Layton DM. Evidence for founder effect of the Glu104Asp substitution and identification of new mutations in triosephosphate isomerase deficiency. Hum Mutat. 1997; 10 (4):290–4. PMID: 9338582
4. Hollan S, Fujii H, Hirono A, Hirono K, Karro H, Miwa S, et al. Hereditary triosephosphate isomerase (TPI) deficiency: two severely affected brothers one with and one without neurological symptoms. Hum Genet. 1993; 92(5):486–90. PMID: 8244340
5. Daar IO, Artymiuk PJ, Phillips DC, Maquat LE. Human triose-phosphate isomerase deficiency: a single amino acid substitution results in a thermolabile enzyme. Proc Natl Acad Sci U S A. 1986; 83 (20):7903–7. PMID: 2876430
6. Ruepp A, Graml W, Santos-Martinez ML, Koretke KK, Volker C, Mewes HW, et al. The genome sequence of the thermoacidophilic scavenger Thermoplasma acidophilum. Nature. 2000; 407 (6803):508–13. PMID: 11029001
7. Wierenga RK. The TIM-barrel fold: a versatile framework for efficient enzymes. FEBS Lett. 2001; 492 (3):193–8. PMID: 11257493
8. Maes D, Zeelen JP, Thanki N, Beaucamp N, Alvarez M, Thi MH, et al. The crystal structure of triosephosphate isomerase (TIM) from Thermotoga maritima: a comparative thermostability structural analysis of ten different TIM structures. Proteins. 1999; 37(3):441–53. PMID: 10591103
9. Xiao L, Honig B. Electrostatic contributions to the stability of hyperthermophilic proteins. Journal of molecular biology. 1999; 289(5):1435–44. PMID: 10373377
10. Dams T, Auerbach G, Bader G, Jacob U, Ploom T, Huber R, et al. The crystal structure of dihydrofolate reductase from Thermotoga maritima: molecular features of thermostability. Journal of molecular biology. 2000; 297(3):659–72. PMID: 10731419
11. Szilagyi A, Zavodszky P. Structural differences between mesophilic, moderately thermophilic and extremely thermophilic protein subunits: results of a comprehensive survey. Structure. 2000; 8(5):493–504. PMID: 10801491
12. Delboni LF, Mande SC, Rentier-Delrue F, Mainfroid V, Turley S, Vellieux FM, et al. Crystal structure of recombinant triosephosphate isomerase from Bacillus stearothermophilus. An analysis of potential thermostability factors in six isomerases with known three-dimensional structures points to the importance of hydrophobic interactions. Protein science: a publication of the Protein Society. 1995; 4 (12):2594–604.
13. Romero-Romero S, Costas M, Rodriguez-Romero A, Alejandro Fernandez-Velasco D. Reversibility and two state behaviour in the thermal unfolding of oligomeric TIM barrel proteins. Physical chemistry chemical physics: PCCP. 2015; 17(32):20699–714. doi: 10.1039/c5cp01599e PMID: 26206330
14. Walden H, Bell GS, Russell RJ, Siebers B, Hensel R, Taylor GL. Tiny TIM: a small, tetrameric, hyperthermostable triosephosphate isomerase. Journal of molecular biology. 2001; 306(4):745–57. PMID: 11243785
15. Otwinowski Z, Minor W. Processing of X-ray diffraction data collected in oscillation mode. Methods Enzymol. 1997; 276:307–26.
16. Vagin A, Teplyakov A. Molecular replacement with MOLREP. Acta Crystallogr D Biol Crystallogr. 2010; 66(Pt 1):22–5. doi: 10.1107/S0907444909042589 PMID: 20057045

17. Emsley P, Lohkamp B, Scott WG, Cowtan K. Features and development of Coot. Acta Crystallogr D Biol Crystallogr. 2010; 66(Pt 4):486–501. doi: 10.1107/S0907444910007493 PMID: 20383002
18. Murshudov GN, Vagin AA, Dodson EJ. Refinement of macromolecular structures by the maximum-likelihood method. Acta Crystallogr D Biol Crystallogr. 1997; 53(Pt 3):240–55. PMID: 15299926
19. Lovell SC, Davis IW, Arendall WB 3rd, de Bakker PI, Word JM, Prisant MG, et al. Structure validation by Calpha geometry: phi,psi and Cbeta deviation. Proteins. 2003; 50(3):437–50. PMID: 12557186
20. Laue TM. Sedimentation equilibrium as thermodynamic tool. Methods Enzymol. 1995; 259:427–52. PMID: 8538465
21. Knott GD. Mlab—a mathematical modeling tool. Comput Programs Biomed. 1979; 10(3):271–80. PMID: 527325
22. John DM, Weeks KM. van't Hoff enthalpies without baselines. Protein science: a publication of the Protein Society. 2000; 9(7):1416–9.
23. Zhang Z, Sugio S, Komives EA, Liu KD, Knowles JR, Petsko GA, et al. Crystal structure of recombinant chicken triosephosphate isomerase-phosphoglycolohydroxamate complex at 1.8-A resolution. Biochemistry. 1994; 33(10):2830–7. PMID: 8130195
24. Alvarez M, Zeelen JP, Mainfroid V, Rentier-Delrue F, Martial JA, Wyns L, et al. Triose-phosphate isomerase (TIM) of the psychrophilic bacterium Vibrio marinus. Kinetic and structural properties. The Journal of biological chemistry. 1998; 273(4):2199–206. PMID: 9442062
25. Williams JC, Zeelen JP, Neubauer G, Vriend G, Backmann J, Michels PA, et al. Structural and mutagenesis studies of leishmania triosephosphate isomerase: a point mutation can convert a mesophilic enzyme into a superstable enzyme without losing catalytic power. Protein engineering. 1999; 12 (3):243–50. PMID: 10235625
26. Noble ME, Zeelen JP, Wierenga RK. Structures of the "open" and "closed" state of trypanosomal triosephosphate isomerase, as observed in a new crystal form: implications for the reaction mechanism. Proteins. 1993; 16(4):311–26. PMID: 8356028
27. Wierenga RK, Kapetaniou EG, Venkatesan R. Triosephosphate isomerase: a highly evolved biocatalyst. Cellular and molecular life sciences: CMLS. 2010; 67(23):3961–82. doi: 10.1007/s00018-010-0473-9 PMID: 20694739
28. Walden H, Taylor GL, Lorentzen E, Pohl E, Lilie H, Schramm A, et al. Structure and function of a regulated archaeal triosephosphate isomerase adapted to high temperature. Journal of molecular biology. 2004; 342(3):861–75. PMID: 15342242
29. Gayathri P, Banerjee M, Vijayalakshmi A, Azeez S, Balaram H, Balaram P, et al. Structure of triosephosphate isomerase (TIM) from Methanocaldococcus jannaschii. Acta Crystallogr D Biol Crystallogr. 2007; 63(Pt 2):206–20. PMID: 17242514
30. Alvarez M, Wouters J, Maes D, Mainfroid V, Rentier-Delrue F, Wyns L, et al. Lys13 plays a crucial role in the functional adaptation of the thermophilic triose-phosphate isomerase from Bacillus stearothermophilus to high temperatures. The Journal of biological chemistry. 1999; 274(27):19181–7. PMID: 10383424
31. Eisenberg D, Schwarz E, Komaromy M, Wall R. Analysis of membrane and surface protein sequences with the hydrophobic moment plot. Journal of molecular biology. 1984; 179(1):125–42. PMID: 6502707
32. Robert X, Gouet P. Deciphering key features in protein structures with the new ENDscript server. Nucleic acids research. 2014; 42(Web Server issue):W320–4. doi: 10.1093/nar/gku316 PMID: 24753421
33. Gopal B, Ray SS, Gokhale RS, Balaram H, Murthy MR, Balaram P. Cavity-creating mutation at the dimer interface of Plasmodium falciparum triosephosphate isomerase: restoration of stability by disulfide cross-linking of subunits. Biochemistry. 1999; 38(1):478–86. PMID: 9890931
34. Mainfroid V, Terpstra P, Beauregard M, Frere JM, Mande SC, Hol WG, et al. Three hTIM mutants that provide new insights on why TIM is a dimer. Journal of molecular biology. 1996; 257(2):441–56. PMID: 8609635
35. Borchert TV, Pratt K, Zeelen JP, Callens M, Noble ME, Opperdoes FR, et al. Overexpression of trypanosomal triosephosphate isomerase in Escherichia coli and characterisation of a dimer-interface mutant. European journal of biochemistry / FEBS. 1993; 211(3):703–10.